IMPERIAL COLLEGE LONDON

SIMULATION OF ULTRASONIC MONITORING DATA TO IMPROVE CORROSION CHARACTERISATION WITHIN HIGH TEMPERATURE ENVIRONMENTS

by

Andrew John Christopher Jarvis

A thesis submitted to the Imperial College London for the degree of

Doctor of Philosophy

Department of Mechanical Engineering
Imperial College London
London SW7 2AZ

March 2013

Declaration of Originality

The content of this thesis is the result of independent work carried out by myself under the supervision of Dr. Frederic Cegla. Appropriate references have been provided wherever use has been made of the work of others.

Andrew Jarvis

06/03/2013

Abstract

Practical applications which involve analyzing how waves scatter from objects with complex shapes span countless scientific and engineering disciplines. Having been the focal point of much research over the past century, many different techniques for simulating such interactions are in common use throughout literature; however there is still an opportunity to improve upon the balance between accuracy and efficiency offered by the most commonly implemented methods. A simulation based on the scalar wave distributed point source method is proposed, exhibiting a large improvement in computational efficiency when compared to the finite element method, and providing greater accuracy than the Kirchhoff approximation by including phenomena such as multiple scattering, surface self-shadowing and edge diffraction. The technique is applied to the problem of simulating how ultrasonic pulses reflect from rough surfaces; the practical application being wall thickness monitoring in high temperature and corrosive environments. Results show that the reflected pulse can take any number of forms, depending on the specific shape of the scattering surface, which can have a dramatic impact on the accuracy of the thickness measurement. Conclusions are drawn about the stability of various time of flight algorithms under conditions of increasing surface roughness. Potential thickness error metrics are also proposed with the aim of estimating measurement uncertainty based on signal shape change. The great efficiency of the simulation technique is further demonstrated by applying it to three dimensional scattering scenarios which would be impossible to carry out using any other method, leading to the proposal of a correction procedure capable of converting results gained in two dimensional geometries to more closely resemble three dimensional results based on the specific transducer and rough surface characteristics. Simulation validation is carried out by comparison to experimental results in both two dimensional and three dimensional scattering scenarios, showing agreement within the experimental error bounds of the shear horizontal ultrasonic waveguide transducers used by the wall thickness sensor. Alternative high temperature structural degradation monitoring applications are also proposed and experimentally verified using an array of waveguide transducers, providing inspection solutions for thermal fatigue crack growth and hydrogen attack.

Acknowledgements

Firstly, I would like to thank my supervisor Dr. Frederic Cegla. Without his email 4 years ago I would never have started this journey and his infectious optimism really helped me during times when felt all was not going to plan! His constant guidance and ingenuity have taught me a lot more than I could ever hope to summarize within this thesis, and it certainly wouldn't have been as enjoyable without his friendship. On that same note I am thankful to all the members of the NDE lab who I have had the pleasure of working with throughout my time here. I will always remember our adventures at QNDE conferences in San Diego, Burlington and Denver which would not have been half as fun or useful without you all! Much credit for this must go to Professor Peter Cawley and Professor Mike Lowe for creating such a fantastic working environment, with the facilities to back up the research being undertaken.

My special thanks go to Attila Gajdacsi, not only for providing much of the data presented in Chapter 7, but also for his constant endeavor for the utmost precision and the countless valuable and challenging discussions I had with him throughout my PhD. Early guidance provided by Dr. Tim Hutt and Dr. Jake Davies was also instrumental in much of my subsequent research. The machining talents of Mr. Philip Wilson and Mr. Guljar Singh must also be praised, without which I doubt any of my experiments would have produced results of any merit. The administrative skills of Miss. Nina Hancock have also made my journey through PhD much smoother than it may well have been!

Of the industrial partners I have had the pleasure of working with my special thanks go to Dr. Jon Allin and Dr. Peter Collins of Permasense Ltd. for providing me with the transducers on which my PhD is based, as well as the frequent opportunities to share my research and receive feedback on the most important avenues of research.

From E.ON I would like to thank Dr. Colin Brett, Mr. Gareth Hey and Mr. Jonathan Spence for entrusting me with their power plant during early prototype trials. From BP I would like to thank Mr. Mark Lozev and Mr. Hamed Bazaz for their frequent input from an industrial perspective, as well as providing various corroded samples.

I would also like thank my family. My Mum for her guidance and unwavering assurance that an educational studies PhD is exactly the same as a mechanical engineering PhD! My Dad who inspired me to get into engineering from a very early age, answering my constant barrage of questions with great patience. My older sister Claire and Chris for introducing me to my nephew Lennon. My twin Sian and Adam who have their first child on the way! And also Tammy for sticking with me throughout my PhD, even though we live 5000 miles apart and I'm not necessarily as interesting to talk to about my work as I think I am! To all of you I dedicate this thesis.

Contents

List of Figures

Nomenclature

α	'2D to 3D' correction factor
γ	Lamé's first parameter
δ_{ij}	Kronecker delta function
ϵ_{ij}	Strain tensor
θ	Incident / reflected angle
λ	Wavelength
λ_0	Correlation length
λ_s	Wavelength of sinusoidal surface
μ	Shear modulus (Lamé's second parameter)
ρ	Density
ρ_{ij}	Correlation coefficient between signals i and j
σ	RMS height
$\overline{\sigma}$	RMS height of average surface
σ_{ij}	Stress tensor
σ_d	Standard deviation
ϕ	Scalar potential
ψ	Acoustic pressure
ω	Angular frequency
a	Point source separation
a_w	Waveguide separation
A	Amplitude
c	Wave speed
C	Autocorrelation function
$\mathbf{C}_{ijkl}$	Elasticity tensor
$d_i, d(x)$	Random number deviation from population mean
$\mathbf{e}$	Unit vector
F_i	Body force per unit volume
G	Green's function
$h_i, h(x)$	Surface deviation from mean plane
$\mathbf{h}$	Vector potential
i	Imaginary variable ($\sqrt{-1}$)

Continued on next page...

– Continued from previous page

$I(i,j)$	Image amplitude at pixel (i,j)
k	Wavenumber
L_F	Fresnel length
L_c	Crack length
$\mathbf{n}$	Unit normal vector
p	probability density function
$\mathbf{r}$	Radial vector
r	Radial distance
r_s	Point source boundary offset
R	Reflection coefficient
s_{ij}	signal received on element i when transmitted from element j
S	Closed surface
t	Time
T	Wall thickness
$\mathbf{u}$	Displacement vector
$w_i, w(x)$	Weights of correlation function

Subscripts

inc	Incident field
L	Longitudinal waves
ref	Reference field
sct	Scattered field
T	Shear (transverse) waves

Abbreviations

BIE	Boundary integral equation
COD	Coefficient of determination
DPSM	Distributed point source method
DSP	Digital signal processing
EDM	Electric discharge machining
EP	Envelope peak detection
FA	First arrival
FEM	Finite element method
FFT	Fast Fourier transform
FMC	Full matrix capture
GMRes	Generalised minimum residual method
IFFT	Inverse fast Fourier transform
IQR	Interquartile range
NAC	Naphthenic acid corrosion
RMS	Root mean squared
SC	Sulphidic corrosion
SH	Shear horizontal
TFM	Total focussing method
TOF	Time of flight
TOFD	Time of flight diffraction
XC	Cross-correlation

Chapter 1

Introduction

1.1 Motivation

Ultrasound refers to acoustic and elastic waves with frequencies higher than the audible range of human hearing, typically ranging from 20kHz to several GHz. It is used in a wide range of medical and engineering applications from real-time three dimensional imaging of structures within the human body [1] to metal and polymer welding [2]. It is this versatility which make it such an important research topic within many scientific disciplines. The focus of the work presented within this thesis will be specifically on its use in the nondestructive evaluation (NDE) of engineering structures, a critical research area which has grown rapidly over the last half century, providing engineers with increasingly rapid, accurate, sensitive and economical means of inspecting structures.

Some of the earliest work utilizing ultrasonic waves for nondestructive testing of engineering structures was carried out during World War II by Firestone for detecting cracks in tank armour plating [3]. Called the 'Supersonic Reflectoscope' [4], the device applied a high frequency voltage to a quartz crystal to enact a small volume change. When coupled to a test specimen using a thin oil film, mechanical waves were transmitted into the specimen which would subsequently reflect from flaws and boundaries. By transmitting bursts of ultrasonic energy into the metallic structure and then displaying the returning echoes on an oscilloscope, an assessment could

be made about whether internal flaws were present or not. This was the earliest implementation of ultrasonic pulse-echo inspection and the fundamental principles of NDE devices using piezoelectric crystals remain largely unchanged to this day. What has changed dramatically however, is the sensitivity of the equipment and the analysis of the data.

The improvement of ultrasonic NDE equipment and its ability to detect smaller flaws, coupled with the development of fracture mechanics as an engineering discipline in the early 1970s lead to the emergence of quantitative nondestructive evaluation (QNDE) as an increasingly important area of research [5]. No longer were inspections aimed solely at detecting whether a defect was present or not, damage tolerant design meant that if a defect could be detected and quantitatively characterised in terms of length, size or severity, stress analysts could make informed decisions whether a structure was within safe operational limits. This is particularly important for in-service inspection of structures whose failure could cause considerable financial burden or loss of human life; for example aircraft, nuclear reactors and ageing civil infrastructure such as bridges, steam power plants and petrochemical processing plants.

Many of the challenges faced within the power generation industry are shared by refineries and chemical processing plants around the world; most notably high operating temperatures, aging equipment, high replacement costs and the requirement for greater efficiency in the face of increasing safety and reliability concerns [6]. As an example, within the UK, deregulation of the electricity market around 25 years ago has lead to power plants, which were originally designed for base load conditions, to be cycled much more rapidly to meet the demands of an increasingly competitive and fluctuating energy market. Known as two-shifting, this mode of operation subjects plants which have already surpassed their deign lives to operate extensively within the regimes where material fatigue and creep damage are of major concern [7, 8]. Failure mechanisms associated with the high temperature operating conditions experienced within power plant and refinery environments arise in a number of ways including creep, hydrogen attack, oxidation, thermal fatigue, low cycle fatigue and thermal shock [9]. Additional to these, there are also damage inducing mechanisms which work over a wider range of temperatures including atmospheric,

galvanic, acidic, biological and erosion corrosion [6, 10]. Oftentimes a number of these mechanisms occur in parallel, causing a multitude of defect morphologies including crevices, cracks, intergranular porosity, pitting and general corrosion causing pipe or pressure vessel wall thickness loss [10].

In an ideal world each inspection method would be tailored precisely to the defect morphology it is designed to detect and monitor in order to extract the maximum sensitivity from the equipment. However, because of the wide range of corrosion mechanisms at work within such environments, it is not always clear what morphology should be expected. As such, ultrasonic wall thickness measurement has become the most widely used NDE technique within the power generation and petrochemical industries as it is robust enough to provide quantitative and reliable measurements over a wide range of corrosion conditions. An example where such data is of great value is in estimating the remaining life of refinery furnace tubing which is coming to the end of its life and suspected of imminent creep rupture. Moss et al [11] describe a method of estimating the remaining life using material properties, temperature and wall thinning rate as inputs; the sensitivity of which is directly related to the accuracy of each of these measures. However, the difficulty in measuring the wall thickness of the in-service furnace reported in this study reflects the primary challenge faced when applying any NDE technique within such hostile environments: standard equipment cannot withstand high operating temperatures. For ultrasonic equipment, the limiting factor is often the Curie temperature (T_c) of the piezoelectric material, beyond which crystal depolarization occurs rendering the transducer useless. This generally limits the use of standard lead zirconate titanate (PZT) ceramics to a maximum temperature of approximately 200°C [12], well below that of the operational temperatures of power plants and refinery furnaces which tend to operate between 300 and 500°C.

There are two main solutions to this problem: non-contact solutions where all hardware is physically separated from the undesirable effects of temperature, or contact solutions which either strive to use piezoelectric materials with higher T_c values or introduce a mechanical connection between the PZT crystal and the workpiece in order to transmit ultrasound. Non-contact solutions cover a range of techniques [13]. Since the late 1970s electromagnetic acoustic transducers (EMATs) have been

developed and used in various applications including high accuracy thickness gauging [14]. However, the requirement for a low separation distance to the workpiece would still make them vulnerable to high temperatures, particularly those utilising permanent magnets which themselves have a maximum T_c in the region of 300°C. Lasers can also be used to generate ultrasonic waves by transient surface heating, as well as detect them through interferometry. Kruger et al demonstrate this by measuring wall thicknesses up to 100mm and 1250°C [15]; however, such systems are generally considered as less sensitive than equivalent piezoelectric devices, and are certainly much more expensive making them unsuitable for mass deployment within plant environments. Theoretically air coupled ultrasonic transducers could also be used to inspect high temperature components; however, the very large difference in specific acoustic impedances of solids and gases makes transmission and detection through metallic components difficult [16]. Achieving sufficient temperature isolation from very high temperature structures over short distances also make the approach unsuited to plant environments.

Solutions where a mechanical connection exists between the piezoelectric crystal come in two forms; those which alter the piezoelectric material to operate at high temperature or those which use a thermally isolating buffer rod. Kirk et al [17] focus on the former and describe the development of transducers constructed using lithium niobate ($LiNbO_3$) which has a T_c =1210°C. Early development focused on replicating ambient temperature designs; however, this approach led to unreliable and expensive transducers since the structure of the piezoelectric, backing block and front face layer became overcomplicated in order for the probes to be able to scan. To overcome this, monolithic arrays with far simpler structures were developed and tested with some success up to approximately 450°C [18, 19]; however, they suffer from complicated and lengthy bonding processes which failed under thermal cycling. The use of many different materials with varying thermal expansion coefficients within one transducer also leads to complications during construction and use at high temperature. Other major limitations to the commercial viability of transducers using $LiNbO_3$ are its low electromechanical coupling coefficient and its tendency to crack during cooling. Schmarje et al [20, 21] describes the development of 1-3 connectivity $LiNbO_3$ composites as a way of improving this by introducing a flexible matrix material. It was found that the electromechanical coupling coefficient of the

composite was roughly double that of crystalline $LiNbO_3$ and that the material was more stable during thermal cycling; however, a reliable coupling method under fluctuating temperature conditions was still lacking. Kelly et al [22] report on a permanently installable TOFD system designed to monitor thermal fatigue crack growth which is constructed using modified sodium bismuth titanate (MNBT) for operation up to 600°C. Diffracted signal amplitudes measured using the probe on an EDM notch were found to be barely visible above the noise floor making crack length estimation unreliable, if not impossible.

Thermal isolation of conventional PZTs using buffer rods, also known as delay lines or waveguides, is an established method of producing ultrasonic transducers capable of measuring physical quantities within high temperature environments including fluid flow [23], component wall thickness for corrosion and crack detection [24–27] and simultaneous measurement of temperature and viscosity [28]. This simple method removes the need for matching thermal expansion coefficients of the transducer and specimen materials; however, it does create the need for a strong and often permanent coupling between the two since acoustic impedance matching coupling mediums such as gel can only be used at temperatures up to approximately 400°C. Cegla [29] describes the development of a waveguide transducer that transmits and receives shear horizontal (SH) waves and investigates the effect that different coupling methods have on the signal quality for thickness gauging purposes in pulse-echo and pitch-catch configurations. Results showed that a welded contact caused spurious signal reflections at the junction between the waveguide and the component introducing large amounts of coherent noise into the signals. Silver soldered contacts were found to perform better but had little signal consistency, even though the same process was carried out for each contact. Dry coupled contacts were found to perform the best, showing good consistency and little signal degradation at high temperatures and during thermal cycling, provided enough pressure was applied at the contact.

This waveguide transducer, whose working principles are described in detail in [26], was subsequently developed into a commercially available wall thickness monitoring sensor [30]. It operates by transmitting a 2MHz 5 cycle Hanning windowed toneburst into the high temperature environment via one waveguide, and then receiving the

pulse which has reflected from the inner surface of the wall along the other waveguide. An estimate of the wall thickness can subsequently be made by calculating the time of flight (TOF) of the pulse within the component wall and using it in conjunction with the ultrasonic wavespeed within the component material (see section 4.3.1). Thickness measurements and full waveforms are then relayed to operators using wireless data connectivity, very well suited to the complicated infrastructure encountered within industrial plant environments where access for inspection is difficult, dangerous and costly. The ability to survive operating temperatures in excess of 550°C and transmit data autonomously represent the major advantages of the sensor; continual wall thickness monitoring at a single location can be carried out, improving dramatically on the repeatability and data content previously offered by periodic inspections which could only be carried out during plant shut down.

The sensor is now established as an industry leader for providing wall thickness monitoring data within high temperature environments, and as such has been deployed in refineries around the world, providing data from many locations subject to a wide variety of corrosive conditions. By inspection of the waveforms recorded by many of the sensors it has become clear that a better understanding of the data is required. If corrosion proceeds in a general manner with approximately uniform wall loss in the vicinity of the sensor, little change in reflected signal shape would occur, it would simply be recorded earlier in time signifying a distance change to the inner surface. However, as described previously, corrosion can proceed through a multitude of different defect morphologies such as localised pitting causing isolated defects and areas or surface roughness. The changes these cause to the shape of the inner surface have a direct impact on the shape of the pulse which is received, and depending on how the TOF is extracted from the waveform, corrosion at the inner surface can have a potentially large impact on the error associated with the final wall thickness estimate. A particularly extreme example of an unexpected thickness trend is shown in figure 1.1 (c), alongside example signals used to calculate the wall thickness. The first pulse seen in Figs. 1.1 (a) and (b) is the surface skimming wave travelling directly from the transmitter to the receiver and the second pulse is the reflection from the inner surface (see Fig. **??**). The thickness was calculated using recorded waveforms using an envelope peak detection TOF algorithm (see section 4.3.1). It is clear that the shape of the reflection from the inner surface (or backwall

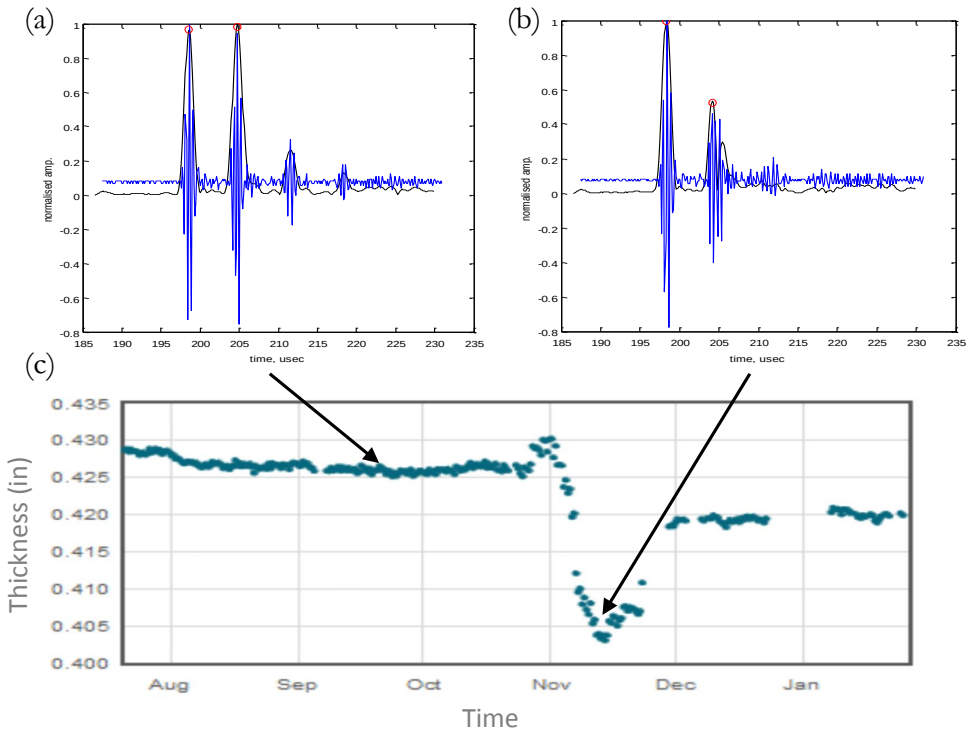

Figure 1.1: Ultrasonic signals recorded at a location showing an unexpected thickness trend in (a) September and (b) November. The first pulse seen within the recorded waveforms is the surface skimming wave and the second pulse is the reflection from the inner surface. (c) Thickness trend as calculated using the recorded waveforms using an envelope peak detection TOF algorithm. Reproduced under permission from Permasense Ltd.

reflection) changes between the dates shown which causes the calculated thickness to increase rapidly by 0.13mm at the end of October, then decrease by 0.7mm only to recover back to a steady wall thickness value of 10.7mm in December, 0.13mm below the value indicated in October. It is expected that corrosion induced surface roughness is the primary factor in determining these apparent errors in thickness measurement.

Although this is not an ideal situation in terms of thickness measurement accuracy based on the TOF algorithm used, it also presents an opportunity; if a relationship between roughness severity / defect size and pulse shape change exists, extra information about the nature of corrosion occurring within the pipe or pressure vessel could be extracted. To derive such a relationship, a simulated study would provide the ideal platform on which to mount an investigation. However, great challenges still exist when trying to accurately and efficiently simulate how ultrasound reflects

from rough surfaces, particularly for three dimensional geometries. Therefore one major objective of this thesis is to overcome these challenges and implement a simulation technique which can offer the required accuracy and efficiency to carry out such an investigation in both two dimensional and three dimensional geometries. In doing so, not only will the explanation of odd trends which are sometimes observed in field data be a priority; mitigating such trends through alternative signal processing techniques will be of primary importance, as well as distinguishing whether there is a way of quantitatively extracting an estimate of the shape of the inner surface based on the shape change of the reflected pulse. Such processing techniques are not possible during probe scanning inspection because much larger signal variability reduces sensitivity to small pulse shape changes, offering additional opportunities for detailed data analysis when using permanently installed sensors as opposed to data acquired during probe scanning.

As discussed previously, it is not only wall thickness loss which is of concern within the high temperature environments experienced within the power generation and petrochemical industries. Thermal fatigue cracks and bulk material degradation through the action of corrosion mechanisms such as hydrogen attack can also cause catastrophic failure. Therefore, another objective is to explore alternative ways of utilising the waveguide transducers to offer means of monitoring structural degradation processes other than wall thickness loss.

1.2 Outline of thesis

This thesis investigates how ultrasonic waves scatter from rough boundaries between materials with very different acoustic impedances. A semi-analytical mesh-free simulation method called the distributed point source method (DPSM) is applied to the problem and used in conjunction with the scalar wave approximation for SH wave scattering in order to produce a simulation technique which provides a better compromise between accuracy and efficiency than any other technique currently offers. The simulation is described in detail and verification of results is carried out using the finite element method (FEM) and experimental investigations for two dimensional and three dimensional geometries. Although focus is paid predominantly

to the application of wall thickness monitoring and the effect corrosion can have on the recorded signals, alternative usage of the high temperature waveguide transducers for monitoring other defect morphologies is also discussed and experimentally verified.

Chapter 2 introduces the governing equations of mechanical wave propagation within solid media, providing a general background to ultrasonic wave interaction along a boundary between two media. The specific problem of scattering along rough boundaries is then explored by reviewing the most commonly implemented techniques appearing within literature today, describing the different approaches and the challenges faced during selection and implementation. The numerical generation of rough surfaces with Gaussian distributed height and length characteristics is described in detail since they are used throughout the thesis to approximate surfaces which could be expected under the corrosive conditions considered. The different contributions within the scattered field from coherent and diffuse sources is then introduced to make the terminology used in the rest of the thesis clear.

The scalar wave DPSM is described in detail in Chapter 3, using the simplified two dimensional geometry of a sinusoidal surface for simulation validation using the FEM, and experimental verification using the waveguide transducers. A detailed comparison to classical Kirchhoff theory is also carried out in order to illustrate the strength of the DPSM over the most commonly implemented technique found in literature. Both monochromatic and time domain simulated cases are considered, showing that although the Kirchhoff approximation ignores phenomena such as multiple scattering, surface self shadowing and tip diffraction, it is the far-field assumption which makes it particularly unsuited to simulating scattering from comparatively large rough surfaces. The spatial frequency content of Gaussian distributed rough surfaces is also shown in order to assess the limits of roughness which are to be considered within this thesis.

The simulation is then applied to the practical problem of wall thickness monitoring in Chapter 4, with the primary goal of assessing how different TOF algorithms perform when confronted by signals reflecting from two dimensional rough surfaces. Three commonly used digital signal processing techniques for calculating TOF are tested: envelope peak detection, cross-correlation and threshold first arrival, indicat-

ing that under low roughness conditions cross-correlation shows the lowest variability and that threshold first arrival is the most stable under increasingly rough conditions. A number of signal quality metrics are also introduced as a way of estimating the most likely error in wall thickness measurement associated with a change in signal shape.

In order to gain a sufficient number of simulated signals to carry out the investigations in Chapter 4, the two dimensional geometry assumption had to be made, approximating a real rough surface as a corrugated (or furrowed) boundary, echoing the approach of a vast majority of literature. The shortcoming this assumption introduces to simulated data is tackled in Chapter 5 by applying the DPSM to a three dimensional rough surface geometry. Particular attention is paid to improving efficiency to ensure a simulation which can be completed within a reasonable timescale. Because of the comparatively large length scales of the scattering geometry being considered, simulation validation can only be carried out by comparison to experimental results, showing good agreement at two different locations above a surface with increasing roughness. Comparison between two dimensional and three dimensional simulated results is subsequently carried out, leading to the proposal of a correction factor capable of converting two dimensional results to more closely resemble those from a three dimensional rough surface given the transducer geometry and statistical properties of the surface being considered.

Chapter 6 focusses on pitted surfaces which cannot be characterized using Gaussian height and length scales, in particular use is made of the flat bottomed hole geometry as a simple approximation of a pitted defect. First, the limits of detection of the sensor are explored using singular localised defects of very small and large length scales; the small being manufactured at a micron scale using a micromachining laser and the large using a milling machine. Comparison is made to the DPSM simulation, again showing agreement within expected experimental error bounds. Then a simulated corrosion model is implemented to more closely approximate how rough and pitted surfaces might evolve over time, and the associated error in corrosion rate is assessed for each TOF algorithm. Similar conclusions are drawn as those for Gaussian distributed rough surfaces in terms of algorithm stability and the difficulty of performing inverse scattering with the limited data available within a single

ultrasonic signal.

The focus of Chapter 7 is therefore exploring applications where the extra information provided by multiple waveguide transducers could be exploited. Two applications are described in detail which use array geometries to monitor structural degradation mechanisms other than wall thickness loss. The first uses the multi total focussing method (TFM) to create an image of thermal fatigue cracks. Experimental validation on EDM notches shows that it performs well on defects of varying lengths and is able to survive temperature fluctuations greater than 500°C for a period of 6 months. This culminated in an opportunity to install a prototype on an operational steam power plant. The second application is the detection and monitoring of hydrogen attack through ultrasonic velocity reconstruction in the area below an array. A proof of concept experimental study was carried out using a transient two dimensional temperature distribution to assess whether the small changes in velocity expected during such bulk material degradation could be detected. Two imaging algorithms are applied, the Kaczmarz algorithm and the assumed distribution technique, both of which were found capable of detecting small velocity changes, providing estimates of distribution position and extent.

Chapter 8 summarizes the conclusions of the thesis. Suggestions of areas for future work are also provided.

Chapter 2

Basic Principles of Bulk Waves and Scattering

2.1 Introduction

The state of every surface of an object is by definition rough, from the microscopic scales caused by irregularities in material structure, up to the macroscopic scales. Applications which involve inspecting surfaces using waves span many scientific disciplines from elastic waves in solid bodies to electromagnetic waves in vacuum. Wave scattering caused by surface roughness can have a large impact on accuracy within such applications; the extent of which is directly related to the wavelength and the associated roughness scales being encountered. The complex nature of this scattering process and the need for detailed understanding has lead to many different simulation methods being proposed.

The aim of the material presented in this chapter is to provide the required background information to justify the work carried out within this thesis, and also to provide relevant information to support the discussion of results presented within the following chapters. First the basic principles of stress waves travelling within elastic media are presented, introducing the equations which must be solved when trying to understand how ultrasonic waves interact with rough boundaries. Then a discussion of approaches taken by others during the investigation of ultrasonic

wave scattering from rough boundaries is carried out, paying particular attention to the issues still faced in solving this very complex problem. Finally, the form of the rough surfaces predominantly being investigated within this thesis will be derived in detail. Much of the relevant literature has been described in my papers [31] and [32], therefore relevant excerpts have been included in the following sections.

2.2 Wave Propagation in Bulk Media

The motion of stress waves within solid media has been extensively studied and covered by many authors. For this reason, only a brief introduction will be provided at this point (see [33–35] for more information). In a Cartesian coordinate system and using tensor notation, the equation of linear momentum is given by

$$\sigma_{ij,j} + F_i = \rho \ddot{u}_i \tag{2.1}$$

Where σ_{ij} is the stress tensor, F_i is the body force per unit volume, ρ is the density of the medium and u represents particle displacement. The constitutive law can be used to relate stress and particle displacement which for any linear material can be written as

$$\sigma_{ij} = C_{ijkl}\varepsilon_{kl} \tag{2.2}$$

Where C_{ijkl} is the elasticity tensor which contains material constants and ε_{kl} is the strain tensor in the solid. If the material can be assumed isotropic Hooke's law is given by

$$\sigma_{ij} = \gamma \varepsilon_{kk}\delta_{ij} + 2\mu\varepsilon_{ij} \tag{2.3}$$

Where γ and μ are the Lamé constant of the material and δ_{ij} is the Kronecker delta function. For small deformation gradients, strain can be defined using the Cauchy strain tensor

$$\varepsilon_{ij} = \frac{1}{2}(u_{i,j} + u_{j,i}) \tag{2.4}$$

Naviers equation of motion is then obtained by substituting equations 2.3 and 2.4 into equation 2.1, assuming a homogeneous medium with uniform temperature in

the absence of body forces.

$$(\gamma + \mu)u_{j,ij} + \mu u_{i,jj} = \rho \ddot{u}_i \tag{2.5}$$

If we take the divergence of equation 2.5, we find that dilatational (longitudinal) motion must satisfy the equation

$$\ddot{\phi} = c_L^2 \phi_{,ii} \tag{2.6}$$

Where ϕ is a scalar potential and c_L is the longitudinal wave speed defined by

$$c_L = \sqrt{\frac{\gamma + 2\mu}{\rho}} \tag{2.7}$$

Similarly if we take the curl of equation 2.5, we find rotational (shear) motion must satisfy the equation

$$\ddot{h} = c_T^2 h_{i,jj} \tag{2.8}$$

Where h is a vector potential and c_T is the shear wave speed defined by

$$c_T = \sqrt{\frac{\mu}{\rho}} \tag{2.9}$$

Therefore, wave motion as described by equation 2.5 can be broken into two constituents that propagate at different velocities independent from one another within unbounded media. The displacement vector at any point within a field can thus be described as a summation of dilatational and rotational components.

$$u = \nabla\phi + \nabla \times h \tag{2.10}$$

Equation 2.10, written in vector notation, is known as the Helmholtz decomposition of the displacement vector. Coupling between wave modes only occurs at the boundaries between two different materials which can lead to mode conversion during reflection and refraction. In the simplest case of normal beam incidence, some of the energy will be reflected back into the medium from which it originated and some will be transmitted into the second medium. This leads to the definition of the normal beam incidence reflection coefficient which can be used to calculate

the amplitude change for an incident wave traveling from medium 1 to 2 which is subsequently reflected at the boundary.

$$R = \frac{\rho_2 c_2 - \rho_1 c_1}{\rho_1 c_1 + \rho_2 c_2} \tag{2.11}$$

This simple analysis only holds when the incident wave is perpendicular to the boundary, approaching from an angle can give rise to reflection, refraction and mode conversion. Snells law, most commonly associated with optical light waves, can be used to describe reflection and refraction angles of the incident waveform. However, unlike electromagnetic waves or waves traveling in fluids, solid materials can sustain waves with both longitudinal and shear components (see equation 2.10). This leads to mode conversion where longitudinal waves incident at a boundary can give rise to reflected and refracted shear waves and vice versa. This phenomenon can be visualized as a wave vector reaching a boundary at an angle. Considered on its own, this vector will give rise to a complicated wave field; however, it can be split into a normal component responsible for longitudinal wave propagation and a tangential component responsible for shear wave propagation. Snells law can still be used to calculate refracted angles for each wave type, ensuring the correct wave velocities are used (see pgs 44-49 of [34]). Figure 2.1 illustrates the polarization directions of the displacements which give rise to each type of reflected or refracted wave.

An important point to note is that in this context, shear waves refer to shear vertical waves which are polarized in the plane of wave propagation and displacements associated with shear horizontal (SH) waves occur perpendicular to this plane. Kino (pg 100 of [35]) highlights the case of SH wave reflection or refraction at a boundary which has a constant cross-sectional shape perpendicular to the plane of propagation as the only case where waves traveling within solids do not undergo mode conversion. No energy is lost as other modes meaning that the elastodynamic waves can be modelled as acoustic waves with a velocity equal to that of the SH wave. This is a powerful simplification which is strictly only valid when dealing with two dimensional reflection and refraction of SH waves which are polarized out of the plane; however, it will be the starting assumption for the modelling of the three dimensional situations considered in this thesis and its validity will be investigated by comparison to experimental results.

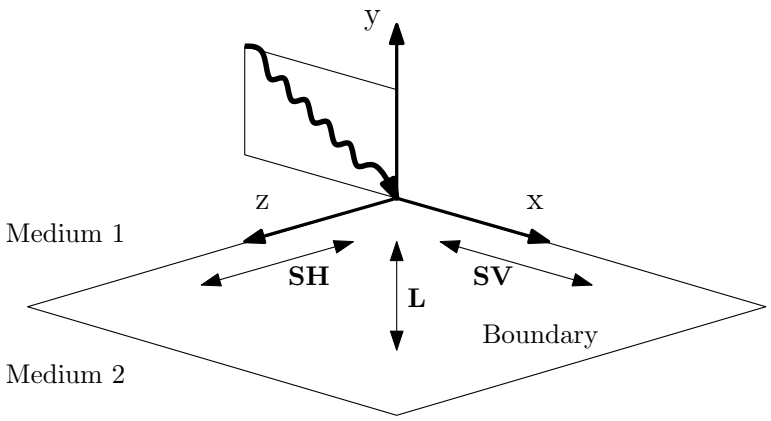

Figure 2.1: Polarization direction of displacements giving rise to longitudinal (L), shear vertical (SV) and shear horizontal (SH) waves.

2.3 Existing Techniques for Modeling Scattering at Rough Interfaces

In 1963 Uretsky described the reflection of plane waves from a sinusoidal boundary as a 'marvelously complex problem' [36]. This complexity has lead to many different models being proposed; what follows is a brief review of the literature (see for example [37–41] for more information). All scattering models are essentially attempting to solve the Helmholtz scattering integral over a closed surface S, which gives the total field ψ at a point $\mathbf{r'}$ away from the surface [42].

$$\psi(\mathbf{r}) = \psi^{inc}(\mathbf{r'}) + \int_S \left(G(|\mathbf{r'} - \mathbf{r}|) \frac{\partial \psi(\mathbf{r})}{\partial \mathbf{n}} - \psi(\mathbf{r}) \frac{\partial G(|\mathbf{r'} - \mathbf{r}|)}{\partial \mathbf{n}} \right) dS \tag{2.12}$$

where $\mathbf{n}$ is the unit inner normal at the surface, $\mathbf{r}$ is a point on the surface, $G(|\mathbf{r'} - \mathbf{r}|)$ is the free space Green's function and the second term in the equation represents the scattered field ψ^{sct}. Figure 2.2 illustrates the problem geometry. The method of solving equation 2.12 and the choice of Green's function depends on the shape of the surface and the application of the theory. Much of the early literature dis-

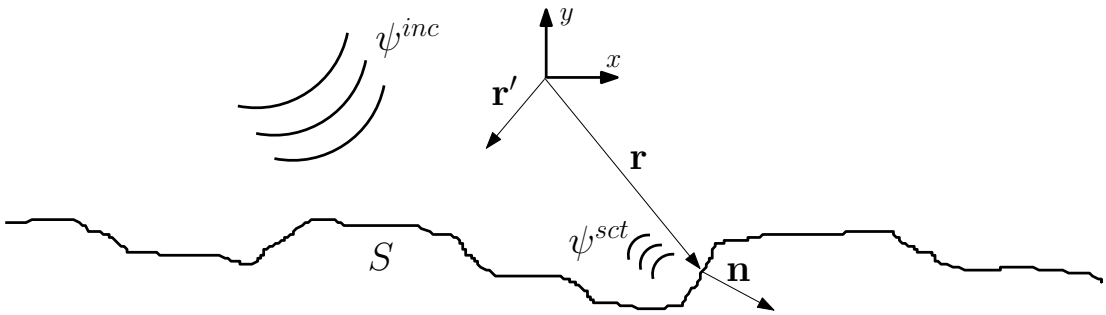

Figure 2.2: Problem geometry of wave scattering by a rough surface.

cussing the scattering of waves by periodic boundaries was concerned with reflection of acoustic waves from the surface of the sea which was assumed instantaneously sinusoidal. In 1878 Rayleigh proposed that the scattered wave from such a surface could be expressed as a sum of infinite plane waves travelling away from each point on the surface [43]. His assumption that this would hold at any point above the surface was heavily criticized making it valid only for small amplitude undulations; his initial method was subsequently altered by many. Marsh for instance generalised the theory and extended application to rough surfaces [44]. Uretsky sought to abolish both assumptions completely and in doing so created a mathematically more rigorous yet complex analytical solution for sinusoidal pressure release surfaces showing satisfactory agreement with experimental results performed by Barnard et al [36, 45].

Today, solutions to the problem of rough surface scattering can be broadly split into two main categories; those which use approximations to simplify analytical scattering models and those requiring no approximation which include numerical and boundary integral equation (BIE) methods. In the absence of sufficient computational capabilities, the majority of early literature focussed on approximate analytical solutions which aimed to reduce complexity, all be it at the cost of accuracy. Elfouhaily and Guérin [39] estimate that over twenty different models exist in literature with little information pertaining to the conditions under which each can be applied and assumed valid. Kirchhoff theory, which is one of the most commonly implemented, approximates the derivative of the wavefield along the boundary by assuming that at each point the reflecting surface acts as an infinite plane reflector with an orientation equal to that of the boundary. Splitting scattered field con-

tributions up in this manner represent the main drawback of this and many other approximate analytical solutions to the scattering integral: any components which have interacted with the boundary multiple times are not calculated. Without alteration phenomena such as surface self-shadowing and diffraction are also generally not well modeled using such approaches, limiting the levels of surface roughness which can be investigated. Information regarding the validity of the Kirchhoff approximation can be found in [46, 47].

Numerical techniques such as the finite element method (FEM) require no assumptions to be made about the field along the reflecting boundary, making the solution exact within stability limits representing their main advantage over approximate analytical techniques. Field variables are calculated at many nodal points making up a mesh which discretises the entire region of interest, often including absorbing boundaries to damp out any unwanted reflections. Zhang et al [48] apply the efficient frequency domain FEM model described by Velitchko et al [49] to the calculation of the far field scattering matrix of longitudinal waves from rough defects and comparing results when using the Kirchhoff approximation. Constructing the mesh only within the near field of the defect and using absorbing boundaries in the method described improves efficiency over the standard FEM; in general however, any method requiring mesh generation around defects still requires greater computational effort than those which calculate field variables only along the boundaries. For three dimensional scattering these computational requirements are particularly apparent, making numerical methods unsuitable for some of the investigations carried out in this thesis.

The final approach to solving equation 2.12 involves formulating a BIE based on the boundary conditions on a rough surface between two homogeneous media which can either be solved directly or by optimizing the solution from a set of fictitious point sources [41]. Direct solution of the analytical expression at a rough boundary is incredibly complex and as such no widely implemented solutions exist. DeSanto [50] presents a BIE for scalar wave scattering from infinite rough surfaces using the analytical expressions in their exact form, finding that the solution reduces down to that expected from a planar reflector at the flat surface limit. However, for Dirichelet boundary conditions it was found that a hypersingular integral equation

results, making the algebra far more complex. Specifying an incident plane wave also makes the approach unsuitable for the investigations carried out in this thesis. A method was thus developed using the distributed point source method (DPSM) [51] which solves the BIE through semi-analytical means by specifying fictitious point sources which are in close proximity to the boundaries.

Initially proposed by Placko and Kundu in 2000, the DPSM is a semi-analytical simulation technique which has been developed to model magnetic, electrostatic, electromagnetic and ultrasonic problems [51]. It operates by placing point sources within close proximity to boundaries; by using the known boundary conditions the complex amplitudes of these point sources can be calculated which are subsequently used to propagate the wavefield to any set of target points within the problem domain. Using the analytical solution of a point source directly in this manner avoids meshing, improving computational efficiency when compared with fully meshed numerical techniques, particularly when considering large three dimensional problem geometries or long time scales. To the authors knowledge the technique has never previously been applied to the problem of rough surface scattering, an application which has been identified through work presented in this thesis as benefitting greatly from the accuracy and efficiency offered by the technique. More information regarding its development by others can be found in section 3.2

2.4 Numerical Creation of Rough Surfaces

A considerable amount of literature exists describing different types of rough surface and methods of numerically generating their shape and a full review is outside the scope of this thesis. The interested reader is referred to [41, 52, 53] for further information. The corrosive processes forming the surfaces investigated in this thesis are assumed to progress as a collection of random events which, over a long enough time scale, combine to obey Gaussian statistics. This is the case even if the localised events do not follow such statistics [54]. In its simplest form the probability density function of the surface height h along the surface is given by equation 2.13

$$p\left(h_i\right) = \frac{1}{\sigma\sqrt{2\pi}} \exp\left(\frac{-h_i^2}{2\sigma^2}\right) \tag{2.13}$$

where $h_i = h(x_i) = h(i\Delta x)$, Δx is a small interval along the surface and σ is the RMS height controlling the vertical deviation of the surface from the mean plane [42]. In order to numerically generate such a surface, first a set of $2N+1$ uncorrelated random numbers with a Gaussian distribution are be generated whose heights are described by equation 2.14

$$\sigma_d^2 = \frac{1}{2N+1} \sum_{i=-N}^{N} d_i^2 \tag{2.14}$$

where σ_d is the standard deviation of the random numbers with deviations from the mean plane described by d_i. Matlab [55] was used to generate these numbers using a multiplicative congruential generator in conjunction with specified seed values in order to create repeatable surface shapes. These numbers are subsequently subjected to a moving average process to form features along the length of the surface using a Gaussian weighted function $C(x)$, defined using the correlation length λ_0.

$$C(x) = \frac{\langle h(x_0)\, h(x_0+x)\rangle}{\langle h^2\rangle} = \exp\left(\frac{-x^2}{\lambda_0^2}\right) \tag{2.15}$$

The correlation length is specified as the distance at which the correlation function has reduced to a value of e^{-1}. For a given set of $2M+1$ elements within vector d, the value in the final rough surface at x_i is given by equation 2.16

$$h_i = \sum_{j=-M}^{M} w_j d_{j+i} \tag{2.16}$$

Where M is linked to the correlation length through $M = 4\lambda_0/(\Delta x\sqrt{2})$, and w_j describe the weights of the Gaussian weighted function which are normalized according to equation 2.17

$$\sum_{j=-M}^{M} w_j = 1 \tag{2.17}$$

which have the form described in equation 2.18

$$w_j = \exp\left(\frac{-2(j\Delta x)^2}{\lambda_0^2}\right) \tag{2.18}$$

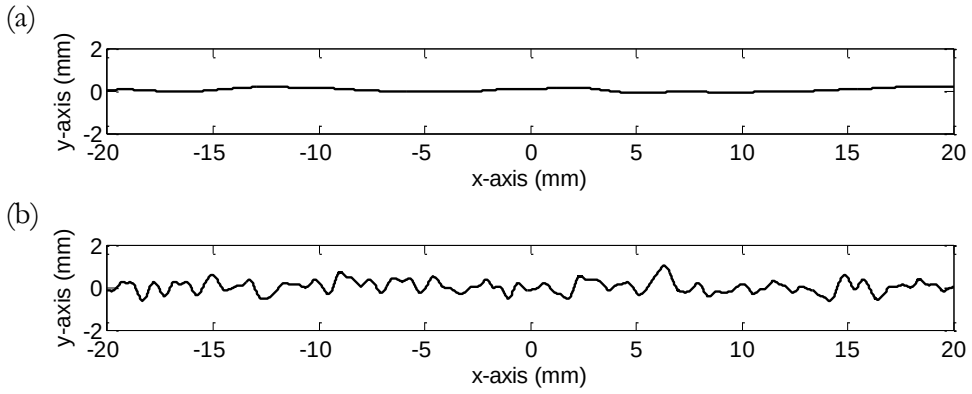

Figure 2.3: Rough surfaces with Gaussian height and length characteristics when (a) σ=0.1mm (λ/16) and λ_0=2.4mm (3λ/2), (b) σ=0.3mm ($\sim \lambda/5$) and λ_0=0.4mm (λ/4).

The RMS height of the final surface is then related to the standard deviation of the uncorrelated random numbers (σ_d) through equation 2.19

$$\sigma^2 = \sigma_d^2 \sum_{j=-M}^{M} w_j^2 \tag{2.19}$$

As such, the values of σ and λ_0 can be used to provide control over the statistics of the generated rough surface; different surfaces with similar statistics can thus be generated simply by changing the value of the seed driving the random number generator. Some examples of rough surfaces generated through this procedure using different σ and λ_0 values are shown in figure 2.3, illustrating the limits of roughness being considered within this thesis (see section 3.5). It is assumed that the centre frequency is 2MHz and the SH wavespeed is 3260ms^{-1}, resulting in an ultrasonic wavelength (λ) of 1.6mm.

Alternative types of rough surface exist, for example those which use an exponential correlation function, or more involved generation procedures [41, 52]. However, without access to experimental data pertaining to the specific forms of surfaces expected over a range of corrosive conditions, it is difficult to know for certain the most likely surface shapes which could be formed under the process conditions being considered. Therefore, this process of numerical generation was selected as the most widespread in rough surface scattering literature; subsequently whenever a roughness is mentioned within this thesis it is assumed to have Gaussian height

and length characteristics unless otherwise stated.

It is important to note that although equations 2.13 through 2.19 only make reference to one axial direction, they are analogous when generating a rough surface which varies in two dimensions (i.e. three dimensional scattering) where instead of a one dimensional bell curve, a two dimensional bell contoured surface is used to correlate the random numbers with each other. Care must be taken however when defining the standard deviation of the original set of uncorrelated random numbers. Equations 2.17 and 2.19 should be used to select the correct value for σ_d. For further information on the numerical generation procedure of rough surfaces detailed in this section please see [42].

2.5 Scattered Wave Field Contributions

Before proceeding, it is important to describe a number of definitions which are used in future sections to describe the scattered wave field from a rough surface. The simulated far-field amplitude of a scattered planar wave from three defects with varying roughness levels are shown in figure 2.4 in order to illustrate this point. A defect length of 6λ was used and absolute amplitudes were calculated in the far field using the scalar wave DPSM (see section 3.2). When the surface is flat (σ=0), all the energy which would be expected to be reflected in the specular direction, in this case at θ=-30° when the wave is incident along θ=30°, is measured predominantly along the specular direction as shown in Fig. 2.4 (a.i). In this case all scattered energy is known as being coherent. However as surface roughness is increased, energy begins to scatter along alternate directions, reducing along the specular direction. Some energy does however still preferentially scatter in the specular direction for intermediate roughness levels. If an average of the scattered wave field is calculated over many rough surfaces with the same σ and λ_0 values (100 surfaces in this case) the most likely reflection results, which is referred to as the coherent contribution to the total scattered field as shown in Fig. 2.4 (b.ii). If this coherent component is subsequently subtracted from the scattered field from an individual rough surface realisation, the component which remains is known as the diffuse field as shown in Fig. 2.4 (b.iii). In the limit of very high roughness, all the scattered energy will

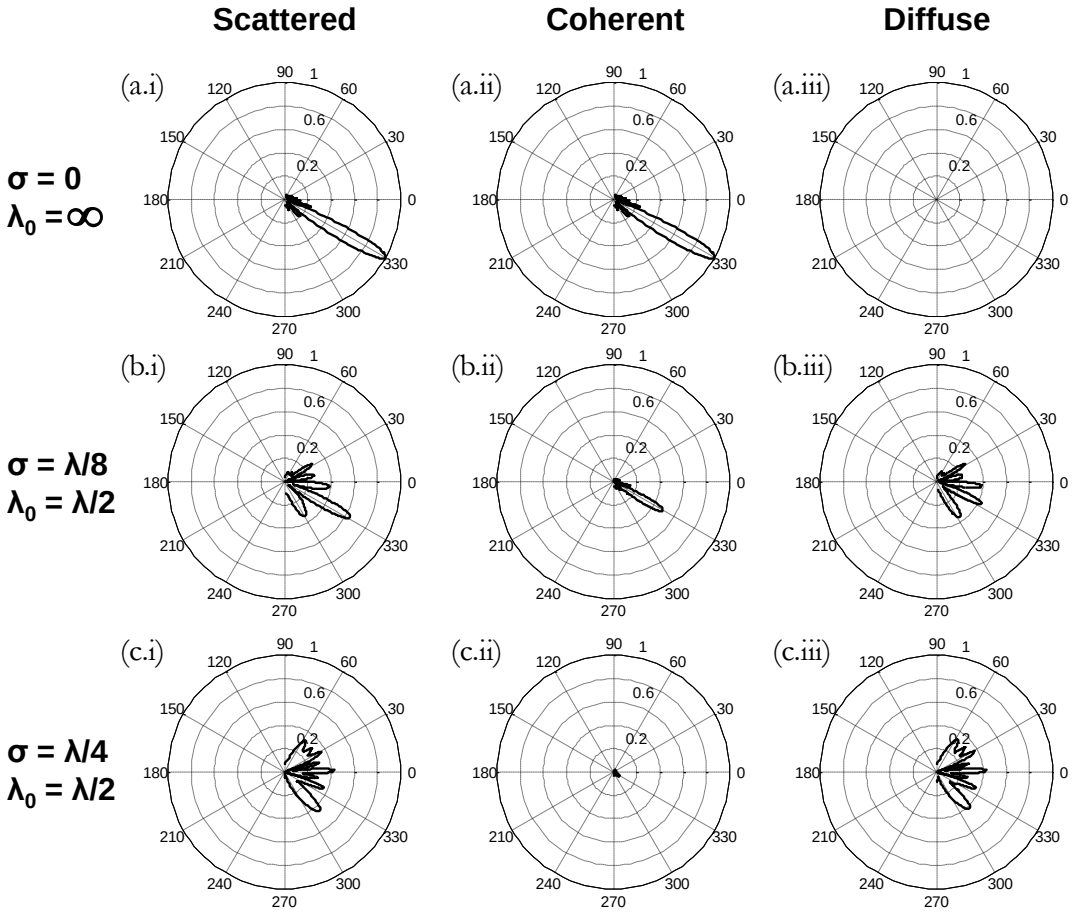

Figure 2.4: Scattered (i) coherent (ii) and diffuse (iii) components of the far field amplitude from a rough defect measuring 6λ in length for a planar incident scalar wave at 30° when (a) $\sigma = 0$ and $\lambda_0 = \infty$, (b) $\sigma = \lambda/8$ and $\lambda_0 = \lambda/2$ (c) $\sigma = \lambda/4$ and $\lambda_0 = \lambda/2$.

exist as part of the diffuse field as shown in Fig. 2.4 (c.iii) and averaging over many surfaces will result in zero coherent contributions to the scattered field.

It is this balance between coherent and diffuse energy which leads to the uncertainty of ultrasonic measurements in monitoring applications; coherent energy accounting for thickness change and diffuse energy adding to measurement uncertainty. Without the ability to take spatial averages over a rough surface through probe scanning, it is unclear whether coherent or diffuse energy dominates within the recorded signal and how this may affect subsequent signal processing. More discussion on this topic is provided in section 4.2.3.

2.6 Summary

The basic principles of wave propagation within elastic solids have been presented, providing sufficient background for the discussion of ultrasonic wave behaviour when scattered by a rough surface. The scalar wave approximation, used when modelling SH wave reflection and refraction at a boundary between two media, is of particular importance, allowing a powerful simplification to be made which permeates through all subsequent simulated investigations carried out within this thesis.

A review of rough surface scattering literature revealed that solution methods can be broadly split into two main categories: approximate analytical solutions which simplify the wave equation to produce a solvable system, and exact solutions which include numerical and BIE techniques. The approximate analytical approach limits accuracy and the applicability of each model depending on the approximations which must be made, leading to a large number of models with poorly defined limits of validity. Numerical techniques such as the FEM suffer from large computational requirements because large areas of the problem domain must be meshed. Exact analytical solutions are very complex and can be applied in only a limited number of applications. Therefore it was decided that a BIE method would be pursued using the analytical solution of a fictitious point source in the hope of maximising simulation accuracy while ensuring minimal computational resources were required.

The process of numerically generating rough surfaces having Gaussian height and length characteristics was described in detail. The form of such surfaces is controlled using just two parameters; the RMS height (σ) and the correlation length (λ_0), where different surfaces with similar statistics are generated by changing the values of a set of uncorrelated normally distributed random numbers. This simple approach of approximating the shape of the inner surface of a pipe or pressure vessel during corrosion forms the basis for all the rough surface investigations carried out in Chapters 3, 4 and 5. The next chapter however, focusses on sinusoidal surfaces in order to assess simulation capabilities when dealing with simpler geometries.

Chapter 3

Two Dimensional Wave Scattering using the DPSM

3.1 Introduction

A review of existing techniques used to study wave scattering by rough surfaces is provided in Chapter 2. The two major factors which must be balanced when selecting a technique are the required simulation time for a single surface realisation and the desired simulation result accuracy. The purpose of decreasing required simulation time as much as possible is a direct result of the random nature of rough surfaces where the objective becomes to simulate the signals from many surfaces with similar height and gradient statistics, subsequently averaging their responses. This ensemble average then provides an approximation of the most likely response from a surface with given statistics, referred to as the coherent part of the response. As a general rule however, as simulation time decreases invariably accuracy must also decrease as is evident when implementing approximate analytical techniques.

A boundary integral equation (BIE) method will be presented which strikes a better balance between accuracy and simulation time than conventional rough surface scattering techniques found within literature. Based on the semi-analytical mesh-free method first proposed by Placko and Kundu in 2000 [51], it calculates field variables using the analytical solution of a point source. Superposing the contributions trans-

mitted by many point sources placed in close proximity to boundaries having known boundary conditions provides the total field at any location in the problem domain. Termed the distributed point source method (DPSM) it has been applied to magnetic, electromagnetic, electrostatic and ultrasonic engineering problems. Avoiding the need for simplifying assumptions about the form of the reflecting surface and incident field represent the main advantage over analytical solutions, providing greater accuracy by inherently including phenomena such as multiple scattering, surface self-shadowing and tip diffraction. Furthermore, calculating field variables only along the boundaries ensures greater computational efficiency than can be achieved with numerical methods which require mesh generation and often absorbing boundaries, particularly within large and three dimensional problem geometries.

The aim of this chapter is to introduce some background behind the DPSM and describe in detail how the simulation method which was developed during the course of this thesis is constructed and applied to the specific monitoring situation being considered. Comparison will then be made to classical scalar wave Kirchhoff theory to highlight the differences in approach and the advantages inherent in using the accurate yet efficient technique. Subsequently it will be compared to simulated results calculated using the finite element method (FEM) and experimental results obtained using the waveguide transducers in order to verify the accuracy of the signals produced by the DPSM simulation. Results will only be carried out for two dimensional scattering to mirror the approach of the vast majority of literature investigating rough surface scattering due to the computational complexity associated with three dimensional scattering. A full description of the relevant literature and the two dimensional DPSM simulation was given in my publication [31]. Relevant excerpts from the paper are included within section **??**.

3.2 Scalar Wave DPSM Simulation

Unlike numerical techniques such as the FEM and the Boundary Element Method (BEM), the DPSM uses the analytical solution for a point source placed in close proximity to boundaries. The form of the wave equation used in numerical methods can lead to prohibitively small element sizes and time steps, particularly in

explicit analyses; however, the direct matrix inversion process used in the DPSM to calculate point source amplitudes given specified boundary conditions makes it very efficient. A comparison between analytical, semi-analytical and numerical techniques for modeling ultrasonic fields was carried out by Kundu et al [56] showing that the DPSM can be far more efficient than the FEM, exhibiting simulation times of minutes rather than hours. Simulation of wave propagation within infinite and semi-infinite media over large distances and times is also far more straight forward since absorbing boundaries are not required.

Over recent years the DPSM has been applied to many ultrasonic applications. Beam profile modelling in a single homogeneous fluid is the simplest case; an example of which can be found in [57] where Ahmad et al study the interaction effect between two phased arrays. Banerjee et al. [58] model ultrasonic beam profiles at a fluid-sold interface, finding that the method correctly calculates the fields produced in the solid and fluid by leaky Rayleigh waves. They then extend this theory to model ultrasonic fields within immersed plates in the presence of internal defects and elastic wave propagation in multilayered nonplanar solid structures, giving a general mathematical formulation in each case [59–61]. Shelke et al. [62] investigate the scattering of ultrasound from a single elliptical cavity within a solid, showing that high stress concentrations at the tips of high aspect ratio ellipses are correctly modelled. Banerjee et al. [63] take this a step further and model scattering within complex geometries using separate scatterer matrices and controlled space radiation point sources to correctly shadow contributions between multiple scatterers. The purpose of the DPSM model presented in this Chapter is to calculate the scattered scalar wave pulse reflected from a traction free boundary in two dimensions while accounting for multiple scattering, surface self-shadowing and edge diffraction. Figure 3.1 shows a schematic of the scattering geometry being considered and the orientation of the axes.

3.2.1 Cylindrical Line Source

A point source in two dimensions can be modelled as an infinitely long line source generating cylindrical waves. In this case the linear scalar wave equation can be

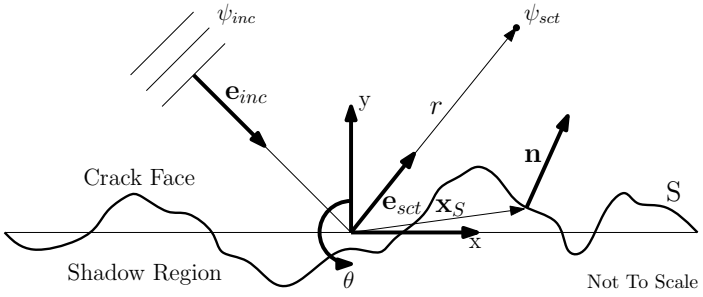

Figure 3.1: Two dimensional scattering geometry

expressed in cylindrical coordinates by equation 3.1 [64].

$$\frac{1}{r}\frac{\partial}{\partial r}\left(r\frac{\partial \psi}{\partial r}\right) = \frac{1}{c^2}\frac{\partial^2 \psi}{\partial t^2} \tag{3.1}$$

where ψ is the pressure at a distance r from the cylindrical axis as a function of time t and c is the wavespeed within the material. The general solution of equation 3.1 takes the form of Hankel functions of either the first or second kind. For purely diverging waves the zero order Hankel function of the second kind can be used.

$$\psi(r,t) = AH_0^{(2)}(kr)\exp[i\omega t] \tag{3.2}$$

where A is a constant, k is the wavenumber, ω is the angular frequency and $i = \sqrt{-1}$. In the far field $(kr \to \infty)$ the Hankel function can be approximated leading to a simplification of equation 3.2.

$$\psi(r,t) = A\frac{\eta}{\sqrt{r}}\exp[i(\omega t - kr)] \tag{3.3}$$

where

$$\eta = \sqrt{\frac{2\exp\left(i\frac{\pi}{2}\right)}{\pi k}} \tag{3.4}$$

Equation 3.3 can thus be used when calculating field variables in the far field in order to decrease computation time when compared to equation 3.2.

3.2.2 Monochromatic Waves

The DPSM is a semi-analytical mesh-free simulation method which calculates field variables at point sources located in close proximity to boundaries. These point sources can be active or passive. Active sources are used at locations which have a predefined input pressure, for example at the transmitting transducer locations. Passive sources are used at boundaries between two media where interactions between the field and boundaries occur, for example the inner surface of the component wall. Target points can then monitor the total field at any point within the problem geometry as the summation of the incident and scattered fields. To my knowledge, other than within my paper [31], all previous literature published using the DPSM relies on simulating in three dimensions, even when results are required in two. The main difference arises in the beam spread of the free space Greens functions which in two dimensions is a function of wavenumber (see equation 3.4) but in three dimensions it is not (see equation 5.1). What follows is a description of how the DPSM has been applied to purely two dimensional situations in order to decrease simulation time as much as possible.

Equation 3.2 or 3.3 can be used to calculate the pressure at a single point at a distance r away from a single transmitting point source with amplitude A. In reality the total pressure at a point within a field is the summation of contributions from multiple waves emanating from various different boundaries. The DPSM casts these single point contributions into a large set of simultaneous equations which can be solved allowing N source points to contribute at M target points. The complex pressure can thus be calculated using equation 3.5.

$$\mathbf{\Psi}_{\mathrm{T}} = \mathbf{Q}_{\mathrm{TS}}\mathbf{A}_{\mathrm{S}} \tag{3.5}$$

where

$$\mathbf{Q}_{TS} = \begin{bmatrix} \frac{\eta \exp(-ikr_1^1)}{\sqrt{r_1^1}} & \frac{\eta \exp(-ikr_2^1)}{\sqrt{r_2^1}} & \cdots & \frac{\eta \exp(-ikr_N^1)}{\sqrt{r_N^1}} \\ \frac{\eta \exp(-ikr_1^2)}{\sqrt{r_1^2}} & \frac{\eta \exp(-ikr_2^2)}{\sqrt{r_2^2}} & \cdots & \frac{\eta \exp(-ikr_N^2)}{\sqrt{r_N^2}} \\ \vdots & \vdots & \ddots & \vdots \\ \frac{\eta \exp(-ikr_1^M)}{\sqrt{r_1^M}} & \frac{\eta \exp(-ikr_2^M)}{\sqrt{r_2^M}} & \cdots & \frac{\eta \exp(-ikr_N^M)}{\sqrt{r_N^M}} \end{bmatrix} \tag{3.6}$$

Bold variables refer to matrix quantities, subscript S refers to source points, sub-

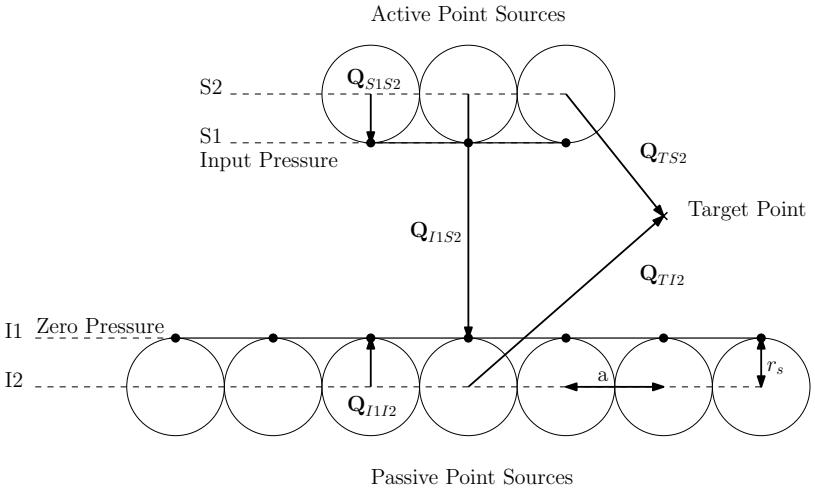

Figure 3.2: Diagram showing how the problem geometry of the DPSM simulation is constructed, illustrating the naming convention of each of the **Q** matrices and boundaries.

script T refers to target points and r_n^m is the distance between source point n and target point m. Since the wave field being calculated is monochromatic the time dependance in equation 3.3 disappears in equation 3.6, therefore the source point amplitudes ($\mathbf{A}_\mathrm{S}$) are set as complex variables in order to include both amplitude and phase information. It is important to note that equation 3.6 is the far-field version of $\mathbf{Q}_\mathrm{TS}$ and a similar expression using equation 3.2 should be used when making calculations in the near field, for example when satisfying boundary conditions in close proximity to the point sources.

Equation 3.5 shows the general case when there are N source points and M target points. This is applied to our single backwall reflection case as illustrated in figure 3.2. In order to simulate multiple interactions between the active and passive sources it is required that a larger matrix is solved over longer boundaries ([51] pg 114)); this was deemed unnecessary in this application where sufficient separation of the pulses in the time domain is expected. The point sources are offset from the true boundaries in order to avoid singularities that would otherwise occur with zero propagation distances. The amplitudes of the active sources are solely a function of the input pressure when simulating a single reflection between the transducer and backwall (or interface). These are calculated by inverting the relevant **Q** matrix and

multiplying by the input pressure boundary condition.

$$\mathbf{A}_{S2} = \left[\mathbf{Q}_{S1S2}\right]^{-1} \mathbf{\Psi}_{S1} \tag{3.7}$$

At the interface, the pressure field created by the passive sources should be equal to the field created by the active sources multiplied by the appropriate reflection coefficients, as given by equation 3.8.

$$R = \frac{\rho_2 c_2 \cos\theta_1 - \rho_1 c_1 \cos\theta_2}{\rho_2 c_2 \cos\theta_1 + \rho_1 c_1 \cos\theta_2} \tag{3.8}$$

where θ_1 is the incident angle and θ_2 is the transmitted angle measured from the normal to the surface and c refers to the wavespeed in the respective media. If the acoustic impedances of the two media are very different (as is the case with SH waves within steel bounded by air) it can be assumed constant over the entire interface at any angle of incidence and can be set equal to -1. During multiple scattering some components of the transmitted field will interact with the surface at incident angles differing from those predicted by the incident wave field alone. A constant reflection coefficient makes the calculation of these extra components trivial; however, when acoustic impedances are more similar this assumption cannot be made. Therefore wherever multiple interactions occur, the reflection coefficient should be recalculated for the solution to remain valid. This would substantially increase the complexity of the simulation. Under such conditions the current simulation would therefore only be valid when low levels of multiple scattering are expected. At the interface

$$\mathbf{Q}_{I1I2}\mathbf{A}_{I2} = \mathbf{Q}^{R}_{I1S2}\mathbf{A}_{S2} \tag{3.9}$$

therefore

$$\mathbf{A}_{I2} = -1\left(\left[\mathbf{Q}_{I1I2}\right]^{-1}\mathbf{Q}_{I1S2}\mathbf{A}_{S2}\right) \tag{3.10}$$

where superscript R denotes multiplication by the reflection coefficient and $\mathbf{Q}$ matrix subscripts should be inferred from Fig 3.2. Equation 3.10 represents the main advantage over other rough surface scattering methods; multiple scattering and shadowing effects are included in a single matrix inversion and multiplication process making it very efficient and simple to implement. The incident field from the transducer face and reflected field from the interface can now be calculated at any set of target

points, hence the total field can be calculated.

$$\mathbf{\Psi}_{\mathrm{T}} = \mathbf{Q}_{\mathrm{TS2}}\mathbf{A}_{\mathrm{S2}} + \mathbf{Q}_{\mathrm{TI2}}\mathbf{A}_{\mathrm{I2}} \tag{3.11}$$

Although Fig 3.2 illustrates the point sources separation (a) as double the offset from the boundary (r_s), the two distances can be set independently. Earlier publications on DPSM have concluded that the upper limit of a should be set at one third of the wavelength and that $r_s = a/\sqrt{2\pi}$ in order to equate the effective hemispherical area of the point sources to the area they occupy on the surface ([56], [51] pg 30). It was found that in two dimensions the value of r_s had little effect on the outcome within certain bounds, determined by the accuracy of the Hankel function over short distances and the minimum radius of curvature of the surface. To ensure each surface was sampled sufficiently to reconstruct their true shape a point source separation of 50μm ($a = \lambda/32$) was selected. An offset to the boundary of 1.6μm ($r_s = \lambda/1000$) was chosen to prevent point source overlap across boundaries which have a low radius of curvature. More rigorous studies into the effects of point source location at the boundaries can be found in [65] and in Chapter 1 of [51].

3.2.3 Extension to the Time Domain

Pulses are used when calculating wall thickness so that the TOF can be determined. To extend the monochromatic DPSM formulation to simulate time domain pulse propagation, first the Fourier transform of the incident pulse $f(t)$ at boundary S1 is determined.

$$F(\omega) = \frac{1}{\sqrt{2\pi}} \int_{-\infty}^{\infty} f(t) \exp(i\omega t)\, dt \tag{3.12}$$

where $F(\omega)$ represents the frequency domain of the incident pulse. The calculations detailed in the previous section are then carried out at each frequency component within the Fourier transform, ensuring the pressure amplitude and phase from $F(\omega)$ are defined in the vector $\mathbf{\Psi}_{\mathrm{S1}}$ in equation 3.7. Once the frequency domain signal is constructed at target point m an inverse Fourier transform is used to transform back to the time domain.

$$\psi_m(t) = \frac{1}{\sqrt{2\pi}} \int_{-\infty}^{\infty} F_m(\omega) \exp(-i\omega t)\, d\omega \tag{3.13}$$

In practice equations 3.12 and 3.13 are replaced with discrete sums and the fast Fourier transform (FFT) and inverse fast Fourier transform (IFFT) are used. Matlab [55] was chosen for writing the simulation since it is well suited to matrix manipulation and it allows the use of complex number matrices which are not always supported in other programming environments. Separating the real imaginary components would allow it to run on such platforms (see for example [66]); however, this would increase the size and complexity of the matrices. The existing FFT, IFFT and Hankel functions in Matlab were also found to perform rapidly and accurately enough for our purposes. An alternative approach to using the DPSM to create time dependent signals has been suggested by Rahani and Kundu [67] where the Green's function is used in the time domain, avoiding the need for Fourier analysis. This approach, termed transient DPSM (t-DPSM), was discounted for the current analysis as it is suited to situations where only a short section of the time domain signal is required.

3.3 Comparison with the Kirchhoff Approximation

Once the DPSM simulation had been completed it was decided that it should be compared with the most common simulation method found in rough surface scattering literature in order to highlight the benefits of the new technique. Approximate analytical solutions making use of the Kirchhoff approximation were found to be the most frequent, however many different forms of Kirchhoff theory exist, differing by incident wave field type, defect boundary conditions, defect types and some which attempt to include shadowing and higher order scattering. For the purpose of this thesis, comparison will be made to classical scalar wave Kirchhoff theory which is the most commonly implemented method used to investigate scalar wave reflection from rough surfaces within literature. Equation 3.14 shows the final result given by Schmerr [68] which calculates the scattered field at an observation point at a distance r away from the crack face given the angle of incidence of the plane wave.

$$\psi_{sct}(\mathbf{r},k) = \psi_0 A(\mathbf{e_{inc}};\mathbf{e_{sct}})\frac{\exp(ikr)}{r} \tag{3.14}$$

where k is the wavenumber of the incident wave, ψ_0 is the incident amplitude, $\mathbf{e_{inc}}$ is the unit normal along the incidence direction, $\mathbf{e_{sct}}$ is the unit normal along the observation direction from the origin and $A(\mathbf{e_{inc}};\mathbf{e_{sct}})$ is the far-field scattered amplitude given by

$$A(\mathbf{e_{inc}};\mathbf{e_{sct}}) = -\frac{ik}{2\pi}\int_S(\mathbf{e_{inc}}\cdot\mathbf{n})\exp[ik(\mathbf{e_{inc}}-\mathbf{e_{sct}})\cdot\mathbf{x_S})]dS \tag{3.15}$$

In deriving equations 3.14 and 3.15 the following assumptions were made:

- Reflection is from a cracklike flaw with zero pressure on the lower surface and a reflection coefficient of -1 on the upper surface.
- The crack is assumed to vary in height in one dimension only, resembling ridges perpendicular to the scattering plane rather than hills which would be expected in reality.
- The incident wave field is made up of monochromatic plane waves approaching along unit vector $\mathbf{e_i}$.
- Amplitude $A(\mathbf{e_{inc}};\mathbf{e_{sct}})$ is calculated in the far-field (r$\gg\lambda$)
- Scattering of waves between multiple parts of the crack is neglected.
- No shadowing of any part of the crack by any other part occurs when viewed along $\mathbf{e_{inc}}$ or $\mathbf{e_{sct}}$.
- Signals diffracted from crack tips are neglected.

Details on the mathematical derivation of equations 3.14 and 3.15 can be found in [68].

3.3.1 Monochromatic Plane Wave Scattering

The simplifying assumption that the scattered amplitude is required only to be calculated within the far-field (often referred to as the Fraunhofer approximation) is commonly used during the derivation of approximate analytical scattering models such as Kirchhoff theory. When considering the case of an ultrasonic transducer,

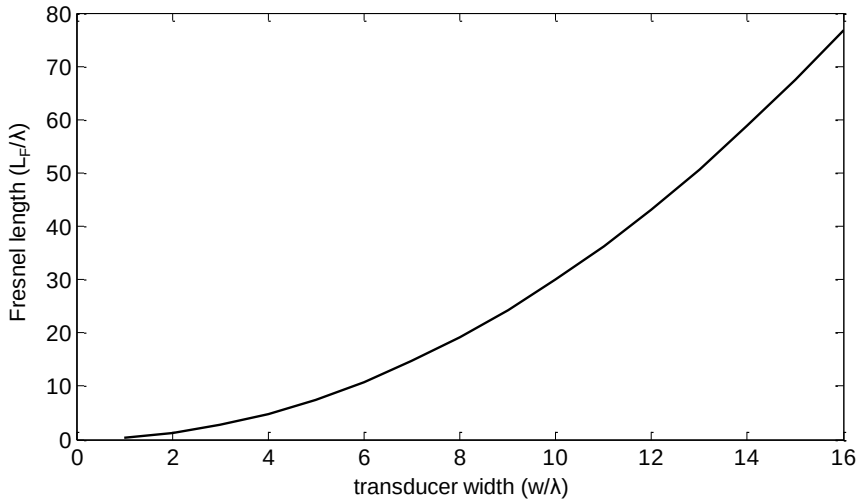

Figure 3.3: Fresnel length of a planar rectangular transducer

the Fresnel length L_F can be used to estimate the distance from the transducer face where the Fresnel zone (near-field) ends and the Fraunhofer region (far-field) begins, beyond which the Fraunhofer approximation is valid. Analytical expressions for this length can only be derived for simplified geometries; for a rectangular transducer which is assumed to be infinite in one direction the Fresnel length is given by equation 3.16 [35] pg 178.

$$L_F = 1.2\frac{(w/2)^2}{\lambda} \tag{3.16}$$

where w is the width of the transducer. By implementing equation 3.16, figure 3.3 illustrates how changing transducer width can have a large impact on the distance where the Fraunhofer approximation can be made. If it can be assumed within our two dimensional simulation that a planar crack under normal plane wave incidence behaves similarly to a rectangular transducer of the same dimensions, Fig. 3.3 also provides an estimate of the distance within which the Kirchhoff approximation cannot be considered valid.

Further to the Fraunhofer approximation, other phenomena neglected during the derivation of classical Kirchhoff theory include multiple scattering, surface self-shadowing and crack tip diffraction. Two simplified geometries shown in figure 3.4 are considered in order to illustrate the impact of ignoring these effects.

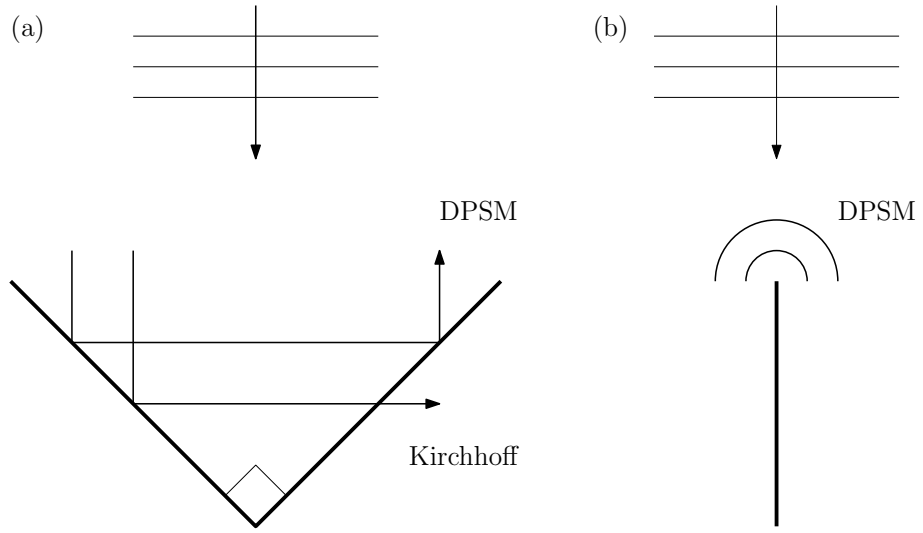

Figure 3.4: Simplified crack geometries (a) 90° angular crack used to demonstrate multiple scattering and surface self shadowing (b) 90° incidence on planar crack used to compare diffracted signal amplitudes.

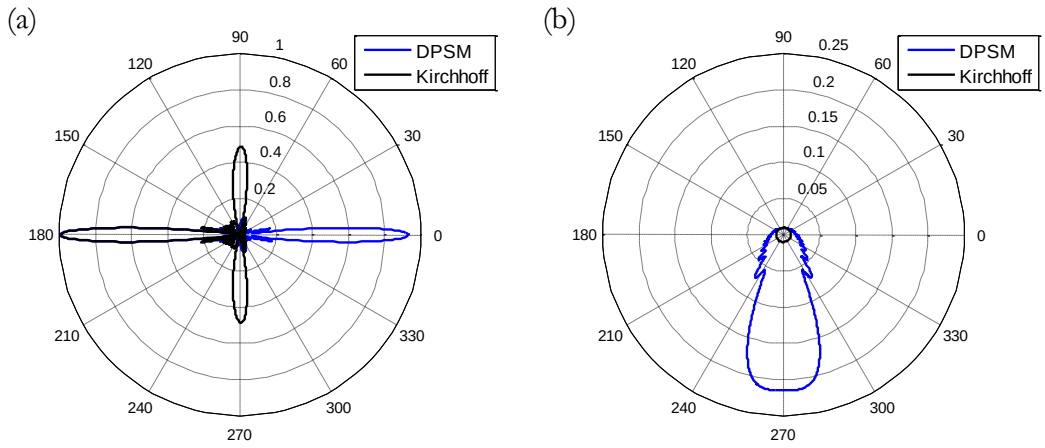

Figure 3.5: Scattered amplitude under normal plane wave incidence (a) 90° concave angled crack (b) 90° incidence on planar crack .

In all cases the simulated response is normalized to the maximum amplitude of the centre frequency of the pulse when incident upon a flat defect of the same length and at the same observation distance. Figure 3.5 shows the far-field scattered absolute amplitude from the defects shown in Fig. 3.4. In the case of the concave angled crack

with an internal angle of 90°, it would be expected that when a plane wave is incident such that it approaches the faces of the crack at 45° that almost all energy would be directed back in the incident direction due to double scattering. The remaining energy would contribute to diffracted waves at the crack tips. This response is clearly demonstrated when using the DPSM simulation shown in Fig. 3.5(a). The Kirchhoff approximation simulation instead shows two lobes perpendicular to the incidence angle, each being half the amplitude of the incident wave. This response illustrates not only that single scattering alone is calculated, it shows that components which are scattered are free to subsequently travel through the crack face. This disregard of self-shadowing is also shown in Fig. 3.5(b) where a lobe within the scattered field downstream of the crack would be expected as indicated by the DPSM in order for a shadow region to exist within the total field. Differences at all angles of incidence in this case also indicate the lack of tip diffracted signals within the scattered field predicted when using the Kirchhoff approximation.

Many authors have published investigations into the validity of the Kirchhoff approximation when modelling wave scattering from rough cracks with Gaussian distributed height and length characteristics; however most only consider the scattered amplitude of monochromatic waves. Our specific application requires knowledge of how the shape of an ultrasonic pulse which has reflected from a rough crack will change, requiring both amplitude and phase to be accurately known. This approach differs from the vast majority of literature on the subject, some examples of which are provided as reference. While investigating acoustic wave scattering, Thorsos [47] provides a thorough investigation into the surface variables which impact on the validity of the Kirchhoff approximation, finding that surface correlation length has a larger effect than the previously assumed RMS radius of curvature. Wombell [69] reports how the Kirchhoff approximation is increasingly violated as RMS height increases, showing rapid deterioration when $\sigma/\lambda \geq 0.2$ while using it to reconstruct rough surface profiles from scattered electromagnetic field data. When considering longitudinal ultrasonic wave scattering from rough cracks, Zhang et al [48] also provide estimates of RMS height, correlation length and scattered angle values beyond which the Kirchhoff approximation can no longer be assumed valid. However, providing definitive limits on the validity criteria of the Kirchhoff approximation and other approximate scattering techniques through rigorous simulation of many

rough surfaces historically has proven very difficult [39]. Therefore a detailed investigation was deemed outside the scope of this thesis and the interested reader is referred to [37] [46] and [53] pg 100 for further information. For the Kirchhoff approximation validity investigations carried out in this thesis a different approach must be taken since it is incident pulse scattering which is of interest. Therefore all subsequent analysis will be carried out by comparing signals in the time domain using the theory in section 3.2.3 to convert monochromatic results.

3.3.2 Time Domain Plane Wave Pulse Scattering

In order to demonstrate how the tip diffracted waves can affect the simulated response of a pulse reflecting from a crack of finite length, the diffracted components must be separated from the main pulse. This can be achieved temporally using equation 3.17 which calculates the crack length L_c required to completely separate the diffracted pulses originating from the crack tips from the pulse reflecting from the crack face.

$$L_c = 2\sqrt{2L_p r + L_p^2} \tag{3.17}$$

Where L_p is the required geometrical distance between the diffracted wave and main pulse along the normal to the crack and r is the observation distance. A planar crack under normal incidence is considered in order to simplify pulse shape and to ensure diffraction is uniform at both tips. Clearly the difference in propagation distance between the center of the crack and the tip tends to zero as observation distance tends to infinity; therefore the simulation must be carried out within the Fresnel zone in order to separate signals in this manner.

Using an observation distance of 5λ and a 2MHz 5 cycle pulse, a crack length of 17λ results in order to completely separate the main pulse from the tip diffracted signals. Figure 3.6(a) shows the scattered response from such a defect, illustrating how using the far field form of the equations inherent within the Kirchhoff approximation can affect the scattered response in the normal direction. In the same way as monochromatic scattering, the simulated response is normalized to the maximum amplitude of the centre frequency of the pulse when incident upon a flat defect of the same length and at the same observation distance. Fig. 3.6(a) shows that the

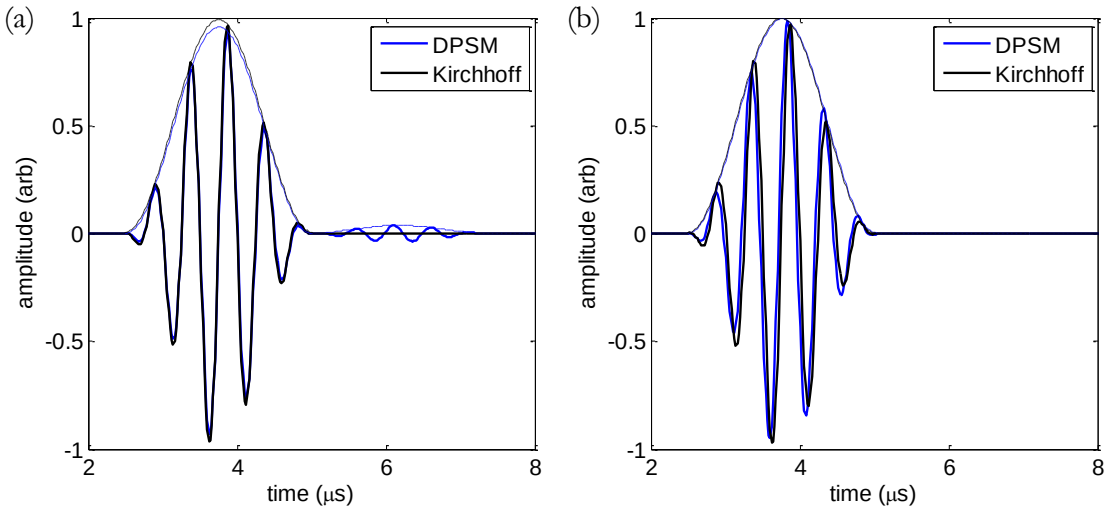

Figure 3.6: Scattered signal at a distance of 5λ normal to the planar crack face under normal incidence with a crack length of (a) 17λ (within near field) (b) 2λ (within far field). Thinner lines show the Hilbert envelopes of each signal.

phase is correctly predicted once diffracted components are removed; however, the amplitude does not reduce by the amount consistent with a loss in energy due to diffraction as is evident within the scattered signal produced by the DPSM simulation. Figure 3.6(b) shows the same result when the observation is made in the far field, obtained by changing the crack to be 2λ in length. It is clear that the diffracted constituents are now incorporated within the main pulse, causing the energy content to be consistent between the two methods; however, the phase predicted by the Kirchhoff approximation alters with respect to the DPSM simulation. Between the near field and far field regions errors in the scattered response when using the Kirchhoff approximation in the normal direction are a combination of amplitude and phase, depending on diffracted signal location with respect to the main pulse.

Considering scattered angles other than the specular direction there are additional errors associated when using the Kirchhoff approximation. Referring to equation 3.14, the position in time of the reflected pulse is calculated by changing the phase of each constituent frequency by multiplying by $\exp(ikr)/r$. This simply moves the far field scattered response to the desired location in time without consideration of near field effects. This has the greatest impact on error in directions other than specular where near field contributions dominate as illustrated in figure 3.7 which

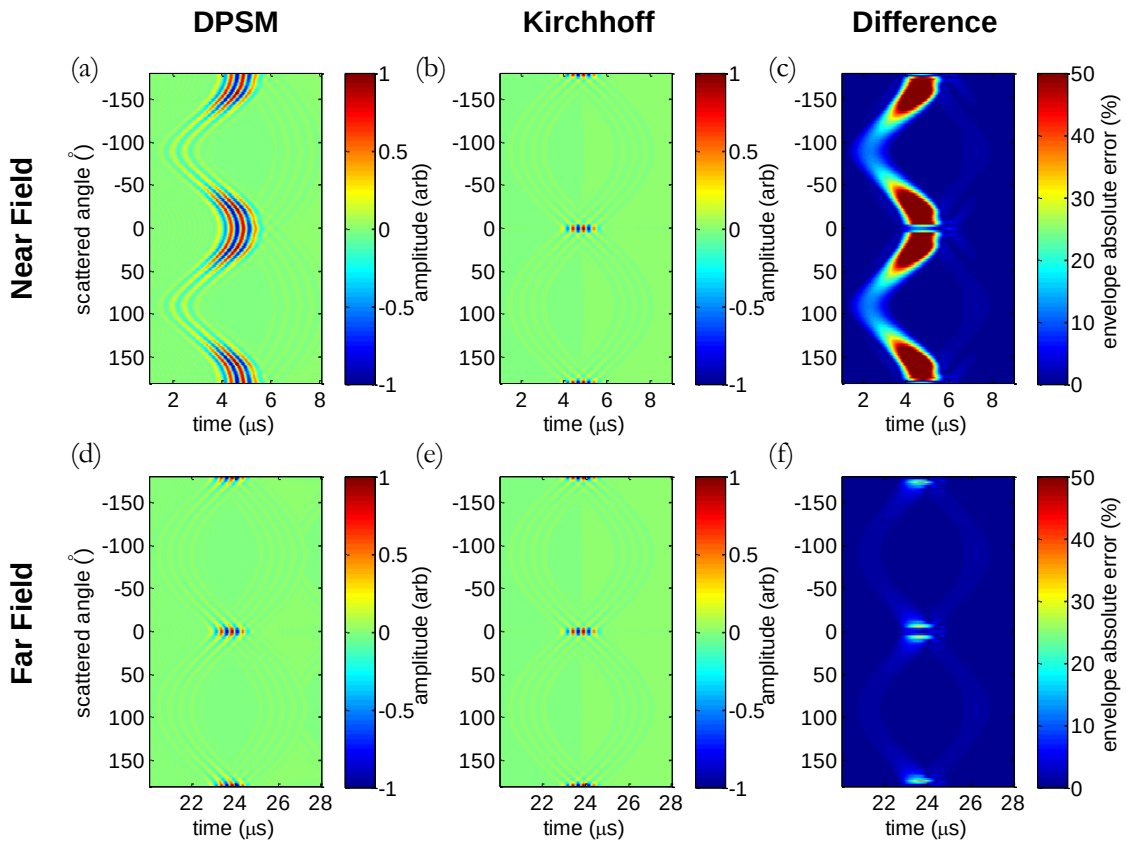

Figure 3.7: Time domain signals for all scattered angles around a planar crack with a length of 10λ. (a) Results from DPSM simulation with $r = 7\lambda$. (b) Results using Kirchhoff approximation with $r = 7\lambda$. (c) Percentage difference in amplitude of the Hilbert envelope results from (a) and (b). (d) Results from DPSM simulation with $r = 45\lambda$ (e) Results using Kirchhoff approximation with $r = 45\lambda$ (f) Percentage difference in amplitude of the Hilbert envelope results from (d) and (e).

shows the scattered pulse recorded at all angles around the crack using the DPSM and Kirchhoff approximation methods. Fig. 3.7(c) compares the amplitude predictions of the two methods by taking the difference of the Hilbert envelopes of their scattered pulses when the planar crack is 10λ in length and the observation distance is 7λ ($L_F/4$). The envelopes were calculated to remove any errors caused by slight variations in phase. Errors larger than 50% occur within 45° either side of the specular reflection, indicating the large impact the far field assumption has on accuracy. Fig. 3.7(f) shows the same results but taken at an observation distance of 45λ ($3L_F/2$), illustrating the improvement in agreement within the Fraunhofer region.

Using the far field assumption when considering a rough crack can have an even

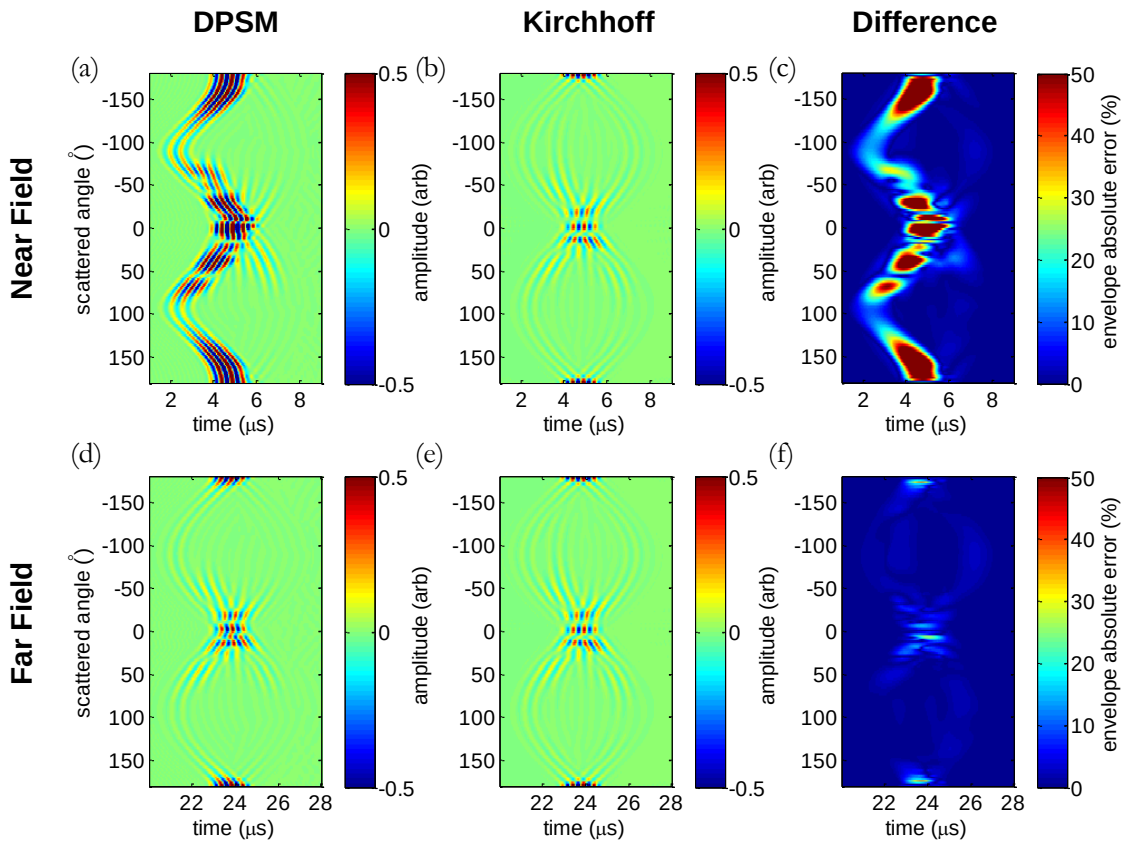

Figure 3.8: Time domain signals for all scattered angles around a rough crack with a length of 10λ, an RMS height of $\lambda/10$ and a correlation length of $\lambda/2$. (a) Results from DPSM simulation with $r = 7\lambda$ (b) Results using Kirchhoff approximation with $r = 7\lambda$ (c) Percentage difference in amplitude of the Hilbert envelope results from (a) and (b). (d) Results from DPSM simulation with $r = 45\lambda$ (e) Results using Kirchhoff approximation with $r = 45\lambda$ (f) Percentage difference in amplitude of the Hilbert envelope results from (d) and (e).

larger impact on pulse shape prediction capability depending on scattered angle and the shape of the particular rough crack. Figure 3.8 shows the scattered pulse shapes at all observation angles around a rough crack with a length of 10λ, an RMS height of $\lambda/10$ and a correlation length of $\lambda/2$. It is clear that when the observation distance is just 7λ, the Kirchhoff approximation is unable to accurately predict pulse shape with amplitude errors generally above 50% at all scattered angles between -90° and 90°, including in the specular direction. However, when calculations are carried out at an observation distance of 45λ, the Kirchhoff approximation is generally within 10% of the amplitude predicted by the DPSM as shown in Fig. 3.8(f). Errors in this case will be caused by other factors such as neglecting multiple scattering, self shadowing at high angles of incidence and tip diffraction which are dependent

on roughness level and are outside the scope of this investigation. By inspecting Fig. 3.3 which gives an estimate of where the Fraunhofer region begins, it is clear that the relationship between crack length and the Fresnel length will be the main limitation on the defect geometries where classical Kirchhoff theory can be applied. The specific case of backwall reflection being investigated in this thesis will now be considered.

3.3.3 Sensor Considerations

The reflection from an infinite backwall can be calculated up to a specified point in time by modelling it as a long crack where the tip diffracted waves occur directly after the total time to be simulated in the time domain signal. The length of this crack can be calculated for a pulse echo inspection when considering only a single backwall reflection from a cylindrical point source in 2D as shown by equation 3.18.

$$L_c = 2\sqrt{\left(\frac{ct_{tot}}{2}\right)^2 - T^2} \tag{3.18}$$

Where T is the wall thickness and t_{tot} is the total time to be simulated. Although the sensor is not strictly pulse echo, equation 3.18 can be used as long as the pitch between the transducers is much smaller than the wall thickness. Therefore, if the wall thickness is 15mm and a simulated time of 15μs is required, a crack length over 39mm results in order to make the simulated result equivalent to that from an infinite backwall. Estimating the Fresnel length using equation 3.16, for a crack length of 39mm a distance greater than approximately 280mm from the crack face would be required to be within the Fraunhofer region of the scattered response and for classical Kirchhoff theory to remain valid. In reality inspection is carried out by the sensor at the upper surface of the wall, well within the Fresnel zone of the backwall making the classical Kirchhoff theory approach unsuitable.

Many corrections have been proposed to improve the accuracy of Kirchhoff theory in specific situations. Melton and Horton [70] investigate the use of the Fresnel correction, further highlighting the importance of accounting for different propagation distances between points on a rough surface and the receiving transducer when calculating phase and amplitude variations within the Fresnel zone. Bruce and Dainty

[71] add an extra term which calculates any rays which have double scattered around features on a rough interface, showing the increase in backscattered amplitude which would be expected on surfaces with large RMS slope. They also include shadowing in the same way as many other authors following the approach taken by Beckmann [72] during early work using shadowing functions which have a value of 1 if the point x_S is illuminated by the incident wave and zero otherwise based on geometrical line of sight. Bistatic shadowing is also included which accounts for shadowing from x_S to the receiver [38, 73]. However, all of these correction factors add to the complexity of the Kirchhoff simulation that would have to be implemented in order to match the accuracy provided by the DPSM.

One further important consideration is that the sensor does not transmit plane waves. For analytical Kirchhoff theory to remain tractable the only alternatives readily available within literature are plane wave beams with finite width and spherical wave fields from point sources. One such example proposed by Berry [74] calculates the pulse scattered from a rough surface by adding contributions from points on the surface at specified geometrical distances away from the transceiver point source to the corresponding location in the time domain signal. Being the closest example found within literature to the situation of interest, it was subsequently applied to the scattering of pulses from sinusoidal surfaces in my paper [31] showing good agreement at low surface RMS heights. Multiple scattering effects do however cause it to breakdown as RMS height increases, exhibiting little discernable improvement in required simulation time when compared with the DPSM. Therefore, based on the rapid simulation time achieved without any need for correction and its ease when handling arbitrary incident fields, the DPSM was deemed superior to the Kirchhoff approximation for the situations under investigation within this thesis and Kirchhoff theory was not pursued any further.

3.4 Simulation Validation

In order to validate the DPSM simulation for use on more complex geometry, the comparatively simple scenario of pulse scattering from a periodic sinusoidal surface whose height varied in the x direction only was investigated. The equation for such

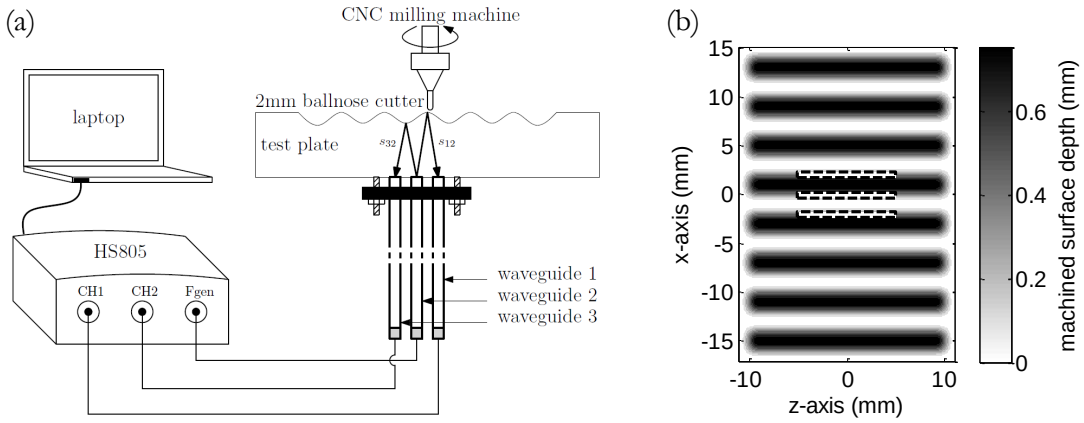

Figure 3.9: (a) Schematic of experimental setup. (b) Plan view of the final stage of the machined sinusoidal surface. Areas within the dashed lines indicate the approximate locations of the contact patches of each waveguide.

a surface is given by equation 3.19

$$h(x) = \sqrt{2}\sigma \cos\left(\frac{2\pi x}{\lambda_s}\right) \tag{3.19}$$

where σ is the RMS height of the sinusoid and λ_s is the wavelength of the surface. The RMS height was increased in stages to investigate how pulse shape changes when compared with a flat surface. The FEM was chosen as the benchmark to compare results to as it is an established numerical method capable of including all scattering interactions along a boundary. Comparison was also made to experimental signals obtained using the waveguide transducers in order to investigate whether the scalar wave assumption can in fact be made when simulating SH wave scattering in two dimensions.

The experimental setup, as illustrated in figure 3.9(a), was designed to investigate the positional sensitivity a sensor made up of two waveguide transducers would have when incident upon a given surface. This was achieved by adding a third waveguide, therefore producing an array which replicated the situation where a single sensor is moved between two positions separated by the pitch of the waveguides. Physically moving the sensor during the experiment was not an option since slight

changes in waveguide coupling would have a large impact on the received waveforms which subsequently could not be compared with any accuracy. The waveguides were assigned numbers from 1 to 3 as illustrated in Fig. 3.9(a), with signal s_{jl} referring to the waveform recorded by waveguide j when a pulse is transmitted by waveguide l. The paths taken by signals s_{12} and s_{32} are shown in Fig. 3.9(a). The 2mm pitch between the waveguides dictated the surface wavelength to be 4mm so that one pair of waveguides would be incident directly above a trough in the surface and the other pair incident above a peak. To mimic a two dimensional scattering situation experimentally the profile shown in Fig. 3.9(b) was machined in 20μm depth increments into the backwall of the 9.88mm thick mild steel test plate up to a maximum RMS height of 0.28mm, beyond which the radius of curvature of the ball nose cutter would cause errors in the machined surface. A full matrix capture (FMC) data set was acquired after each machining stage using a TiePieSCOPE HS805 which performed the roles of function generator and digital data acquisition unit controlled using Matlab. The two dimensional plane modelled during simulation was taken as the xy plane ($z = 0$) in Fig. 3.9(b), around which the beam profile in the waveguide width direction is assumed symmetrical.

The FEM simulation, written using Abaqus explicit [75], was constructed using the same backwall geometry and zero pressure boundary condition as the DPSM simulation. Four node linear 2D acoustic quadrilateral elements were used with a nominal node separation of 50μm and a simulation time step of 5ns which was stable up to an RMS height of 0.26mm, beyond which increased mesh deformation required smaller time steps. It was found that the built in non-reflecting acoustic boundary conditions within Abaqus did not sufficiently damp out edge reflections; therefore the problem domain was expanded to the minimum size required for no reflections to encroach up to a total signal time of 10μs, resulting in a problem geometry containing approximately 360000 elements. When run on a machine which had 256GB random access memory and 4 quad-core 2.7GHz processors (AMD Opteron, Sunnyvale, CA) a simulation time of 130 seconds was achieved. On the same machine the equivalent DPSM simulation using the same point source separation as the node separation (see section 3.2.2) took just 3 seconds, two orders of magnitude more rapid than the FEM highlighting the efficiency of the technique.

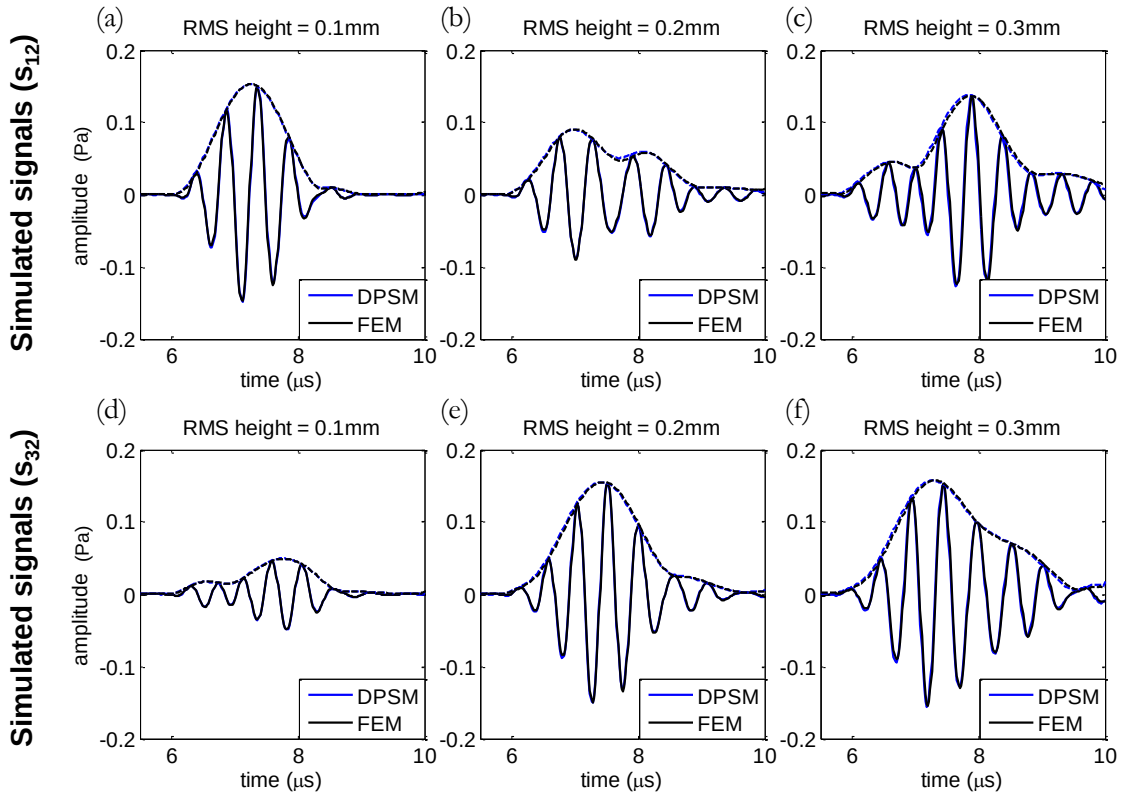

Figure 3.10: Simulated signals s_{12} obtained using the DPSM and FEM simulations with an input pressure amplitude of 1, showing the unscaled reflected scalar wave pulse from a sinusoidal surface with RMS heights of (a) 0.1mm, (b) 0.2mm and (c) 0.3mm. Similar results for signals s_{32} and RMS heights of (d) 0.1mm, (e) 0.2mm and (f) 0.3mm. Dotted lines show the Hilbert envelopes of each signal.

Simulated signals from both pairs of waveguides within the array are shown in figure 3.10 which have not been scaled from the raw outputs produced by the FEM or the DPSM simulations based on an input pressure amplitude of 1Pa at the transmitting waveguide. To calculate the final signal an average of all the signals calculated at the nodes / target points within the 0.5mm long receiver contact patch was taken. The results from the DPSM are almost indistinguishable from the FEM, illustrating no need for amplitude scaling as is reported for the DPSM in three dimensional scattering problems [76]. This is most likely because ignoring contributions between point sources at the surface has a much reduced effect in two dimensions because of the large reduction in effective area being ignored. Using denser point sources distributions along a boundary produces the same simulated result. Based on such strong agreement and much improved efficiency, the DPSM was used to carry out all future two dimensional scalar wave simulated results presented within this thesis.

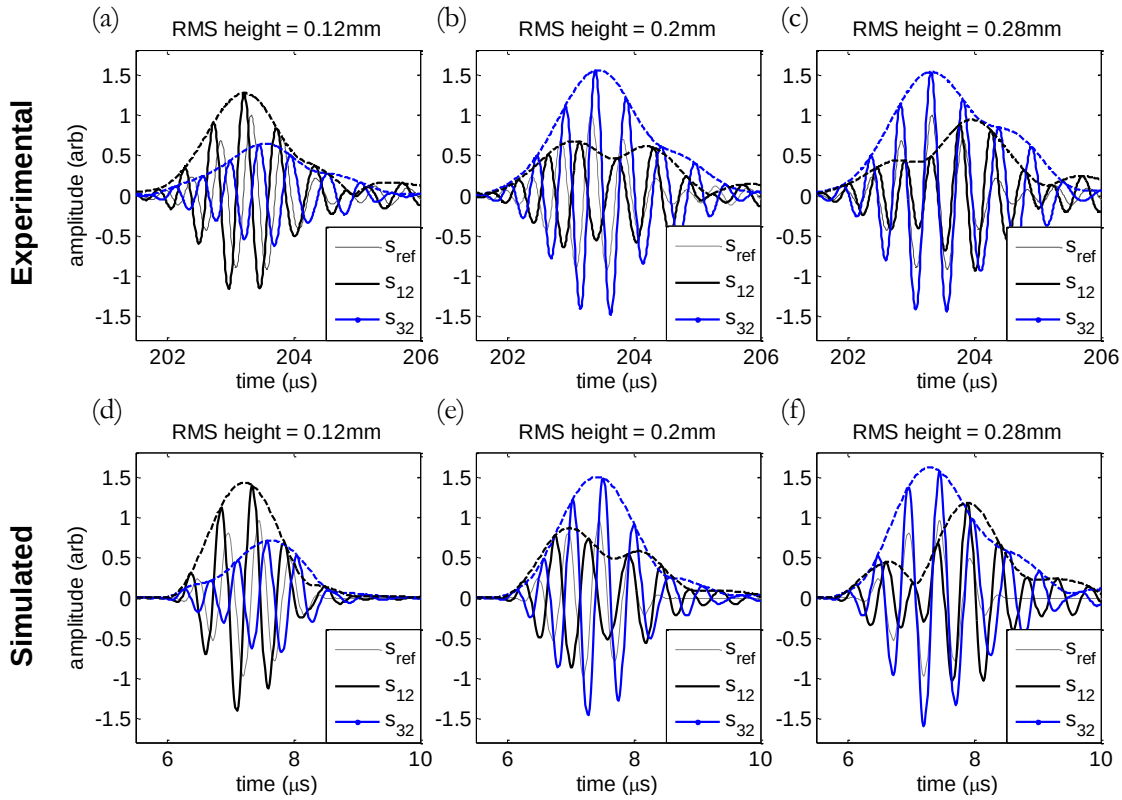

Figure 3.11: Experimental signals showing the reflected SH wave pulse from a one dimensional sinusoidal surface with a surface wavelength of 4mm and RMS heights of (a) 0.12mm, (b) 0.20mm and (c) 0.28mm. Simulated signals obtained using the two dimensional scalar wave DPSM model from the same surface with RMS heights of (d) 0.12mm, (e) 0.20mm and (f) 0.28mm. Dotted lines show the Hilbert envelopes of each signal.

Experimental signals from both waveguide pairs at RMS heights of 0.12, 0.2 and 0.28mm are shown in figure 3.11 alongside equivalent signals calculated using the DPSM simulation. In each case the signals were normalized to a reference signal s_{ref}, taken as the reflected pulse when the backwall was flat which is also shown in Fig. 3.11 for amplitude and phase comparison. Additionally, it was found that because of the comparatively long length of the waveguides that ambient temperature changes occurring during the course of the experiment caused the arrival times of the surface skimming wave which travels directly from transmitter to receiver to change by up to 0.1μs. In order to isolate changes in pulse shape caused by backwall shape change from those caused by external environmental factors, the temperature compensation strategy presented by Croxford et al [77] was implemented using the surface skimming waves as reference signals since in theory they should not be affected during machining.

It is clear by comparing the shape of the Hilbert envelopes of the signals in Fig. 3.11 that the majority of physical interactions occurring during reflection at the backwall are captured using the scalar wave approach. Taking s_{12} for example, the initial increase in amplitude and subsequent split into two smaller amplitude peaks with the later arriving peak constructively interfering to be higher in amplitude as RMS height approaches 0.28mm is predicted well using the simulation. Similarly for s_{32} the simulation closely matches the experimental results showing the initial decrease in amplitude and subsequent large increase in both pulse maximum amplitude and tail length caused by energy being backscattered from areas on the surface further from the receiver. By inspection the relative phase changes from s_{ref} to s_{12} and s_{32} also appear to match closely.

However differences are clearly evident which are thought to be primarily caused by insufficient mode purity within the waveguide transducers. While experimentally assessing SH0* mode purity within similar transducers by looking at the pulse echo signals reflected from the end of the waveguide, Cegla reports that higher order modes which are around 30dB weaker than the primary mode are observed [26]. These modes which are evident immediately following the surface skimming wave, as illustrated in figure 3.12, have a larger impact when performing pitch catch inspection of a backwall, being on average only 22dB weaker than s_{ref}. Through constructive and destructive interference it is expected that these modes will cause amplitude errors, represented as error bars in figure 3.13 which illustrate the bounds within which the envelope maximum amplitude is expected to lie as RMS height increases. Experimental results for RMS heights lower than 0.12mm have been omitted because it was clear by visual inspection of the machined surfaces that the CAM software used by the milling machine failed to generate the required tool paths.

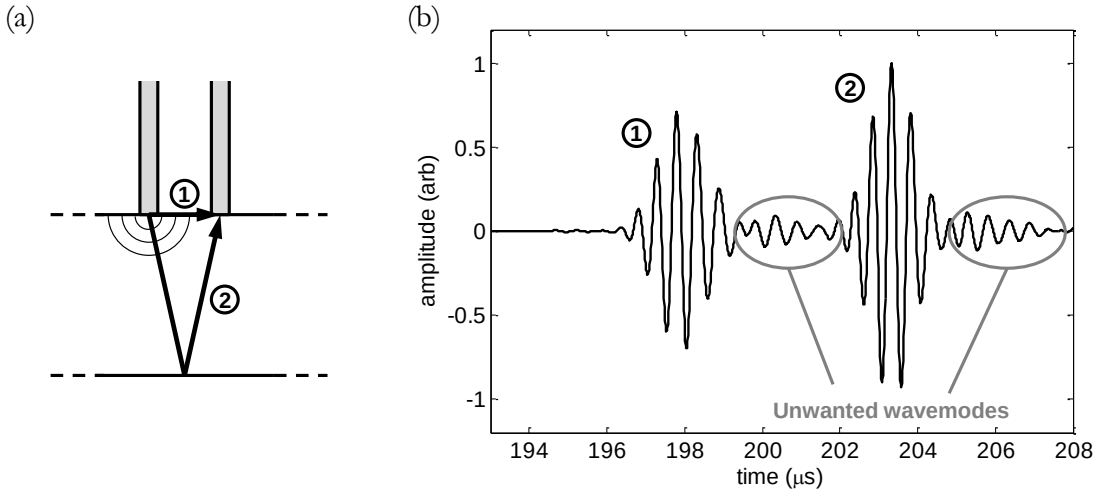

Figure 3.12: (a) Diagram of paths taken by the surface skimming wave and backwall reflection from the transmitter to the receiver. (b) Experimental signal taken when backwall was flat, illustrating the unwanted modes travelling along the waveguides adding coherent noise which is on average 22dB lower than the amplitude of the backwall reflection.

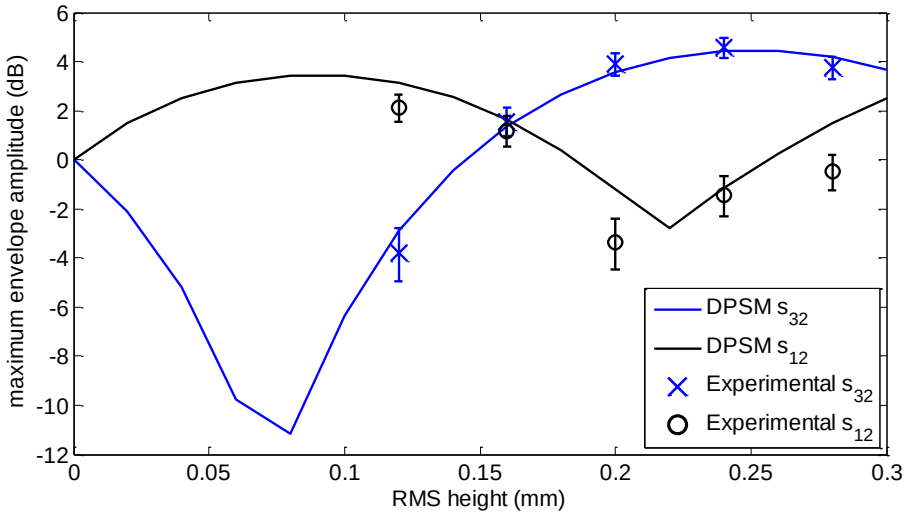

Figure 3.13: Comparison of the maximum envelope amplitude measured experimentally and calculated using the two dimensional scalar wave DPSM simulation for both waveguide pairs within the 3 waveguide array. Error bars represent the -22dB amplitude error that could be introduced by unwanted modes travelling within the waveguides.

The simulated amplitude trend for s_{32} shown in Fig. 3.13 is within 0.9dB of experimental results at all RMS heights; however, agreement is not so close for s_{12}. A 20% reduction in amplitude of the reference signal between waveguides 1 and 2 indicates that coupling quality, and therefore signal quality, is the most likely cause. However, in both cases the amplitude trends and signal shape changes produced using the DPSM simulation match experimental results closely, indicating that the scalar wave approach is valid for predicting SH wave scattering in two dimensional geometries. The large decrease in simulation complexity associated with making the scalar wave assumption is particularly beneficial when studying the effects of surface roughness where ensemble averaging must carried out, therefore making it an important approximation within all subsequent work presented in this thesis.

3.5 Rough Surface Spatial Frequency Content

Before proceeding onto pulse scattering from rough surfaces, it is important to assess the limits of roughness which will have an impact on the shape of the scattered pulse. Many non-dimensional numbers have been suggested as a way of defining the level of roughness, in particular for the purpose of advising when diffuse components will dominate over coherent reflections. The most commonly used is the Rayleigh criterion in conjunction with the Rayleigh parameter, derived by considering plane waves scattering from sinusoidal surfaces. By summing contributions at a target location within the scattered field from all points along a surface, it was proposed that a rough surface could be considered smooth if:

$$k\sigma cos\theta < \frac{\pi}{4} \tag{3.20}$$

where k is the wavenumber, θ is the incident and reflected angle and the value of the left hand side of the equation is known as the Rayleigh parameter [53]. Otherwise the surface should be considered rough and the diffuse field will dominate. For a 2MHz SH wave in steel under normal incidence this suggests that RMS heights above 0.2mm ($\lambda/10$) can be considered rough. As such RMS heights up to 0.3mm ($\sim \lambda/5$) will be considered within this thesis to ensure that the majority of signal coherency is lost. However, the Rayleigh parameter does not consider horizontal length scales

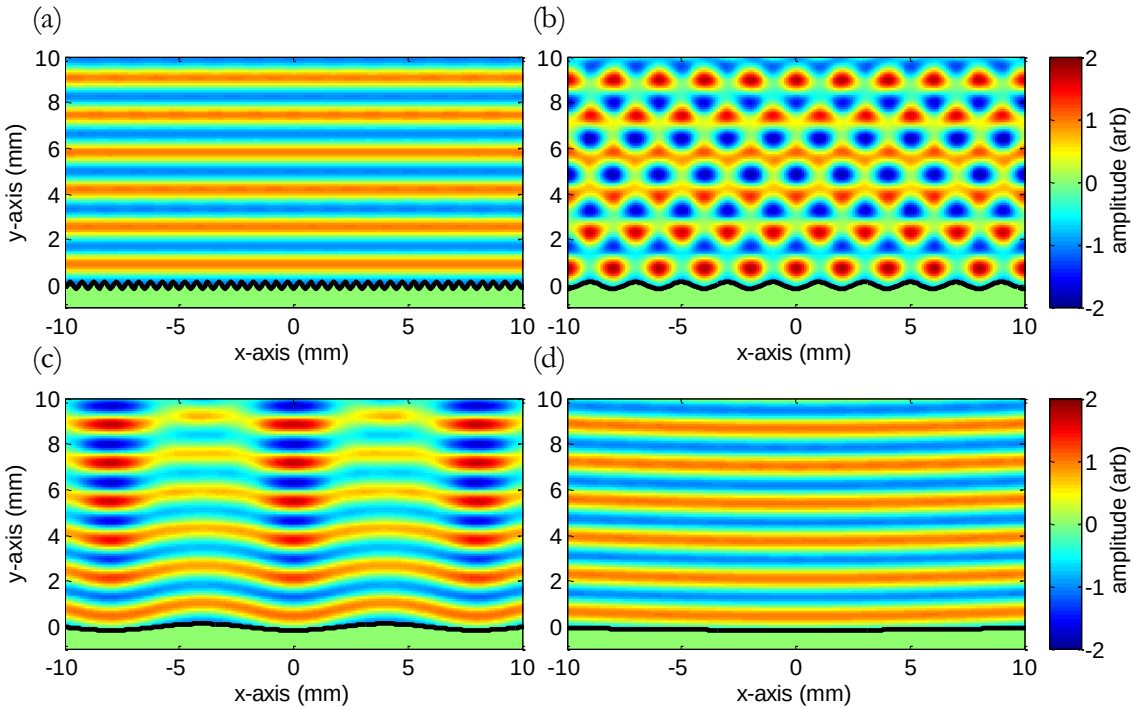

Figure 3.14: Scattered field when a 2MHz plane wave with a velocity of 3260ms^{-1} is normally incident upon a sinusoidal backwall with an RMS height of 0.1mm and a surface wavelength (λ_s) of (a) 0.5mm, (b) 2mm, (c) 8mm and (d) 50mm.

which are more difficult to define in terms of a transition to surface roughness. Factors such as the RMS slope and RMS curvature which incorporate horizontal length measures have been used to define limits on the validity of the Kirchhoff approximation [47, 54], mainly for reasons of multiple scattering; however, they give no indication of the horizontal feature length limits outside which a surface should be considered rough. The challenge faced in defining such a limit is illustrated in figure 3.14, which shows the near field amplitude of the scattered wave field when a normally incident plane wave reflects from sinusoidal surfaces with RMS heights of 0.1mm but with different surface wavelengths (λ_s).

When horizontal feature lengths are much smaller than the incident wavelength, as can be seen in Fig. 3.14 (a), the ultrasound cannot interact with the small features and reflection is identical to that which would be experienced if the surface was flat along the peaks of the sinusoid. Conversely if the features are much larger than the incident wavelength, as can be seen in Fig. 3.14 (d), the surface is essentially flat from the point of view of the incident wave and reflection behaviour is very similar to that of a flat backwall. In between these two limits however, the interference field

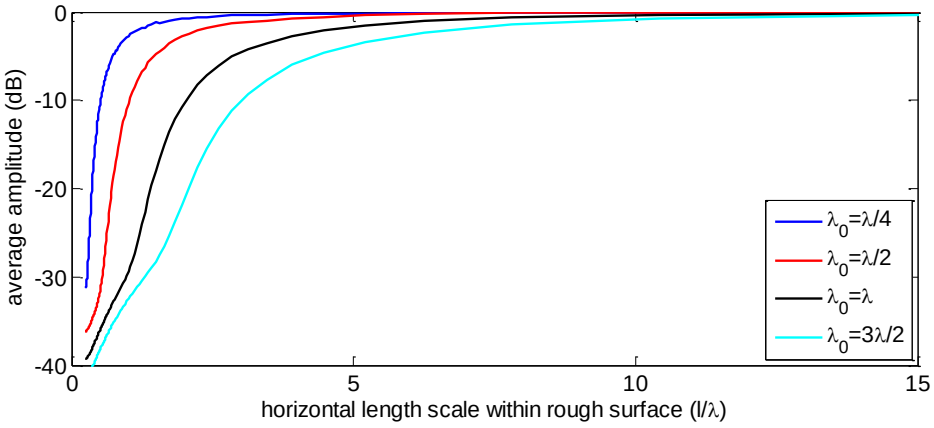

Figure 3.15: Average Fourier transforms of 5000 rough surfaces with the same correlation lengths for various correlation length values, indicating the length scales of features present within the surfaces. Amplitudes are relative to the length scale with the largest contribution to the average spatial frequency content.

can have a very complex structure which is difficult to predict and dependent on the surface wavelength.

When considering rough surfaces, the interference patterns become much more difficult to predict since the surface structure contains features of varying length scales. This is illustrated in figure 3.15 where the spatial frequency content of rough surfaces described using Gaussian height and length characteristics has been analysed by calculating the Fourier transform of 5000 rough surfaces generated using the same correlation lengths and RMS heights and averaging their result. The relationship illustrates that the correlation length parameter performs as expected, effectively acting like a length-scale high pass filter, allowing features with longer lengths to remain in the final rough surface during the moving average procedure described in section 2.4. However, it also indicates that various length scales act concurrently during ultrasonic wave reflection from rough surfaces to produce very complex scattered fields. Therefore it can be concluded that RMS height is the dominant factor in establishing whether a surface should be considered rough using equation 3.20, and whether diffuse energy will dominate. Correlation length simply has to be of a similar order of magnitude to the incident wavelength in order for diffuse energy to exist within the scattered field. Within this thesis correlation length will be varied from 0.4mm ($\lambda/4$) up to 2.4mm ($3\lambda/2$) to produce a wide range of surface shapes

for analysis (see Fig. 2.3).

3.6 Summary

The DPSM has been presented as an alternative simulation method for use when investigating how scalar waves interact with rough surfaces in two dimensions. Scattering simulations using classical Kirchhoff theory were identified as the most commonly implemented within literature; therefore a comparison was carried out to highlight the benefits of the new technique. It was found that although multiple scattering, surface self-shadowing and tip diffraction all affect the accuracy of the Kirchhoff approximation, it was the far-field assumption and the need for an arbitrary incident field which most limited its applicability for the rough backwall situation being investigated within this thesis. In all cases the DPSM showed improved accuracy with little increase in required simulation time.

Comparison was also made to simulated results produced using the FEM in order to validate the true accuracy of the technique. A sinusoidal backwall was chosen rather than a rough backwall in order to produce repeatable results with potentially high reflected pulse shape variability based on sensor position. Without any need for scaling, the results produced by the DPSM were indistinguishable from those produced using the FEM at RMS heights up to 0.3mm ($\sim \lambda/5$), providing confidence in the accuracy of the technique. When carried out on the same machine the DPSM calculated each simulated waveform within 3 seconds whereas the FEM took around 130 seconds, approximately two orders of magnitude slower. Based on its accuracy and efficiency the DPSM simulation was the clear choice for carrying out future roughness investigations in two dimensions.

Comparison with experimental results on the same sinusoidal surface was carried out in order to verify that the scalar wave approximation was a valid approach when simulating SH wave scattering in two dimensions. Good agreement in both pulse shape and envelope maximum amplitude trends as RMS height increased was achieved. Unwanted modes travelling within the waveguide transducers were found to be the main source of error; however, the close agreement indicates that the scalar

wave approximation is valid when simulating SH wave scattering in two dimensions by periodic corrugated surfaces. Now that the technique has been experimentally validated, the focus of the next chapter will its application to the practical problem of wall thickness monitoring and what impact corrosion at the reflecting surface can have on thickness estimate based on the ultrasonic data.

Chapter 4

Thickness Monitoring and Surface Roughness Detection

4.1 Introduction

The previous chapter discussed how the DPSM simulation was developed for modelling ultrasonic pulse reflection from rough surfaces. In this chapter it will be used to investigate the uncertainty in measured wall thickness caused by diffuse energy being introduced into the pulse by the rough surface. The altered shape of the reflected pulse affects how accurately the time of flight (TOF) algorithm can distinguish when the pulse is received by the sensor, and therefore the wall thickness estimate produced. This is demonstrated by the simulated results shown in figure 4.1 which shows the working principles of the ultrasonic waveguide sensor, as well as the simulated signal when the inner surface is flat and an example when the inner surface has an RMS height of 0.2mm ($\sigma = \lambda/8$) and a correlation length of 0.8mm ($\lambda_0 = \lambda/2$).

The sensor [30] operates by sending a pulse down one waveguide and receiving along the other (pitch-catch mode) to overcome high coupling losses on transmission into the component wall. If the distance to the inner surface is larger than the separation between the transmitter and receiver, the received signal will record two distinct pulses; the first is the surface skimming wave directly between the trans-

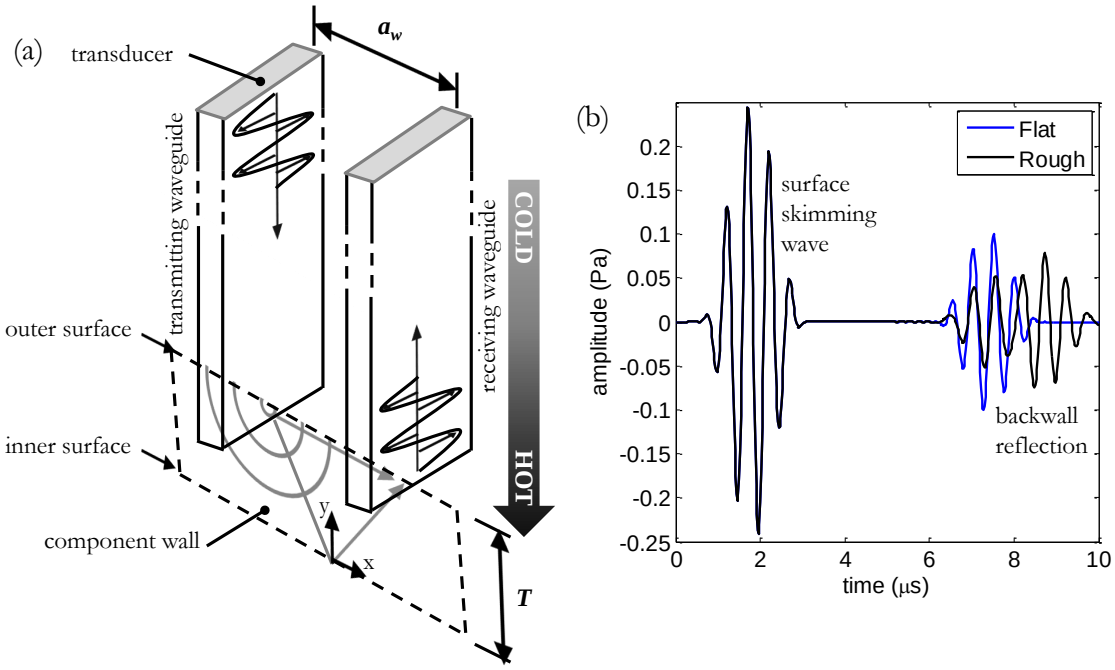

Figure 4.1: (a) Schematic of wall thickness sensor showing paths taken by surface skimming wave and backwall reflection. (b) Simulated signals from a flat backwall and a rough backwall when $\sigma = 0.2$mm and $\lambda_0 = 0.8$mm showing the surface skimming wave and backwall reflection which would be received and used to calculate wall thickness.

mitter and receiver and the second is the reflection from the inner surface (ignoring any material backscatter and multiple reflections between inner and outer surfaces that arrive at later points in time). Once the TOF of the surface skimming wave t_1 and the backwall reflection t_2 are determined, the estimated wall thickness T can be calculated using equation 4.1

$$T = \frac{1}{2}\sqrt{[(t_2 - t_1)c + a_w]^2 - a_w^2} \tag{4.1}$$

Where a_w is the separation between the transmitter and receiver and c is the wavespeed which is linearly dependent on temperature and can be corrected for using known material properties and temperature values [30, 78]. Simply through observation of the rough surface signal in Fig. 4.1 (b) it is clear that any operator or TOF algorithm would struggle to accurately determine the arrival time of the reflected pulse; the value produced depending on what aspect of the signal is being used to make the estimate. Three commonly implemented TOF algorithms will be introduced and applied to simulated signals produced by the DPSM simulation and in doing so will provide stability limits for each algorithm.

Additional to determining the stability of each TOF algorithm under corrosive conditions, it will also be investigated whether the shape change caused by diffuse energy introduced by surface roughness can be used directly to evaluate the uncertainty limits on the thickness estimate. This would increase both information content and confidence in the final value provided. All results presented are for two dimensional scattering from Gaussian distributed rough surfaces and as such should be treated as a worst case scenario for the RMS height and correlation length values quoted. It is expected that for a surface with similar surface statistics in three dimensions that spatial averaging should reduce the extreme effects of roughness (see Chapter 5).

4.2 Scattered Pulse Shape Change Caused by Surface Roughness

The majority of investigations into the effects of surface roughness found in literature consider only monochromatic plane wave scattering, primarily focussing on signal amplitude and reflection coefficient change with incident and reflection angle. In isolation these results give no indication of the shape changes that can occur to pulses in the time domain when reflecting from such surfaces. This severely limits the applicability of such research when signal shape is of primary concern, such as the situation being investigated within this thesis. Therefore, unlike the vast majority of literature our approach focusses on reflected pulse shape change in the time domain, making the results more relevant in practical TOF applications.

4.2.1 DPSM Simulation

A simulation that replicates the sensor setup was created: the separation between the transmitter and receiver was 2mm with estimated 0.5mm contact lengths at the locations where each waveguide couples to the test specimen. To create a single signal at the receiver the reflected pulse is calculated at each target point along the contact and an average signal is calculated. A point source separation of 50μm was used ($a = \lambda/32$), similarly to section 3.2.2, resulting in 533 passive point sources

making up the inner surface which were separated from the true boundary by 1.6μm ($r_s = \lambda/1000$). At each combination of RMS height (0.02 to 0.3mm in 0.02mm increments) and correlation length (0.4, 0.8, 1.6 and 2.4mm) 500 surfaces were generated having the same mean wall thicknesses and the corresponding signals were simulated. Similar results are shown in my paper [31] which used a mean wall thickness of 15mm. To remain consistent with other results given in this thesis, simulations were rerun using a mean wall thickness of 10mm showing little difference in terms of scattered signal shapes and TOF algorithm stability. Therefore relevant excerpts from [31] have been reproduced in sections 4.2.2 and 4.3.2, changing only some numerical values quoted in the results.

4.2.2 Individual Signal Analysis

Figure 4.2 (a), (b) and (c) show the scattered pulses and surface profiles of three realizations of surfaces with an RMS height of 0.2mm ($\sigma = \lambda/8$) and a correlation length equal to the incident centre frequency wavelength ($\lambda_0 = \lambda$). The flat backwall response is shown as a blue line in each plot to serve as reference for the change in pulse shape. It is clear that surfaces with similar statistics can produce scattered pulses with very large fluctuations in amplitude. Figures 4.2(a) and (b) show the signals with the highest and lowest amplitudes in the data set when $\sigma = \lambda/8$ and $\lambda_0 = \lambda$, caused by constructive and destructive interference at the receiver respectively. The shapes of these signals are also quite distorted from the incident pulse; however, Fig. 4.2(c) illustrates that a response can equally show little evidence of scattering by a rough surface. This result indicates that the inverse scattering problem of reconstructing a surface profile from its reflected response would be impossible from a fixed position using a single thickness sensor.

If the correlation length is decreased, other effects can be observed in the signals as illustrated in Fig. 4.2 (d), (e) and (f) which show three signals and corresponding surfaces having the same RMS height ($\sigma = \lambda/8$) but a correlation length of half the incident centre frequency wavelength ($\lambda_0 = \lambda/2$). In this case more features exist on the surface which are further away from the transmitter that act to reflect energy back to the receiver, culminating in more pronounced tails on the signals as illustrated in Fig 4.2(d). This leads to other effects such as pulse stretching and

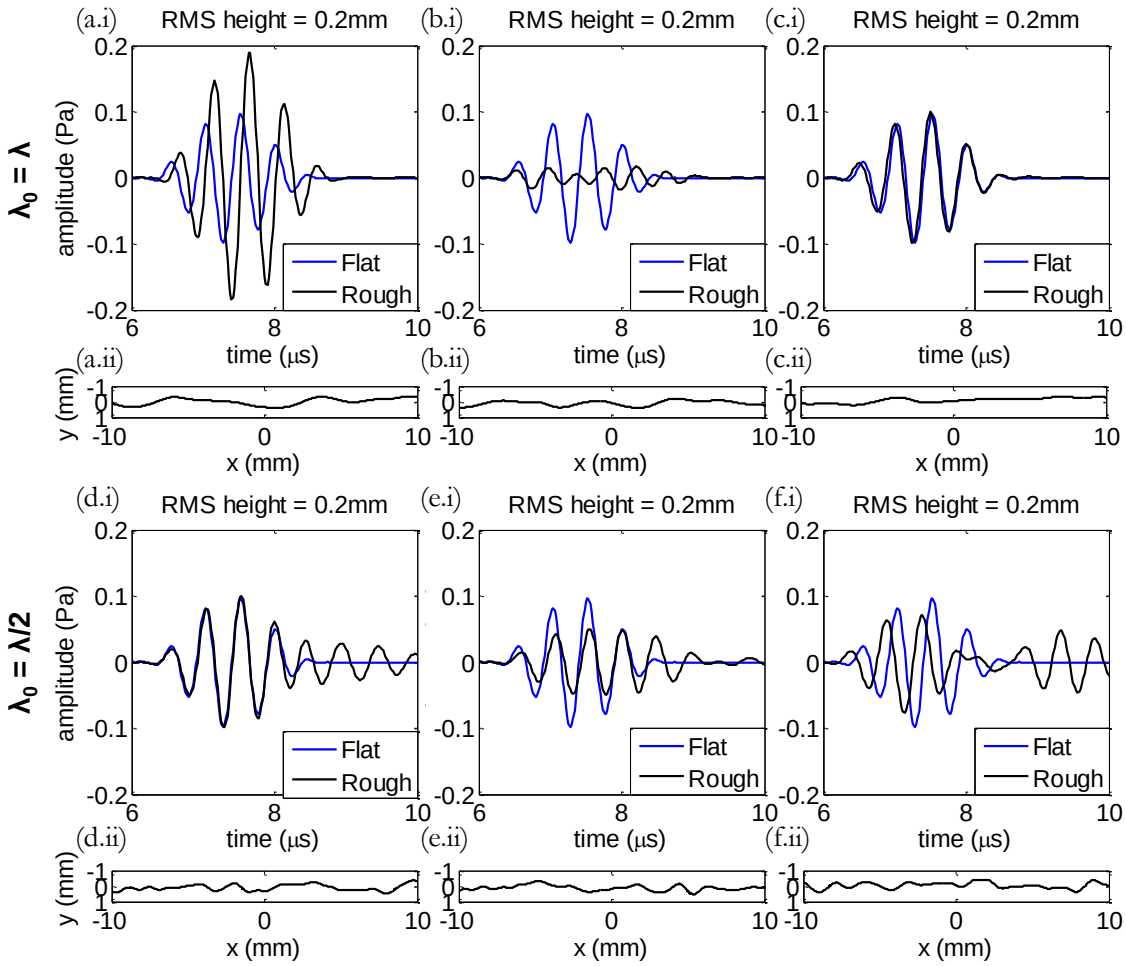

Figure 4.2: Simulated scattered pulse shapes and surface profiles for three surfaces where $\sigma = \lambda/8$ and $\lambda_0 = \lambda$ illustrating examples of (a) high ampltiude (b) low amplitude, and (c) similarity to flat backwall response. Simulated Signals with the same σ value but $\lambda_0 = \lambda/2$ showing examples of (d) energy in signal tail, (e) stretched/offset pulse, and (e) multiple pulses. Each signal is shown alongside the specific surface from which it reflected.

apparent increases in arrival time and overestimation of wall thickness (see Fig. 4.2(e)), the extent of which is dependent on the choice of TOF algorithm. Multiple pulses can also be observed in many signals such as those in Fig 4.2(f), casting doubt over final thickness values and phantom defect responses.

This short summary of potential signal shapes illustrated in Fig 4.2 is by no means exhaustive or representative; the majority of signals contain varying levels of diffuse energy creating an almost infinite number of possible scattered pulse shapes. The general conclusions that can be drawn however are that RMS height has a much greater impact on signal shape and amplitude than correlation length, imparting greater levels of diffuse energy as it is increased. This is further illustrated in Fig

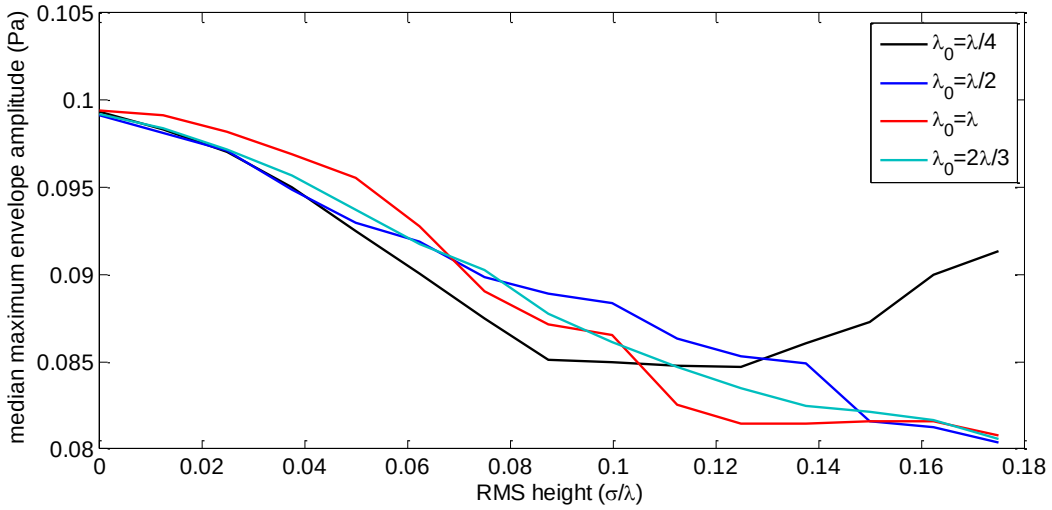

Figure 4.3: Comparison of the median maximum amplitude of Hilbert envelope of reflected pulses from surfaces with RMS heights up to 0.3mm ($\sigma < \lambda/5$) and correlation lengths between 0.4mm and 2.4mm ($\lambda/4 < \lambda_0 < 2\lambda/3$).

4.3 where the maximum amplitude from each reflected pulse is used as a measure of pulse change due to surface roughness. Taking the median value of the distribution at each RMS height decreases the impact of outliers and indicates the most likely change in amplitude which could be expected. It can be observed that pulse amplitude decreases as RMS height increases; this is caused by energy being preferentially scattered away from the receiver as roughness normal to the incident wave increases. However, changing correlation length is seen to have little effect on the most probable amplitude change. The results given in Figs 4.2 and 4.3 clearly illustrate the variability in scattered pulse shape a TOF algorithm might encounter when monitoring the wall thickness of corroded components.

4.2.3 Ensemble Averaged Results

Ensemble averaging is carried out by calculating many signals from surfaces possessing the same σ and λ_0 values and averaging their result. This produces the coherent constituent of the reflected signal, signifying on average what the most likely reflected response would be from such a surface. Subsequently subtracting this coherent constituent from an individual scattered response provides the diffuse

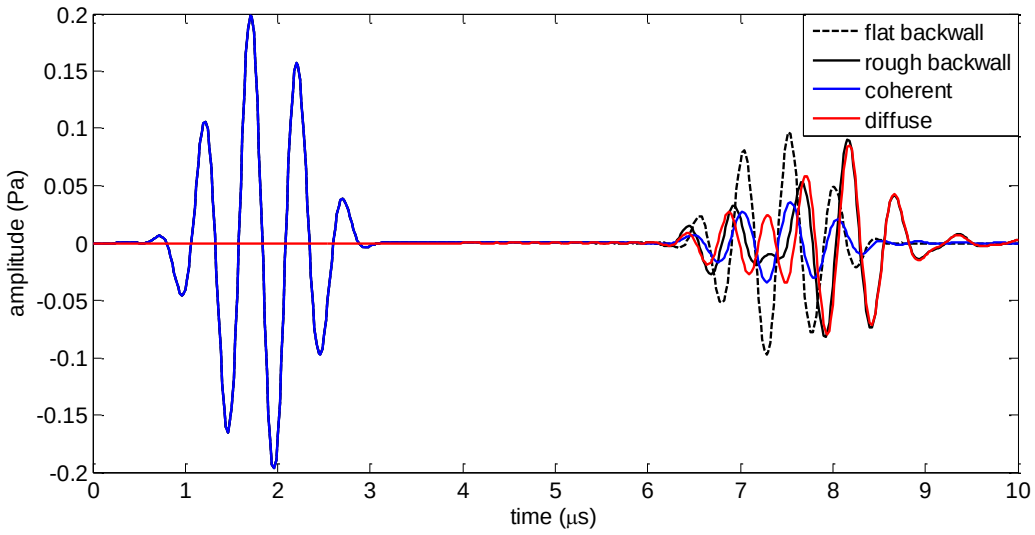

Figure 4.4: Example rough backwall simulated signal, showing the coherent component calculated using 500 simulated signals and the diffuse component.

component of the reflected signal. In general as roughness increases it is expected that coherency should reduce, while diffuse components which scatter from many points on the surface should increase depending on the position of the observer. A comparison of these signal constituents for a time domain pulse is shown in figure 4.4 for a surface with an RMS height of 0.2mm ($\sigma = \lambda/8$) and a correlation length of 0.8mm ($\lambda_0 = \lambda/2$).

Many (if not all) authors who have published work investigating the effects of surface roughness use ensemble averaging to damp out the large variations in amplitude and phase that can occur, thereby producing clear conclusions on the most probable trends that might be observed under given conditions. In a practical sense these results cannot be utilised without the possibility of averaging over a given surface, usually spatially by scanning a probe. In permanently installed monitoring situations this is clearly impractical where signals are only available from a single location. In this case a temporal average could be taken; however, the surfaces are not independent through time, therefore features developing on the surface (assuming gradual change) will affect the signals in a similar way, not allowing ensemble averaging to take place. Accounting for this lack of applicability, ensemble averaged results can give insight into expected changes to signals and therefore will be examined briefly.

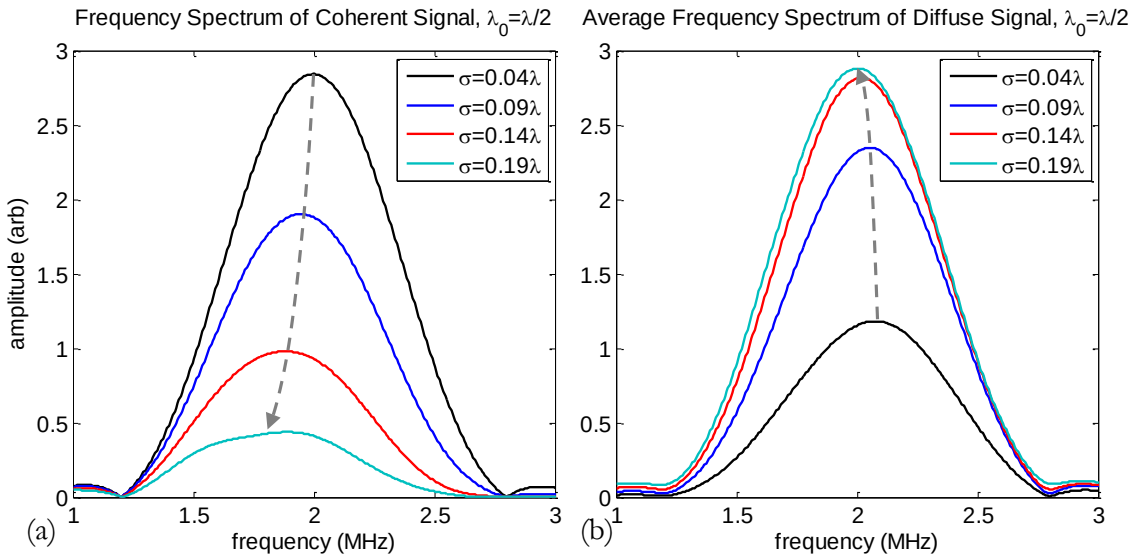

Figure 4.5: (a) Frequency spectra of coherent pulses reflected from rough surfaces with correlation lengths of 0.8mm ($\lambda_0 = \lambda/2$) and RMS heights of 0.06, 0.14, 0.22 and 0.3mm ($\sigma = 0.04\lambda, 0.09\lambda, 0.14\lambda and 0.19\lambda$). (b) Average frequency spectra of diffuse components from the same surfaces.

The coherent pulse is first calculated as the average of all 500 simulated signals from rough surfaces with a particular RMS height and correlation length. Figure 4.5 (a) shows how the frequency spectrum of the coherent pulse changes as RMS height increases for a correlation length of 0.8mm ($\lambda_0 = \lambda/2$). The diffuse component can then be extracted by subtracting the coherent pulse from each scattered pulse. Fig. 4.5 (b) shows the average frequency spectrum of the diffuse components from all 500 simulated results. The peak of the coherent signal shifts towards lower frequencies because the higher frequencies are preferentially scattered leaving only low amplitude, low frequency components. The peak of the diffuse component on average decreases slightly as lower frequency components start to get affected by increasing RMS height; however, it is clear that under these conditions all components are scattered to a similar extent indicating that frequency components within a single signal could not be used as indicators of the level of roughness.

Figure 4.6 (a) compares results from other correlation lengths (from $\lambda_0 = \lambda/4$ to $\lambda_0 = 2\lambda/3$), showing that the peak frequency in the coherent pulse is very similar below an σ/λ value of around 0.14. Above this value the location of the peak frequency was found to vary; however this was due to very low coherent amplitudes

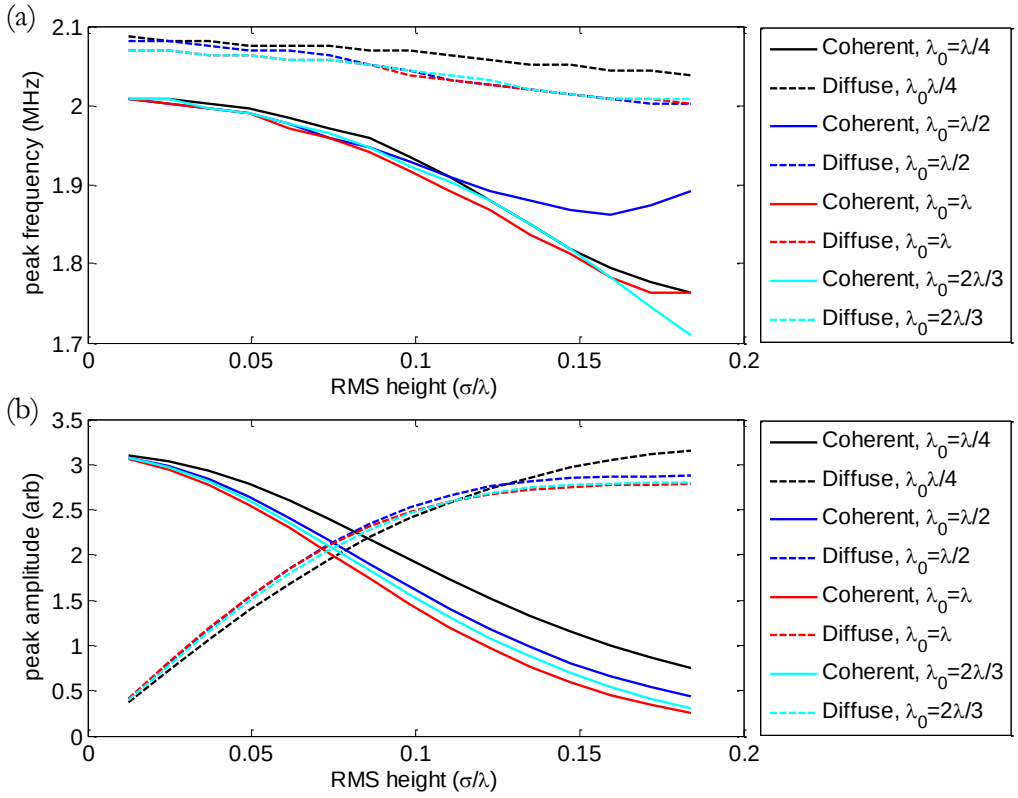

Figure 4.6: (a) Peak frequencies in frequency spectra of coherent pulse and average frequency spectra of diffuse components for all RMS height values (0.02 to 0.3mm in 0.02mm increments) and correlation length values (0.4, 0.8, 1.6 and 2.4mm) investigated. (b) Amplitudes at peak frequencies.

affecting peak location markedly. The peak frequency in the diffuse components are also very similar when $\lambda_0 \geq \lambda/2$ regardless of σ; however below this value the peak doesn't migrate as rapidly towards the lower frequencies which can be seen when $\lambda_0 = \lambda/4$. This is most likely caused by longer wavelength (low frequency) components not interacting as strongly with the shorter features along the rough surface with low λ_0 values.

Figure 4.6 (b) compares the amplitude at the peak within the frequency spectrums for the same simulated results. It can be seen that the coherent amplitude is significantly higher when $\lambda_0 = \lambda/4$. This is likely to be caused by more of the surface on average being orientated such that energy is directed towards the receiver with a low correlation length. With a long correlation length it's more likely that a majority of the signal is directed away from the receiver be it diffuse or coherent, therefore

over many surfaces less coherent energy is received. There could also be an affect of increased multiple scattering at low correlation lengths simply increasing the energy content of the received pulse. Looking at the diffuse component it can be observed that for short correlation lengths and high RMS heights where multiple scattering effects cannot be ignored ($\lambda_0 < \lambda/2$) the diffuse component of the scattered pulse is on average larger in amplitude than the scattered pulse under flat backwall conditions. In general the results in Fig .4.6 show that the frequency content of the coherent and diffuse components within the scattered pulse are much more sensitive to RMS height than correlation length. This is also illustrated by the transition from coherent energy to diffuse energy domination within the scattered pulses occurring consistently at RMS heights around 0.08λ for each of the correlation lengths considered.

4.3 Wall Thickness Gauging

4.3.1 Time-of-Flight Algorithms

The wall thickness measurement estimate produced by an ultrasonic sensor is only as good as the method used to calculate the time of arrival of the reflected pulse, be it an automated algorithm or operator controlled. Many techniques exist for such a purpose; however, only the three most commonly employed digital signal processing (DSP) TOF algorithms will be investigated in this thesis: envelope peak detection, cross-correlation and threshold first arrival:

Envelope Peak Detection (EP) To avoid any errors due to phase uncertainties and frequency shifts the envelope of the pulse is calculated. The time at which the maximum amplitude of the envelope occurs is taken as the TOF. The Hilbert transform was used to calculate the envelope as it is a simple and robust method when dealing with noisy signals.

Cross-correlation (XC) The transmitted signal $f(t)$ is cross-correlated with the received pulse $g(t)$, ensuring that the phase reversal due to backwall reflection is accounted for by multiplying by -1 prior to cross-correlation. For a digitally

sampled signal where $f(t)$ is J samples in length the cross-correlation $C_{fg}(t)$ at sample k is given by equation 4.2.

$$C_{fg}(k) = \sum_{j=0}^{J} g(k+j) f(j) \tag{4.2}$$

The maximum point of the cross-correlation thus gives the point in time where the two signals are most similar in shape, this is then taken as the TOF. Cross-correlation is the optimal DSP technique when trying to isolate a signal hidden by incoherent noise [79]; however it is unclear how well it will deal with coherent noise introduced by corrosion.

Threshold First Arrival (FA) First an envelope is calculated for the pulse to avoid errors which could be caused by phase differences due to noise. Then a threshold amplitude value is selected and the point in time where the envelope first crosses this amplitude value is taken as the TOF. The threshold value is determined by taking the maximum amplitude of the envelope and decreasing in amplitude by a predefined amount, usually between 6 and 20dB depending on signal quality.

To increase precision above the sampling rate the TOF values for each algorithm were calculated using linear interpolation.

4.3.2 Wall Thickness Results

Each of the algorithms described in section 4.3.1 were applied to the scattered pulse data sets. Figure 4.7 shows the box plots for each of the data sets with correlation lengths of 0.8mm ($\lambda_0 = \lambda/2$), indicating the probability distributions of each algorithm at RMS height values approaching 0.3mm ($\sigma < \lambda/5$). Similar box plots for each of the other correlation lengths investigated are included in the Appendix. The interquartile range (IQR) provides a measure of the spread of the wall thickness estimates at each RMS height giving the bounds within which 50% of the results lie; this can be interpreted as the length of the box in the plot. The line within the box gives the median of the distribution and the whiskers represent the range which is identified as not containing any outliers which in this case corresponds to

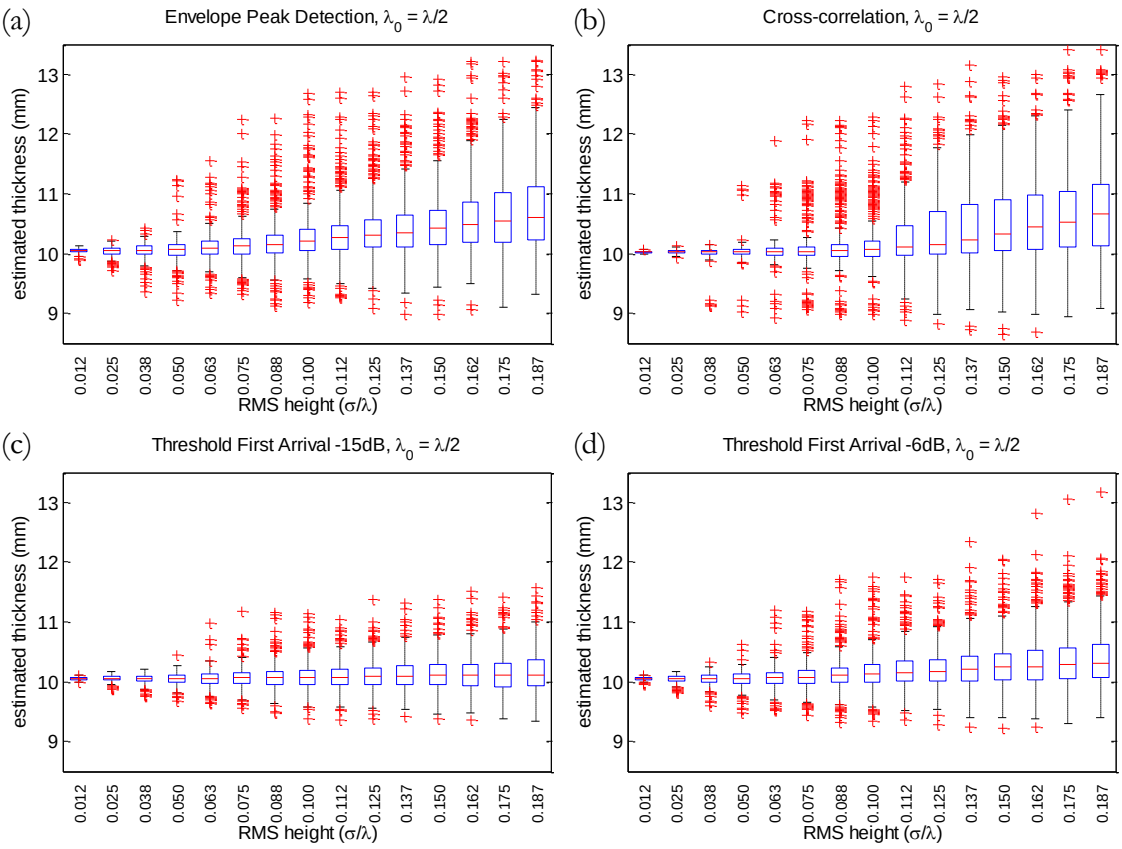

Figure 4.7: Box plots showing the statistical distribution of estimated wall thickness values obtained for a 10mm thick wall with RMS heights approaching 0.3mm ($\sigma < \lambda/5$) and a correlation length of 0.8mm ($\lambda_0 = \lambda/2$ using (a) envelope peak detection (b) cross-correlation (c) threshold first arrival with a -15dB threshold, and (d) threshold first arrival with a -6dB threshold.

99.3% data coverage if it was normally distributed (see for example [55]). Any other results are taken as outliers and plotted individually.

Fig. 4.7 (a) shows that the stability of the envelope peaks method decreases steadily from an IQR of 0.04mm at 0.02mm RMS height to 0.89mm at 0.3mm RMS height. The median value also increases from 10.04mm to 10.60mm, indicating a trend to overestimate the wall thickness. Multiple scattering effects and single scattering from features further from the transmitter increases energy content in the scattered pulses later in time than would be expected for a flat backwall response causing this apparent thickening effect. Fig. 4.7 (b) shows the estimated wall thickness values when using the cross-correlation TOF algorithm on the same data. Contrary to the steady increase of IQR exhibited by the envelope peaks method, cross-correlation performs well up to an RMS height of 0.16mm with an increase in IQR of only

0.25mm and a more stable median value. However, past this point it too fails and the IQR rapidly increases to a value of 1.03mm at 0.3mm RMS height, similar to that of the envelope peak detection algorithm. The reason both of these algorithms become progressively worse at estimating the wall thickness at increasing RMS height values is because they rely on pulse shape in order to calculate the TOF, a feature which can be completely altered by the introduction of diffuse energy due to roughness. Cross-correlation performs better at low values of roughness because it is a superior method at distinguishing pulse shapes within signals; however, when almost all coherence is lost (at $\sigma \approx \lambda/10$) both algorithms exhibit similar probability distributions as they are simply finding the location in time where the most amount of energy is detected within the received pulse.

Referring to the signals shown in Fig 4.2, one feature that remains roughly constant is the time of first arrival. This is because the points on the surface which contribute earliest to the reflected pulse have the shortest cumulative distance from the transmitter and back to the receiver. Irrespective of scattering elsewhere, these points of closest approach are generally going to occur in the same area; directly below the two pitch-catch transducers. Fig. 4.7 (c) and (d) show how this first arrival methodology performs on the same data as the envelope peak detection and cross-correlation algorithms, displayed on the same axes scales to allow for direct comparison. Fig. 4.7 (c) shows the distribution when a -15dB threshold level is taken as the point of first arrival, exhibiting a much improved IQR of 0.43mm at 0.3mm RMS height and a median value that remains within 0.11mm of the nominal value at all levels of roughness. This improvement in both accuracy and precision is closely linked to how low the threshold level can be set to find the earliest arrival in the signal. If the noise floor is high and the level must be raised, it starts to intersect the signal at amplitudes where the shape of the pulse is changing due to diffuse energy emanating from various points on the surface. The algorithm reverts to being a shape detecting method similar to envelope peak detection and cross-correlation and stability suffers as a result. This is illustrated in Fig. 4.7 (d) where a -6dB level is taken giving an IQR of 0.55mm at 0.3mm RMS height and a median that increases with roughness, a distribution shape more similar to that of the envelope peak detection method shown in Fig. 4.7 (a). It is therefore important to reduce other forms of noise as much as possible when implementing TOF algorithms based

on detecting the earliest arrival of a pulse.

4.4 Surface Roughness Detection

Many methods of extracting information about the nature of the reflecting surface were investigated during the course of this thesis. For example, methods of directly extracting RMS height and correlation length values using pulse similarity factor [80] and pulse width were found to work only marginally using worst case signals from the two dimensional DPSM simulation free from any other forms of noise. Frequency scanning of the incident pulse from 1MHz to 3MHz was also investigated, showing limited surface characterisation potential. As such only the most promising technique developed for determining the error bounds of a thickness estimate based on the shape of the reflected pulse will be discussed in any detail here.

4.4.1 Signal Quality Metrics

Unlike array imaging or probe scanning applications, permanently installed ultrasonic thickness monitoring suffers from a lack of data because only a single A-scan is available from which information can be extracted about the reflecting surface. Ignoring how the reflected signal may change over time from a corroding surface (a situation dealt with in section 6.4), only a single signal is available from which an estimate of the thickness measurement uncertainty could be extracted. Therefore only the change in shape of the signal from that which was transmitted to what is subsequently received can be used in such a situation. Three signal quality metrics were found to show some level of correlation with error distribution in the estimated thickness, potentially providing a means of quantifying uncertainty when nothing is known about the state of roughness of the reflecting surface.

Pulse Amplitude The Hilbert envelope of the backwall reflection is calculated to avoid any influence of phase change during reflection. The peak amplitude of the envelope is then divided by a reference amplitude, in this case the envelope peak amplitude when the backwall is flat. A change in pulse amplitude

from what is expected for a particular wall thickness is indicative of corrosion occurring at the inner surface.

Pulse Width Similarly, the Hilbert envelope of the backwall reflection is calculated. The two points in time where the amplitude of the envelope crosses a predetermined threshold (15dB below the envelope peak amplitude in this case) are calculated and the time difference is taken as the pulse width. The pulse width is then divided by the pulse width of the transmitted waveform at the same amplitude level. Increased scattering caused by surface roughness will in general increase the energy within the pulse causing it to increase in length, hence providing a measure of roughness.

Correlation Coefficient First the cross-correlation between the transmitted signal $f(t)$ and the received pulse $g(t)$ is calculated (see equation 4.2). The product of the mean values of each signal is subtracted. The resulting signal is subsequently divided by the standard deviations of $f(t)$ and $g(t)$ and squared to eliminate any negative values.

$$\rho_{fg}(t) = \left[\frac{C_{fg}(t) - \mu_f \mu_g}{\sigma_f \sigma_g}\right]^2 \tag{4.3}$$

Equivalent to the Pearson correlation coefficient [81], $\rho_{fg}(t)$ provides a quantity between 0 and 1 which signifies how similar the received signal $g(t)$ is to the transmitted signal $f(t)$ at time t; 1 representing a perfect match and 0 representing zero shape similarity. This value is calculated at all time samples along the received signal and the maximum value is taken as the quality metric. Lower values indicate increased shape distortion from what is expected based on the transmitted pulse, hence providing a measure of roughness.

Alternative quality metrics were also investigated such as the change in phase angle of the centre frequency and the bandwidth of the reflected pulse; however they were found to show very low correlation to estimated thickness error. The same simulated results as detailed in section 4.2.1 were used, totalling 30000 individual signals scattered from surfaces with all combinations of RMS height (0.02 to 0.3mm in 0.02mm increments) and correlation length (0.4, 0.8, 1.6 and 2.4mm).

4.4.2 Uncertainty Plots and Thickness Error Estimation

To create a plot from which the error in the estimated thickness can be extracted, first the results of thickness error and quality metric for all 30000 simulated signals are placed in order of increasing quality metric; in the case of correlation coefficient this means ordering them from 0 to 1. Figure 4.8 (a) shows the correlation coefficient and the error in estimated wall thickness which occurs when using the envelope peaks TOF algorithm plotted alongside each other after sorting. It is clear that as correlation coefficient decreases, the tendency of the TOF algorithm is to overestimate the thickness, increasing thickness variance as it does so, regardless of the RMS height or correlation length of the surface. To provide quantitative values of the spread of the thickness error data, the full data set is split into sections containing 10% of all the simulated signals (along the x axis in Fig. 4.8 (a)). The 5^{th}, 25^{th}, 50^{th}, 75^{th} and 95^{th} percentiles of each section containing 3000 results is subsequently calculated, along with the mean value of the quality metric within each section of data. Fig. 4.8 (b) shows these values as calculated using results in Fig. 4.8 (a). Figure 4.9 then shows these quantities plotted against one another.

It is proposed that uncertainty plots such as that shown in Fig. 4.9 could be used to estimate the error in calculated thickness when nothing is known about the state of the inner surface of a corroding component. To use the plot an operator or an automated algorithm would first calculate the thickness value and quality metric from the received signal; then, referring to the plot, a line is drawn vertically from the calculated quality metric value, providing an estimate of the error of the calculated thickness based on where the line intersects the percentile values. As an example shown in Fig. 4.9, if the thickness was calculated to be 10mm and the signal correlation coefficient calculated to be 0.95, the most likely thickness would actually be 9.89mm with 50% confidence that the thickness will be between 9.72 and 10.07mm and 90% confidence that the thickness will be between 9.48 and 10.43mm assuming an incident wavelength of 1.6mm (SH wave in mild steel).

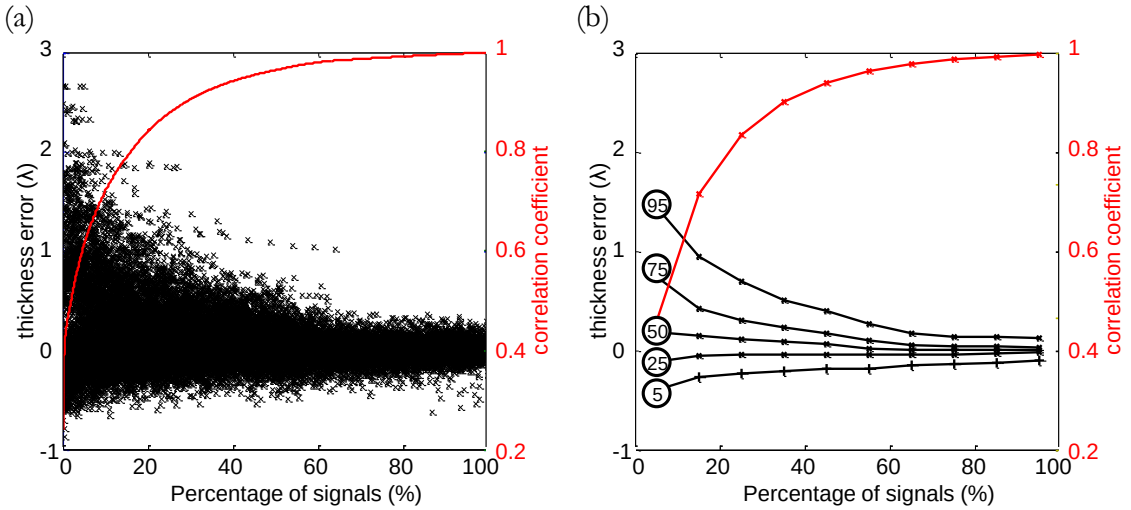

Figure 4.8: (a) Error in thickness estimation relative to incident wavelength when using envelope peak TOF algorithm plotted against corresponding correlation coefficient values for all 30000 simulated results. (b) Black lines show percentile values for each section containing 10% of the signals, percentiles are indicated by the value in the circle. Red line shows the mean values of the correlation coefficient in each 10% section.

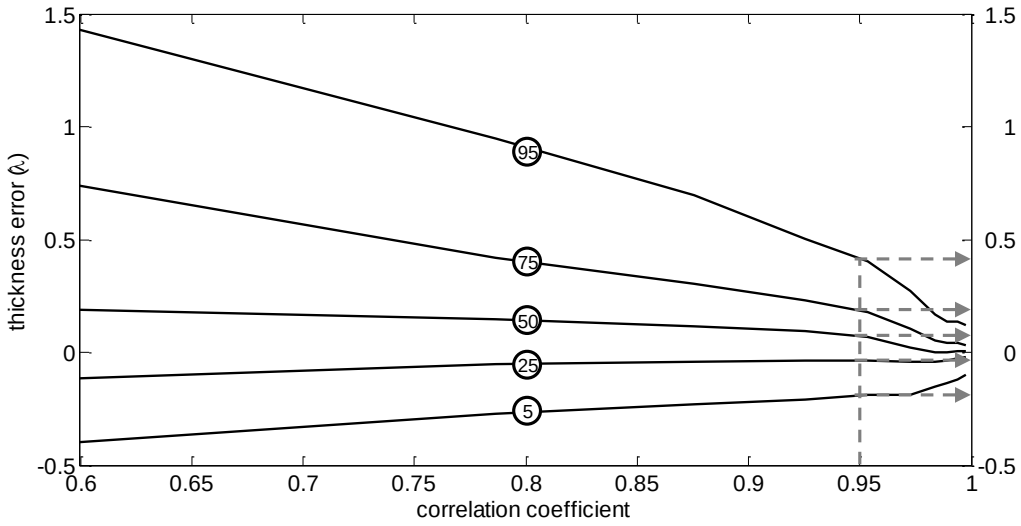

Figure 4.9: Uncertainty plot when using envelope peak detection TOF algorithm for thickness evaluation and correlation coefficient as error metric. Black lines represent the percentile values indicated in the circles. Dotted lines represent an example of how the error bounds are estimated for a correlation coefficient value of 0.95.

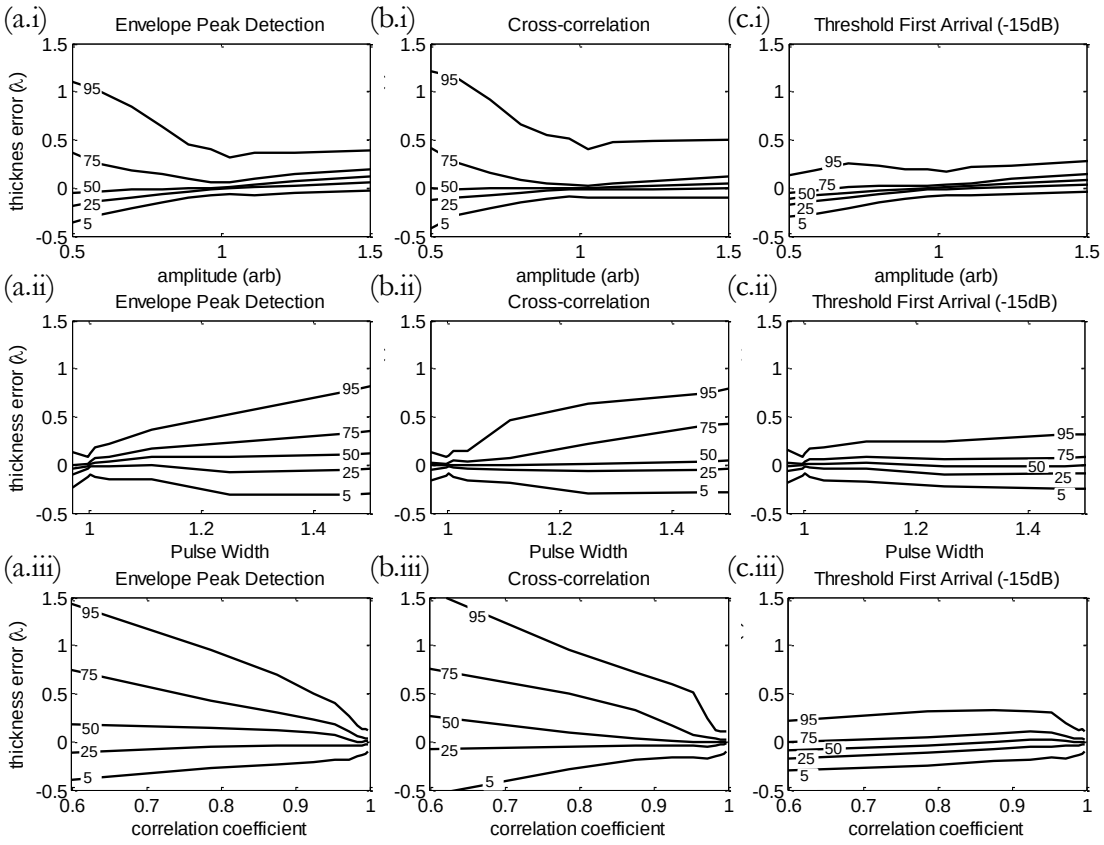

Figure 4.10: Uncertainty plots for (a) envelope peak detection, (b) cross-correlation and (c) threshold first arrival TOF algorithms when using (i) reflection amplitude, (ii) pulse width and (iii) correlation coefficient quality metrics. The black lines from top to bottom in each plot represent the 95^{th}, 75^{th}, 50^{th}, 25^{th} and 5^{th} percentiles respectively.

Each uncertainty plot will differ depending on the TOF algorithm and quality metric being utilised; figure 4.10 shows all combinations of TOF algorithm and quality metric being investigated in this thesis. A number of conclusions can be drawn about the effects of surface roughness on wall thickness estimation by inspecting the plots in Fig. 4.10; the most clear being that the expected variance of thickness estimation reduces when using TOF algorithms based on pulse first arrival, similar to the result shown in Fig. 4.7. Referring to Figs. 4.10 (a.i) and (b.i), if the amplitude of the reflected pulse is higher than expected, the thickness error remains relatively steady; however thickness error increases rapidly as amplitude decreases below the expected level using the envelope peak detection and cross-correlation TOF algorithms. Figs. 4.10 (a.ii) and (b.ii) indicate that in general roughness causes pulse width to increase and as it does so thickness error also increases. It is clear that comparing 4.10 (a.iii) and (b.iii) to the other uncertainty plots that correlation

coefficient is the best technique at distinguishing thickness error based on the clear percentile trends and wider error bounds. However, in practice the choice of quality metric and TOF algorithm depends greatly on the situation being considered and a combination of techniques may be the best option when determining the true thickness and associated error based on signal shape.

4.5 Summary

Results from the DPSM simulation have been analysed in order to provide insight into the reflected signal shape changes that could be expected when ultrasonic thickness measurements are subject to corrosion. Roughness normal to the incident wave (controlled using the RMS height) was found to influence the amplitude and shape of the pulse greatly, whereas features in the orthogonal direction (controlled using the correlation length) determined energy content within the tail of the reflected signal. Analysis of the frequency spectra of ensemble averaged results indicated that the frequency content of a single scattered pulse can not be used to assess the level of roughness of the reflecting surface. An evaluation of three different TOF algorithms concluded that those based on signal first arrival would be the most stable under increasing roughness conditions. Envelope peak detection and cross-correlation both became progressively unstable because they are reliant on signal shape to provide the time of arrival estimate, an aspect of the reflected signal which can be altered significantly by the introduction of diffuse energy by surface roughness. A method for determining error bounds on a thickness estimate when subject to surface roughness was also proposed which uses reflected pulse shape change to asses the most likely error regardless of surface statistics. Calculation of a reflected signals similarity to the transmitted pulse using the correlation coefficient was found to be the most promising measure of error, while signal amplitude and pulse width could also be used with the advantage of being more easily implemented in practical implementations.

It is important to note that simulated signals have been used in this chapter to evaluate TOF algorithm stability and roughness detection methods which are free from other sources of noise, as well as external environmental factors such temperature

and coupling condition. It is expected that these sources of error will alter the stability limits of each algorithm in practice. Of these, unwanted modes propagating along the waveguides, as experimentally observed (see Fig. 3.12), are expected to have the greatest impact, altering the lower amplitude constituents of the reflected pulse making low amplitude threshold first arrival analysis impractical. However, the conclusions drawn from the comparison between each of the TOF algorithms can be used in practice since it is expected other forms of noise should impact all algorithms to a similar extent. The conclusions drawn can also be applied in a more general sense to alternative transducer geometries since it is the shape of the recorded waveform which affects TOF stability, not the architecture of the sensor creating the signal. One further limitation of the results presented in this Chapter is that they have been derived using the assumption of two dimensional scattering. The next chapter will address this by investigating signal scattering in three dimensions.

Chapter 5

Three Dimensional Simulation and Size Considerations

5.1 Introduction

Previous chapters have considered scattering only from rough surfaces in two dimensions; an approach which the vast majority of associated literature also follows due to the complexity of modelling wave scattering in three dimensions. The difference in simulated geometry of each approach is illustrated in figure 5.1. Assuming scattering occurs in two dimensions limits the reflecting surface to vary only over one dimension, causing the equivalent surface in three dimensions to appear corrugated in shape as illustrated in Fig. 5.1 (a). Although this a very powerful approximation for reducing simulation complexity, it has limited relevance when modelling scattering from rough surfaces which are formed by real corrosive processes which have features that vary in shape over two dimensions as illustrated in Fig. 5.1 (b).

The aim of the work presented in this Chapter is to change the DPSM simulation to produce scattered signals from more realistic three dimensional surfaces. In doing so it is expected that the results will more closely match what would be expected when corrosion occurs in reality. However, the complexity of simulating ultrasonic wave propagation in three dimensions make this very challenging and simulation efficiency becomes of primary importance. To illustrate the scale of this problem,

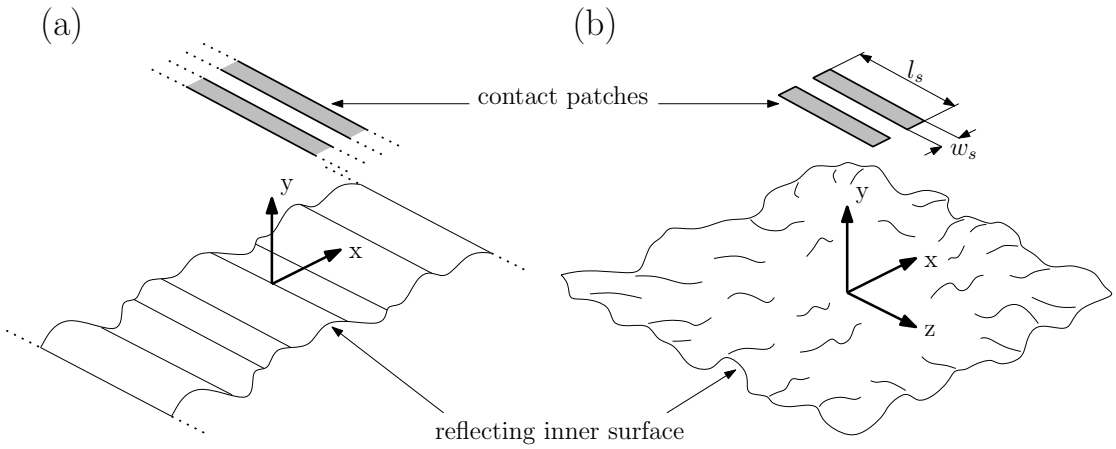

Figure 5.1: Geometry of reflecting inner surface and waveguide contact patches for (a) two dimensional scattering and (b) three dimensional scattering.

if equivalent simulations to those presented within this Chapter were carried out using a standard FEM model, in excess of 40 million degrees of freedom would be required, severely limiting the number of simulated results that could be extracted within a given time frame based on the computational resources available. Kundu et al [56] further demonstrate the implications of requiring so many degrees of freedom by comparing the time taken to calculate the pressure field transmitted by a square transducer in three dimensions, showing that the DPSM is around three orders of magnitude faster and more stable than the FEM. The DPSM simulation for use in three dimensional situations will be presented alongside several efficiency enhancing measures in order for statistical analysis of the scattered data to be carried out within realistic timescales.

The size and complexity of the situation under investigation also limits the current simulation to use only scalar waves. Although this is equivalent to SH wave scattering in two dimensions as described in section 2.2, severe mode conversion due to features in the z direction can make the scalar wave assumption inappropriate in three dimensions, the extent of which is linked to the level of mode conversion being experienced. Simulated results calculated using the scalar wave approximation and experimental results gained using the SH wave transducers are compared to asses the levels of roughness below which the scalar wave assumption can be assumed to be close to valid.

Investigations into the effects of roughness similar to those in the previous chapter are subsequently presented, allowing direct comparison between two dimensional and three dimensional approaches. Upon observation it was found that the shape of the scattered pulses from each approach can be related to one another through an approximate correction procedure, allowing scattered pulse shapes gained by considering scattering in only two dimensions to more closely match those when scattering occurs in three dimensions. TOF algorithm stability analysis and error estimation is then carried out on the simulated results from the previous Chapter after being corrected, therefore improving applicability when considering scattering from real corroded surfaces while reducing the time it would otherwise take for three dimensional simulations by over three orders of magnitude.

5.2 Three Dimensional Scalar Wave DPSM Model

Extending the DPSM simulation that was presented in Chapter 3 from two dimensional geometries to three dimensional is straight forward. Only two major aspects of the way in which the simulation is constructed must be changed:

1. The Greens function for a spherically radiating point source must be used for scattering in three dimensions.
2. The location of the point sources with respect to boundaries becomes increasingly important.

Other than these changes which are detailed in section 5.2.1, the mathematical framework presented in Chapter 3 can be used directly and will not be repeated here.

5.2.1 Spherical Point Source

The DPSM simulation domain is constructed in the same way as in Chapter 3 with the only real difference geometrically being that the third co-ordinate in the z-direction must also be included, as shown in figure 5.2. From a mathematical point of

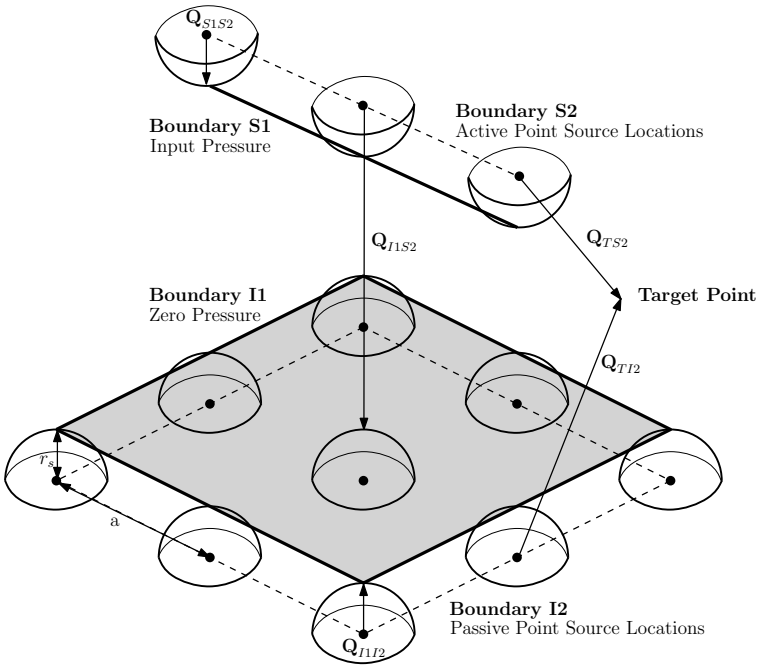

Figure 5.2: Diagram showing how the problem geometry of the DPSM simulation is constructed in three dimensions, illustrating the naming convention of each of the **Q** matrices and boundaries.

view the free space Greens function must also change since propagation is no longer from infinitely long cylindrical sources; instead it is from point sources transmitting waves spherically. The complex amplitude ψ at a target point r distance away from point source m transmitting scalar waves is given by

$$\psi_m(r_m) = A_m \frac{\exp(ikr_m)}{r_m} \tag{5.1}$$

Where A is the amplitude of the point source and k is the wavenumber of the transmitted wave [51]. This equation is simply substituted into equation 3.6 to create the three dimensional scattering version of the DPSM simulation. However, unlike two dimensional scattering where it was found that point source location along a boundary had little impact on signal amplitude, point source location is found to have an inherent inaccuracy in the DPSM simulations capability when predicting reflection amplitude. As shown by Rahani and Kundu [76], this is caused by contributions between source points being ignored making the apparent acoustic pressure transmitted by the transducer have peaks and troughs, averaging to a lower amplitude than intended (around 35% lower than predicted using the analytical solution for

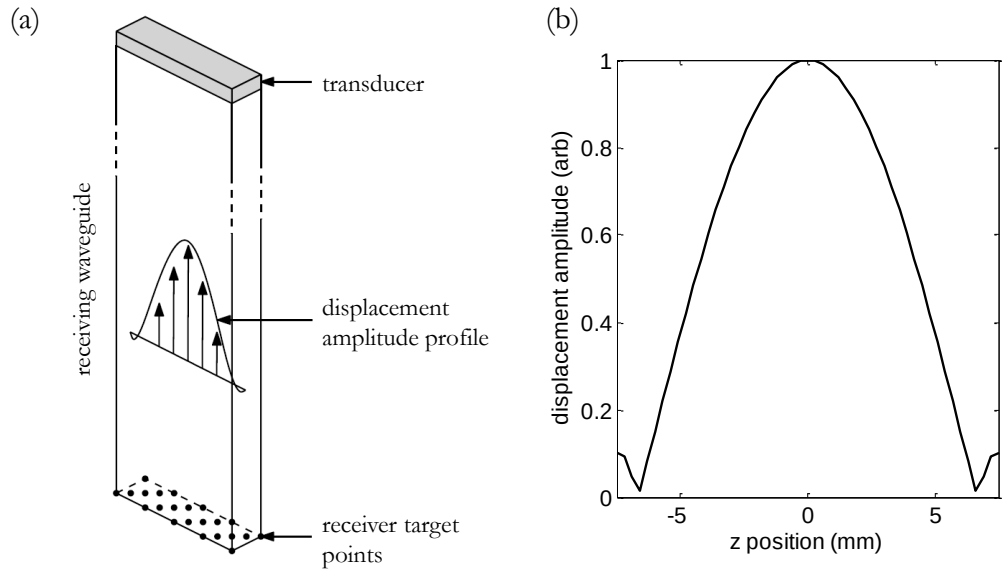

Figure 5.3: a) Illustration of the displacement amplitude distribution as the pulse travels along the waveguide. (b) Amplitude distribution of an SH0* plane wave propagating within a 15mm thick semi-infinite plate as calculated using Disperse.

acoustic pressure along the centreline of a piston source). They propose a method of correcting this without requiring large numbers of point sources by introducing child sources around each parent source to create a Gaussian distributed amplitude profile around each source. Placed in close proximity to ensure these contributions overlap, a uniform amplitude profile over the whole surface of the transducer can be achieved, producing results which closely match analytical theory. However, this process adds another level of complexity to the simulation which takes extra time to solve. It was also determined that relative amplitude would be of primary interest for results presented in this thesis; therefore, although this method could provide more accurate absolute amplitude predictions, it was deemed unnecessary. The approach of the majority of other publications on the DPSM was adopted which was to equate the area of the hemispherical point sources to the equivalent area they occupy on the surface which for sources in a grid arrangement equates to $r_s = a/\sqrt{2\pi}$. Further information on point source location along boundaries can be found in [65] and Chap. 1 of [51].

Following the same steps as outlined in Chapter 3, the signal can then be simulated using the three dimensional version of the DPSM at all the target points making up the contact patch of the receiving waveguide. To produce a single simulated signal an

average of each of these constituents must be calculated based on the transduction properties of the waveguide. Cegla [26] has shown that wave propagation along wide and thin waveguides can be accurately modelled by assuming plane strain conditions within wide plates remote from any edge effects. Figure 5.3 shows the normalized displacement profile of a 2MHz SH0* (the * representing a strip mode) plane wave propagating within a steel plate measuring 15mm in width as calculated using Disperse [82], giving a good estimate of the amplitude distribution as the pulse travels down the waveguide. Once each of the constituent signals are weighted based on their location within the contact patch, they are averaged to give an estimate of the final signal detected by the piezoelectric element.

5.2.2 Simulation Efficiency

The separation between the transmitting and receiving waveguides of the sensor is 2mm and the transmitted pulse is an SH wave 5 cycle Hanning windowed toneburst with a centre frequency of 2MHz and a wave speed of 3260ms^{-1}. To ensure sufficient temporal separation between the surface skimming wave travelling directly from the transmitter to the receiver and the backwall reflection, a wall thickness greater than 5mm is required. A thickness of 10mm was specified as it was within the operational range of the sensor and provided good quality experimental signals. In order to include the majority of the reflected signal up to the start of the second backwall reflection a simulated signal length of 10μs was defined. Using trigonometry this value resulted in an x-axis length of the reflecting surface of 28mm (17λ). The z-axis surface length was specified by inspection of the beam profile in the yz plane; a value of 16mm (10λ) ensured the simulated result would be almost identical to that of an infinite surface.

The generalized minimum residual (GMRes [83]) method was used to solve equation 3.10 to decrease simulation time as much as possible. Running different frequency components in parallel on 12 processors also improved speed; however when using a point source separation of 100μm it was found that memory requirements exceeded what was available on the machine which had 256GB random access memory and 4 quad-core 2.7GHz processors (AMD Opteron, Sunnyvale, CA). Therefore a method was sought which could improve computational efficiency with minimum impact on

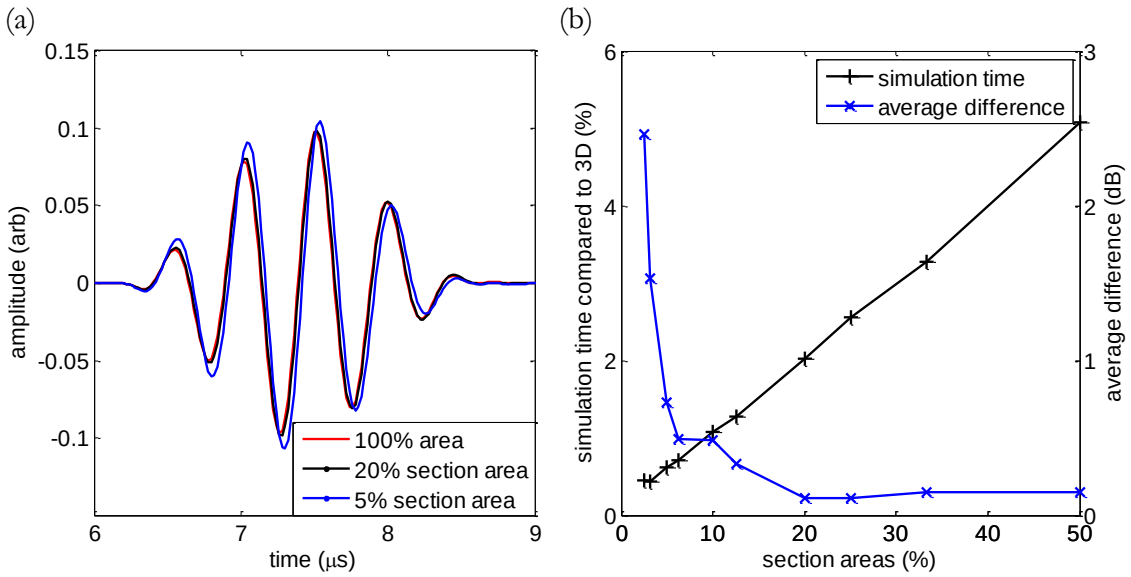

Figure 5.4: (a) Change in reflected pulse shape from a flat surface as subdivided section areas decrease. (b) Average absolute difference of amplitudes within a 20dB bandwidth of the centre frequency as section area decreases compared with original surface, also showing a comparison of simulation time with that of original surface.

simulated result accuracy.

The majority of the time taken is during the solution of equation 3.10 when large matrices are being considered. Similar in theory to the beam superposition technique [84] a method of subdividing the singular large surface into many sections was developed which could decrease memory allocation requirements. During solution the incident field remained constant and the reflected field from each section of the surface was calculated and summed in the frequency domain at all of the receiving target points. Subsequent conversion to the time domain results in a signal which in theory would have reflected from the original surface, minus any interactions between sections such as multiple scattering. In reality the major source of error originates from large calculated amplitudes along edges caused by disregarding reflected contributions from other sections of the surface. The edge sources for each section were made to coincide with the same locations along the joins between sections to mitigate these effects as much as possible.

Figure 5.4 (a) shows how the shape of the reflected pulse from a flat reflector with a passive point source separation of 200μm changes as the number of sections is increased, and Fig. 5.4 (b) compares the time taken and the average absolute

difference in amplitude. The impact on simulation time is considerable; decreasing to 5% of the time that would be required for the original surface simply by splitting it into two sections. The associated difference in pulse shape is also very slight for section areas below 20% being on average below 0.15dB for all frequency components within a 20dB bandwidth of the centre frequency. Above this point differences start to increase rapidly; therefore during all subsequent work presented in this thesis this method was used to split original surfaces into 5 sections, incurring minimal error while decreasing simulation times by approximately 95%. It is understood that rewriting the simulation in alternative programming languages such as c++ or fortran could improve efficiency still further; however the simulation was developed as a proof of concept and built to be as flexible as possible. Using the efficiency enhancing methods described a simulation time of around 1500 seconds per signal from a three dimensional rough surface was achieved, making statistical analysis of rough surface signals a viable option for future investigations into three dimensional scattering.

5.3 Simulation Validation

Numerical methods such as the FEM are unsuitable for large three dimensional simulations at the roughness levels and surface sizes being considered since the mesh would require so many nodes that the simulation would become unfeasible, if not impossible to solve. Considering the inaccuracy of approximate analytical methods in the near field as described in Chapter 3, it was decided that DSPM simulation validation could only be carried out by comparison to experimental results. The added advantage of this approach is that not only would it provide an example of how well the simulation could predict signal shape, it would also give an indication of how well the scalar wave approximation works when predicting SH wave scattering in three dimensions. The same experimental equipment and signal post-processing was used as detailed in section 3.4 and for the sake of brevity will not be repeated here. Further details of this experiment have been submitted for publication in [P6]; as such the relevant excerpts are reproduced in sections 5.3.1 and 5.3.2.

5.3.1 Rough Surface Selection and Setup

A surface with a Gaussian roughness profile was selected for the three dimensional scattering experiment to closely approximate the impact real corrosion can have on reflected pulse shape. For two dimensional scattering from rough surfaces, the coherent component of the signal drops significantly (approximately 7 to 13dB dependent on scattered wavemodes) when $\sigma \approx \lambda/10$, while the incoherent component increases and acts to distort the shape of the reflected pulse [31, 54]. Therefore a maximum RMS height of 0.3mm ($\sigma \approx \lambda/5$) was defined to ensure almost all signal coherence was lost by the end of the experiment. A correlation length of 1.6mm ($\lambda_0 = \lambda$) resulted from calculations of the minimum radius of curvature of the surface, the milling cutter dimensions and the objective of minimising correlation length.

One aim of this experiment was to test the capability of the simulation when predicting reflected pulse shapes in a worst case scenario; this was defined as the surface which exhibited the greatest pulse amplitude difference between neighboring waveguide pairs. The final surface was selected using a sample of 50 simulated results with RMS heights of 0.2mm (selected as the intermediate value where much coherency should be lost) and correlation lengths of 1.6mm. The RMS height of the selected surface was subsequently increased from 0.02mm to 0.3mm in 0.02mm increments while CAD files were created using the same point cloud data as used by the DPSM simulation. These were used to program the CNC milling machine to create each surface sequentially while signals were acquired throughout. The mean plane was adjusted to ensure the entire surface was machined based on the lowest point when viewed by the array.

Figure 5.5 (a) shows a plan view of the depth of the selected surface after the final stage of machining as specified using Matlab. The rectangles shown on Fig. 5.5 (a) are the approximate positions of the three waveguide contact patches before the experiments were carried out. The contact patch location and dimensions can only be approximated beforehand because of difficulties in accurately positioning the array and evenly applying contact pressure to all three waveguides using the welded studs. However, shear couplant which was primarily applied to improve the signal-to-noise ratio of the acquired signals also aided in determining the true location of the array. The areas of highest contact pressure were clearly visible

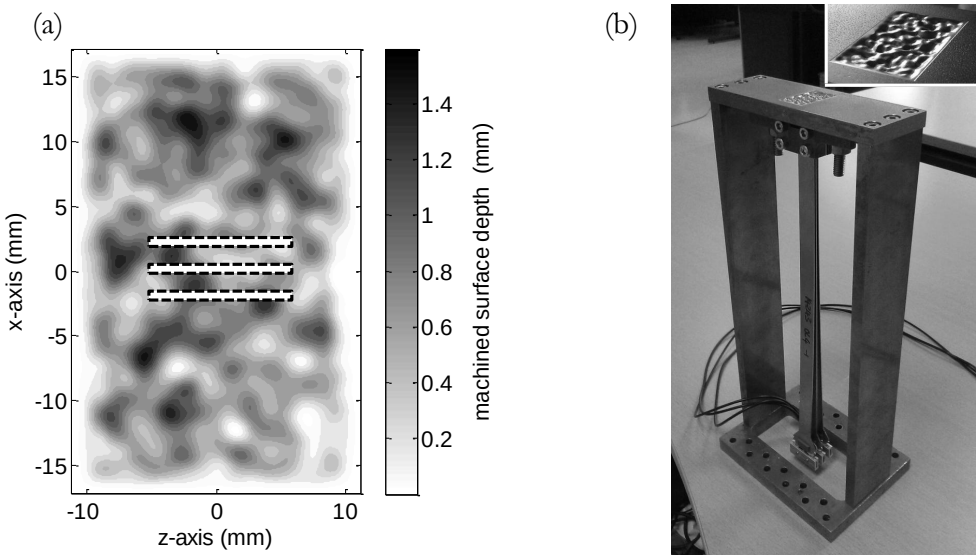

Figure 5.5: (a) Plan view of the final stage of the rough surface machined with RMS height of 0.3mm ($\sigma \approx \lambda/5$) and a correlation length of 1.6mm ($\lambda_0 = \lambda$). Areas within the dotted lines indicate the approximate positions of the contact patches of each waveguide within the array. (b) Photograph of holding jig, array of three waveguides and the test sample after machining, also showing detail view of machined rough surface (inset).

in the couplant once the array was removed, giving an indication of contact patch dimensions and positions. This couplant is not required within high temperature environments where more contact force can be applied. A photograph of the work holding jig used during the experiment is shown in Fig. 5.5 (b) just after the final stage of machining.

5.3.2 Experimental Results

The position of the array and size of the waveguide contact patches were determined by inspection of the shear couplant which remained on the surface of the test sample once the array was removed. An average contact patch measuring 0.5x7mm was defined for each of the waveguides which were offset from their intended position above the centre of the rough surface by 2mm in the z direction (see Fig. 5.5 (a)). These measurements were subsequently used to produce the simulated signals using the DPSM simulation for scattering in three dimensions.

A comparison of experimental and simulated signals at RMS heights of 0.1, 0.2 and

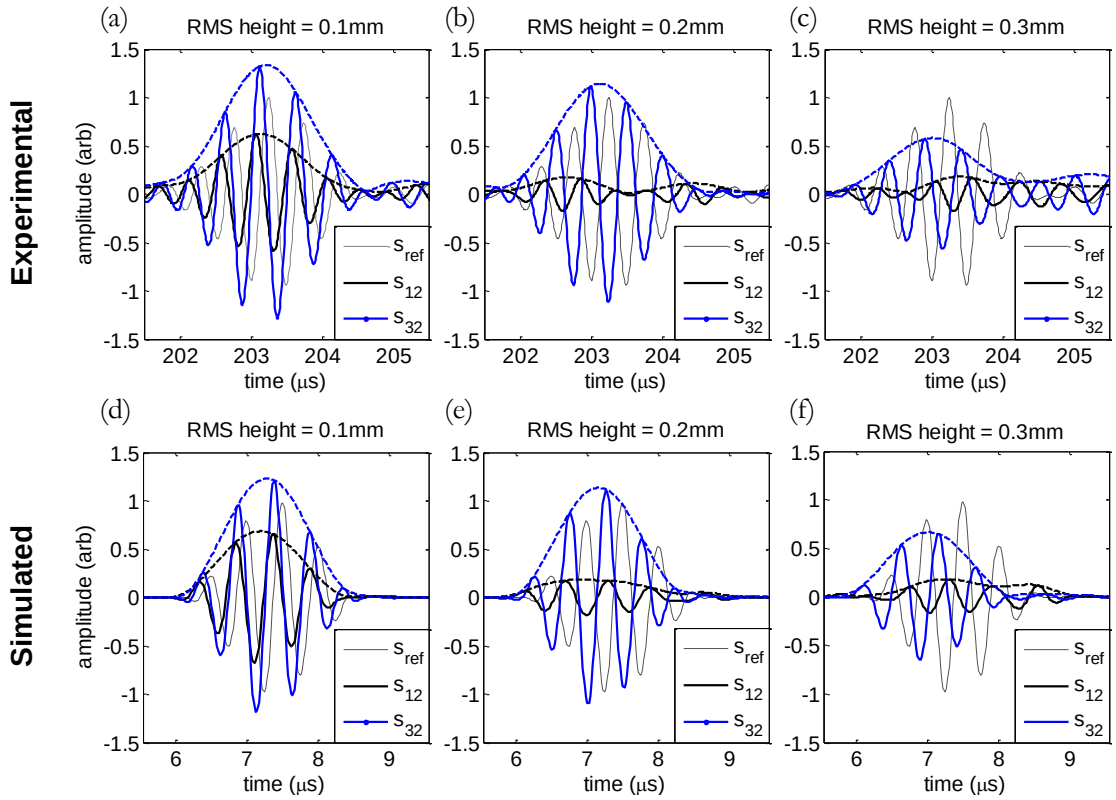

Figure 5.6: Experimental signals showing the reflected SH wave pulse from a rough surface with a correlation length of 1.6mm ($\lambda_0 = \lambda$) and RMS heights of (a) 0.1mm, (b) 0.2mm and (c) 0.3mm. Simulated signals obtained using the scalar wave DPSM model in three dimensions from the same surface with RMS heights of (d) 0.1mm, (e) 0.2mm and (f) 0.3mm. Dotted lines show the Hilbert envelopes of each signal.

0.3mm is shown in figure 5.6 for both of the waveguide pairs within the array. The large difference in amplitude between s_{12} and s_{32} which was predicted and used to select this specific rough surface is evident in both the simulated and experimental signals. At an RMS height of 0.2mm s_{12} has almost disappeared, dropping in amplitude by 15dB due to destructive interference while s_{32} looks relatively similar to the reference signal reflected under flat backwall conditions (s_{ref}) with an amplitude increase of 1dB. Over the range of RMS heights the predicted envelope shapes are very similar to experimental results; for example s_{12} reduces in amplitude dramatically and stretches along the time axis caused by multiple scattering and backscattering of the pulse from areas further from the receiver. In contrast s_{32} retains a pulse-like shape, initially increasing in amplitude but eventually reducing in amplitude, also exhibiting signs of pulse elongation. Similar to results in section 3.4, unwanted modes travelling within the waveguides around 22dB weaker than

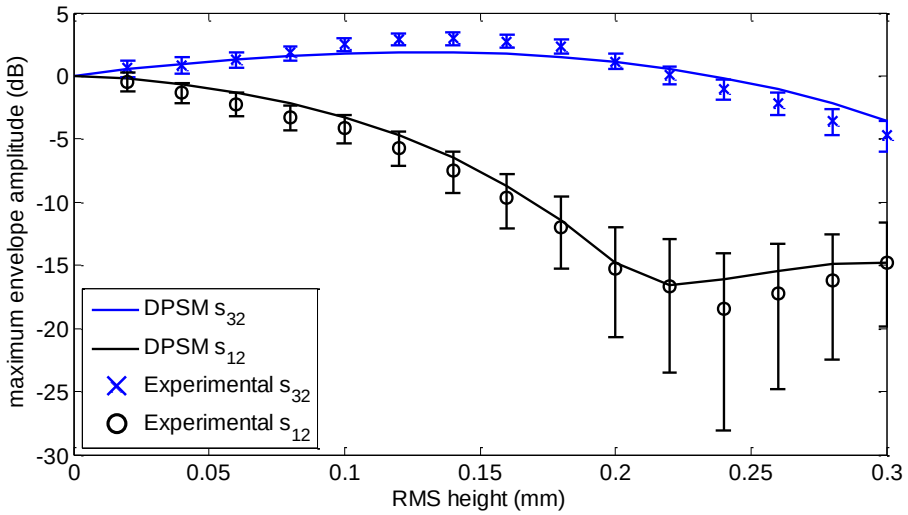

Figure 5.7: Comparison of the maximum envelope amplitude measured experimentally and calculated using the DPSM simulation for both waveguide pairs within the 3 waveguide array. Error bars represent the -22dB amplitude error that could be introduced by unwanted modes travelling within the waveguides.

the reference signal can be observed preceding the backwall reflection changing the shape of the recorded pulse.

The maximum amplitude of the envelopes of each of the waveguide pairs recorded during the experiment as the RMS height of the rough surface is increased by increments of 0.02mm is shown in figure 5.7 alongside simulated results. The error bars represent the amplitude of the weaker unwanted mode signals evident between the surface wave and backwall reflection which corrupt the true shape of the reflected SH wave pulse. The predicted amplitude change of s_{12} is within these error bounds, dropping rapidly by a maximum of 18dB over the range of RMS heights investigated. The amplitude change for s_{32} is also well predicted to within 1.4dB at all RMS heights; however, some results are outside the error bounds indicating other sources of error for which there are multiple possibilities. Most likely is incorrectly specifying the contact shape and dimensions of each of the waveguides during simulation; unlike the rectangular contacts of equal size which were defined, inspection of the shear couplant suggest elliptical ends to the contacts with varying dimensions between waveguides. Not simulating mode conversion is also an obvious source of discrepancy between simulated and experimental results. However, the similarity of

results for this simplified case proved sufficient for our purposes.

The similarity of experimental and simulated results show that the scalar wave assumption is valid in this case for SH wave scattering from a rough surface with a correlation length of 1.6mm ($\lambda_0 = \lambda$) and RMS heights less than 0.3mm ($\sigma <\approx \lambda/5$), suggesting it too is valid for similar surfaces and those with reduced roughness and mode conversion effects along the reflecting surface. Additional experimental results would be required to accurately define validity under increased roughness conditions and other SH wave transducer types. The results shown in Figs. 5.6 and 5.7 should be taken as being close to a worst case scenario for the amplitude and pulse shape variation that could be observed between neighboring waveguide positions. Based on simulated results the pulses received at each position are in general more similar and amplitudes tend to lie between the bounds indicated on Fig. 5.7.

5.3.3 Positional Sensitivity

Simply by comparing signals received from the neighboring pairs of transducers in the three waveguide array it is clear that moving an actual sensor by only 2mm (1.25λ) along a surface with a correlation length of 1.6mm (λ) can have large repercussions on the received waveform. A simulated study was therefore carried out to assess how dependent amplitude values are for this particular rough surface when the array was moved within a 1.8x4mm area around the nominal position. The contact patch size for each waveguide was taken as 0.5x10mm and the RMS height was fixed at 0.1mm, all other variables remained the same as those in section 5.2.2.

The maximum amplitude of the envelope of s_{12} and s_{32} are shown in figure 5.8(a) and (b) respectively. It is clear that sensitivity of pulse amplitude to sensor position is higher in the x axis which can be attributed to the contact dimension being narrower in this direction. Averaging of the received signal in the orthogonal direction over a longer contact reduces the impact of roughness; even so a change in position of 4mm in the z axis from the position occupied during the experiment would have yielded reflected pulses of equal amplitude for both pairs of waveguides. This is clearly illustrated in Fig. 5.8(c) which shows the difference in amplitude between s_{12} and s_{32}, varying by over 8dB within the comparatively small scan area above

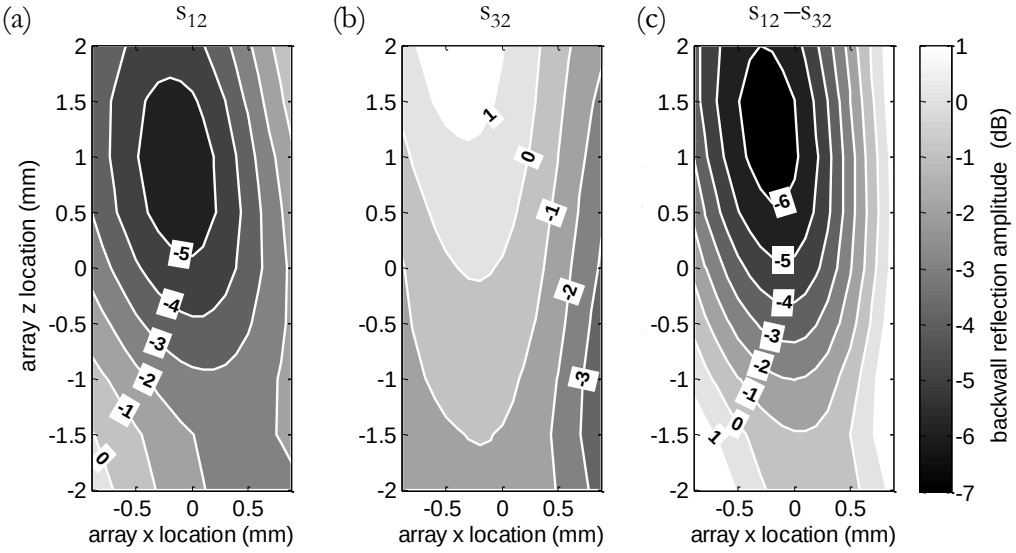

Figure 5.8: Simulated results showing the backwall reflection envelope maximum amplitude when the array is incident upon different positions above the rough surface with an RMS height of 0.1mm for (a) s_{12} and (b) s_{32}. (c) The difference in amplitude between neighboring positions within the array.

the rough surface.

The contour plots shown in Fig. 5.8 only correspond to this particular rough surface which was selected as a worst case scenario based on its reflected pulses having the largest amplitude difference within a sample of 50 results at a single RMS height and sensor position. The sensitivity of reflected pulse amplitude to sensor position is clearly dependent on the specific surface being considered and its associated correlation length, as well as the transducer contact patch dimensions. The results in Fig. 5.8 should therefore only be taken as an example of what could happen when moving a sensor over different positions on a rough surface, not necessarily as the most likely occurrence. The results simply illustrate the dependence reflection amplitude can have on surface roughness, changing by as much as 7dB with a positional change of only 1.25λ in the x axis in this particular case ($\sigma = \lambda/16$, $\lambda_0 = \lambda$). Referring to the experimental results shown in Fig. 5.7 a maximum difference in amplitude of 17dB was observed at an RMS value of 0.24mm, further illustrating the dependence received pulse amplitude can have on sensor position.

5.4 Comparison with Two Dimensional Results

Although a simulation time of under 30 minutes was achieved for each three dimensional scattering simulation, it was still deemed too long for enough simulations to be carried out to ensure ensemble average accuracy over the range of rough surface statistics being investigated. As an example, if simulations were to be carried out in three dimensions over the same number of surfaces, σ values and λ_0 values as in section 4.3, it would take nearly 2 years to complete them all rather than 1 day which it would otherwise take in two dimensions. Therefore an investigation was carried out into whether it would be possible to make simulated results produced in two dimensions more closely match three dimensional results for scattering from rough surfaces with Gaussian height and length characteristics. The availability of a '2D to 3D' correction factor would allow two dimensional results which could be acquired very rapidly to be applied to three dimensional situations more confidently without the need for restrictively long simulation times at all RMS height and correlation length combinations. In a wider sense it could also be used in situations were reflector roughness is an issue but simulations can only be carried out in two dimensions; for example, when using numerical simulations such as the FEM where simulation times would be far too high in three dimensions. For this reason and to be as general as possible, the amplitude averaging process described in section 5.2.1 has not been carried out and it is assumed that the signals received at all points on the transducer face contribute equally to the final result.

5.4.1 Correction Factor

Fifty simulated results were acquired for scattering in three dimensions in order to form ensemble average results at RMS heights of 0.1, 0.2, and 0.3mm (σ = $\lambda/16, \lambda/8, \lambda/5$) and correlation lengths of 0.4, 0.8, 1.6 and 2.4mm (λ_0 = $\lambda/4, \lambda/2, \lambda$ and $3/2\lambda$) with source lengths of 4, 8 and 12mm (l_s = $2.5\lambda, 5\lambda$ and 7.5λ) totalling 1800 simulations. A visual inspection of the signals clearly shows that the predominant difference is that the reflected pulse amplitude and shape variation is much higher in two dimensions. This is illustrated in some example signals shown in figure 5.9. Calculation of the coherent pulse as the ensemble average over all signals at

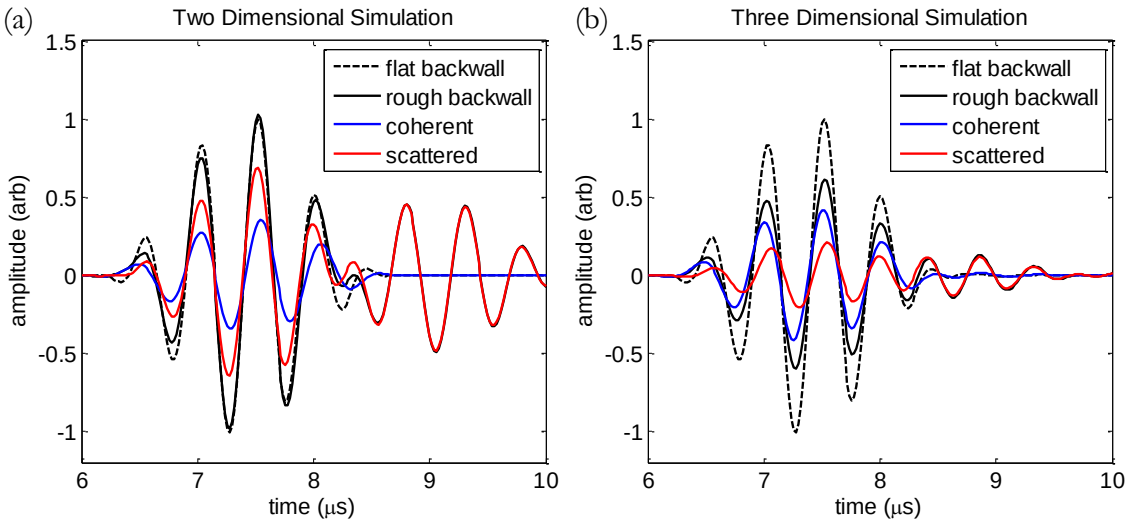

Figure 5.9: Example backwall reflected signals from a rough surface with an RMS height of 0.2mm (σ = $\lambda/8$) and a correlation length of o.8mm (λ_0 = $\lambda/2$) calculated using a (a) two dimensional simulation (b) three dimensional simulation.

a particular RMS height and correlation length (50 in three dimensions and 500 in two dimensions) reveals that these differences are carried predominantly within the diffuse component of each signal since the coherent signals are almost equal between two dimensional and three dimensional results. The measure of signal shape variation was subsequently defined as the ratio of the maximum amplitude of the diffuse component A_{dif} over the maximum amplitude of the coherent component A_{coh}. It is this ratio which defines how much diffuse component should be present within the final reflected pulse at a given RMS height and correlation length value and by altering two dimensional results so that this amplitude ratio more closely approximates the ratio of three dimensional results, so too the shapes of the resulting signals should better approximate what is expected in reality.

The corrugated surface formed by the simplifying assumption is the reason diffuse energy is higher in two dimensional results. A lack of out of plane signal averaging means that the effects of roughness are amplified in the resulting signal with large variations not being damped out as they should be in reality. The reflecting wave interacts with many more points on a rough surface in three dimensions; therefore interactions occurring at the extremities of the surface contribute less to the total signal. It was therefore investigated whether an average of a rough surface in the z

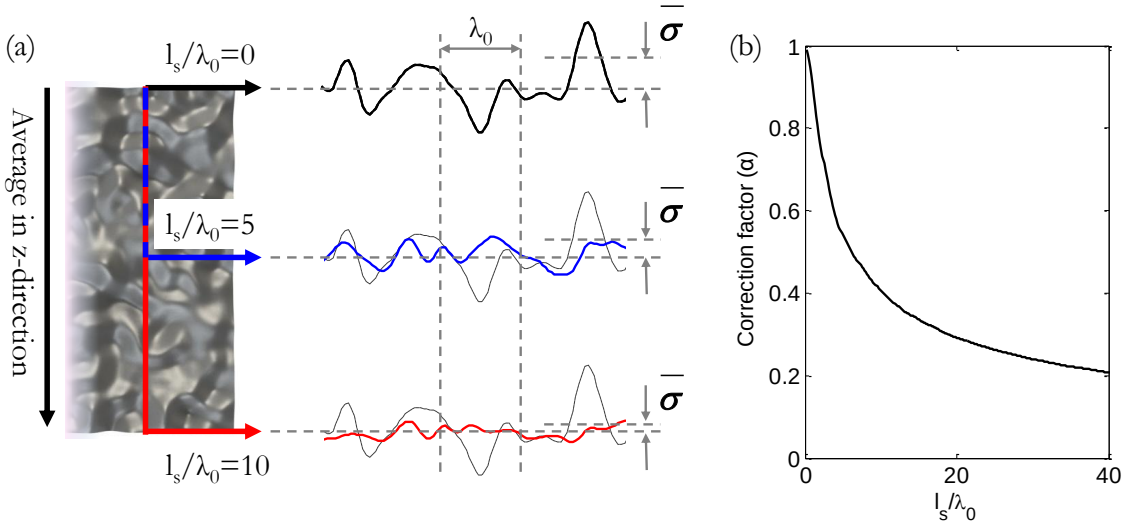

Figure 5.10: (a) Schematic illustrating how correction factor is derived by averaging a Gaussian distributed rough surface along one direction. (b) Correction factor versus source length to correlation length ratio; can be used for any RMS height, correlation length and source length combination.

direction would indicate a reduction in effective RMS height that the sensor would observe because of signal averaging over the length of the waveguides' contact patch. This was carried out by simulating a very large rough surface in three dimensions and calculating the statistics of the resultant two dimensional surface as it was averaged over increasing source lengths in the z direction. The method in which this process was carried out is illustrated in figure 5.10 (a). It can be observed that as source length increases the RMS height of the average surface $\overline{\sigma}$ decreases, the rate of which is directly linked to how many correlation lengths occur within a certain source length. Furthermore, the correlation length remains constant. When plotted against the ratio of source length over correlation length as shown in Fig. 5.10 (b), it is found that the value of $\overline{\sigma}$ when compared with the original three dimensional surface is independent of the initial RMS height σ. The relationship shown in Fig 5.10 (b) is therefore applicable to any RMS height, correlation length and source length combination. This relationship was subsequently used to correct the amplitude of the scattered component in the two dimensional results by defining the correction factor α in equation 5.2

$$\alpha = \frac{\overline{\sigma}}{\sigma} \tag{5.2}$$

The correction factor α represents the reduction in the effective RMS height the sensor observes in three dimension when converted to an equivalent two dimensional surface. Therefore, since diffuse energy is highly dependent on RMS height, this correction factor can also be used to approximate how much the diffuse energy within a two dimensional result should be reduced in order to more closely approximate three dimensional results. For a single two dimensional simulated signal this is carried out in the following steps:

1. The coherent component is calculated as the ensemble average from many simulations on surfaces with similar statistics. This is very straight forward in two dimensions since simulation time is very rapid.

2. The individual signal to be corrected is selected and the coherent component is subtracted leaving only the diffuse component.

3. The diffuse component is multiplied by the correction factor α to reduce its amplitude to what would be expected for three dimensional scattering.

4. The corrected diffuse component is then summed with the coherent component to produce the new corrected scattered signal.

This correction procedure was applied to two dimensional simulated results carried out at the same RMS height and correlation length as the three dimensional simulation, the only difference being that 500 signals were simulated instead of 50 and RMS heights of 0.05, 0.15 and 0.25 were also included to produce smoother distributions to compare three dimensional results to. At each RMS height the diffuse amplitude to coherent amplitude ratio was calculated and the median value taken as the representative value and the interquartile range used to assess data spread. These quantities were chosen in order to minimise the impact of outliers which for distribution populations as small as 50 can have a large impact on alternative measures such as distribution mean. The results for all simulated combinations are shown in figure 5.11 with error bars representing half of the interquartile range about the median value of the distributions.

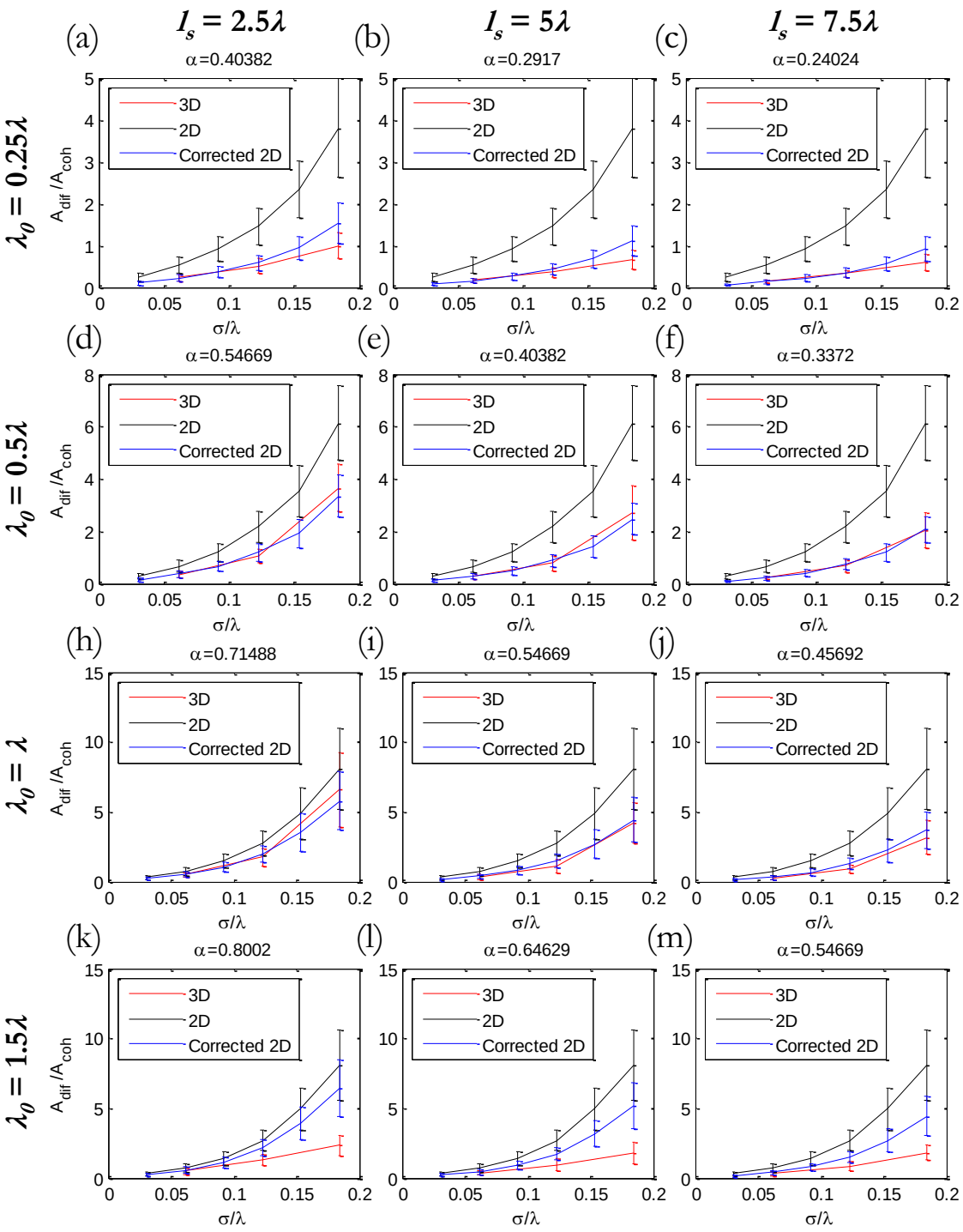

Figure 5.11: Comparison of scattered to coherent amplitude ratio of two dimensional, three dimensional and two dimensional with correction simulated results when (a) $l_s = 2.5\lambda$ and $\lambda_0 = 0.25\lambda$ (b) $l_s = 5\lambda$ and $\lambda_0 = 0.25\lambda$ (c) $l_s = 7.5\lambda$ and $\lambda_0 = 0.25\lambda$ (d) $l_s = 2.5\lambda$ and $\lambda_0 = 0.5\lambda$ (e) $l_s = 5\lambda$ and $\lambda_0 = 0.5\lambda$ (f) $l_s = 7.5\lambda$ and $\lambda_0 = 0.5\lambda$ (h) $l_s = 2.5\lambda$ and $\lambda_0 = \lambda$ (i) $l_s = 5\lambda$ and $\lambda_0 = \lambda$ (j) $l_s = 7.5\lambda$ and $\lambda_0 = \lambda$ (k) $l_s = 2.5\lambda$ and $\lambda_0 = 1.5\lambda$ (l) $l_s = 5\lambda$ and $\lambda_0 = 1.5\lambda$ (m) $l_s = 7.5\lambda$ and $\lambda_0 = 1.5\lambda$.

Clearly without correction the amplitude ratio is consistently higher for two dimensional results as expected; however, once correction has been applied the amplitude ratio of the two dimensional results matches those of the three dimensional results very well for correlation lengths less than 2.4mm ($\lambda_0 < 2/3\lambda$). When the correlation length becomes significantly larger than the incident wavelength, rather than the roughness causing general scattering over the entire sensor footprint leading to signal averaging, few scattering features act more as large isolated defects. As a result the ensemble averaging process becomes increasingly unreliable with insufficient numbers of simulated results, especially for short source lengths where very limited signal averaging occurs along the width of the contact patch. Two dimensional signal correction through the use of an average RMS height is therefore only viable when $\lambda_0 \leq \lambda$. Furthermore, at very short correlation lengths and large RMS heights ($\lambda_0 = \lambda/4$ and $\sigma = \lambda/5$) it can be seen that the corrected results do not match three dimensional results as closely. It is suspected that increased multiple scattering may be the cause since the simple signal averaging methodology does not account for additional scattered components other than those that have made a single interaction at the reflecting surface. All other results show very good agreement indicating that signal correction using this method can be used to approximate how results gathered using two dimensional geometries should look when scattering actually occurs in three dimensions.

It should be noted that this is an approximate technique based on observation and thus direct use of the results shown such as the correction factor relationship should be treated with caution. This process has only been carried out on rough surfaces with Gaussian distributed height and length characteristics; there is no guarantee it would work on surfaces with alternate statistics and full analysis should be carried out in each case. However, the methodology is straight forward and could be applied to a range of other circumstances where three dimensional simulations would be difficult or time consuming; for example alternative transducer geometries, elastic wave scattering etc.

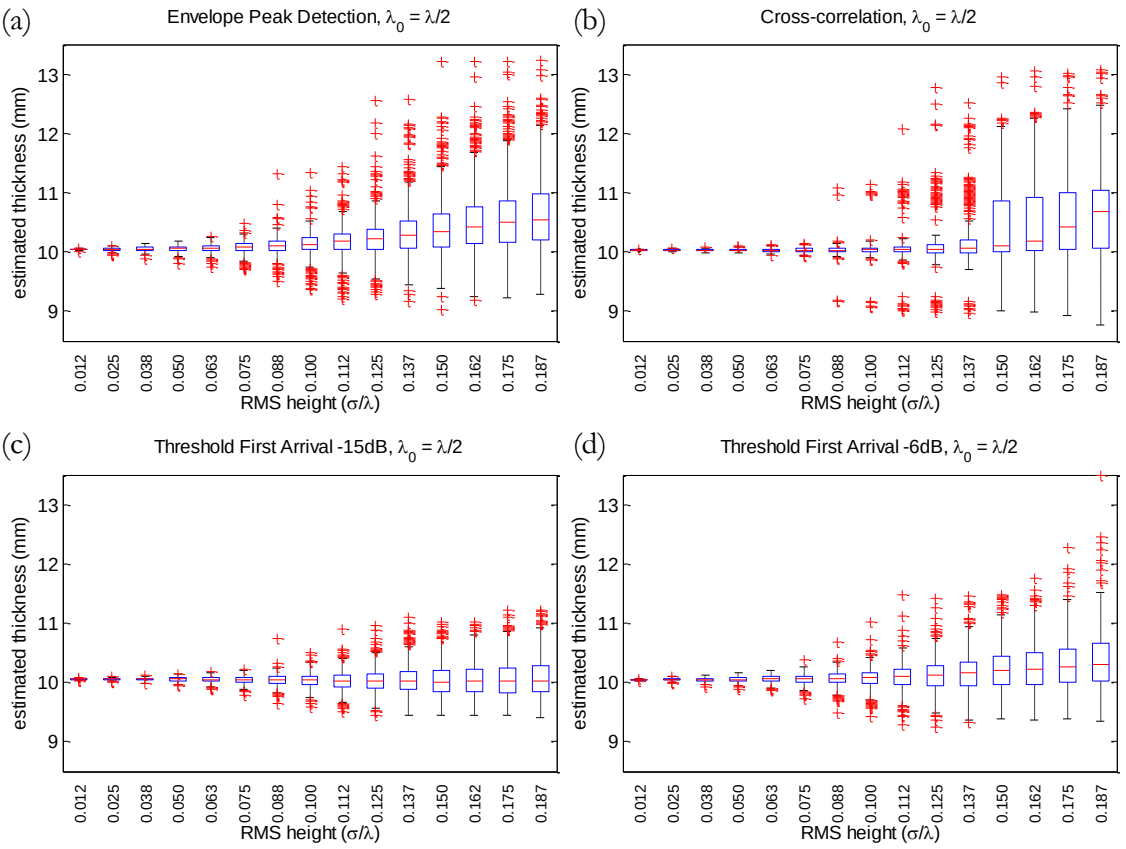

Figure 5.12: Box plots showing the statistical distribution of estimated wall thickness values obtained for a 10mm thick wall with RMS heights approaching 0.3mm ($\sigma < \lambda/5$) and a correlation length of 0.8mm ($\lambda_0 = \lambda/2$ using (a) envelope peak detection (b) cross-correlation (c) threshold first arrival with a -15dB threshold, and (d) threshold first arrival with a -6dB threshold. Simulated signals were obtained using the two dimensional DPSM simulation and corrected using '2D to 3D' correction factor for an assumed source length of 12mm.

5.4.2 Wall Thickness and Roughness Detection

Decreased diffuse energy within scattered signals in three dimensions changes the stability limits of the wall thickness estimation techniques presented in Chapter 4. As such the analysis carried out on the TOF algorithms in section 4.3 has been repeated on the two dimensional simulated results with '2D to 3D' correction applied. The boxplots of each TOF algorithm for surfaces with a correlation length of 0.8mm ($\lambda_0 = \lambda/2$) and an assumed source length of 12mm ($l_s = 7.5\lambda$) are shown in figure 5.12 which is the equivalent of Fig. 4.7 for the simulated results without correction. Similar box plots for correlation lengths up to 1.6mm ($\lambda_0 = \lambda$) have been included in the Appendix.

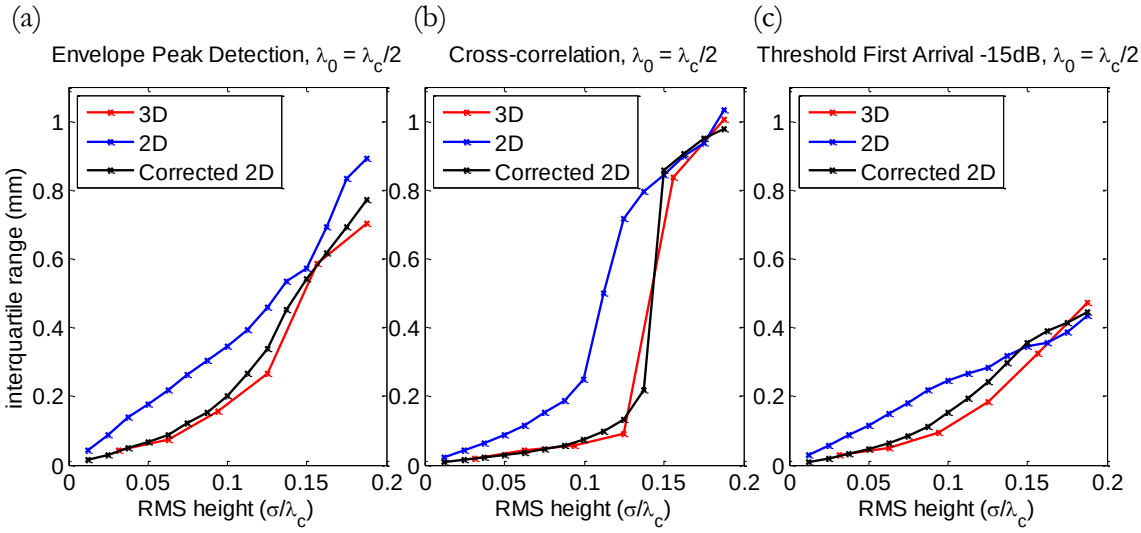

Figure 5.13: The values of the interquartile range for three dimensional, two dimensional and two dimensional with correction as RMS height increases for (a) envelope peak detection, (b) cross-correlation and (c) threshold first arrival with a threshold of -15dB.

Comparing Fig. 5.12 and Fig. 4.7 it is clear that the stability of the TOF algorithms improves for three dimensional scattering, showing more stable median values and reduced spread in the thickness estimate data. This is most evident when comparing the variability of estimated thickness values by using the IQR (length of the box in the plots) which provides the spread of the data within which 50% of the results lie. To illustrate this point more clearly, figure 5.13 compares this quantity for three dimensional results, two dimensional results and two dimensional results with correction.

For each TOF algorithm the value of the IQR as RMS height increases is much more similar when correction is applied. Referring to Fig. 5.13 (a), the almost linear increase in IQR observed for envelope peak detection in two dimensions transforms to a more curved and lower amplitude trend for both three dimensional and two dimensional results with correction. The cross-correlation results in Fig 5.13 (b) show that the transition between low IQR to high IQR and algorithm instability is delayed until an RMS height of around 0.21mm, rather than 0.16mm observed in two dimensional results. The lower IQR values observed in three dimensional results at RMS heights below the instability limit are also accurately predicted using the correction procedure on two dimensional results. Similar to envelope peak detection,

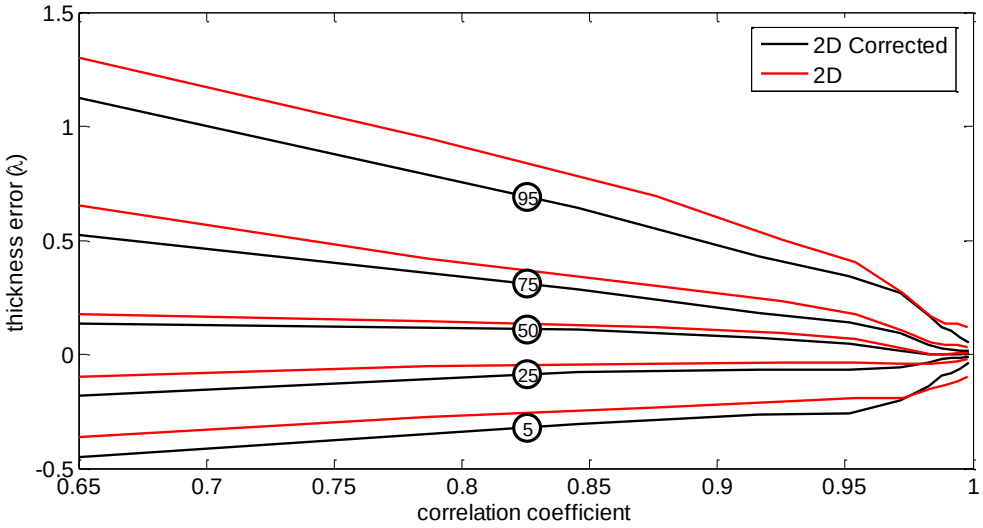

Figure 5.14: Uncertainty plot when using envelope peak detection TOF algorithm for thickness evaluation and correlation coefficient as error metric. Black lines represent the percentile values indicated in the circles when '2D to 3D' correction is applied to results from the two dimensional DPSM simulation. Red lines show the equivalent percentile values for the same results without correction.

threshold first arrival also exhibits a curved trend in IQR as RMS height increases for three dimensional results as illustrated in Fig. 5.13 (c), a trend that is recreated by application of the correction procedure from the otherwise linear trend seen in two dimensional results. Not only do the results in Fig. 5.13 provide confidence that the correction procedure is altering the shape of the scattered pulses in the manner expected if scattering truly was occurring in three dimensions, they also indicate more accurately what stability limits would be expected when the TOF algorithms are applied to field data.

The proposed error estimation technique presented in section 4.4 is also affected by the initial assumption of two dimensional scattering. Carrying out the same procedure as outlined in section 4.4, the equivalent uncertainty plot to that shown in Fig. 4.9 is given in figure 5.14 for two dimensional results with '2D to 3D' correction applied. The black lines show the percentile values as calculated after correction and the red lines are the same as those shown in Fig. 4.9 for two dimensional results to allow direct comparison. The spread of the percentile values is very similar for the two dimensional results with and without correction which is expected since signal shape (correlation coefficient) is what determines error, not the process by which that

particular signal shape occurs. However there is a negative offset for all percentile values after correction. This is caused by the higher amplitude diffuse components in two dimensional results tending to move the energy content of the pulse later in time, therefore causing the thickness error to increase. Similar conclusions can be drawn about the equivalent uncertainty plots as those shown in Fig. 4.10 for corrected results.

5.5 Summary

The DPSM has been applied to scalar wave scattering from a rough surface measuring 17x10λ, equivalent to an infinite surface for a wall thickness of 6.25λ, a wave velocity of 3260ms^{-1} and a simulated signal length of 10μs. Techniques such as beam superposition, frequency component parallelization and GMRes all combine to produce a very efficient simulation resulting in a required simulation time of less than 30 minutes. Comparison to experimental results indicate that for surfaces with roughness satisfying $\sigma < \lambda/5$ and $\lambda_0 = \lambda$, SH wave scattering is accurately modelled using the scalar wave approximation. General trends in reflected pulse shape change as RMS height increases are predicted well with envelope maximum amplitudes being within 2.2dB under all conditions and in general much closer. Unwanted wave modes travelling within the waveguides were found to be the predominant source of experimental error. Comparison of results between neighboring transducer pairs in a three waveguide array illustrates the positional dependence a wall thickness sensor can exhibit when incident upon a rough surface, differing by as much as 17dB in amplitude with a change in position of 2mm (= 1.25λ_0). Simulated results also illustrate the sensitivity pulse amplitude has to sensor location, varying between 1 and -6dB when $\sigma = \lambda/16$.

The shape of scattered pulses obtained from two and three dimensional scenarios were compared. It was found that the coherent components from surfaces with the same σ and λ_0 values had the same shapes and amplitudes, whereas the diffuse components were higher in amplitude but similar in shape when scattering occurs only in two dimensions. Neglecting diffuse components out of the plane amplifies the effect surface roughness has in two dimensions, the level of which is directly linked to

the source length over which the final signal is averaged in three dimensions and the correlation length of the surface. A correction procedure was proposed which is based on the effective RMS height a sensor would observe which reduces as source length increases relative to correlation length. Reducing the diffuse component of the signal by the same amount resulted in the diffuse to coherent amplitude ratio of the signals which were calculated using the two dimensional simulation to much more closely match those from the three dimensional simulation when $\lambda_0 \leq \lambda$. Application of each TOF algorithm showed that wall thickness estimation stability improved when compared with the results of the previous chapter after correction is applied. The trend of the IQR in each case was also well predicted after correction is applied, indicating that the procedure is altering the shape of the scattered pulse in a way which is consistent with actual three dimensional scattered results.

It should be noted that all the results presented so far in this thesis including all TOF algorithm stability boxplots, error estimation uncertainty plots and '2D to 3D' correction have assumed rough surfaces with Gaussian distributed height and length characteristics. This is because they are straight forward to generate numerically using only two control parameters (σ and λ_0) and it has been assumed that the corrosive process creating the rough surfaces proceeds as a collection of random events which over a large area and time span combine to obey Gaussian statistics, even if the individual processes do not follow such statistics [54]. In reality it would be rare to find a corroded surface which truly adheres to both Gaussian distributed height and length characteristics, for instance those which are subjected to predominantly localised corrosion such as pitting. Such surfaces will be the focus of the next chapter.

Chapter 6

Corrosion Propagation and Characterisation

6.1 Introduction

All the rough surfaces created and analyzed in previous chapters have been described by normally distributed random numbers controlled using the RMS height and a Gaussian autocorrelation function controlled using the correlation length. This form of rough surface is widely used in literature as it is a relatively simple and convenient method (as outlined in section 2.4) of fully defining a rough surfaces' shape using just two parameters. However, in reality the shape of corroding surfaces can rarely be described so simply [85]; the focus of this chapter will be on alternative approaches to modelling corrosion propagation in the hope of producing more realistic predictions of how reflected pulse shape may change over time in a single location.

A vast amount of literature exists investigating how different corrosion mechanisms initiate, propagate and cause mechanical components to fail within industrial environments; for instance intergranular, atmospheric, erosion, fretting, formicary, microbiological, pitting, stress, cavitation, hydrogen embrittlement etc. [10]. What follows is a brief summary of the relevant literature relating to naphthenic acid corrosion (NAC), chosen as one particular example of a corrosion mechanism which is observed within high temperature crude oil refinery environments which can in-

fluence ultrasonic wall thickness data gathered by sensors currently installed in the field. Such corrosion mechanisms can lead to areas of pitting which contain localised defects of different shape and size, enacting ultrasonic signal shape changes which differ from those observed during scattering from rough surfaces with Gaussian height and length characteristics. Additional to the safety implications, an independent experimental investigation into such mechanisms was deemed outside the scope of this thesis because of the difficulties that would otherwise be encountered when dealing with highly corrosive substances at elevated temperatures.

As high grade crude oil reserves deplete, refineries are being forced to accept lower grades from 'sour' oil fields [86] with higher sulphur and naphthenic acid contents. The influence of such substances on the reliability of refinery distillation units therefore is becoming an increasingly important issue. Process variables such as metallurgy [87], local flow conditions [88] and temperature [89] all affect NAC which has historically been controlled by blending crude oils with high total acid number (TAN) with other crude oils and those containing sulphur compounds, altering the interaction between NAC and sulphidic corrosion (SC) [90]. Clearly this is not a viable solution in the future where crude oils with higher acid and sulphide content will increase corrosion rates, therefore requiring more frequent low temperature plant inspections in order to ensure no failures occur. However, with greater understanding of how an ultrasonic pulse reflects from a surface subjected to NAC and SC over time, not only would permanently installed sensors provide more accurate corrosion rate estimates improving maintenance scheduling, it could also be possible that information about the size and location of localised defects could be extracted and used to further improve minimum wall thickness estimation. Accurate corrosion rate estimates would also provide an opportunity to implement a feedback loop when using chemical inhibitors [91] to control corrosion, altering their upstream concentration depending on downstream corrosivity.

NAC can be differentiated from SC by the morphology of the attack. SC usually corrodes the exposed area relatively evenly causing more uniform wall loss, a mechanism which is straight forward for the ultrasonic sensors to track. However NAC is typically characterised by more localised areas of attack which often occur where flow rate is particularly high or where condensation of concentrated acid vapors

form in the distillation unit [92]. Damage usually occurs with unexpectedly high corrosion rates forming localised defects and areas of pitting. Such defects are more challenging to accommodate using ultrasonic sensors as it is unclear exactly where the pits are, how large they are and how they will change the shape of the reflected pulse and the associated wall thickness estimate. Trying to quantify the level of reflected pulse shape change that could be expected by introducing localised defects at the inner surface of the wall is the main aim of the work presented in this chapter.

Initial work focusses on a simplified localised defect geometry, specifically a flat bottomed hole (FBH), and the change in reflected pulse amplitude and shape as the diameter and depth of the FBH are varied using the three dimensional DPSM simulation. Experimental work will then be presented which examines the extremes of signal change caused by such defects by machining micron-scale ($\sim \lambda/10$) and millimetre-scale ($\sim \lambda$) pit-like features into test samples as ultrasonic signals are measured. Comparison to the simulated results then provides further guidance on the scalar wave models validity when simulating SH wave scattering from three dimensional features. Focus is then switched to more realistic corrosion geometries and propagation mechanisms. A realistic geometry is selected using scan data taken from a field sample which has been subjected to corrosion within a refinery environment, which is subsequently used to machine profiles of increasing RMS height into a test sample as experimental signals are taken and compared with simulated results. A more realistic propagation mechanism based on a diffusion limited reaction is then presented, allowing conclusions to be drawn about the ability of the TOF algorithms presented in section 4.3.1 to calculate accurate corrosion rates. The possibility of tracking severe corrosion through its effects on reflected pulse shape through time using a single wall thickness sensor is subsequently discussed.

6.2 Localised Defect

The shape and size of localised defects can vary greatly, depending on how corrosion initiates and propagates within the component material. This variety makes specifying a single shape for experimental investigations particularly challenging. Therefore, a single flat bottomed hole (FBH) located directly beneath the thickness

sensor (see Fig. 4.1) was specified for initial investigations as a simple and easily defined geometry from which conclusions could be drawn about the sensitivity the sensor has to such localised defects growing at the inner surface.

To assess the change in reflected pulse shape that could be expected, a simulated investigation was carried out for FBH depths and diameters up to 2λ in size using the three dimensional scalar wave DPSM simulation. A source length of 10mm was defined for all simulated results presented in this chapter with a wall thickness of 10mm to remain consistent with previous results within this thesis. The amplitudes of the Hilbert envelope over the main backwall reflection are compared in figure 6.1 (a), as are the pulse widths at an amplitude level 15dB below the peak amplitude in Fig. 6.1 (b).

Below an FBH diameter of approximately 1.6mm (λ), the depth of the FBH has little impact on the amplitude or pulse width of the backwall reflection. This is because the top surface of the FBH is not large enough to reflect a portion of the pulse of appreciable amplitude to interfere with the main pulse reflecting from the rest of inner surface. Above this FBH diameter however the amplitude of this pulse becomes large enough to cause destructive and constructive interference with the main pulse causing the ripple in amplitude seen for FBH depths of approximately less than 1.6mm (λ). In the region where both FBH depth and diameter are larger than λ it can be seen that only diameter has an effect on amplitude; however, pulse width can be used to distinguish FBH depth since the pulse reflected from the top surface of the FBH is high enough in amplitude to be detected by the -15dB threshold and is arriving earlier in time as depth increases. Simulated signals for the two extreme cases are shown in Figs. 6.1 (c) and (d), defined as the lowest amplitude pulse and the longest pulse width having a FBH diameter of 3.2mm (2λ) and depths of 0.4mm ($\lambda/4$) and 3.2mm (2λ) respectively.

The results shown in Fig. 6.1 illustrate the large impact a single FBH in a fixed position can have on the reflected pulse, depending both on its depth and diameter. Experimental validation of these results was subsequently carried out in order to find the limits of detectability for small defects using the waveguide transducers, as well as to estimate the localised defect size beyond which the scalar wave assumption cannot be used.

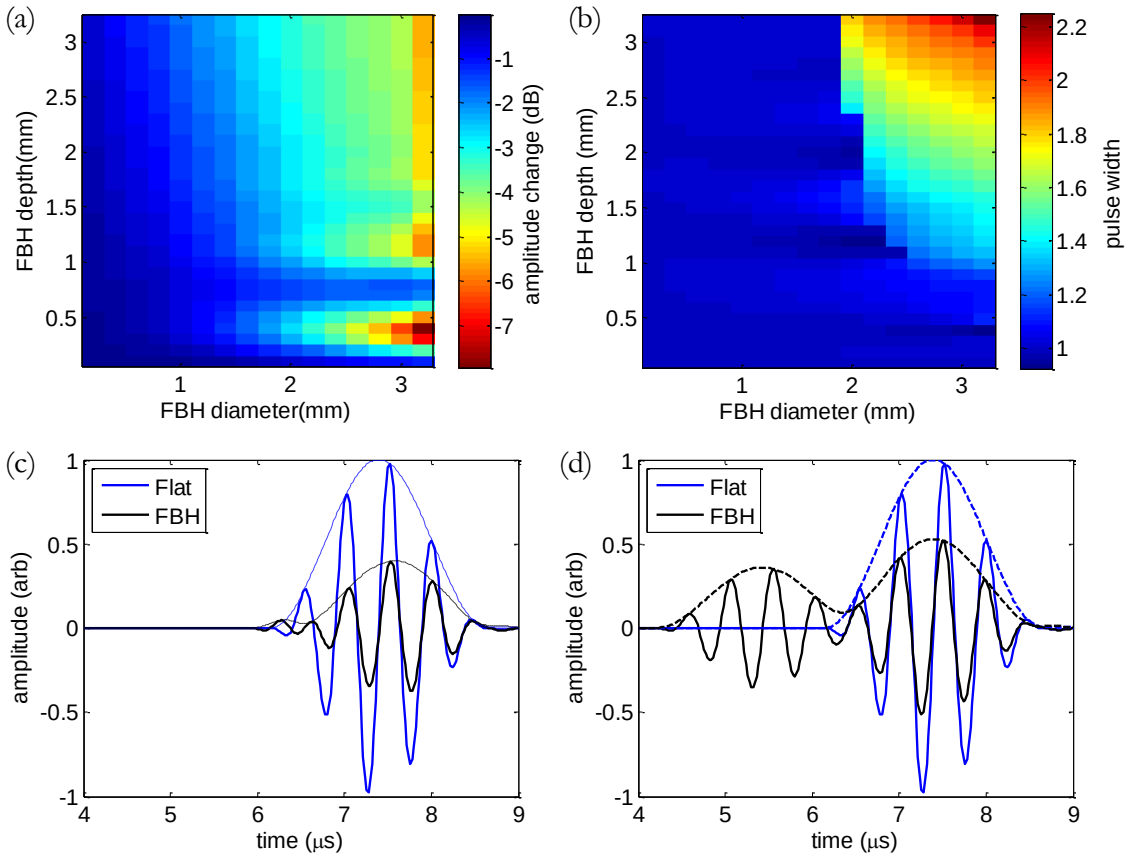

Figure 6.1: (a) Amplitude change of backwall reflection compared with flat backwall conditions. (b) Change in pulse width 15dB below peak amplitude relative to pulse width under flat backwall conditions. Comparison of simulated backwall reflection signals when the inner surface is flat and has a FBH located directly beneath the wall thickness sensor with a diameter of 3.2mm (2λ) and a depth of (c) 0.4mm ($\lambda/4$) and (d) 3.2mm (2λ). Dashed lines represent the Hilbert envelopes of the associated signals.

6.2.1 Small Defect: Laser Micromachined Pit

NAC initiates as small circular defects, often at locations with high flow or concentrated acid condensates. If these vulnerable locations in the stream are predictable, a sensor can be installed to monitor such areas which are expected to have particularly high corrosion rates and localised defect growth occurring. An experiment was carried out to asses the reflected pulse shape and amplitude changes which could be expected in the early stages of NAC initiation. Qu et al [90] show that NAC tends to initiate as hemispherical indentations measuring less than 50μm ($\lambda/32$) in diameter. Using a CNC milling machine to create such a defect would have been unfeasible, therefore it was decided that laser micromachining would be utilised to create small hemispherical indentations in a test sample as ultrasonic signals were taken using

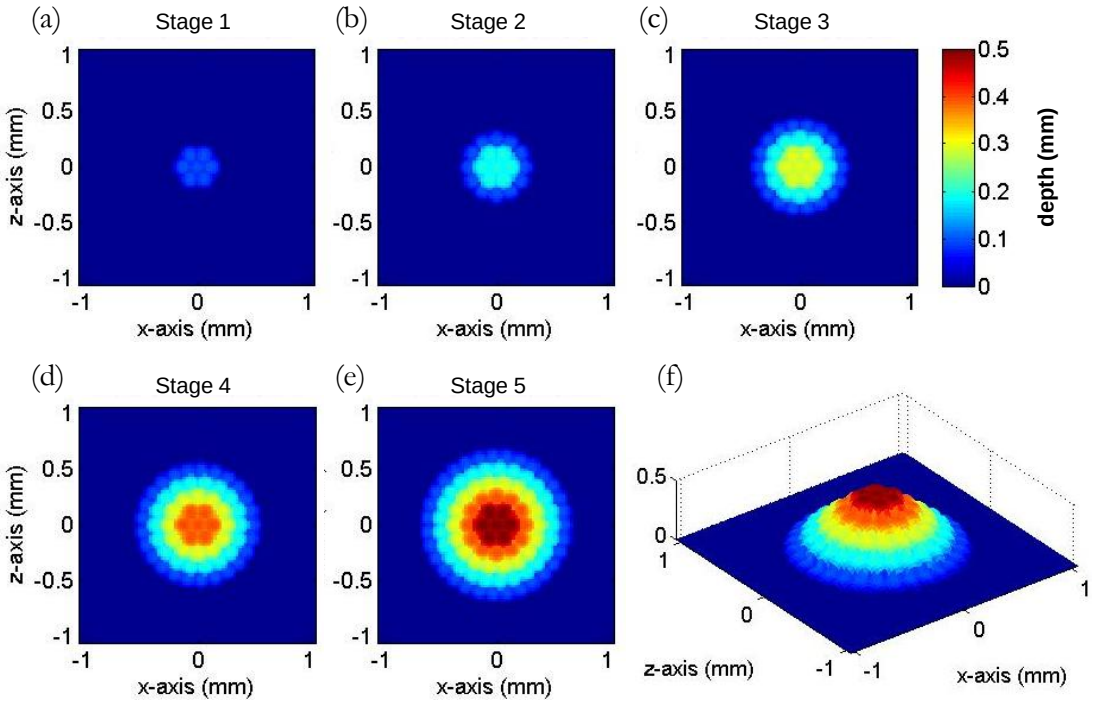

Figure 6.2: Plan view showing the depth of conical pit during machining during stage (a) 1 (max depth of 100μm) (b) 2 (max depth of 200μm) (c) 3 (max depth of 300μm) (d) 4 (max depth of 400μm) (e) 5 (max depth of 500μm). (f) Isometric view of conical pit after the final stage of machining.

the waveguide transducers. Unlike the experimental setup described in section 3.4, only two waveguide transducers were used to mimic the actual wall thickness sensor and ensure sufficient contact pressure could be applied equally between the waveguides to produce signals with high SNR without the need for shear couplant. All other aspects of the experimental setup remained the same as described in section 3.4.

It was decided that the laser would be used to incrementally 'grow' a defect directly below the thickness sensor to simulate NAC initiation. Based on the simulated results shown in Fig. 6.1, it is clear that a defect diameter of 50μm, two orders of magnitude smaller than the incident wavelength, would cause almost indistinguishable change to the reflected signal. It was therefore assumed that the very earliest stages would be impossible to detect using the current sensor and the smallest hemispherical indentation to be machined during the experiment would have a diameter of 200μm. In order to 'grow' the defect in stages, indentations were machined in circular loci to form a conical shaped pit over five stages with pit dimensions start-

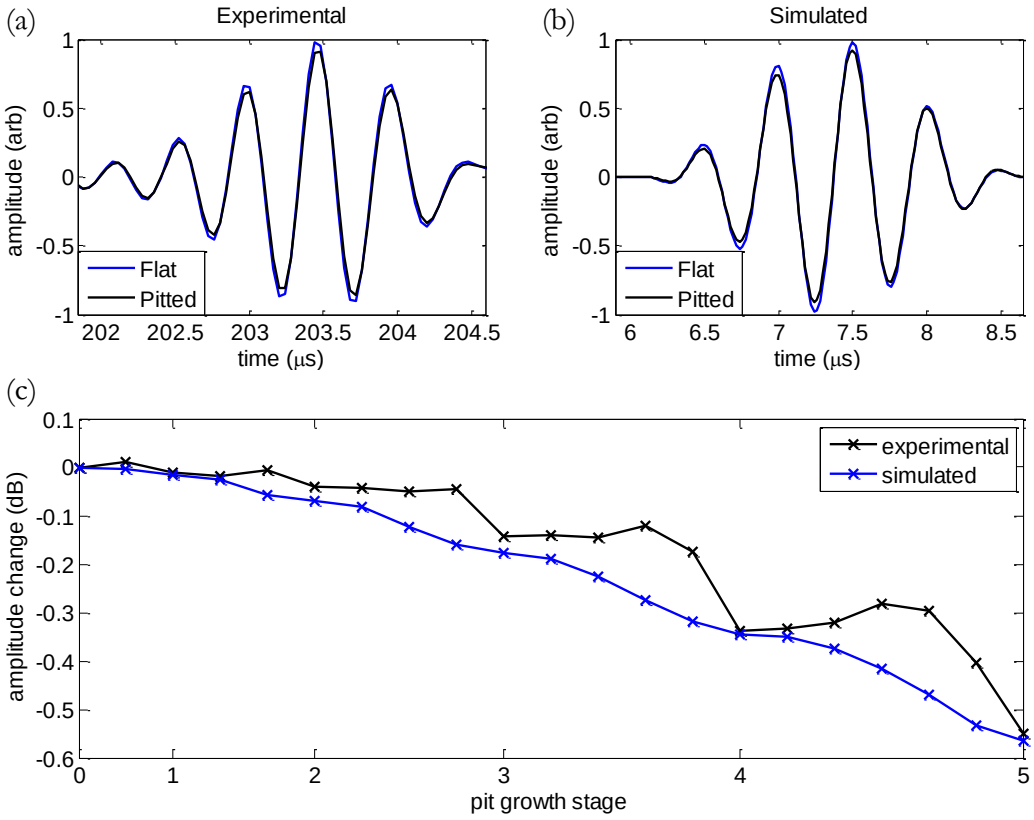

Figure 6.3: Signal comparison when the backwall is flat and with the largest conical pit (stage 5) for (a) experimental results (b) simulated results. (c) Comparison of amplitude change calculated using the DPSM simulation and recorded using the thickness sensor for all defect geometries machined during the experiment.

ing with a diameter of 200μm and a depth of 100μm, ending with a diameter of 1400μm and a depth of 500μm. The conical shape was selected to ensure material would be properly ejected from the test sample during machining and the shape is a close approximation of what might be expected during the initial stages of NAC. The depth profile of the five stages of the conical pit are illustrated in figure 6.2 as predicted using Matlab.

Reflected pulse amplitude has been used in figure 6.3 (c) to track signal change during the experiment since pulse shape and phase were not seen to vary by any appreciable amount as illustrated in Fig. 6.3 (a) and (b). It can be seen that an undulating amplitude pattern exists in Fig. 6.3 (c). Comparison to simulated results confirmed that it was the way in which the pit was built up using circular loci of smaller indentations during laser micromachining that caused this amplitude

undulation; this effect would not be expected in reality. The largest difference between experimental and simulated results occur when the sides of the pit are almost vertical, hinting that this error could be caused by mode conversion effects not being properly simulated or that point source placement was not optimal during simulation since gaps between them are largest at these stages. However, the general trend is predicted well to within 0.17dB at all stages and it can be concluded that small changes in signal shape can be accurately simulated. Error bars similar to those shown in Fig. 5.7 have been omitted since a significant change in arrival time of any part of the pulse is not expected for such small features. This makes the error associated with the pulse traversing over unwanted modes within the recorded signal negligible. The extent of observed reflected pulse shape change is so slight in both experimental and simulated signals that detection of a single small defect within an industrial environment subject to other forms of signal changing phenomenon (coupling condition, temperature, incoherent noise, ADC conversion process etc) would be very challenging.

6.2.2 Large Defect: Flat Bottomed Hole

To enact a large change in signal shape of an amplitude that could be easily detected in the field a larger defect was selected. Based on the results in Fig. 6.1, a FBH with a diameter of 3mm was selected as it should show significant amplitude undulation and pulse width increase. The experimental setup was identical to that in section 6.2.1, other than the defect itself which was machined in 0.1mm depth increments up to a maximum depth of 3mm using a manual milling machine and a 3mm diameter end mill cutter. Results from the experiment are shown alongside simulated results produced by the DPSM simulation in figure 6.4. The signal produced by the DPSM simulation has been averaged using the method described in section 5.2.1, accounting for the transduction properties of the waveguide.

A significant change in reflected pulse shape and amplitude can be seen in Fig. 6.4 (a) and (b) from the expected response if the inner surface was flat. Rather than one distinct pulse, two pulses are recorded; one from the top of the FBH arriving earlier, and another from the rest of the backwall. It is the interaction between these two pulses as FBH depth increases which cause the amplitude undulation seen in Fig.

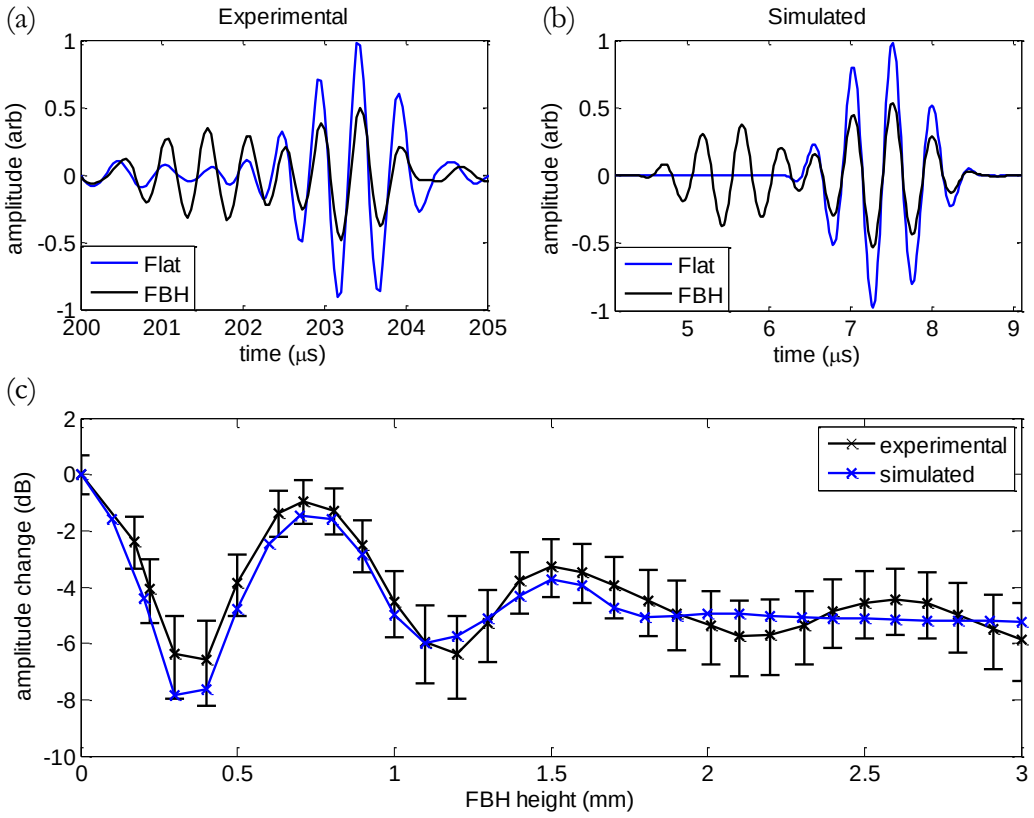

Figure 6.4: Signal comparison when the backwall is flat and with a 3mm diameter FBH with a depth of 3mm directly below the thickness sensor for (a) experimental results (b) simulated results. (c) Comparison of amplitude change calculated using the DPSM simulation and recorded using the thickness sensor for all FBH depths. Error bars represent the amplitude error that could be introduced by unwanted modes travelling within the waveguides which are on average 22dB weaker than the backwall reflection when the inner surface is flat.

(c), a pattern reproduced accurately by the DPSM simulation below an FBH depth of approximately 1.6mm (λ). As FBH increases still further, low amplitude undulations occur in the experimental results which don't occur in the simulated case. It is likely that these are caused by ultrasound which has mode converted into longitudinal waves along the sides of the FBH, interfering with the first backwall reflection once they have converted back into SH waves during the second reflection with the inner surface and FBH. The higher velocity of the longitudinal mode cause these secondary SH waves to arrive earlier than expected, causing increased coherent noise between the first and second backwall reflections. Even so, the DPSM simulation predicts amplitude change at all FBH depths to be within expected experimental error bounds, based upon unwanted wave modes travelling within the waveguides

which are 22dB weaker than the primary SH0* mode in pitch catch configuration (see Fig. 3.12).

It can be concluded that the scalar wave simulation predicts reflected pulse shape change well for the FBH depths investigated. Even though mode conversion effects are expected to be a source of error when using the scalar wave DPSM in three dimensions, amplitude predictions are within expected experimental error bounds based on the unwanted modes which travel along the waveguides. Without an alternative elastodynamic simulation technique capable of modelling three dimensional SH wave scattering from comparatively large surfaces, deterministic conclusions related to the bounds of validity of the scalar wave approximation cannot be drawn. However, the experimental results presented in sections 6.2.1 and 6.2.2 indicate that for the defect sizes of interest, the scalar wave approximation provides sufficient accuracy to simulate SH wave scattering in three dimensions when using the waveguide transducers.

6.3 Multiple Defects

The evolution of a corroded surface can rarely be described so simply as a single defect growing at any particular point in time; a situation investigated in the previous section. Real corroded features are made up of many localised corrosion events occurring in parallel, causing the surface as a whole to have a much more complex shape. It was decided that the wall thickness sensor should be installed to inspect a surface with many different features growing in parallel in order to investigate how reflected pulse shape changes in a more realistic pitting-type scenario and whether the DPSM simulation would continue to provide accurate predictions. To allow for such a comparison, the shape of the inner surface being inspected by the sensor must be known at all times. This was achieved by machining the inner surface of the sample in stages using a CNC milling machine while ultrasonic signals were taken, mimicking the effect real corrosion would have during wall thickness monitoring. To make the scenario as realistic as possible the surface to be machined was selected using scan data taken from a corroded field sample taken from a refinery environment (received with thanks from M. Lozev and H. Bazaz at BP). A linear

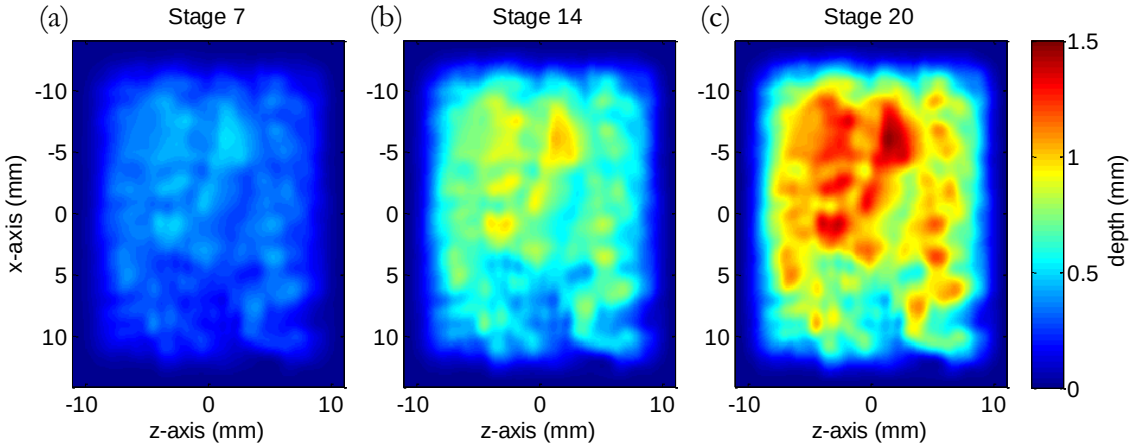

Figure 6.5: Plan view of the depth of the machined surface directly below the sensor at stage (a) 7 (b) 14 and (c) 20.

progression from flat to fully corroded over 20 stages was used to simulate corrosion propagation, as well as a 0.05mm uniform depth increase per stage to mimic additional mean wall loss. A plan view of the depths of three of the surfaces machined during the course of the experiment as predicted using Matlab are shown in figure 6.5.

The original corroded sample was scanned using a GOM ATOS III Triple Scan white light scanner which provided point cloud data with higher concentrations of data points around areas with a low radius of curvature (provided by C.Brett and R.Bell at E.ON). Interpolation by Kriging [93] was carried out to convert the data points into a grid format, helping in CAD surface generation and improving simulated result accuracy obtained using the DPSM. Features with a low radius of curvature on the original corroded surface were also filtered from the machined surface using a two dimensional FFT within Matlab to ensure the 2mm diameter ball nose cutter could machine the required surface profiles. The data retrieval and analysis procedures remained the same as in section 6.2. Results of the experiment are shown alongside simulated results in figure 6.6.

The signals shown in Fig. 6.6 (a) and (b) show two main changes to the backwall reflection from flat to fully 'pitted'; it arrives earlier in time and with reduced amplitude. The uniform thickness loss of 0.05mm per stage is the predominant factor in changing the arrival time of the pulse. The corroded shape of the inner

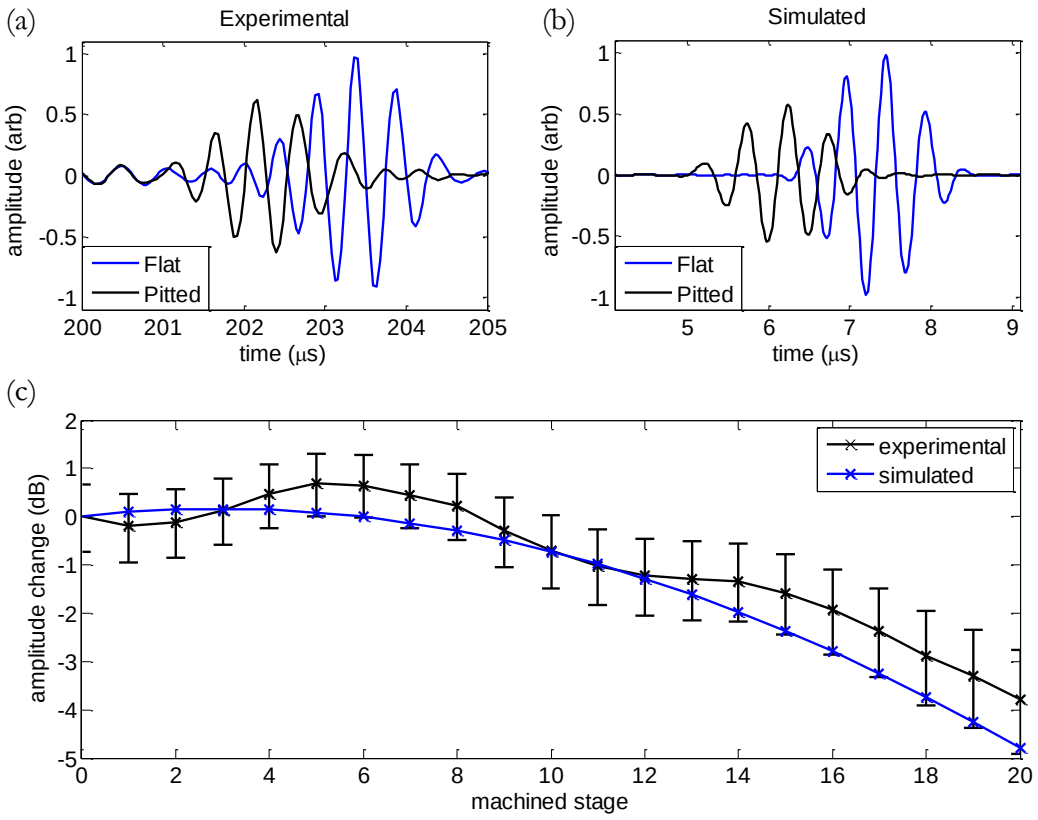

Figure 6.6: Signal comparison when the backwall is flat and the final stage of corrosion machining (stage 20) for (a) experimental results (b) simulated results. (c) Comparison of amplitude change calculated using the DPSM simulation and recorded using the thickness sensor for all machined corrosion stages. Error bars represent the amplitude error that could be introduced by unwanted modes travelling within the waveguides which are on average 22dB weaker than the backwall reflection when the inner surface is flat.

surface enhances scattering of the pulse, directing ultrasonic energy away from the receiver, therefore reducing the amplitude of the recorded pulse as the severity of the pitting increases. Referring to Fig. 6.6 (c), the amplitude of the pulse again undulates as the machined surfaces become deeper. The size of this undulation is consistent with unwanted modes travelling within the waveguides; as the reflected pulse traverses the recorded signal during thickness reduction, it constructively and destructively interferes with these lower amplitude modes. The simulated results are within these expected errors, indicating that the scalar wave DPSM performs well on reflecting surfaces made up of many localised features without the need for a more complex elastodynamic wave approach. The reflected pulse shape changes observed for this pitted surface are consistent with the level of change seen when considering rough surfaces with Gaussian height and length characteristics. It is

expected that the conclusions drawn within Chapters 4 and 5 are therefore applicable when considering corroded surfaces made up of more localised features with similar RMS heights and length characteristics.

6.4 Corrosion Propagation

The process by which a rough or corroded surface attains its particular shape has been largely ignored so far in this thesis. A linear progression from flat to fully corroded where all features grow in parallel with the same rate was assumed in section 6.3; however, this is unlikely to be the true manner in which the corroded surface was originally formed during corrosion. The aim of this section is to investigate a more realistic material loss mechanism in order to evaluate the corrosion rate estimation capabilities for each of the TOF algorithms described in section 4.3.1.

6.4.1 Simulated Corrosion

Extensive amounts of literature exist describing different corrosion mechanisms and the varied ways in which their propagation can be simulated or statistically predicted. A full review was considered outside the scope of this thesis and as such only the relevant theory for the model implemented will be described in any detail. For more information on alternative pitting corrosion models used in the oil and gas industries please see [94–99].

The model proposed by Meakin et al [100] was chosen because it is relatively simple to implement and it focusses specifically on the morphology of localised pit-type defects, describing the structure of the corrosion front as the defect develops. It describes both uniform (smooth brightening pits) and non-uniform (rough 'etching' pits) corrosion processes by introducing passivation and depassivation rates which act to change the characteristics of material at specific sites within the simulated domain. It is based on a two dimensional cross-section of the material being subdivided into a square lattice in which each site in the lattice can be one of four different states:

1. Unreactive fluid (empty).
2. Corrosive fluid or particle.
3. Reactive metal.
4. Passive non-reactive metal.

Corrosion is assumed to be the result of a diffusion limited reaction between mobile corrosive sites and the unprotected metal surface. The mobile corrosive sites are controlled using a random walk algorithm which causes them to come into contact with metal along the corrosion front. If the site is reactive then the two reagents combine and the site becomes unreactive fluid, therefore causing material loss. If the site is passive nothing happens and the corrosive site stays where it was to be moved to another potentially reactive metal site along the corrosion front. To establish non-uniform pit growth spontaneous random events are introduced which are characterised by the passivation and depassivation rate constants (k_p and k_d respectively). The passivation rate controls whether previously reactive metal sites along the corrosion front spontaneously become passive and the depassivation rate controls whether previously passive sites along the corrosion front spontaneously becomes reactive again. Two pits are shown in figure 6.7 to illustrate the difference between pit shapes caused by uniform and non-uniform pit growth, controlled using these parameters. The time variable is arbitrary and controlled using the number of corrosive site movements per unit time. Singular pits were generated in these cases by only allowing corrosive sites to enter through a single empty site on the inner surface.

A three dimensional approach was deemed unnecessary during this initial investigation into corrosion rate estimation capabilities of the TOF algorithms because of the large increase in computational resources and time which would otherwise be required. Using two dimensional DPSM in conjunction with the pitting simulation (also written using Matlab) allowed simulated ultrasonic signals from many corroding surfaces to be acquired very rapidly. The results should therefore be taken as a worst case scenario as it is expected that diffuse components of the reflected pulse will be amplified by of a lack of spatial averaging in two dimensions, as was the case with Gaussian distributed roughness shown in Chapter 5.

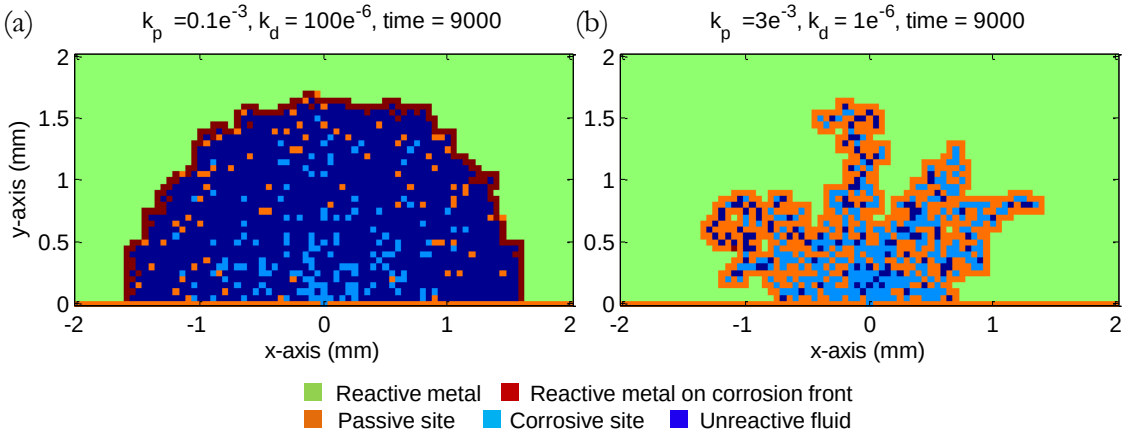

Figure 6.7: Examples of single pits resulting from conditions of (a) uniform growth (b) non-uniform growth.

6.4.2 Corrosion Rate Estimation

To simulate behaviour similar to the interaction between SC and NAC during real corrosion where both uniform was loss and localised defects occur, it was decided that initially all sites on the corrosion front would be reactive and k_p and k_d would be used to alter corrosion propagation through time. Initially uniform wall loss occurs, representing a situation where SC is dominant; however, as corrosion proceeds and passive sites begin to appear, so too do localised features representing a change to a more NAC dominated scenario. For a grid size of 100μm, values of k_p = $0.25e^{-3}$ and k_d = $100e^{-6}$ were found to produce the desired corrosion characteristics up to a mean wall loss of 1mm (10%), beyond which the passivation rate halted corrosion almost entirely. The mean wall loss was defined as the area of material lost below the corrosion front divided by the horizontal length of the surface being corroded. The DPSM simulation calculated signals at 50 stages during the corrosion of a particular surface, each separated by 0.02mm mean wall loss. The random numbers used to generate the trajectories of the corrosive sites were altered to produce different corroding surfaces, 950 of which were simulated. An example of a corroding surface produced by the pitting simulation is shown in figure 6.8, alongside the signals calculated using the DPSM simulation. More results have been shown for greater levels of wall loss because of the greater surface RMS height and associated signal distortion.

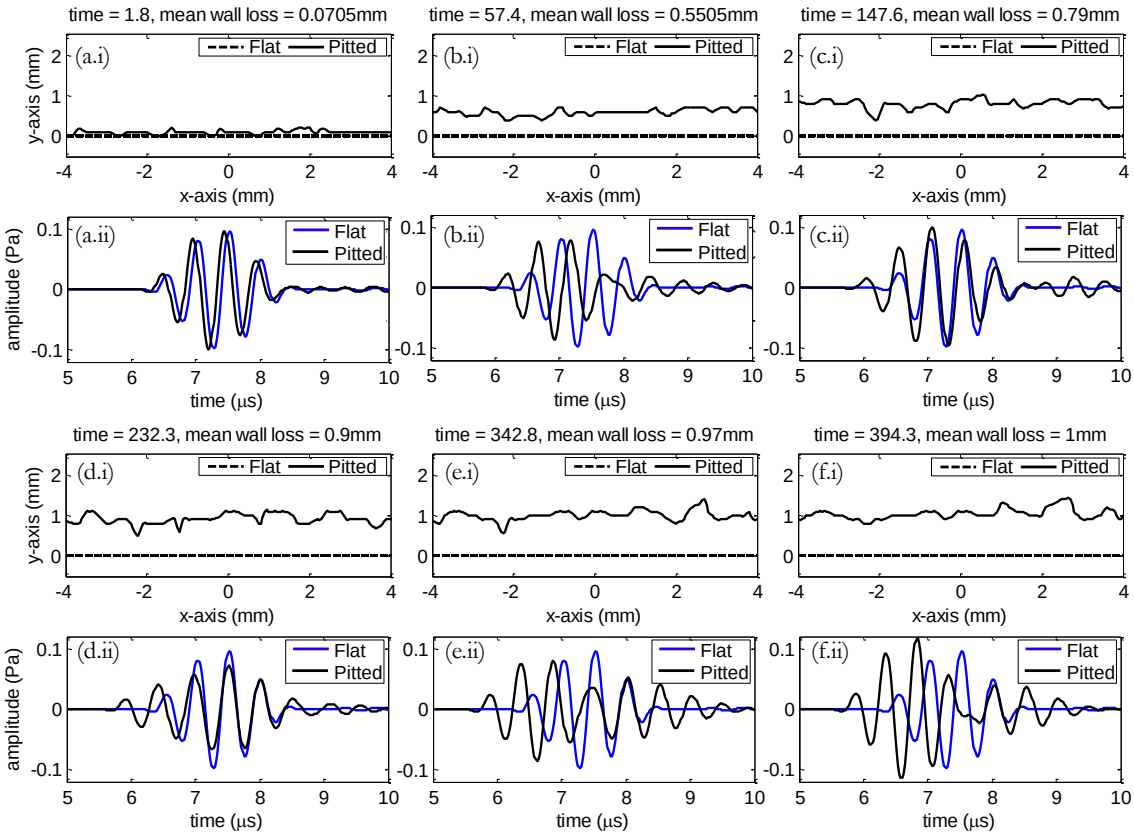

Figure 6.8: Example of a corroding backwall shown alongside the simulated pulse reflected from the surface calculated using the DPSM for a mean wall loss of (a) 0.07mm (b) 0.55mm (c) 0.79mm (d) 0.9mm (e) 0.97mm and (f) 1mm.

The surface profiles of the corroding surface initially have low RMS height and the localised defects tend to be small as they are made up of only a few squares of the material lattice. However, it can be seen in Fig. 6.8 that as corrosion proceeds, the height and length characteristics of localised features increase because passive sites restrict growth from occurring uniformly along the surface. The associated reflected pulse distortion also tends to increase as these features grow in size, therefore impacting on the behaviour of the TOF algorithms. Each algorithm (as described in section 4.3.1) was applied to all the signals produced by this particular corroding surface and the results are shown in figure 6.9, alongside the linear corrosion gradient estimations. In this idealised case where the material loss within the wall is accurately known, a corrosion gradient has been used rather than a corrosion rate in order to remove any influence of the arbitrary time variable used within the corrosion model. The corrosion gradient is defined as the estimated wall loss over the actual mean wall loss; therefore a value of 1 corresponds to the TOF algorithm

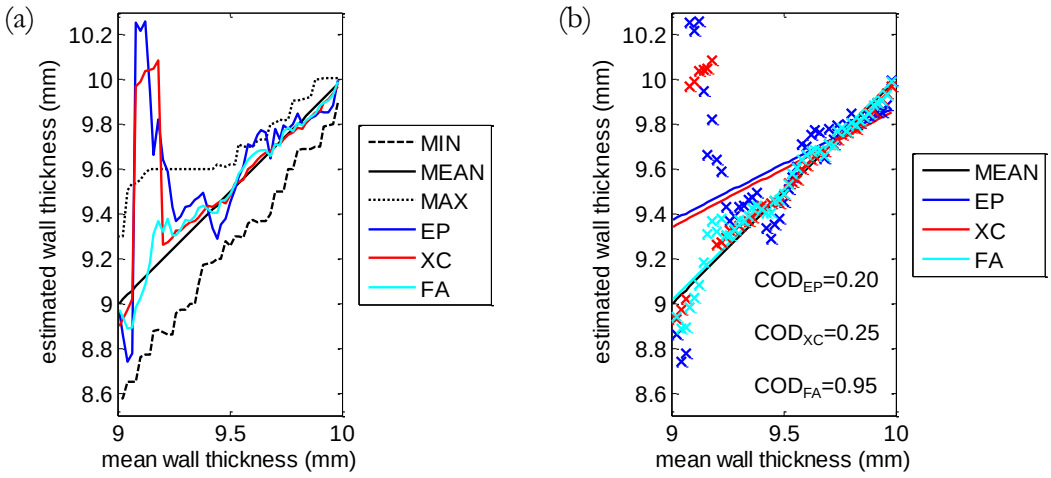

Figure 6.9: (a) Comparison of estimated wall thickness trends for envelope peak detection (EP), cross-correlation (XC) and threshold first arrival (FA) TOF algorithm. A 15dB threshold was used for FA. Lines have been included showing the actual minimum, maximum and mean wall thickness of the surface calculated using the surface profiles. (b) Comparison of linear regression lines and their associated COD values for each TOF algorithm. The data points show the wall thickness estimates from which the linear regression lines have been calculated.

finding the mean wall loss exactly. The value of the coefficient of determination (COD) has also been included for each TOF algorithm in Fig. 6.9 (b) to indicate how well the linear regression lines fit the estimated wall thickness data; a value of 1 corresponding to a perfect linear fit and a value of 0 to zero shape similarity.

A discontinuity in thickness estimate occurs for both envelope peak detection and cross-correlation, caused by signal amplitude in the tail of the pulse exceeding that of the main pulse. If included in the linear regression, such discontinuities can have a large impact on corrosion gradient estimates, which for envelope peak detection and cross-correlation were 0.50 and 0.52 respectively. The COD values also indicate the very low correlation between the linear regression and observed thickness trends. Threshold first arrival is not as sensitive to energy in the tail of the reflected pulse, therefore it is found to perform far better, calculating a corrosion gradient of 0.99 with a COD of 0.95. Values for the COD and corrosion gradient for all 950 corrosion simulations carried out are shown in figure 6.10 (a) and (b) respectively. It can be seen that because threshold first arrival is not affected so strongly by

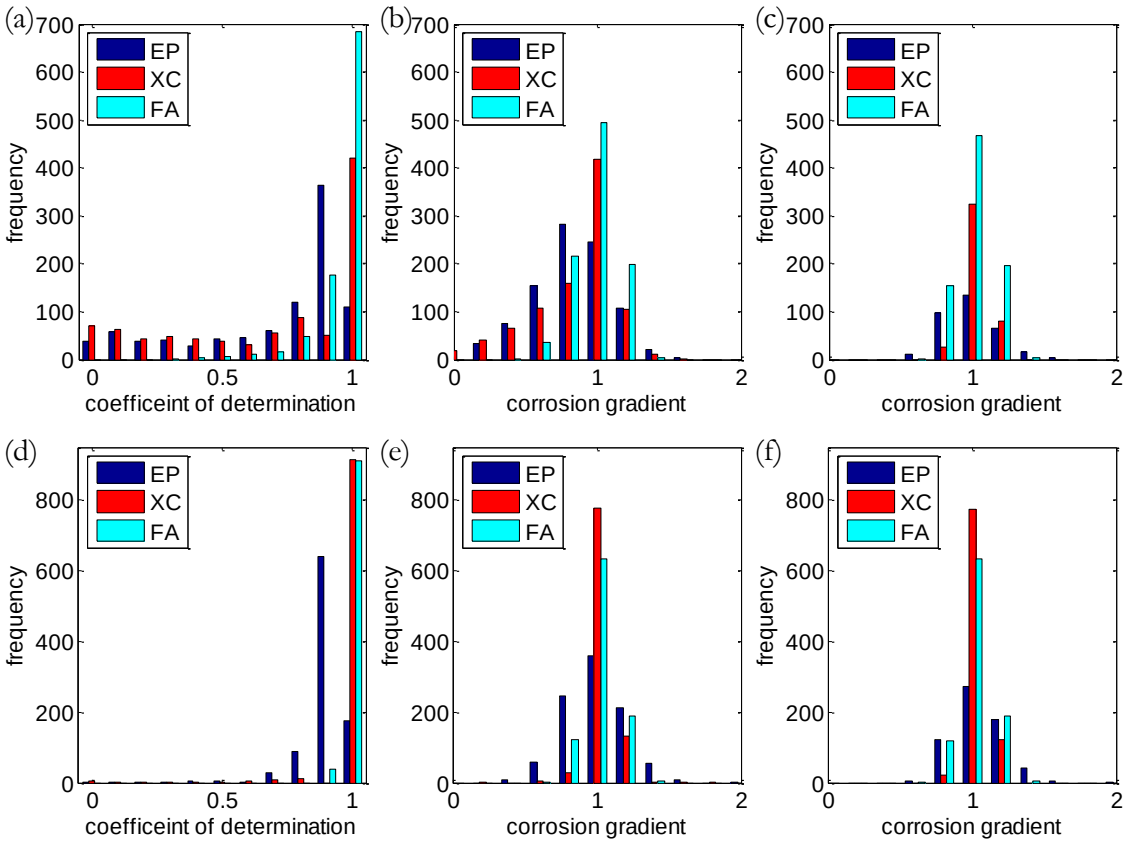

Figure 6.10: (a) COD values for all simulated results. (b) Corrosion gradient values for all simulated results, (c) for linear regression lines with COD values greater than 0.9. (d) COD values for simulated results up to a mean wall loss of 0.75mm. (e) Corrosion gradient values for simulated results up to a mean wall loss of 0.75mm, (f) for linear regression lines with COD values greater than 0.9.

diffuse energy in the pulse that it consistently outperforms envelope peak detection and cross-correlation, calculating COD and corrosion gradient values of around 1 more frequently. Both envelope peak detection and cross-correlation also tend to underestimate corrosion gradient, indicating that an increase in apparent thickness is the main source of error as corrosion propagates. However, if only those corrosion gradients with COD values greater than 0.9 are selected, most of these erroneous corrosion gradients are removed as shown in Fig. 6.10 (c). This process reduced the population of results to 34%, 45% and 87% of the original 950 results for envelope peak detection, cross-correlation and threshold first arrival respectively.

The comparatively large number of results with COD values less than 0.9 is caused by the RMS height of the surface increasing rapidly as localised features establish and propagate during the final stages of corrosion. If results for mean wall thickness

losses greater than 0.75mm are omitted during the corrosion gradient calculation (corresponding to RMS heights greater than approximately 0.1mm), these large jumps in thickness rarely affect the final result. This is evident in Fig. 6.10 (d) where almost all COD values are above 0.95 for threshold first arrival and cross-correlation. Envelope peak detection also improves; however the majority of the linear regression lines have a value between 0.85 and 0.95, indicating that the TOF algorithm is the least accurate of the three tested. This is also clearly illustrated in Fig. 6.10 (e) where the distribution of corrosion gradients is spread more widely than for both cross-correlation and threshold first arrival. By ignoring wall losses greater then 0.75mm, cross-correlation is now found to be more precise than threshold first arrival, indicated by a tighter distribution around the correct corrosion gradient. Both show a positive skew, tending to slightly overestimate corrosion gradient, a situation which is more favourable than the reverse in a safety critical oil refinery environment.

Coupled with the results presented in Chapter 4, the main conclusions that can be drawn from these simulated results which are free from other forms of noise are that under low RMS height conditions where rapid changes in estimated wall thickness are not expected, cross-correlation would be the optimum method for calculating corrosion rates. If however large jumps in thickness are observed, TOF algorithms based on the earliest arrival time of a pulse would be the most stable. As such, for operation in the field a combination of both should be implemented to ensure maximum precision during the early stages of corrosion and the best possible accuracy during the later stages of severe corrosion. Other methods of detecting and removing large jumps in estimated thickness could also be implemented to improve corrosion rate estimation such as alternative regression models or roughness detection as an indicator of ongoing and potentially severe corrosion.

6.5 Inverse Scattering with Limited Data

It has already been shown in section 4.2.2 that reconstructing a rough surface using information contained in the only A-scan available at any particular time during permanent wall thickness monitoring would be impossible. It could be possible

using a lookup table type method if assumptions could be made about the form of the features on the inner surface causing the pulse to change shape; however, as the previous sections have described, corroded features are rarely fully predictable in shape. This leaves only one option: tracking how pulse shape changes through time as corrosion propagates. Such a method could also provide a means of advising when operation should switch from one type of TOF algorithm to another.

Referring back to the work presented in section 4.4, it was found that calculating the correlation coefficient between the transmitted and received pulse provided the most promising method of measuring the extent of reflected pulse shape change and the impact this can have on estimated thickness error. It could therefore also be used to track signal shape change through time in order to provide information on how the condition of the surface deteriorates as corrosion proceeds. This has been carried out for the corroding surface shown in Fig. 6.8 as an example, shown alongside the mean change in correlation coefficient for all 950 simulated cases as corrosion propagates in figure 6.11. It can be seen that for an individual surface that the correlation coefficient of the reflected pulse can alter quite substantially through time, both increasing and decreasing as the reflected signal alters to become more or less similar in shape to the ideal transmitted pulse. Over many corroding surfaces these variations average out and the decrease in correlation coefficient mirrors how the average RMS height of the corroding surfaces increases. It should be noted that the average results shown in Fig. 6.11(b) and are only included to illustrate the most common trends; the change in correlation coefficient for individual surfaces can vary substantially from this result as illustrated in Fig. 6.11(a).

The results shown in Fig. 6.11 (b) should be treated with caution since any particular rough surface will have its own unique trend, not necessarily showing a substantial decrease in correlation coefficient even with a large increase in RMS height. Furthermore, applying the technique directly to real signals can have added complications. To illustrate these points the correlation coefficients of the experimental signals presented in section 5.3.2 have been calculated and are shown in figure 6.12. These particular experimental results were chosen because of the substantial change in signal shape exhibited as RMS height increases and the comparison which can be made from signals reflecting from the same surface but recorded at locations

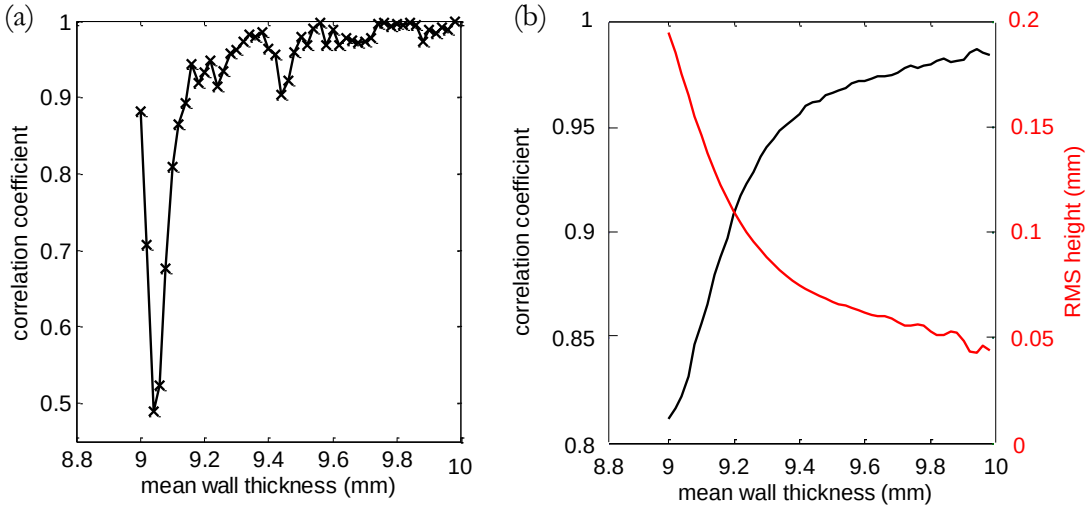

Figure 6.11: (a) Correlation coefficient of simulated signals as pitting corrosion proceeds for example surface. (b) Average correlation coefficient and RMS height as corrosion proceeds over 950 surfaces.

separated by only 2mm (1.25λ).

The first conclusion that can be drawn from experimental results is that even under flat backwall conditions, the correlation coefficient is not equal to 1. This is because the ideal transmitted pulse which has been compared with is free from any noise, whereas even the best quality experimental signal is subject to noise, most notably caused by unwanted modes travelling within the waveguides. To correct this, the initial experimental signal could be used instead of the ideal transmitted pulse; therefore subsequent comparison will indicate change from the initial state now corresponding to a correlation coefficient value of 1. However, when using an ideal pulse for comparison, any increase in correlation coefficient value from the sensors initial state could be an indicator of improving coupling conditions, for example when temperature cycling ensues. Comparison to a less ideal state in this case would undermine the usefulness of the technique, therefore it is advised that comparison should always be made to the ideal transmitted signal and changes in correlation coefficient should be monitored as an indication of signal quality and the potential onset of severe corrosion. Not being able to use absolute values of the correlation coefficient in the field does however mean that direct use of the uncertainty plots presented in section 4.4.2 would be unadvisable. In cases where severe corrosion

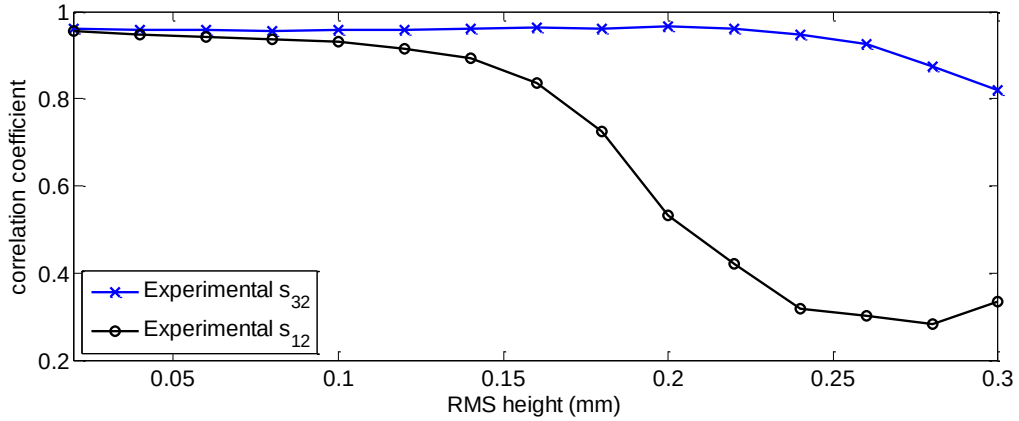

Figure 6.12: Correlation coefficient values for experimental signals reflecting from a three dimensional Gaussian distributed rough surface with a correlation length of 1.6mm ($\lambda_0 = \lambda$) as RMS height increases.

is detected through correlation coefficient deterioration, it is therefore advised that the error in thickness estimate derived from such uncertainty plots should be based on correlation coefficient change from a high quality signal, ideally when the inner surface shape is known to be approximately flat and uncorroded.

It is also clear from Fig. 6.12 that the shape of a single reflected pulse cannot be measured using methods such as the correlation coefficient and used directly to assess the level of corrosion beneath a wall thickness sensor. For instance, for a correlation coefficient value of 0.85, the array which effectively represents two thickness sensors separated by 2mm indicates that this value occurs at RMS heights of 0.16mm and 0.29mm for signals s_{12} and s_{32} respectively. If these signals were recorded in the field, it would most likely be assumed that s_{32} came from a section which was corroding very heavily from an early stage and that s_{12} was from a section where corrosion was not as severe and onset initiates much later in time. However, these signals come from the same surface with nominally the same RMS height and correlation length characteristics at each of the sensor locations. Therefore, although tracking reflected pulse shape change through time is a useful indicator of the onset of corrosion, if information is only available from a single location within a single A-scan, definitive conclusions cannot be drawn about the shape and location of multiple defects which may be growing on the inner surface. Techniques such as the uncertainty plots presented in section 4.4.2 provide the best opportunity

for data extraction in applications such as wall thickness monitoring since they provide probabilistic rather than deterministic estimates of corrosion induced errors in situations where data is very limited.

It is important to note that these conclusions have been drawn from worst case scenarios, be it from two dimensional simulated results or experimental results where the surface was specifically chosen to show signal disparity between neighboring sensor positions. It is expected that the majority of cases seen in the field will show reduced levels of reflected pulse shape change and the thickness estimates they produce will be less sensitive to the levels of corrosion expected within petrochemical refinery environments.

6.6 Summary

Building upon the work presented in previous chapters which investigated ultrasound reflection from rough surfaces with Gaussian height and length characteristics, alternative defect morphologies and growth mechanisms have been investigated. Simplified geometries such as a FBH showed that a single localised defect could influence reflected pulse shape greatly, changing amplitudes by up to 8dB for defect sizes up to 2λ. Comparison of experimental and simulated results for a micron-scale laser micromachined conical pit-like defect and a 3mm diameter FBH indicated that the scalar wave approach predicted amplitude trends closely, within the expected errors introduced by imperfect mode purity in the waveguide transducers. Without an alternative three dimensional elastodynamic simulation technique, the experimental results indicated that the scalar wave DPSM is sufficiently accurate to simulate SH wave scattering from pit-like features of comparable size to the incident wavelength using the waveguide transducers.

More realistic defect geometries and propagation mechanisms were investigated through experimental and simulated studies. Scan data taken from a real sample taken from a corrosive refinery environment was used to machine a pitted surface below a wall thickness sensor which was linearly increased in height to approximate increasingly corroded conditions. The change in pulse shape as the experiment pro-

gressed was found to be consistent with that found in Chapter 5, suggesting that conclusions drawn about ultrasound reflection from rough surfaces with Gaussian height and length characteristics are equally valid for those subject to pitting corrosion with comparable feature sizes. A two dimensional simulation based on a diffusion limited reaction was implemented to more closely approximate how material is lost during pitting corrosion; simulated signals were subsequently calculated at each stage using the DPSM. Corrosion rates calculated using the envelope peak detection, cross-correlation and threshold first arrival TOF algorithms echo the conclusions made for discrete wall thickness calculations in Chapter 4; for severe corrosion, algorithms based on determining the earliest arrival of a pulse are more stable, otherwise cross-correlation is found to be the most accurate, providing precise corrosion rate estimates.

Based on the results found, some recommendations about algorithm deployment in the field have been provided. Primarily, reliance on a single TOF algorithm is unadvisable as each can be affected by corrosion in different ways; a better strategy is to employ cross-correlation and threshold first arrival and track how the estimated corrosion rates change through time. A large difference between them is a likely to indicate the onset of severe corrosion and results given by threshold first arrival should be taken as the most stable. Measuring how pulse shape changes through time using methods such as the correlation coefficient provides a useful probabilistic indicator of corroded feature development on the inner surface, and therefore the reliability of the estimated thickness. However, with only a single ultrasonic signal to extract information from, definitive conclusions about the true nature of the inner surface cannot be drawn. Application of an array of waveguides within a high temperature environment would increase the information content about a defect, allowing more deterministic conclusions to be drawn about its size and location. This situation will be the focus of the next chapter.

Chapter 7

Alternative Remote Monitoring Methods using Waveguide Arrays

7.1 Introduction

Previous chapters have focused on monitoring material degradation and corrosion by measuring localised wall thickness loss using a sensor made up of two ultrasonic waveguide transducers setup in pitch-catch configuration. The comparative lack of information available in a single signal from a single location makes deterministic conclusions about the exact nature of the reflecting surface impossible to draw. Methods to increase positional data content such as probe scanning are not possible in permanent monitoring applications, therefore the only approach to increase positional information is by means of an array, allowing defects to be interrogated from multiple directions.

In the following sections two of the most promising structural degradation monitoring applications which have been identified as benefitting from the increase in data available from an array of waveguides will be presented. The first is monitoring thermal fatigue crack growth within a high temperature, high pressure steam power plant environment. It will be shown that the additional data can be manipulated to create an image of a crack, indicating both position and length relative to the array. Simulated studies are carried out in order to define the working en-

velope of the array, with comparison to experimental results providing validation of hardware design and prototype readiness for industrial implementation. The second application investigates how a two dimensional velocity distribution can be reconstructed using ultrasonic data in order to isolate areas of material degradation such as hydrogen attack which can alter bulk material properties. A proof-of-concept experimental investigation was carried out using a transient heat distribution to simulate the effect such corrosion mechanisms could have, providing feedback on velocity change detectability limits, as well as the positional resolution of a limited view array geometry.

7.2 Thermal Fatigue Crack Growth Monitoring

The way in which power plants are operated throughout the UK has changed a great deal in the past few decades. Deregulation has led to plants which were originally designed to operate under base load conditions to endure far more frequent load changes and start cycles (known as two-shifting) in order to match supply with fluctuating demand in a competitive energy market. This increase in load cycles, coupled with the age of many plants has caused circumferential thermal fatigue cracks to grow in the chrome moly vanadium (CMV) steel steam pipework butt welds [7]. Left unchecked these cracks could grow to the point of failure, presenting a safety hazard and incurring large maintenance and repair costs.

Upon discovering such defects, conventional ultrasonic inspection has been employed to measure their extent in an attempt to monitor their development, and to provide stress analysts with information vital in deciding whether a plant is safe to operate in its current condition. However, because conventional ultrasonic transducers cannot withstand elevated temperatures, current inspection techniques can only occur when the plant is shut down during planned maintenance cycles which generally occur years apart. This leads to poor repeatability because of the potential for operator, equipment and positioning variance. Furthermore, crack undersizing due to tip closure can occur at low temperature [101]. An improved strategy would be to permanently monitor small, subcritical cracks that have been identified during routine inspection. This would allow more accurate and repeatable evaluation of

the defect size, prevention of unplanned shut downs due to component failure and more efficient scheduling of component replacements, all of which increase plant availability and hence maximise revenue.

Currently, permanently installable ultrasonic crack monitoring devices that can survive high temperatures (above 200°C) are not commercially available and the construction of such a device has formed the motivation for the work presented in this section. Much of the work presented has previously been reported in our papers [102] and [103], as such some relevant excerpts have been included in section 7.2.

7.2.1 Fatigue Crack Monitoring Strategy

Many techniques can be used to measure the size of a crack using ultrasonic waves. The most commonly used method is time of flight diffraction (TOFD) [104–106]. Such applications usually employ longitudinal waves which diffract strongly from crack tips. By scanning two transducers of fixed separation across the outer surface of a component containing a crack, simple geometric considerations can be used to size the crack based on the arrival time of the diffracted signal. The advantage of this monitoring strategy is that only two transducers are needed to size the crack; however, as described by Chapman [107], the expression for the far field diffracted amplitude A of a plane SH wave within an infinite medium incident upon a semi-infinite planar crack is given by:

$$A(\theta) = \frac{cos^2(\theta/2)}{2\pi cos(\theta)} e^{i\pi/4} \sqrt{\frac{\lambda}{r}} e^{ikr} \tag{7.1}$$

Where the incident and reflected angles are assumed to be equal (θ) and r is the observation distance. If this equation is plotted as shown in figure 7.1 it is clear that the amplitude of the diffracted SH wave would be below the detectability limit (often around -40dB for standard equipment) when inspecting at angles greater than 130°. This is the case when the transducers are installed on the outer surface of the component inspecting a crack initiating on the inner surface, such as would be the case in a steam power plant environment. Experimental studies were carried out to verify TOFD would be unsuitable using the waveguide transducers, the details of

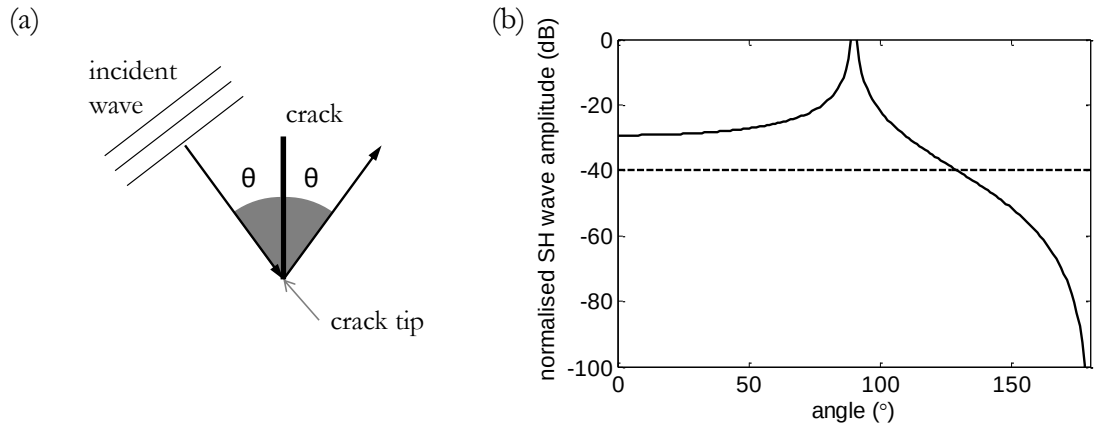

Figure 7.1: (a) Geometry considered for diffraction of a plane wave from a crack tip when the incident angle θ is equal to the receiving angle. (b) Diffracted SH wave amplitude when the observation distance (r) is 30mm and λ=1.6mm. The dashed line represents the typical signal to noise ratio for standard equipment (-40dB).

which can be found in our paper [103].

An alternative monitoring strategy is to use waves which have reflected from the crack face via the backwall. Termed the multi-synthetic aperture focussing technique (multi-SAFT) [108, 109], it takes advantage of higher amplitude components being received by an array of waveguides caused by lower incidence angles. The received waveforms can subsequently be used to construct an image of the crack based on the distance travelled from the transmitter to the receiver via the backwall and crack face. These distances are calculated using equations 7.2 and 7.3 assuming a plate geometry with thickness T.

$$d_{tx} = \sqrt{(x_{tx} - x)^2 + (T + (T - y))^2} \tag{7.2}$$

$$d_{rx} = \sqrt{(x_{rx} - x)^2 + y^2} \tag{7.3}$$

where subscript tx refers to the transmitter and subscript rx refers to the receiver. Once a full matrix capture (FMC) data set is acquired, the total focussing method (TFM) [110] can be used to construct the image $I(x, y)$ of the crack using equation 7.4.

$$I(x, y) = \left| \sum_{tx} \sum_{rx} g_{tx,rx}\left(\frac{d_{tx}}{c} + \frac{d_{rx}}{c}\right) \right| \tag{7.4}$$

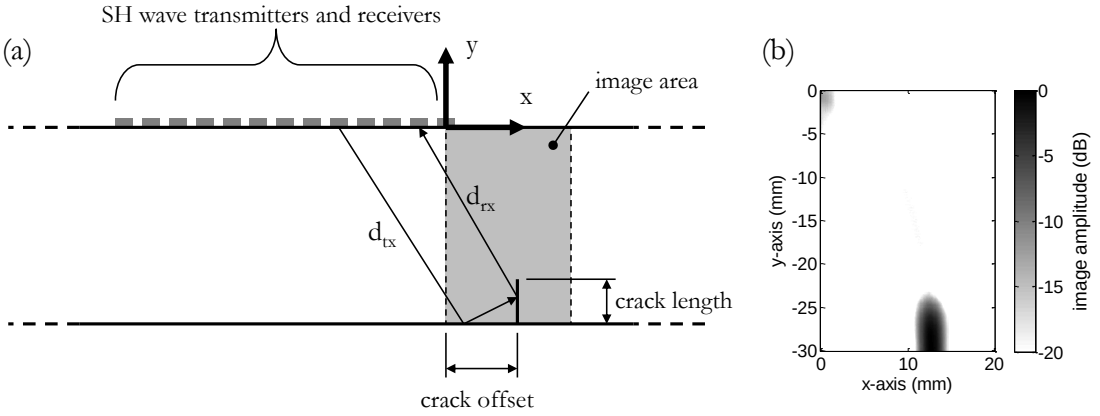

Figure 7.2: (a) Array geometry considered showing the path analyzed during TFM imaging. (b) Example TFM image calculated using simulated signals.

Where $g_{tx,rx}(t)$ is the time dependent signal recorded at transducer rx when transducer tx is transmitting. Areas in the image which have a high amplitude represent areas in the original geometry which have strong reflections associated with them based on the sum of the propagation distances given by equations 7.2 and 7.3. The TFM was used because it uses data from all possible combinations of transmit-receive waveguide pairings when creating an image, requiring no predetermined focussing laws or complicated electronics. A schematic of the inspection geometry is shown in figure 7.2, alongside an example image of a crack calculated using simulated data. It should be noted that the axis system is different from previous chapters in this thesis since it was decided the crack position should be calculated relative to the first element in the waveguide array.

7.2.2 Simulated Investigation of Array Working Envelope

The two dimensional scalar wave DPSM simulation described in Chapter 3 for modelling rough surface scattering is equally valid when simulating SH wave scattering from a crack-like defect which is constant in cross-section across the width of the array. As such the theory will not be repeated here; however, one important simplifying assumption was made to improve simulation efficiency in this particular application since N^2 signals are needed to simulate a FMC data set for an array made up of N waveguides. In order to reduce the number of passive sources, the

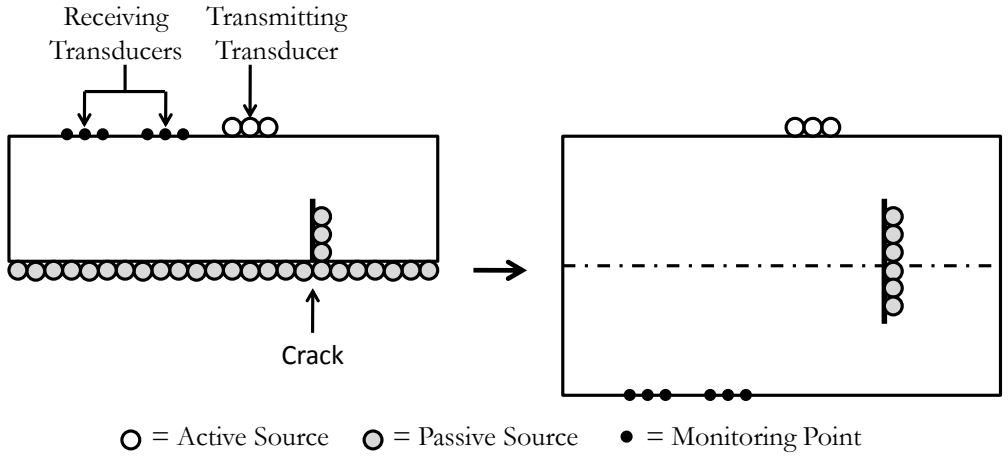

Figure 7.3: Sketch showing the DPSM model geometry after the simplifying assumption that the backwall acts as a perfect reflector

backwall was assumed to be a perfect reflector, in effect transforming the simulation into a through thickness inspection with the receiving array mirroring the transmitting array about the backwall plane as illustrated in figure 7.3. This allowed a FMC data set to be simulated within a matter of seconds because of the large decrease in matrix size which was necessary to invert (see equation 3.10).

It was decided to use the DPSM model to simulate the performance of the array for a range of parameters which were chosen to closely match experimental investigations. The centre frequency of the excited 5 cycle Hanning windowed toneburst was changed to 1.6MHz to reduce wave attenuation within the thicker plate than has previously been used in this thesis. A constant element pitch of 2mm and a plate thickness of 30mm were used throughout. Figure 7.4 (a) shows how the calculated defect size changes for a defect 10mm away from the array for arrays of constant pitch but with different size. It illustrates that at a given position, defect length estimation using the TFM is accurate up to about 40 percent of the wall thickness, provided there is a sufficient number of transducers in the array. The wavelength of the excited wave determines the smallest defect lengths the array can image explaining the lower limit to the range. The upper limit is determined by the aperture of the array. A short array is unable to receive reflections from the defect tip travelling beyond the final transducer, therefore vital information for defect length estimation is not obtained.

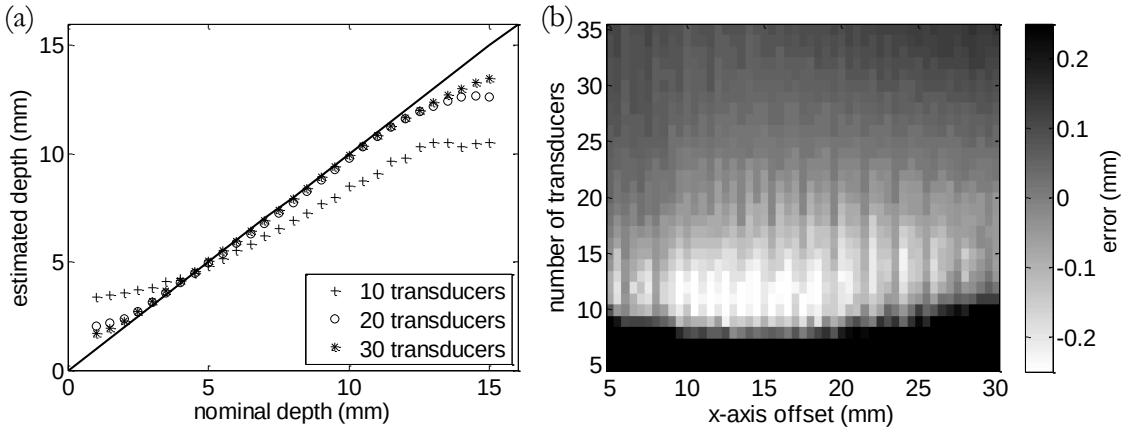

Figure 7.4: (a) Estimated crack lengths for various sizes of array in a 30mm thick plate containing a defect placed 10mm away from the array. (b) Error in defect length estimation for a 5mm defect in a 30mm thick steel plate due to the number of transducers within the array for various defect positions. Results are based on simulated data from the DPSM simulation

Furthermore, Fig. 7.4 (b) illustrates the effect that the number of waveguide transducers has on the error in estimating a 5mm defect at various positions from the array. The results indicate that accurate defect length estimation requires a minimum number of waveguides, approximately 15 in this case, to stay within 0.25mm of the nominal dimension. Reducing the x-axis offset from the array to the crack is also a good strategy to minimise errors. However, it is important to have some offset to avoid backwall reflections from interfering with the image of the crack. It is also clear that there is an optimum number of waveguides that retains estimate precision while decreasing array aperture, found to be between 20 to 25 waveguides depending on array offset. It was decided to use 20 waveguides in all future investigations to mimic experimental conditions where the minimum was decided upon to reduce system complexity. Investigating the relationship between these factors and the final defect length estimate provides a method for specifying the operating envelope of a particular array and test piece configuration.

7.2.3 Waveguide Array Experimental Setup and Results

An array of 20 waveguides was clamped to the surface of 30mm thick mild steel plates (300mm long and 150mm wide) that contained different sizes (5mm, 10mm and 15mm) of vertical notches. All notches were 0.3mm wide and machined using electric discharge machining (EDM). The notches were uniform across the width of the plate. The array was attached by a purpose made clamp that individually clamped each SH transducer onto the surface of the metal plate. The clamp separated the waveguides by a uniform spacing of 2mm in the x-direction. The array location was chosen to be on the opposite plate surface relative to the notches with a horizontal offset from the notch location of approximately 10mm. Figure 7.5 shows a picture and a schematic of the setup. A purpose made multiplexer (Omega Engineering Ltd, OME-DB-24R/24) was used to connect each waveguide transducer to the transmitter/receiver device (Handyscope HS3, TiePie Engineering Ltd). This arrangement allowed one transmitter/receiver to transmit and receive signals from all possible transmitter-receiver combinations within the array. The multiplexer and transmitter/receiver were both controlled by a program written in Matlab so that the experimental data was read directly into the signal processing platform. Once the signals were received, the imaging algorithm described by equation 7.4 was used to compute an image of the sample. The measurements were repeated several times to determine the repeatability of the experiments.

A comparison between experimental and simulated waveforms and the resultant images is shown in figure 7.6, illustrating that the DPSM simulation results correlate very well with experimental results. Differences in waveguide coupling and piezoelectric element characteristics both contribute to the variations between A-scan amplitudes, apparent in Fig 7.6 (a.i). The array was subsequently clamped on similar steel plates containing different sized EDM notches in order to verify the array performed as predicted when inspecting defects of increasing length. Figure 7.7 (a.i), (b.i) and (c.i) show the images processed from the data when the array was clamped to a 30mm plate sample containing a 5, 10 and 15mm deep notch respectively. Fig 7.7 (a.ii), (b.ii) and (c.ii) show the corresponding -6dB contours used to size the notches. As expected, the size of the notch image is larger for larger notches. Weak artefacts (<-15dB) above the tip of each notch can also be seen in

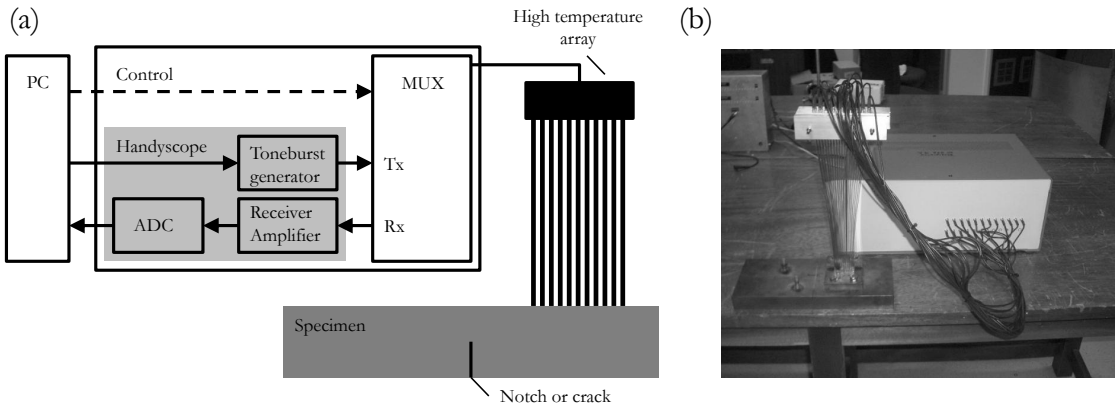

Figure 7.5: (a) Schematic of the SH waveguide array and transmit-receive equipment (b) photo of the prototype waveguide array coupled to a 30mm thick steel plate with a 5mm notch

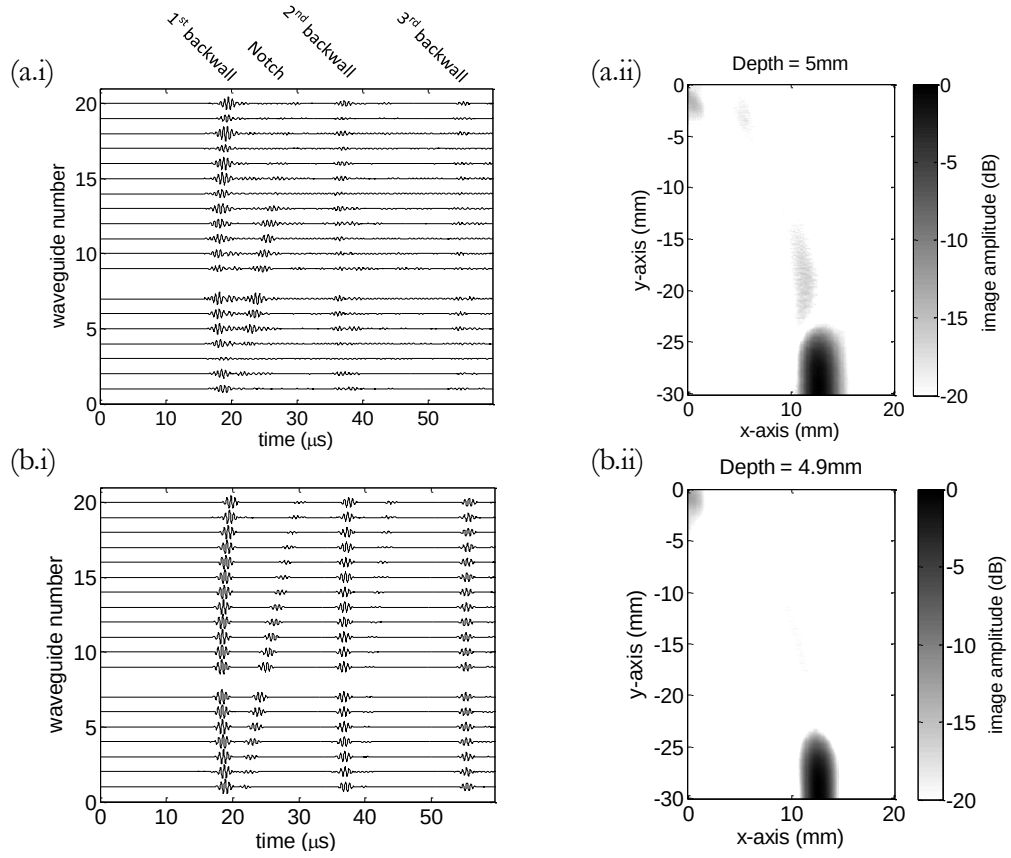

Figure 7.6: Comparison of experimental and simulated results for a 5mm notch in a 30mm thick steel plate, (a.i) experimental pitch-catch signals for transmitting transducer number 8. (a.ii) Image using experimental data. (b.i) Simulated pitch-catch signals for transmitting transducer number 8. (b.ii) Image using simulated data.

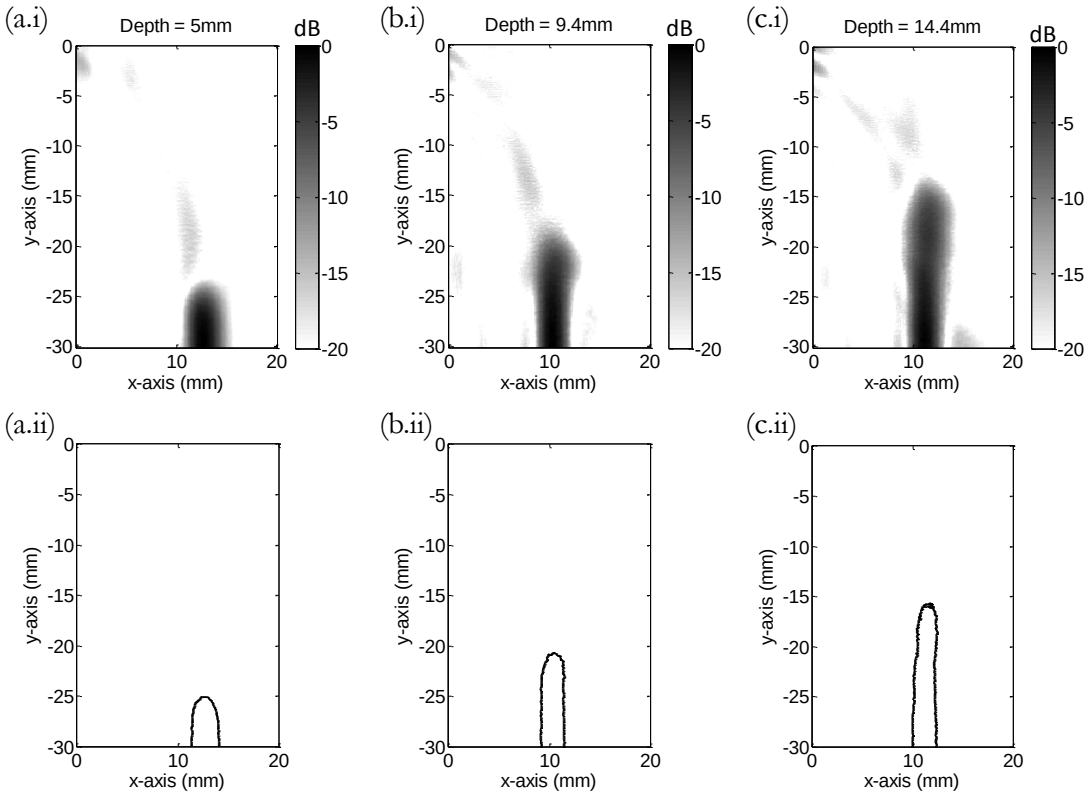

Figure 7.7: Images processed from data acquired when the SH array was clamped to a 30mm thick steel plate containing (a.i) a 5mm deep notch, (b.i) a 10mm deep notch, (c.i) a 15mm deep notch. (a.ii), (b.ii) and (c.ii) show the corresponding -6dB contour plots. (dB values are relative to the maximum values in the image, all notches were 0.3mm wide).

each of the images. They occur at points in the image which have the same propagation distances associated with them as the specular reflections from the crack face, as calculated by equations 7.2 and 7.3. The relatively large amplitude of these signals means that the artefacts do not completely cancel out during image averaging over the transmitting transducers. These artefacts also exist in images created using simulated data; however, because of the absence of noise they are lower in amplitude (<-22dB).

The repeatability of the size measurements for the 10 and 15mm notches was checked with and without un-clamping the array between each measurement by taking 10 data sets and calculating the mean and standard deviation. The mean notch size determined from ten repeat measurements of the sample containing a 10mm notch was 9.49mm with a standard deviation (σ_d) of 0.14mm. Similarly ten repeat mea-

surements on the 15mm notch resulted in a mean of 14.25mm with standard deviation 0.26mm for the measured notch size. In both cases re-clamping the array did not considerably influence the measurements. The repeatability data shows that the measurements are repeatable to within approximately ±0.25mm ($2\sigma_d$). Both notches are undersized which is a result of the particular sizing technique using the 6dB drop method; determining length at a lower amplitude would result in a longer notch length estimation.

An experiment to asses how the array performs under conditions expected in steam power plant environments was also carried out. A 30mm thick stainless steel plate containing a 5mm deep EDM notch was instrumented with the waveguide array and mounted in a furnace so that the waveguides could protrude out of a hole in the furnace door as illustrated in figure 7.8 (a). Any air gaps in the hole were stuffed with mineral wool in order to contain the heat in the furnace. The sample was then heated rapidly to 550°C, held at this temperature for 24 hours and allowed cool over 48 hours to 40°C; this process was repeated 48 times over a period of 6 months while measurements were taken by the array every 2 hours. Temperature cycling was performed in order to simulate conditions the array may be subject to during cyclic loading of a steam power plant. When the images were processed care was taken to adjust for a change in ultrasonic velocity with temperature. Ultrasonic velocity is temperature dependent [111] and has to be corrected for in order to use the correct parameters to process a defect image. The new velocity was determined by taking the mean of the measured TOF to the backwall of the plate for each transmit-receive combination of transducers. The plate thickness was known to be 30mm so that the ultrasonic velocity could be calculated and the values throughout the experiment are shown in Fig 7.8 (c).

It was noticed throughout the experiment that the amplitudes of the received waveforms varied with temperature and time as illustrated in Fig. 7.8 (d). During the initial high temperature cycle, the amplitude (taken as the maximum of the Hilbert envelope over the first backwall reflection relative to the value during initial installation) of all transmit-receive combinations of waveguides was found to increase by an average of 9.5dB for each pitch-catch signal. During subsequent temperature cycles, amplitudes were found to fluctuate by approximately 0.7dB while gradu-

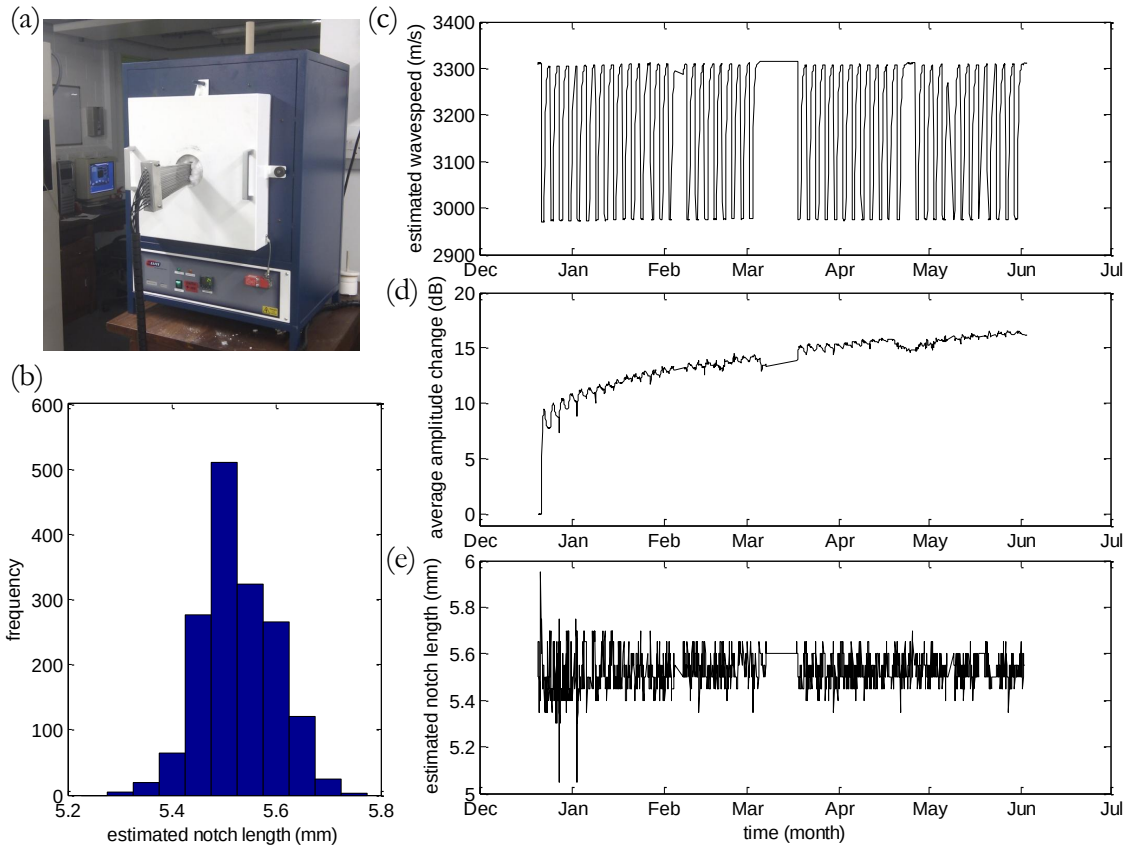

Figure 7.8: (a) Photograph of the experimental setup showing the array and furnace. (b) Histogram of estimated notch lengths showing distribution throughout experiment. (c) Calculated wavespeed throughout experiment. (d) Average amplitude change of first backwall reflection of all pitch-catch signals throughout experiment relative to initial amplitude. (e) Estimated notch length derived from -6dB contour around defect image.

ally increasing, ending at an average increase of 16.5dB. The likely cause of this initial improvement in signal quality is thermal cycling; material at the contacts between the waveguides and the substrate plastically deforms at high temperature and contact pressure, improving the transduction quality between the contacting interfaces (see for example [112]). Continued plastic and elastic deformation during subsequent temperature cycles acts to further improve the contact characteristics. It can be seen in Fig 7.8 (e) that temperature does cause small fluctuations of approximately 0.15mm in crack length estimate; this is likely caused by not taking the increase in plate thickness due to thermal expansion into account, therefore changing how equation 7.4 calculates the notch image. For stainless steel with a thermal expansion coefficient of $16\text{x}10^{-6}$, the approximate plate thickness increase would be 0.25mm. If the relationship between temperature and ultrasonic wavespeed was pre-

cisely known within the component material, as well as the current wall thickness, this error could be removed; however, a detailed knowledge of these parameters at any one time is unlikely to be available within a steam power plant environment where other forms of corrosion or erosion may affect the inner surface of the pipe or pressure vessel. As such this temperature compensation strategy has been identified as the most applicable for industrial implementation, providing a repeatability of ±0.15mm ($2\sigma_d$). The overestimation of the mean notch length of being 5.53mm is caused by the choice of amplitude level at which the notch length is estimated (-6dB). This is not of primary importance since it is the change in fatigue crack length and measurement repeatability which would be of greatest concern for monitoring applications.

7.2.4 Prototype Array Industrial Implementation

Following on from experimental validation of the waveguide array under high temperature cyclic loading conditions, an opportunity became available to install a prototype array on an operational steam power plant at a location identified as containing a thermal fatigue crack during low temperature inspection. The crack was identified as a circumferential defect, initiating at the butt weld between two CMV steel pipes feeding steam from the boiler. The plant itself is a former coal-fired station which is in the process of being converted to fire biomass. Installation was carried out over a two day period, the first day was taken up with the installation itself, taking approximately 4 hours to weld the studs and attach the array, ensuring all waveguides were sufficiently clamped to give good quality signals through the 70mm wall thickness. The second day was predominantly used for data retrieval and analysis, as well as supervision while insulation was reinstalled around the array. The array was installed axially along the pipe with a 20mm offset from the estimated location of the crack which was sized using TOFD to be approximately 2-3mm in length over the width of the array. Although this crack length is shorter than the ideal length for the array to detect, it gives scope for detecting an appreciable amount of growth if it does indeed occur during normal operating conditions. Data acquisition hardware remained the same as that described in section 7.2.3 for

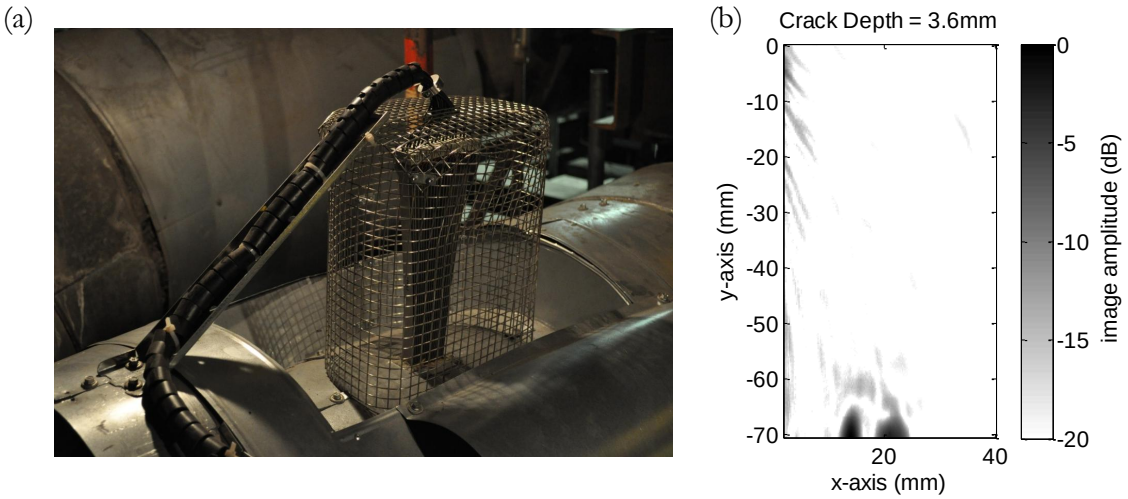

Figure 7.9: (a) Photograph of the final array installation (b) Latest crack image, calculated using data taken in January 2012

this initial prototype installation. Connection ports were installed on an adjoining walkway, 5 metres away from the array in preparation for operator access during data retrieval using a portable multiplexer and laptop.

A photograph of the final installation is shown in figure 7.9 (a), alongside the latest crack image. The crack was calculated to be 3.6mm in length, slightly longer than initially estimated during installation (2.6mm using the array and 2-3mm using TOFD) which may be due to crack tip opening at high temperature, which was estimated to be around 210°C at the time of measurement based on the calculated ultrasonic wavespeed. It is also clear that two reflectors are present in the image; the stronger reflector with the longest length is taken as the crack with a length of 3.6mm, with the lower amplitude reflector possibly being an additional crack or some other reflection caused by a change in pipe cross-sectional area or material property changes within the butt weld. A definitive conclusion to the cause of this lower amplitude reflection is difficult to draw without full knowledge of the true nature of the defect within the weld, as such the higher amplitude reflector has been taken as the life-limiting defect which should be monitored for future growth. Data sets were acquired up until January 2012 when conversion to biomass firing commenced. The main lessons learnt from this initial industrial implementation are as follows:

- The array survived initial temperature cycling, providing consistent crack size estimations over a period of 4 months. It is expected that it will still be in working order once the first data set is taken following plant conversion to biomass firing.
- Array installation was straight forward using standard drawn-arc stud welding equipment, requiring minimum surface preparation using an angle grinder.
- It is advised that future installations include an independent temperature measurement of the test structure using a thermocouple in order to verify velocity calculations and measure the exact temperature conditions the array has been subjected to.
- Implementation of autonomous or wireless data collection would remove the need for continued operator access, identified as the limiting factor for more frequent crack size measurements.

7.3 Velocity Mapping for Detecting Bulk Material Degradation

Another application which benefits greatly from the increase in information content and spatial resolution offered by the array of waveguides is ultrasonic velocity distribution reconstruction, aimed at detecting and monitoring changes in bulk material properties. An example of a material degradation mechanism which can cause such changes is hydrogen attack which often occurs in petrochemical refinery environments. This form of corrosion is of particular concern when carbon steel is subjected to high temperatures (>200°C) and high partial pressures (>690KPa) when in contact with solute hydrogen (H_2) which reacts with iron carbide (Fe_3C) to form methane (CH_4). The gaseous methane cannot diffuse externally because of the large molecule size, therefore micro-voids and fissures are formed within the material structure, often along grain boundaries compromising structural integrity and in some cases leading to catastrophic failure [113]. The conventional approach to avoid such failures has been to use materials which are resistant to this type of degradation, such as low carbon steels containing carbide-forming alloying elements

such as chromium and molybdenum [10]. The Nelson curves serve as a graphical representation of long-term refinery experience, providing guidance on which alloys are most resistant under various operating conditions [10]; however, failures continue to occur with the curves requiring periodic revision [114]. As such an active nondestructive technique for monitoring hydrogen attack within vulnerable areas of a structure would be of great value within the petrochemical industry.

Ultrasonic techniques have previously been applied to the detection of hydrogen attack; specifically techniques based on attenuation, back-scatter and velocity have been investigated [115]. Both attenuation and backscatter increase in areas subject to hydrogen attack because of increased scattering caused by micro-defects, however because the individual defects are around three orders of magnitude smaller than the ultrasonic wavelength (~2-60μm [116]), the effect they have on the material as a whole is to reduce the apparent ultrasonic velocity. Because of the complexity of the corroded structures formed during hydrogen attack, as well as alternative material properties such as inclusions and varying grain structure which can cause very similar changes to ultrasonic signals, conventional detection techniques using scanning probes suffer from poor measurement repeatability, often leading to false or missed calls [117]. This represents the major advantage of using the waveguide array in this application: it can be installed permanently in a vulnerable area operating at high temperature, allowing very small changes in the measured ultrasonic signals to be accurately detected, removing any influence of equipment or operator variance.

Based on the accuracy of cross-correlation when calculating the TOF of pulses in low roughness conditions (see section 4.3.2) and the uncertainty associated with measuring pulse backscatter, it was decided that velocity calculation would be used to reconstruct an image of a localised area of material degradation using the array. The first task was to develop a monitoring strategy based on the expected data quality and volume, coupled with potential imaging algorithms. Subsequently an experimental feasibility study was carried out in order to investigate whether the array is capable of detecting the velocity changes expected during hydrogen attack in an experimental setting. This was achieved by introducing a transient heat distribution into a test specimen, mimicking the effect an area of hydrogen attack could have on the velocity distribution within the material. Much of the work presented

has previously been reported in our paper [118], from which some results in the following sections have been reproduced.

7.3.1 Material Degradation Monitoring Strategy

During hydrogen attack the wall thickness of a pipe or pressure vessel often shows no decrease in thickness [10], degradation simply develops within the structure. If this is the case, it is possible to locate areas of differing velocities by calculating the TOF of pulses reflected from the backwall at different positions within a waveguide array. Using 20 waveguides this totals 380 pitch-catch signals from which data can be extracted about the velocity distribution below the array. Two possible ray paths which travel though the same point on the backwall are illustrated in figure 7.10, each providing extra information about the form of the defect through which the waves are travelling. Taking all transmit-receive combinations into account, multiple ray paths will intersect each image pixel (depending on the assumed width of the ray and pixel size) providing enhanced information about the velocity experienced within the material at that point, leading to an an overdetermined system. The task of the imaging algorithm is to convert the calculated velocity values for each individual signal into a graphical representation of defect size and location by reconstructing the most likely spatial distribution of velocity based on the observed data. The algorithm must do this while remaining stable and achieving the best possible resolution given the quality of the measured data.

Many different techniques exist which vie to reconstruct images of scatterers based on wave projections through or from their structure using TOF tomography. A full review is outside the scope of this thesis; however, the interested reader is referred to [119–122]. What follows is a description of two methods which were found to provide the best reconstruction properties based on the form and expected quality of the data produced by the array. The main challenge faced was a direct result of the array geometry as illustrated in Fig. 7.10. Comparatively few projections through the defect structure are available in this limited view setup, with information content being preferentially distributed along the horizontal direction because of geometrical limitations. As such, algorithms which are potentially stable with the minimum number of projections subject to noise were sought.

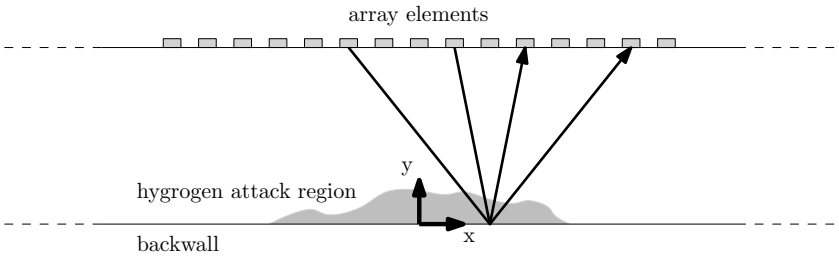

Figure 7.10: Schematic of array geometry incident upon an area of hydrogen attack showing two possible ray paths through the area of degradation.

The first, based on the Kaczmarz algorithm (algebraic reconstruction technique), was selected because it had the potential of utilizing data contained in all 380 signals recorded by the array and is very often used when solving overdetermined systems using an iterative procedure [123]. It became clear however that as noise in the data increased, errors in reconstruction increased dramatically. Therefore a second algorithm was implemented which circumvents the lack of vertical resolution provided by the limited view array by assuming a vertical exponential velocity distribution (assumed distribution method), as could potentially be the case for the diffusion limited propagation of hydrogen within steel. This algorithm has the advantage of requiring only 19 signals (one between each neighboring waveguide pair), attaining much greater stability at the expense of approximating the vertical velocity distribution. Further details about the implementation of each of these algorithms will not be included within this thesis since it was A. Gajdacsi who undertook the majority of the work in algorithm development; however, results will still be presented to illustrate the performance of each technique. The interested reader is referred to our paper [118] for further details.

7.3.2 Temperature Distribution Model

In order to carry out a feasibility study into whether the array could provide accurate enough velocity calculations to make image reconstruction possible, without requiring a complex and potentially expensive hydrogen attack rig, an alternative approach

was proposed. Since temperature has a similar effect on ultrasonic wavespeed to hydrogen attack, a localised heat source was used to produce a transient temperature distribution within a test specimen. Reconstructing the instantaneous temperature distribution using ultrasonic data therefore simulates the scenario of reconstructing an area of material degradation caused by hydrogen attack. However, before selecting suitable temperatures to subject the test specimen to it was necessary to estimate the level of ultrasonic velocity change expected during hydrogen attack. Based on theory presented by Chatterjee [124], the decrease in shear wave velocity which might be expected in areas of hydrogen attack was estimated to be linearly dependent with increasing void fraction, decreasing by approximately 1.5% for a void fraction of 3%. The void fraction represents the volume of material within the area of degradation which is replaced by micro-scale voids which are randomly distributed within the area of degradation. These cause a reduction of the material shear modulus and hence the shear velocity in the material, replicating the effect early stages of hydrogen attack would have.

An experiment was carried out using the same array setup as described in section 7.2.3 in order to determine the true temperature-wave speed relationship. The steel sample was uniformly heated using a hot plate as ultrasonic signals were taken using the array and temperature measurements taken using a k-type thermocouple. The velocity at each temperature was calculated as the average from all pitch-catch signals using the TOF of the first backwall reflections. The results of this experiment are shown in figure 7.11, illustrating a linear trend over the temperatures experienced. Furthermore, the results indicate temperature differentials no larger than 100°C are required to simulate void fractions below 3%. It was therefore concluded that the controllable temperature range within which the experiment would be carried out would be consistent with velocity changes experienced during early onset hydrogen attack.

In order to evaluate the ideal imaging capability of each algorithm, a simple steady-state two dimensional heat conduction simulation was carried out using theory from [125]. The ideal values of the TOF for each pulse propagating through this temperature distribution were subsequently extracted by integrating time along each ray path, avoiding any requirement for a more complicated wave propagation simula-

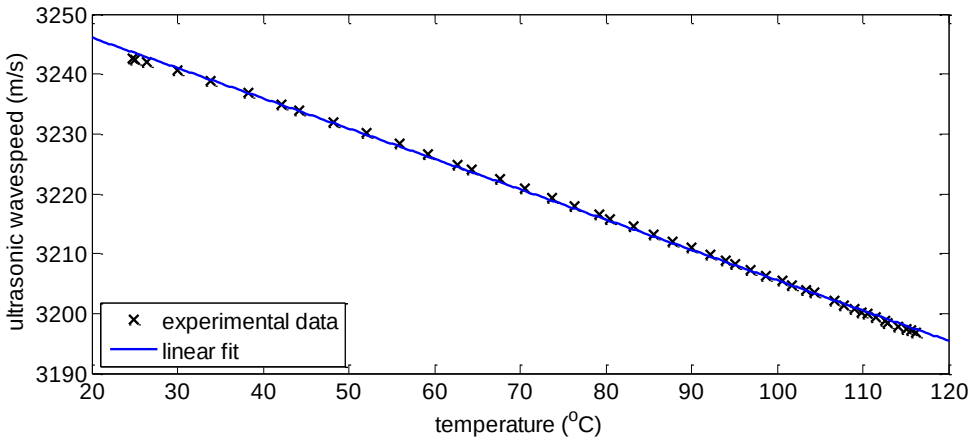

Figure 7.11: Relationship between ultrasonic shear wave velocity and temperature of mild steel test specimen.

tion using a technique such as FEM since ultrasonic wave refraction was found to be negligible. These TOF values could then be supplied to the imaging algorithms to ascertain the capabilities of each in an ideal situation, the results of which are shown in figure 7.12. It can be seen that in the absence of noise, both algorithms are able to produce a reconstruction of the true temperature distribution, correctly locating the hot spot. However, the lack of information available about the distribution in the vertical direction within the projection data has caused the final solution provided by the Kaczmarz algorithm to preferentially calculate higher temperatures closer to the array than they actually occur. This has a knock on effect of reducing the accuracy of the distribution in the horizontal direction, underestimating the temperature at the hot spot by 20°C. The assumed distribution technique avoids this limitation by assuming a vertical distribution, providing a hot spot temperature estimate within 3°C of the true value, as well as a more accurate temperature distribution estimate along the full length of the array.

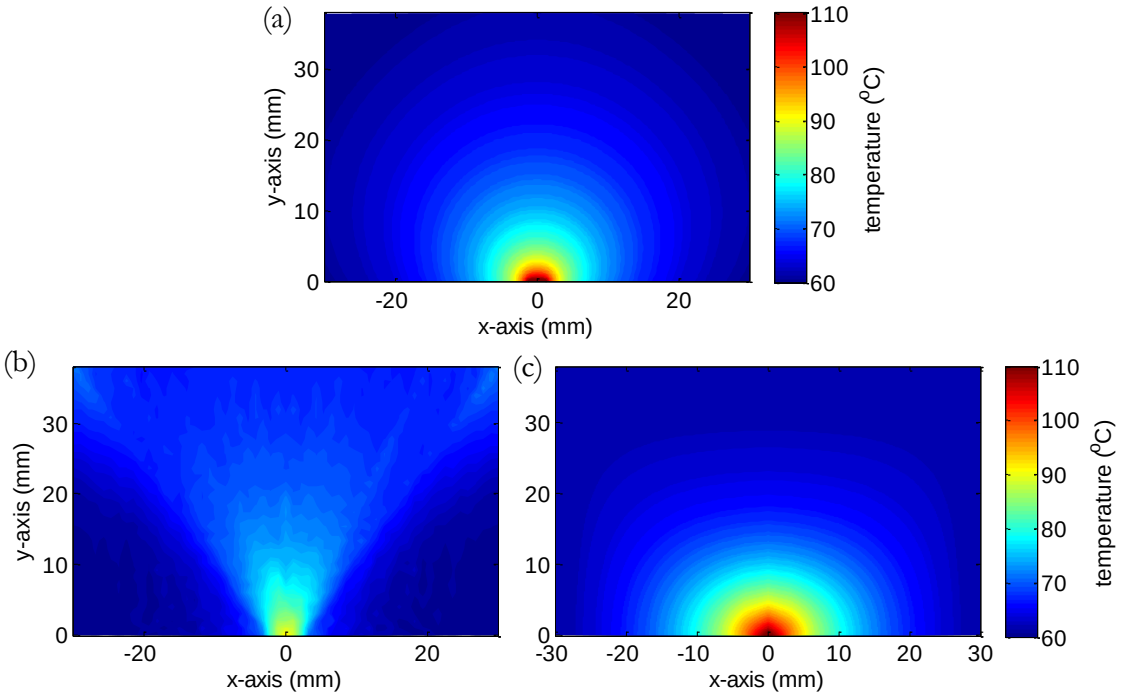

Figure 7.12: (a) Steady state heat conduction simulated temperature distribution. Reconstruction of temperature distribution using (b) Kaczmarz algorithm (c) assumed distribution method.

7.3.3 Experimental Setup and Temperature Reconstructions

An experimental rig was designed which could apply a transient temperature distribution to a test specimen in order to investigate the performance of each algorithm using data produced by the array. A transient temperature distribution was used because of the high conductivity of the mild steel sample, the steady state distribution within such a material would not have a large enough temperature gradient to simulate the void fractions which are of interest. This required the FMC data sets used by the imaging algorithms to be captured very rapidly, in order for the distribution not to change substantially from the first to the last measured signal. This was achieved using an M2M MultiX LF fully parallel array controller (M2M S.A., Les Ulis, France) which was capable of capturing the required data in less than a second using a repetition rate of 0.5kHz and 16 averages for each measured waveform. Without the capability of transmitting an arbitrary signal, a square wave

was defined using the in-built function generator with a centre frequency of 2MHz, producing good quality signals ready for processing using cross-correlation (more details of which can be found in [118]).

In order to create a localised temperature distribution which was approximately constant along the width of the array, a 500W cylindrical cartridge heater (Fast Heat Ltd., Eastborne, UK) with a length of 100mm and a diameter of 9.5mm was used to act as a line source for heat to conduct into the test specimen. A schematic of the experimental setup is shown in figure 7.13, alongside a photograph of the final rig. Five k-type thermocouples were attached to the outside surface of the test specimen in order to assess the form of the temperature distribution, although it is expected to differ slightly from the distribution within the test specimen at the array location because of edge convection and a slightly non-uniform heat distribution along the length of the heating element. Once clamped to the test specimen using springs to allow for thermal expansion, the heating element was insulated to ensure maximum heat transfer efficiency at the contact patch. The heating element was powered using an Elektro-Automatik PS 8000 DT power supply (Viersen, Germany) set to provide 400W as 60 FMC data sets were taken over a 10 minute period using the array controller, as well as temperature measurements using a Pico Technology USB TC-08 thermocouple data logger (Eaton Socon, UK). The pitch between the waveguides was increased to 3mm to provide a larger array aperture, increasing the potential area of inspection for the same investment in hardware.

Reconstructions of the temperature distributions provided by Kaczmarz algorithm and the assumed distribution method using data measured when the hot spot was at its highest temperature as measured by the thermocouple (115°C) are shown in figure 7.14. Also shown are the reconstructed temperature distributions calculated at the same hot spot temperature when the heating element was offset from the centre for the array by 10mm, demonstrating the positional capabilities of each algorithm. It can be seen in each case that the general location of the hot spot is correctly identified; however, Kaczmarz algorithm is much more susceptible to noise within the calculated velocity data, which is evident from the poor temperature resolution within the final images. This equates to a hot spot accuracy of approximately ±30°C which was found to be independent of the actual hot spot temperature. In

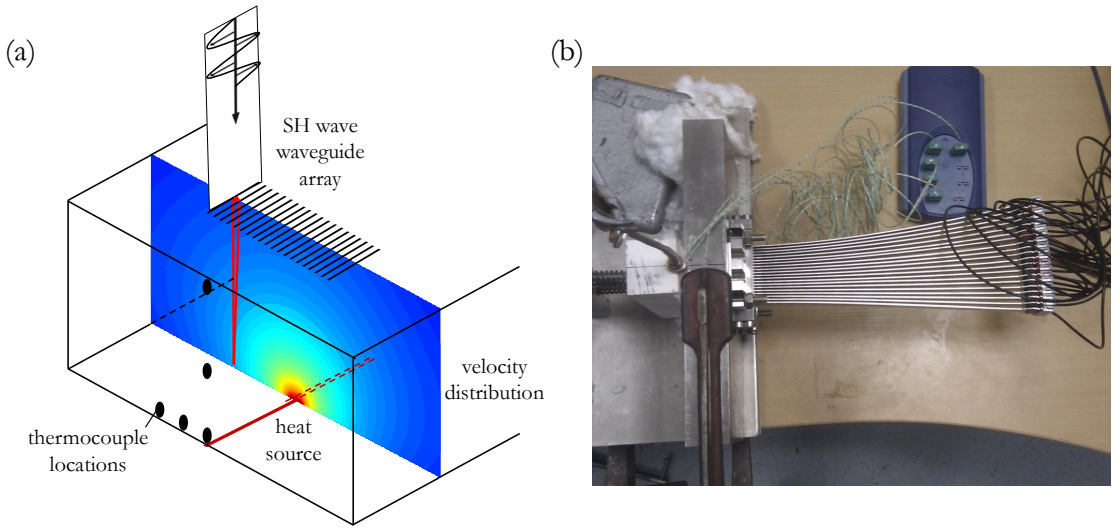

Figure 7.13: (a) Schematic of heating arrangement to produce a two dimensional temperature distribution below the array. (b) Photograph of experimental setup.

contrast the assumed distribution model has an accuracy of approximately ±5°C, 6 times better while requiring less data and image processing. The main cause of difference between each algorithm is the limited view of the array which is a geometrical limitation that cannot be overcome for a plate geometry. Increasing the length of the array would improve information content along the vertical direction; however, large levels of beam spread and attenuation expected in petrochemical plant materials would limit the allowable array aperture greatly. As such it is advised that in this limited view arrangement that some assumption should be made about the vertical velocity distribution (for example if not exponential, a linear, polynomial or step function could also be assumed) in order to provide more accurate conclusions about the extent of the attack being experienced within the monitored component. Alternative imaging algorithms specifically designed for limited view array geometries could also be implemented [126].

The results of this feasibility study were very encouraging, showing that very small changes in velocity could be measured using the waveguide array and used to produce an image of possible material degradation. The results are reported in our paper [118] which describes the imaging algorithm work carried out by A.Gajdacsi in much greater detail. All future development of the monitoring concept was subsequently handed over to A.Gajdacsi as part of his PhD studies. Recent work within the

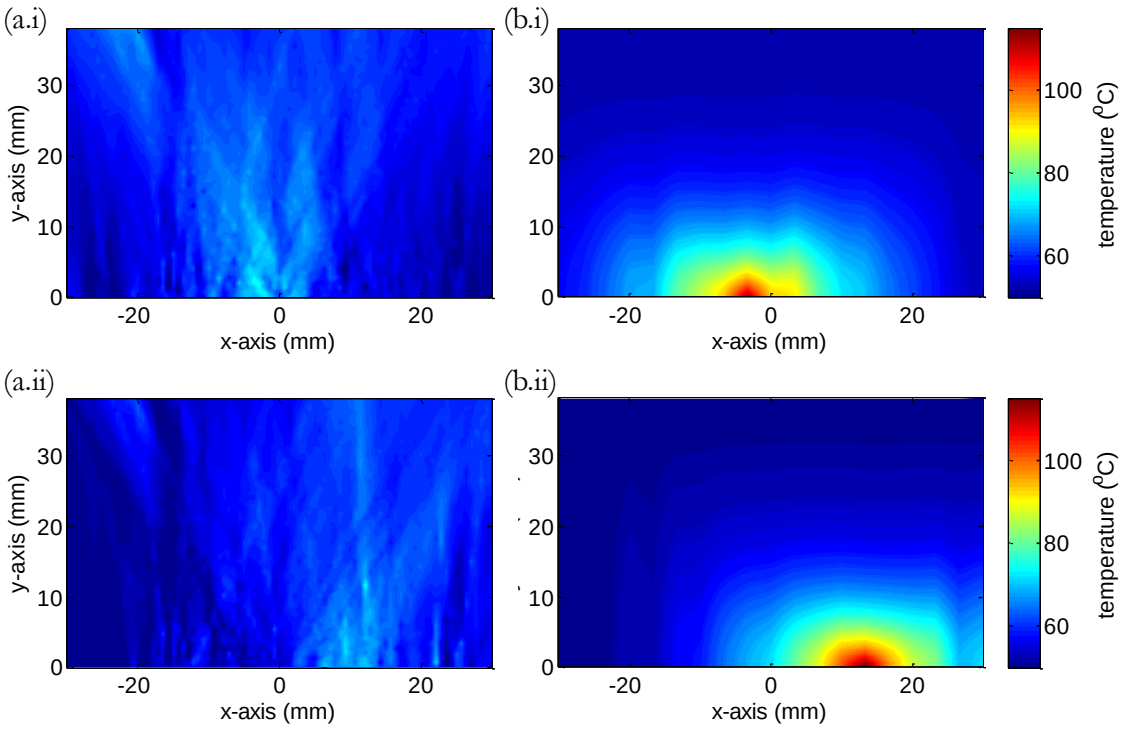

Figure 7.14: Reconstructions of temperature distribution at the end of the experiment using (a) Kaczmarz algorithm and (b) the assumed distribution method for (i) centralised heat source and (ii) 10mm offset heat source. The array is located along the top of the images.

project has focussed on the implementation of an experimental corrosion rig to simulate real hydrogen attack conditions more accurately, as well as more accurate signal processing techniques and temperature compensation.

7.4 Summary

Two different applications of an array of waveguide transducers have been investigated and experimentally verified, illustrating the benefits that increased levels of information can provide when monitoring different forms of corrosion within high temperature environments. The first of these applications was monitoring circumferential thermal fatigue crack growth at the weld between two sections of piping, caused by load cycling of a steam power plant. By using the TFM on ultrasonic signals which had reflected from the crack face via the backwall, it was shown that an image of a fatigue crack could be produced, from which its location and length could

be estimated and monitored for growth. A simulated study was carried out using the DPSM to assess the working envelope of the array. The main conclusions were that a minimum of 15 waveguide transducers would be necessary for measurement error to be within ±0.25mm and that the defect should be placed in close proximity to one end of the array, ensuring some offset exists so that backwall reflections do not encroach upon the defect image. An array of 20 waveguide transducers was specified for experimental investigations in order to design in some redundancy if individual transducers fail.

Temperature cycling of a test specimen containing a 5mm long EDM notch was carried out from 40°C to 550°C, 48 times over a 6 month period, producing a measurement repeatability of ±0.15mm ($2\sigma_d$). The success of this experiment lead to an opportunity to install a prototype array on an operational coal fired power plant which has subsequently been converted to biomass firing. Installation was straight forward and good quality signals were achieved, producing an image of a defect in the expected location with an initial length estimate of 2.6mm which was within the 2-3mm estimate provided by an external contractor using conventional TOFD inspection. Upon temperature cycling this length increased to 3.6mm, possibly caused by crack tip opening at high temperature. This estimate remained stable for 4 months until the plant was shut down in preparation for conversion to biomass firing. It is hoped that the success of this initial industrial implementation of the technology will pave the way for future development, particularly in the area of data extraction since operator access is limited while the plant is under load.

The second application which has been investigated is monitoring bulk material degradation caused by hydrogen attack within high temperature, high pressure petrochemical refinery environments. Micro-voids caused by trapped methane alter the shear modulus of the material, causing ultrasonic wavespeed to decrease. An experimental proof of concept study was carried out to asses whether the signals produced by the waveguide array using existing signal processing techniques would be sensitive enough to the small velocity differentials expected under early onset hydrogen attack. To simulate these conditions experimentally a two dimensional temperature distribution was applied to the test specimen using a cylindrical cartidge heater, producing SH wave velocity distributions which would be equivalent

to void fractions within hydrogen attacked regions of up to 3%.

Two TOF tomography imaging algorithms were selected as the most applicable within the high noise, limited view geometry offered by the array: the Kaczmarz algorithm and the assumed distribution technique. Both were found to successfully locate the hot spot within the experimental data; however the lack of information within the projections related to the vertical velocity distribution caused the Kaczmarz algorithm to underestimate the temperature of the hot spot by approximately 30°C. Noise in the data also greatly affected the images produced by the algorithm. The assumed distribution method circumvented this lack of vertical information by assuming an exponential form to the temperature below the array, producing hot spot temperature estimates to within 5°C of that indicated by thermocouple measurements. However, the simplicity of the assumed distribution technique requires an approximation to be made and only 5% of the information held in the FMC data set is exploited. Further work should be carried out investigating alternative imaging algorithms for use in limited view geometries, as well as better simulation of the actual hydrogen attack environment. The success of this experiment at detecting very small changes in ultrasonic velocity indicates that a robust monitoring technique could be developed using the waveguide array; however, further study is outside the scope of this thesis and future work will be carried out by A.Gajdacsi.

The two practical applications of a high temperature waveguide array presented in this chapter show promise for future structural degradation monitoring within extreme environments, however they are not the only opportunities provided by the technology. It is hoped that the work presented in this chapter will provide a footing for others to expand upon and develop solutions to a wider range of non-destructive corrosion monitoring problems encountered within various challenging operating conditions.

Chapter 8

Conclusions

8.1 Thesis review

A new approach to simulating ultrasonic wave scattering from rough surfaces has been presented in this thesis, developed using the semi-analytical mesh-free DPSM. A reduction in simulation time of around three orders of magnitude over the FEM is a clear indication of the improvement in efficiency over meshed numerical techniques. The inclusion of multiple scattering, surface self-shadowing and edge diffraction also improve accuracy over approximate analytical techniques such as classical Kirchhoff theory. The ability to define arbitrary incidence fields, as well as calculate field variables within the near-field are also great advantages offered by the technique. The results from the simulation were subsequently used to improve the quantitative analysis of ultrasonic signals gathered during wall thickness monitoring of corroding components within high temperature environments.

Chapter 2 outlined the challenges still faced when modelling ultrasound scattering from rough surfaces. It began by presenting the equations which must be solved when simulating mechanical wave propagation within solid structures, introducing the powerful simplification that the scalar wave approximation can bring when considering SH wave propagation in two dimensional geometries. A description of current techniques concluded that although many exist, few strike a good balance between simulation complexity, efficiency and accuracy. Chapter 3 then introduced

the DPSM as an alternative which was comparatively simple to implement, required equations to be solved only along problem boundaries and inherently included multiple scattering, surface self-shadowing and edge diffraction within the boundary integral matrix equation. Results produced by the DPSM were indistinguishable from those produced using the FEM, and further validation against experimental results gained using the waveguide transducers also indicated that the scalar wave approximation was sufficient to capture SH wave scattering behaviour in two dimensional geometries.

Chapter 4 then focussed on using the simulation to assess TOF algorithm stability for wall thickness monitoring within corroded environments using rough surfaces with Gaussian distributed height and length characteristics. It was found that roughness can have a large impact on reflected pulse shape, and TOF algorithms based on earliest signal arrival are most stable under high roughness conditions ($\sigma > 0.1\lambda$). Signal quality metrics were also proposed as probabilistic measures of the error in thickness measurement based on the shape change of the pulse. Correlation coefficient showed the most promise; however, it was clear that insufficient information is carried within a single reflected pulse to determine characteristics of the surface itself.

The efficiency of the DPSM was then exploited fully by applying it to scattering in three dimensions from comparatively large (10x17λ) and rough reflectors in Chapter 5. Efficiency enhancing techniques such as GMRes, beam superposition and parallel processing all combined to produce a simulation time of approximately 30 minutes, which is currently impossible to achieve using the FEM with comparable simulation objectives and computing power. Validation could only be carried out by comparison to experimental results, showing agreement in both amplitude and pulse shape within expected experimental error bounds even when using the scalar wave approximation. Furthermore, having access to simulated results from both two dimensional and three dimensional rough surface geometries allowed direct comparison, leading to the proposal of a correction procedure which could be used to convert results gained rapidly in two dimensions to more closely resemble those from rough surfaces in three dimensions.

Alternative corroded surface geometries were considered in Chapter 6, focussing on

localised pitting. Experimental results illustrated the extremes which could be expected for signal change from singular defects over micron and millimetre length scales. Comparison to experimental results using a surface taken from a real corroded sample again showed the simulation capable of predicting signal shape change under increasingly corroded conditions. A corrosion model was subsequently taken from literature and used alongside the DPSM to describe how defect morphology through time can change ultrasonic signal shape and corrosion rate predictions using different TOF algorithms.

Monitoring of structural degradation mechanisms other than wall thickness loss was explored in Chapter 7 using array geometries to increase data availability. Two applications were considered: thermal fatigue crack monitoring and bulk material degradation through hydrogen attack. Both were shown to be possible using an array architecture and the current waveguide transducer; it is hoped that similar application of the technology could provide monitoring solutions for other defect morphologies within high temperature environments.

8.2 Main findings

Accurate simulation of how waves interact with rough boundaries during reflection is a very complex problem to solve. Applications involving such interactions span many scientific and engineering disciplines making it the focal point of much literature. This importance and complexity has lead to many different techniques being proposed with associated strengths and weaknesses. The main aim of the work presented in this thesis was to present an alternative which maximised efficiency with a minimum impact on the accuracy of the final simulated result; the practical application being the NDE of wall thickness using permanently installed ultrasonic sensors within high temperature and corrosive environments. This was achieved by developing a simulation based on the DPSM, a semi-analytical mesh-free BIE technique which previously had not been applied to the problem of rough surface scattering. It allowed simulations to be carried out within the near field of comparatively large reflectors, including effects such as multiple scattering and surface self-shadowing, within timescales appropriate for statistical analysis investigations to be performed.

The alteration to standard DPSM for application to purely two dimensional geometries was described in detail (as published in [P5]), as well as comparison of the three dimensional model to experimental results (to be published in [P6]). Its simplicity, efficiency and accuracy make it a strong candidate for future use by researchers investigating wave scattering, from electromagnetic waves to ultrasonic waves.

The scalar wave approximation has been utilised throughout this thesis as a simplifying assumption which is mathematically only valid for SH wave scattering in two dimensional geometries. It was shown by comparison to experimental results that this was indeed the case; however, for the surface geometries and waveguide transducers considered, it was also found that the amplitude and pulse shape changes predicted using the scalar wave model in three dimensions agreed within the experimental error bounds of the SH wave transducers. Therefore, the extra complexity associated with a full elastodynamic analysis of SH wave scattering in three dimensions was shown to be unnecessary since the majority of the physical interactions are captured using much simpler scalar waves. The experimental results of scattering from a three dimensional rough surface also served to illustrate the large variability that can exist in scattered response when a sensor is installed at different locations separated by only 1.25λ (to be published in [P6]).

Analysis of signals produced using the simulation was carried out in order to assess the levels of roughness beyond which various TOF algorithms became unstable. It was found that cross-correlation is superior to envelope peak detection and threshold first arrival in accurately determining wall thickness when $\sigma < 0.1\lambda$; however, as roughness increases and diffuse energy acts to completely distort the shape of the scattered pulse, algorithms based on finding the earliest arrival of the pulse become the most stable. The performance of such algorithms is directly linked to how low the detection threshold can be set, potentially limiting their application in field results (as published in [P2] and [P5]). The limited data available within a single reflected pulse was also shown to be insufficient for deterministic conclusions to be drawn about the nature of the surface causing the shape change. The correlation coefficient could potentially be used to estimate thickness measurement uncertainty; however, direct application to field results would be challenging.

Another novel investigation which was carried out in this thesis thanks to the simu-

lation developed was the comparison between results gained using both two dimensional and three dimensional geometries. It was found that although coherent energy within the scattered pulses was similar for comparable RMS height and correlation length parameters, diffuse energy dominated two dimensional results because of a lack of out-of-plane spatial averaging. This means that for given surface statistics, two dimensional results should always be considered as a worst case scenario. It was found that the reduction in the RMS height of the average surface beneath the sensor contact patch could be used directly to reduce the diffuse energy component within two dimensional results to produce simulated results which much more closely approximated what would be expected in three dimensions. The correction procedure was found to work well when $\lambda_0 \leq \lambda$ and $\sigma < \lambda/5$ for sensor widths greater than 2.5λ and less than 7.5λ.

The extra information available in an array geometry allowed the waveguide transducer to be applied to other high temperature NDE monitoring applications. The TFM was applied to thermal fatigue crack monitoring and shown experimentally to produce repeatable and accurate measurements of EDM notches during sustained temperature cycling over a 6 month period (as published in [P1] and [P3]). A prototype was subsequently installed on an operational power plant and shown capable of producing stable estimates of crack length and position, the first such implementation in the world. A method of monitoring hydrogen attack by reconstructing ultrasonic velocity using backwall reflections in the limited view array geometry was also presented. An experimental feasibility study, carried out using a transient two dimensional temperature distribution to simulate the effect localised hydrogen attack could have, indicated that the levels of velocity change expected during such degradation could be measured using the current transducers (to be published in [P7]). Temperature distribution reconstructions carried out using two different algorithms (Kaczmarz algorithm and the assumed distribution technique) successfully detected the location and approximate temperature of the hot spot; however, further work is necessary to utilise all the data available within the limited view FMC data set.

8.3 Areas for future work

Although experimental results presented in this thesis suggest the scalar wave approximation is sufficient for modelling SH wave scattering from the rough surfaces considered using the waveguide transducer geometry described, to the authors knowledge no simulation technique exists which is capable of modelling elastic wave scattering from large rough three dimensional reflectors within the near field. This makes formal comparison of simulated elastic and scalar wave results impossible. The validity of the scalar wave approximation when modelling elastic wave scattering from surfaces with increasing levels of roughness and alternative defect morphologies will therefore remain uncertain. To address this issue, one future avenue of research could be the development of a simulation technique which is capable of efficiently and accurately simulating elastic wave scattering at rough boundaries. Based on the success of the scalar wave DPSM, the obvious choice would be use its elastodynamic form as described in Chapter 4 of [51]; however, the results from an initial implementation carried out using Matlab indicate a potential problem as illustrated in figure 8.1.

The simple scenario of a point load within an infinite solid medium under plane strain conditions was chosen to verify results given by the elastic DPSM were the same as the FEM before the simulation was developed any further. It was found that in the near field there was a large difference between calculated displacements produced by the elastic DPSM and the FEM as illustrated in Fig. 8.1 (b) which becomes negligible for propagation distances greater than approximately 3.7mm (2.3λ). Accuracy of the equations within the near field is imperative for the final scattered field to remain correct since point sources must be placed in close proximity to the boundaries. Since a reason for this discrepancy was not forthcoming and because it was not necessary for the results presented within this thesis, further development was halted. However, future work could pick up where this simulation left off and improve upon the near field behaviour of the elastic DPSM.

Of the TOF algorithms investigated in Chapter 4 of this thesis, cross-correlation was found to provide the most accurate wall thickness estimates when RMS height was low ($\sigma < 0.1\lambda$), and threshold first arrival was the most stable over the full range of

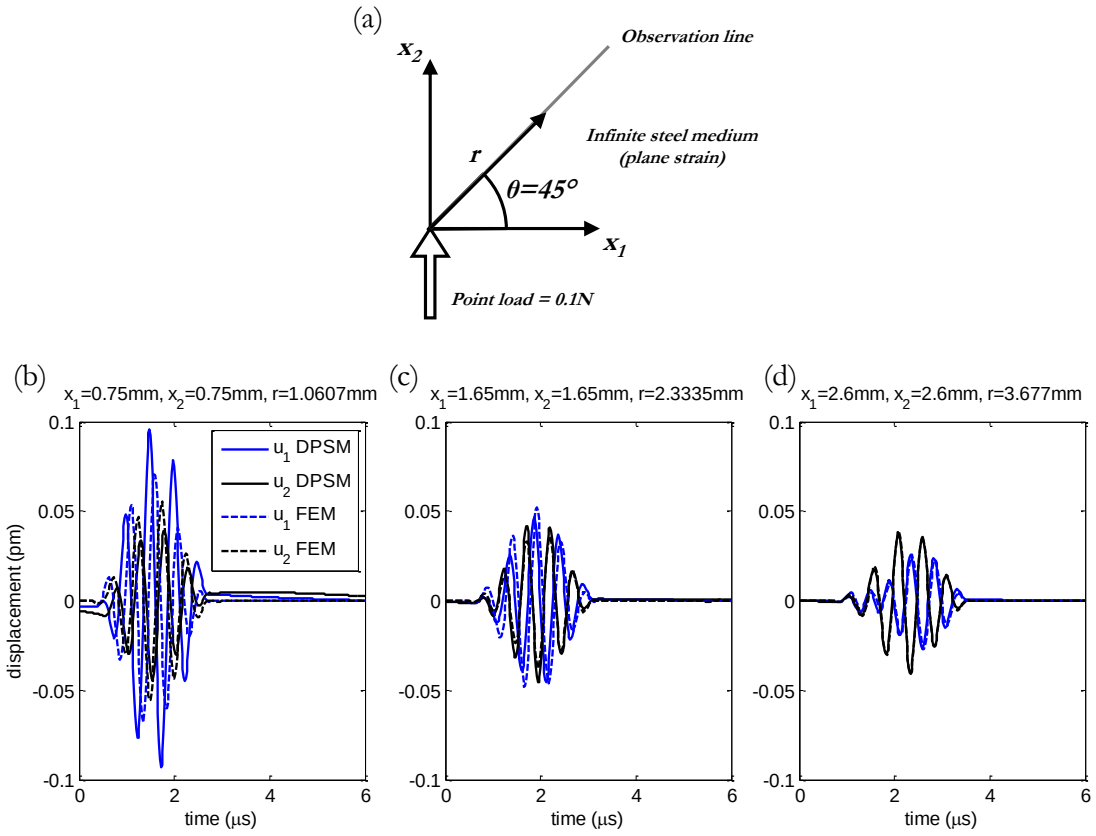

Figure 8.1: (a) Schematic of simple simulated case. Simulated signals showing horizontal displacement (u_1) and vertical displacement (u_2) produced by the elastic DPSM simulation and the two dimensional plane strain FEM simulation using a 2MHz input Hanning windowed toneburst point load at an observation point where (b) $x_1 = x_2$ =0.75mm, (b) $x_1 = x_2$ =1.65mm and (c) $x_1 = x_2$ =2.60mm.

surface roughnesses considered. The correlation coefficient was also shown to be the most promising error metric when trying to ascertain a probabilistic measure of the uncertainty in thickness measurement based on the shape of the reflected pulse. Following on from these simulated studies, the algorithms described should be applied to field results in order to improve confidence in the corrosion rate estimates, and to determine whether thickness measurement uncertainty estimation is a possibility when dealing with real signals. There is also scope for alternate TOF algorithm development, aimed at combining the strengths of cross-correlation and threshold first arrival to produce a single algorithm possessing the best possible accuracy over all roughness levels.

A correction procedure was proposed in Chapter 5 of this thesis which could correct the high levels of diffuse energy in two dimensional simulations to levels which

would be more likely in reality based on the characteristics of the scattering surface and transducer geometry. This concept is potentially very powerful in that it can reduce the time required for simulated investigations which would otherwise need to be carried out in three dimensions by several orders of magnitude. Currently it has only been applied to rough surfaces with Gaussian distributed height and length characteristics using rectangular strip-like transducer contact patches. Future work could be carried out to apply the diffuse enrgy correction concept to alternative scenarios; for example piston or square transducer geometries, rough surfaces described by other statistics or even to other wave scattering problems such as grain boundary scattering in highly attenuative materials.

As described in Chapter 7, further development work has already been undertaken to improve on the performance of the waveguide array designed to monitor bulk material degradation such as hydrogen attack in high temperature environments. Work is still ongoing on designing an electrochemical corrosion rig to simulate more realistic corrosion environments, as well as the development of more accurate signal processing techniques to isolate the signal changes caused by hydrogen attack from those caused by temperature change or thickness loss. The thermal fatigue crack monitoring array is also currently the subject of further experimental investigations to see whether the growth of an actual fatigue crack can be measured using a high temperature fatigue rig. Continued analysis of data from the prototype array on an operational steam power plant will also provide further proof that the waveguide array operates consistently within industrial environments and is a candidate for future commercial development.

Appendix

Wall Thickness Box Plots

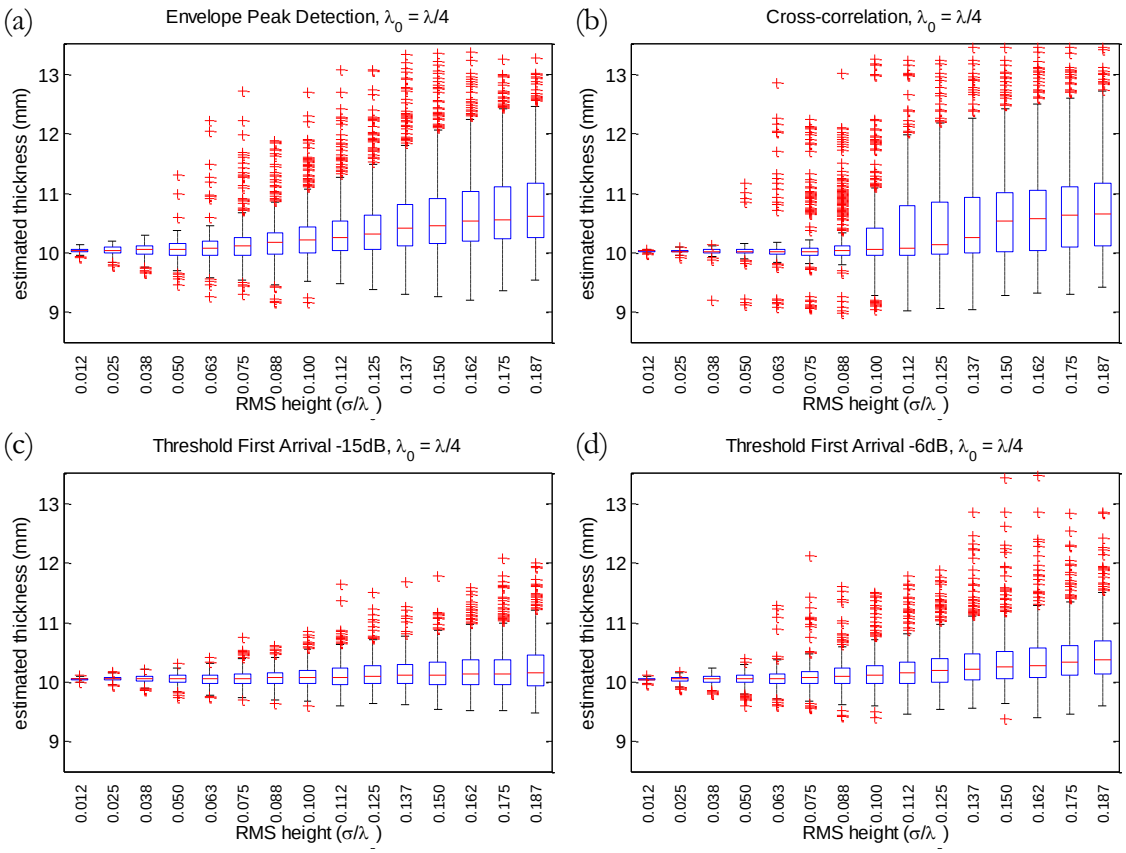

Figure 8.2: Box plots showing the statistical distribution of estimated wall thickness values obtained using the two dimensional DPSM simulation for a 10mm thick wall with RMS heights approaching 0.3mm ($\sigma < \lambda/5$) and a correlation length of 0.4mm ($\lambda_0 = \lambda/4$ using (a) envelope peak detection (b) cross-correlation (c) threshold first arrival with a -15dB threshold, and (d) threshold first arrival with a -6dB threshold.

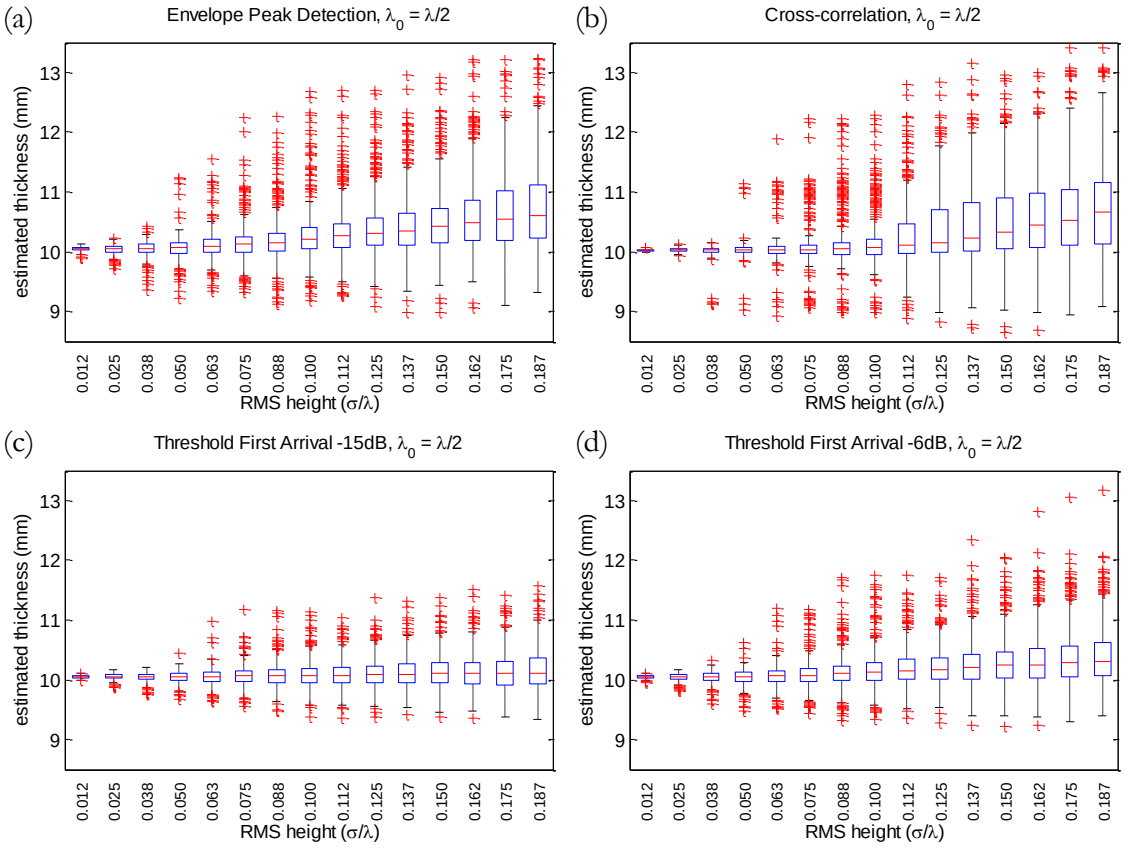

Figure 8.3: Box plots showing the statistical distribution of estimated wall thickness values obtained using the two dimensional DPSM simulation for a 10mm thick wall with RMS heights approaching 0.3mm ($\sigma < \lambda/5$) and a correlation length of 0.8mm ($\lambda_0 = \lambda/2$ using (a) envelope peak detection (b) cross-correlation (c) threshold first arrival with a -15dB threshold, and (d) threshold first arrival with a -6dB threshold.

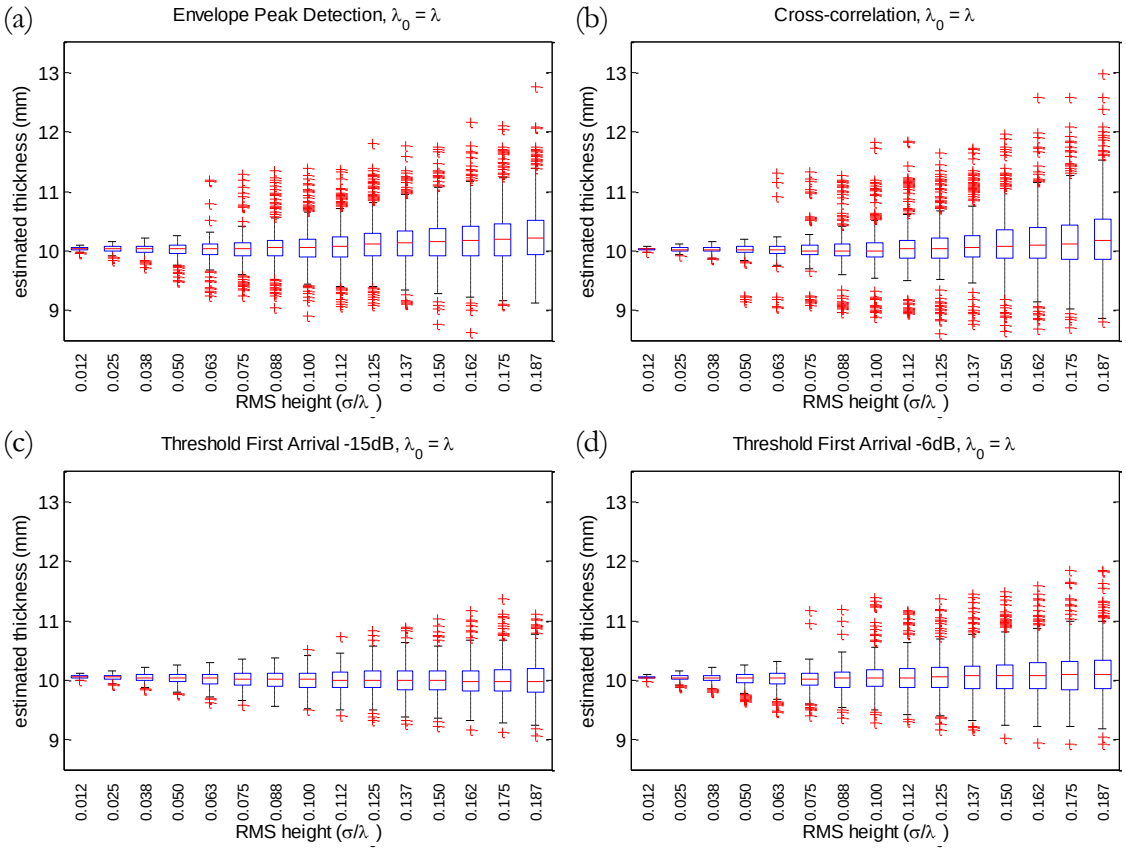

Figure 8.4: Box plots showing the statistical distribution of estimated wall thickness values obtained using the two dimensional DPSM simulation for a 10mm thick wall with RMS heights approaching 0.3mm ($\sigma < \lambda/5$) and a correlation length of 1.6mm ($\lambda_0 = \lambda$ using (a) envelope peak detection (b) cross-correlation (c) threshold first arrival with a -15dB threshold, and (d) threshold first arrival with a -6dB threshold.

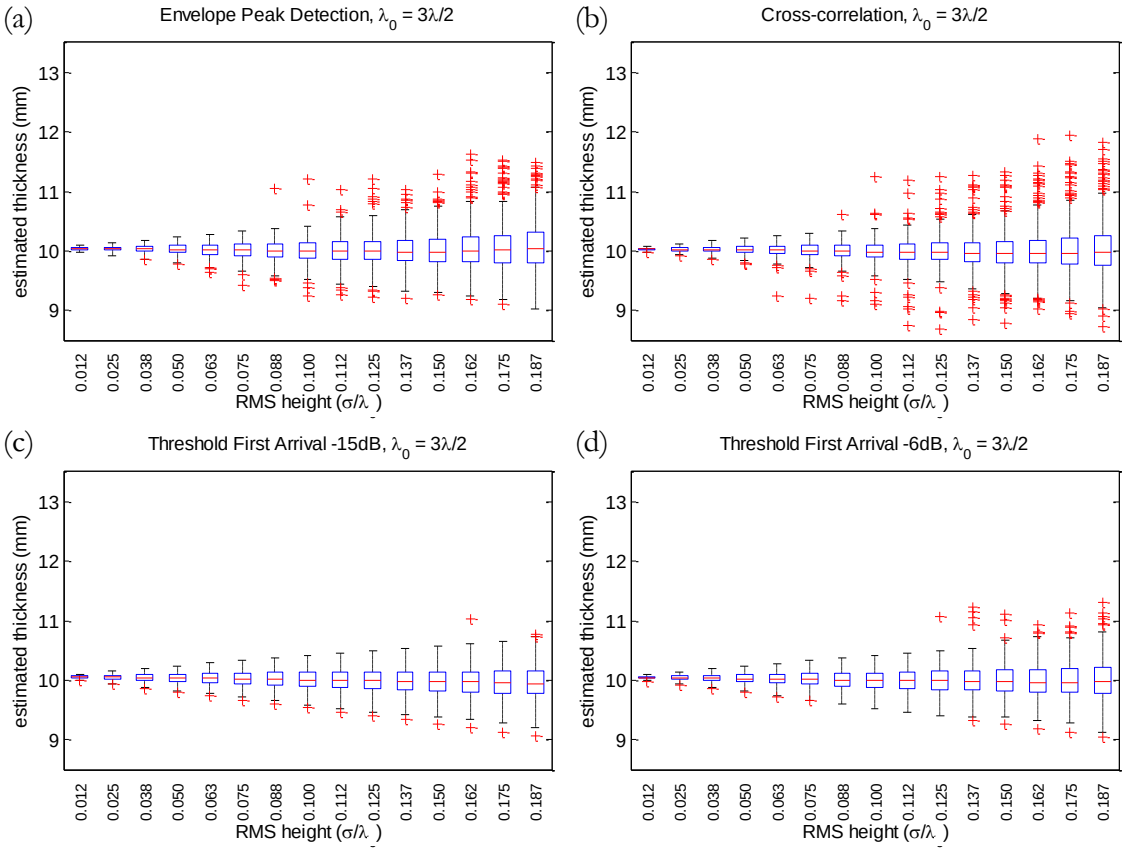

Figure 8.5: Box plots showing the statistical distribution of estimated wall thickness values obtained using the two dimensional DPSM simulation for a 10mm thick wall with RMS heights approaching 0.3mm ($\sigma < \lambda/5$) and a correlation length of 2.4mm ($\lambda_0 = 3\lambda/2$ using (a) envelope peak detection (b) cross-correlation (c) threshold first arrival with a -15dB threshold, and (d) threshold first arrival with a -6dB threshold.

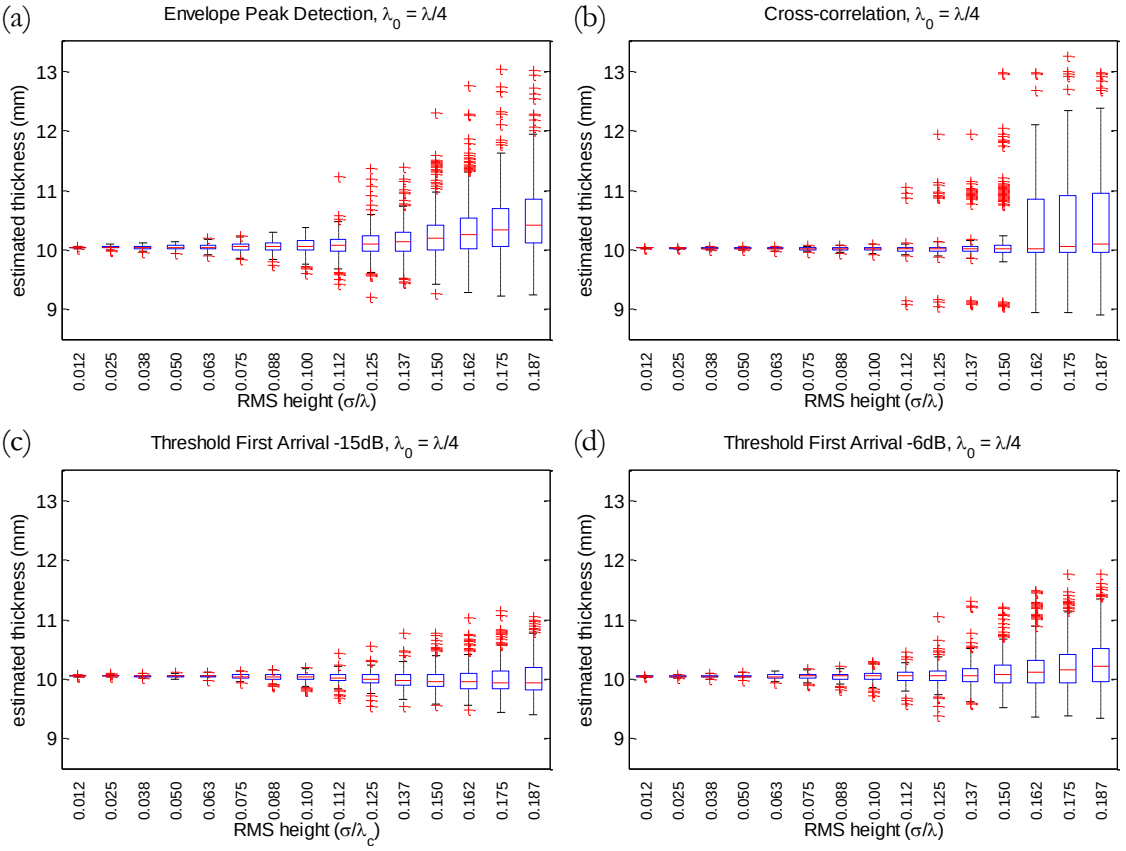

Figure 8.6: Box plots showing the statistical distribution of estimated wall thickness values obtained using the two dimensional DPSM simulation with '2D to 3D' correction and an assumed source length of 12mm for a 10mm thick wall with RMS heights approaching 0.3mm ($\sigma < \lambda/5$) and a correlation length of 0.4mm ($\lambda_0 = \lambda/4$ using (a) envelope peak detection (b) cross-correlation (c) threshold first arrival with a -15dB threshold, and (d) threshold first arrival with a -6dB threshold.

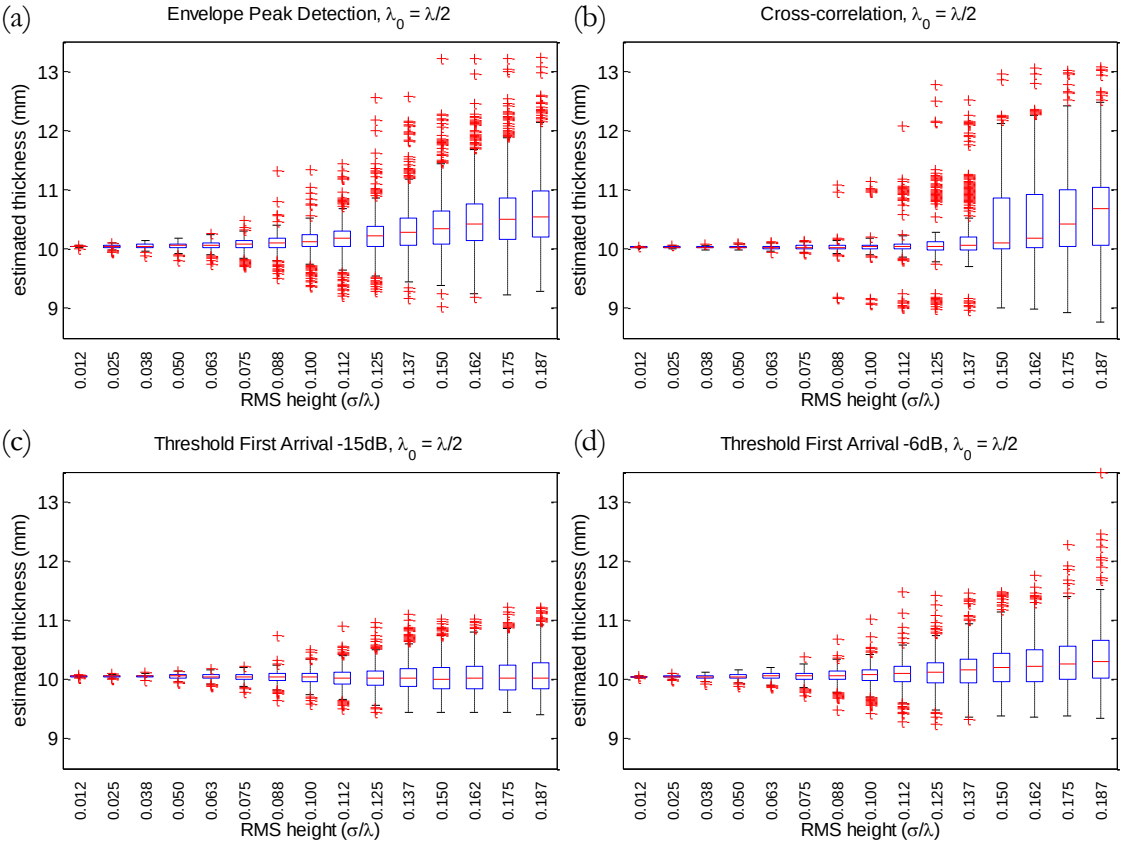

Figure 8.7: Box plots showing the statistical distribution of estimated wall thickness values obtained using the two dimensional DPSM simulation with '2D to 3D' correction and an assumed source length of 12mm for a 10mm thick wall with RMS heights approaching 0.3mm ($\sigma < \lambda/5$) and a correlation length of 0.8mm ($\lambda_0 = \lambda/2$ using (a) envelope peak detection (b) cross-correlation (c) threshold first arrival with a -15dB threshold, and (d) threshold first arrival with a -6dB threshold.

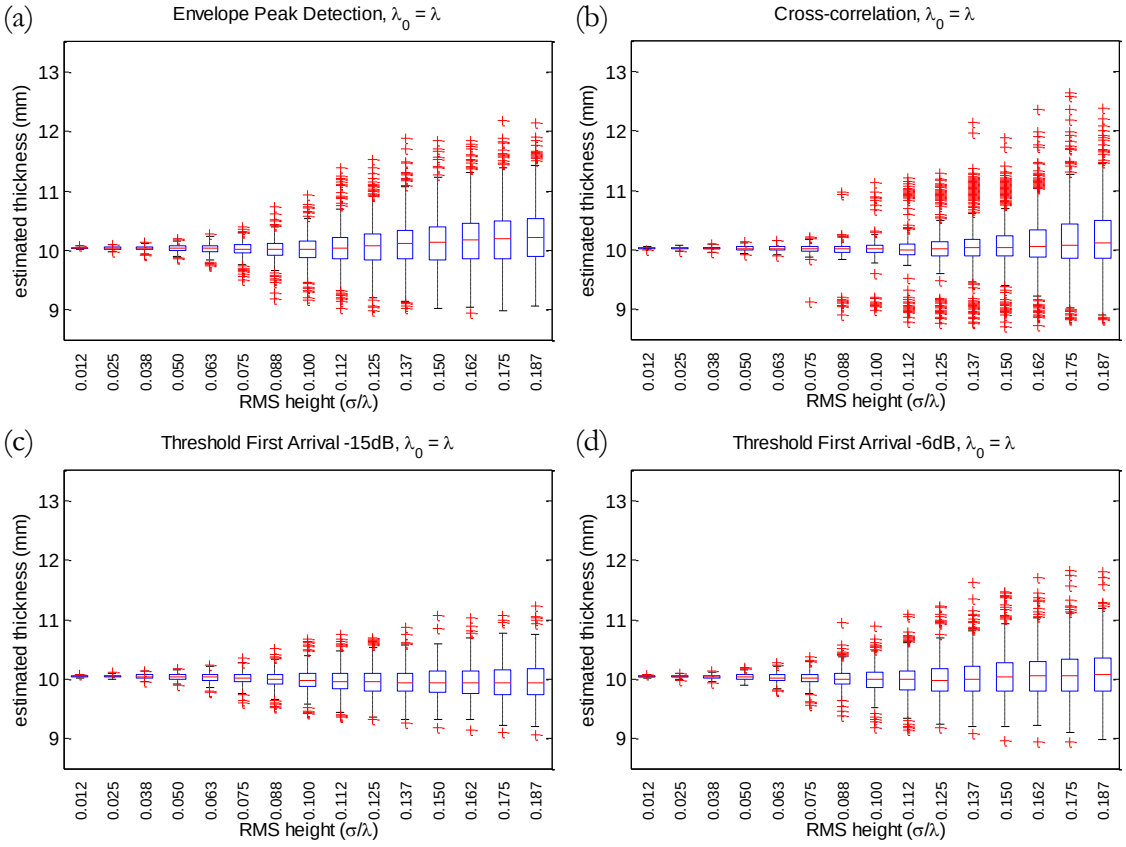

Figure 8.8: Box plots showing the statistical distribution of estimated wall thickness values obtained using the two dimensional DPSM simulation with '2D to 3D' correction and an assumed source length of 12mm for a 10mm thick wall with RMS heights approaching 0.3mm ($\sigma < \lambda/5$) and a correlation length of 1.6mm ($\lambda_0 = \lambda$ using (a) envelope peak detection (b) cross-correlation (c) threshold first arrival with a -15dB threshold, and (d) threshold first arrival with a -6dB threshold.

References

[1] A. Fenster and D.B. Downey. 3-D Ultrasound Imaging : A Review. *IEEE Engineering in Medicine and Biology Magazine*, 15(6):41–51, 1996.

[2] S. Krüger, G. Wagner, and D. Eifler. Ultrasonic Welding of Metal/Composite Joints. *Advanced Engineering Materials*, 6(3):157–159, 2004.

[3] A.M.K. Thomas, A.K. Banerjee, and U. Busch. *Classic Papers in Modern Diagnostic Radiology*. Springer, Berlin, Germany, 2005, pp. 162-170.

[4] F.A. Firestone. The Supersonic Reflectoscope, an Instrument for Inspecting the Interior of Solid Parts by Means of Sound Waves. *The Journal of the Acoustical Society of America*, 17(3):287–299, 1946.

[5] J.D. Achenbach. Quantitative nondestructive evaluation. *International Journal of Solids and Structures*, 37:13–27, 2000.

[6] H.C. Furtado and I.L. May. High Temperature Degradation in Power Plants and Refineries. *Materials Research*, 7(1):103–110, 2004.

[7] C. Johnston, M.A. Cooper, and R.J. Martin. An Approach to Power Station Boiler and Turbine Life Management. *Insight*, 46(10):606–610, 2004.

[8] J. Melville and G. Foster. A pictorial review of failures in conventional boiler plant. *International Journal of Pressure Vessels and Piping*, 3(1):1–25, 1975.

[9] I.L. May, T.L. Silveira, and S.K.P. Cheung-Mak. Uncertainties in the evaluation of high temperature damage in power stations and petrochemical plant. *International Journal of Pressure Vessels and Piping*, 59:335–343, 1994.

[10] L. Garverick. *Corrosion in the Petrochemical Industry*. ASM International, Material Park, OH, 1994, pp. 339-341.

[11] C.J. Moss, P. Barrien, and A. Walczynski. Life management of refinery furnace tubing. *International Journal of Pressure Vessels and Piping*, 77:105–112, 2000.

[12] R. Kažys, A. Voleišis, and B. Voleišiene. High temperature ultrasonic transducers : review. *Ultrasound*, 63(2):7–17, 2008.

[13] R.E. Green. Non-contact ultrasonic techniques. *Ultrasonics*, 42(1-9):9–16, 2004.

[14] S. Dixon, C. Edwards, and S.B. Palmer. High accuracy non-contact ultrasonic thickness gauging of aluminium sheet using electromagnetic acoustic transducers. *Ultrasonics*, 39:445–453, 2001.

[15] S.E. Kruger, M. Lord, and J.P. Monchalin. Laser Ultrasonic Thickness Measurements of Very Thick Walls at High Temperatures. volume 25, pages 240–247, 2006.

[16] W.A. Grandia and C.M. Fortunko. NDE Applications of Air-Coupled Ultrasonic Transducers. In *IEEE Ultrasonics Symposium*, volume 1, pages 697–709, 1995.

[17] K.J. Kirk, A. Mcnab, A. Cochran, I. Hall, and G. Hayward. Ultrasonic Arrays for Monitoring Cracks in an Industrial Plant at High Temperatures. *IEEE Transactions on Ultrasonics, Ferroelectrics and Frequency Control*, 46(2):311–319, 1999.

[18] A. Mcnab, K.J. Kirk, and A. Cochran. Ultrasonic transducers for high temperature applications. *IEEE Proceedings - Science, Measurement and Technology*, 145(5):229–236, 1998.

[19] K.J. Kirk, C.K. Lee, S. Cochran, A. McNab, and G. Shepherd. Condition monitoring with ultrasonic arrays at elevated temperatures. *Insight*, 45(2):130–133, 2003.

[20] N. Schmarje, J.F. Saillant, K.J. Kirk, and S. Cochran. Imaging with lithium niobate/epoxy composites. *Ultrasonics*, 42:439–442, 2004.

[21] N. Schmarje, K.J. Kirk, and S. Cochran. 1-3 Connectivity Lithium Niobate Composites for High Temperature Operation. *Ultrasonics*, 47:15–22, 2007.

[22] S.P. Kelly, I. Atkinson, C. Gregory, and K.J. Kirk. On-Line Ultrasonic Inspection at Elevated Temperatures. In *IEEE Ultrasonics Symposium Proceedings*, pages 904–908. IEEE, 2007.

[23] Y. Liu, L.C. Lynnworth, and M.A. Zimmerman. Buffer waveguides for flow measurement in hot fluids. *Ultrasonics*, 36:305–315, 1998.

[24] Y. Ono, C.K. Jen, and M. Kobayashi. High temperature integrated ultrasonic shear and longitudinal wave probes. *Review of Scientific Instruments*, 78(2):024903–1–024901–5, 2007.

[25] M. Kobayashi, C.K. Jen, J.F. Bussiere, and K.T. Wu. High-temperature integrated and flexible ultrasonic transducers for nondestructive testing. *NDT & E International*, 42(2):157–161, 2009.

[26] F.B. Cegla. Energy concentration at the center of large aspect ratio rectangular waveguides at high frequencies. *The Journal of the Acoustical Society of America*, 123(6):4218–4226, 2008.

[27] F.B. Cegla and J.O. Davies. Ultrasonic Crack Monitoring At High Temperatures Using SH Waves (¿500C). volume 29, pages 980–987, 2010.

[28] K. Balasubramaniam, V.V. Shah, R.D. Costley, G. Boudreaux, and J.P. Singh. High temperature ultrasonic sensor for the simultaneous measurement of viscosity and temperature of melts. *Review of Scientific Instruments*, 70(12):4618–4623, 1999.

[29] F.B. Cegla. *Ultrasonic Waveguide Sensors For Fluid Characterisation And Remote Sensing*. PhD thesis, Imperial College London, 2006.

[30] F.B. Cegla, P. Cawley, J. Allin, and J.O. Davies. High-Temperature (> 500°C) Wall Thickness Monitoring Using Dry-Coupled Ultrasonic Waveguide Transducers. *IEEE Transactions on Ultrasonics, Ferroelectrics and Frequency Control*, 58(1):156–167, 2011.

[31] A.J.C. Jarvis and F.B. Cegla. Application of the distributed point source method to rough surface scattering and ultrasonic wall thickness measurement. *Journal of the Acoustical Society of America*, 132(3):1325–1335, 2012.

[32] A.J.C. Jarvis and F.B. Cegla. Scattering of SH Waves by Sinusoidal and Rough Surfaces in 3D: Comparison to the Scalar Wave Approximation. Submitted to. *NDT & E International*, 2013.

[33] J.A. Hudson. *The Excitation and Propagation of Elastic Waves*. Cambridge University Press, Cambridge, 1980.

[34] J.L. Rose. *Ultrasonic Waves in Solid Media*. Cambridge University Press, Cambridge, 1999.

[35] G.S. Kino. *Acoustic Waves: Devices, Imaging and Analog Signal Processing*. Prentice-Hall, inc., New Jersey, 1987.

[36] J.L. Uretsky. Reflection of a Plane Sound Wave from a Sinusoidal Surface. *Atomic Energy*, 290(1930):1293–1294, 1963.

[37] L. Fortuin. Survey of Literature on Reflection and Scattering of Sound Waves at the Sea Surface. *The Journal of the Acoustical Society of America*, 47(5B):1209–1228, 1970.

[38] J.A. Ogilvy. Wave scattering from rough surfaces. *Reports on Progress in Physics*, 50:1553–1608, 1987.

[39] T.M. Elfouhaily and C. Guérin. A critical survey of approximate scattering wave theories from random rough surfaces. *Waves in Random Media*, 14(4):R1–R40, 2004.

[40] K.F. Warnick and W.C. Chew. Numerical simulation methods for rough surface scattering. *Waves in Random Media*, 11(1):R1–R30, 2001.

[41] M. Saillard and A. Sentenac. Rigorous solutions for electromagnetic scattering from rough surfaces. *Waves in Random Media*, 11(3):R103–R137, 2001.

[42] J.A. Ogilvy. Computer simulation of acoustic wave scattering from rough surfaces. *Physics*, 21:260–277, 1988.

[43] J.W. Strutt (Lord Rayleigh). *The Theory of Sound*. Macmillan, London, 1-504, 1878.

[44] H.W. Marsh. Exact Solution of Wave Scattering by Irregular Surfaces. *The Journal of the Acoustical Society of America*, 33(3):330–333, 1961.

[45] G.R. Barnard, C.W. Horton, M.K. Miller, and F.R. Spitznogle. Underwater-Sound Reflection from a Pressure-Release Sinusoidal Surface. *The Journal of the Acoustical Society of America*, 39(6):1162–1169, 1966.

[46] D.F. McCammon and S.T. McDaniel. Application of a new theoretical treatment to an old problem; sinusoidal pressure release boundary scattering. *The Journal of the Acoustical Society of America*, 78(1):149–156, 1985.

[47] E.I. Thorsos. The validity of the Kirchhoff approximation for rough surface scattering using a Gaussian roughness spectrum. *The Journal of the Acoustical Society of America*, 83(1):78–92, 1988.

[48] J. Zhang, B.W. Drinkwater, and P.D. Wilcox. Longitudinal wave scattering from rough crack-like defects. *IEEE Transactions on Ultrasonics, Ferroelectrics and Frequency Control*, 58(10):2171–80, 2011.

[49] A. Velichko and P.D. Wilcox. A generalized approach for efficient finite element modeling of elastodynamic scattering in two and three dimensions. *The Journal of the Acoustical Society of America*, 128(3):1004–1014, 2010.

[50] J.A. DeSanto. Exact boundary integral equations for scattering of scalar waves from infinite rough interfaces. *Wave Motion*, 47(3):139–145, 2010.

[51] D. Placko and K. Kundu. *DPSM for Modeling Engineering Problems*. John Wiley and Sons, Inc., New Jersey, 1-372, 2007.

[52] J.A. Ogilvy and J.R. Foster. Rough surfaces: gaussian or exponential statistics? *Journal of Physics D: Applied Physics*, 22(9):1243–1251, 1989.

[53] J.A. Ogilvy. *Theory of Wave Scattering From Random Rough Surfaces*. IOP Publishing Ltd., Bristol, UK, 1991.

[54] J.A. Ogilvy. Theoretical comparison of ultrasonic signal amplitudes from smooth and rough defects. *NDT International*, 19(6):371–385, 1986.

[55] *MATLAB Reference Manuals, Version 7.9.0.529*. The Mathworks, Inc., Natick, MA, 2009.

[56] T. Kundu, D. Placko, E. K. Rahani, T. Yanagita, and C. M. Dao. Ultrasonic Field Modeling : A Comparison Numerical Techniques. *IEEE Transactions on Ultrasonics, Ferroelectrics and Frequency Control*, 57(12):2795–2807, 2010.

[57] R. Ahmad, T. Kundu, and D. Placko. Modeling of phased array transducers. *The Journal of the Acoustical Society of America*, 117(4):1762, 2005.

[58] S. Banerjee, T. Kundu, and N. Alnuaimi. DPSM technique for ultrasonic field modelling near fluid-solid interface. *Ultrasonics*, 46(3):235–50, 2007.

[59] S. Banerjee and T. Kundu. Ultrasonic field modeling in plates immersed in fluid. *International Journal of Solids and Structures*, 44(18-19):6013–6029, 2007.

[60] S. Banerjee and T. Kundu. Semi-analytical modeling of ultrasonic fields in solids with internal anomalies immersed in a fluid. *Wave Motion*, 45(5):581–595, 2008.

[61] S. Banerjee and T. Kundu. Elastic wave field computation in multilayered nonplanar solid structures: a mesh-free semianalytical approach. *The Journal of the Acoustical Society of America*, 123(3):1371–82, 2008.

[62] A. Shelke, S. Das, and T. Kundu. Distributed Point Source Method for Modeling Scattered Ultrasonic Fields in Presence of an Elliptical Cavity. *Structural Health Monitoring*, 0(0):1–13, 2010.

[63] S. Banerjee, S. Das, T. Kundu, and D. Placko. Controlled Space Radiation concept for mesh-free semi-analytical technique to model wave fields in complex geometries. *Ultrasonics*, 49(8):615–22, 2009.

[64] S. Wooh and Y. Shi. Optimum beam steering of linear phased arrays. *Wave Motion*, 29(3):245–265, 1999.

[65] T. Yanagita, T. Kundu, and D. Placko. Ultrasonic field modeling by distributed point source method for different transducer boundary conditions. *The Journal of the Acoustical Society of America*, 126(5):2331–9, 2009.

[66] J. Cheng, W. Lin, and Y. Qin. Extension of the distributed point source method for ultrasonic field modeling. *Ultrasonics*, 51(5):571–580, 2010.

[67] E.K. Rahani and T. Kundu. Modeling of Transient Ultrasonic Wave Propagation Using the Distributed Point Source Method. *IEEE Transactions on Ultrasonics, Ferroelectrics and Frequency Control*, 58(10):2213–2221, 2011.

[68] L.W. Schmerr. *Fundamentals of Ultrasonic Nondestructive Evaluation.* Plenum Press, New York, 1998.

[69] R.J. Wombell and J.A. DeSanto. Reconstruction of rough-surface profiles with the Kirchhoff approximation. *Journal of the Optical Society of America A*, 8(12):1892–1897, 1991.

[70] D.R. Melton and C.W. Horton. Importance of the Fresnel Correction in Scattering from a Rough Surface . I . Phase and Amplitude Fluctuations. *Journal of the Acoustical Society of America*, 47(1B):290–298, 1970.

[71] N.C. Bruce and J.C. Dainty. Multiple Scattering from Random Rough Surfaces Using the Kirchhoff Approximation. *Journal of Modern Optics*, 38(3):579–590, 1991.

[72] P. Beckmann. Shadowing of Random Rough Surfaces. *IEEE Transactions on Antennas and Propagation*, 13(3):384–388, 1965.

[73] R.J. Wagner. Shadowing of Randomly Rough Surfaces. *The Journal of the Acoustical Society of America*, 41(1):138–147, 1967.

[74] M.V. Berry. On deducing the form of surfaces from their diffracted echoes. *Physics*, 5:272–291, 1972.

[75] *ABAQUS Reference Manuals, Version 6.9.* ABAQUS Inc., Providence, RI, 2010.

[76] E. K. Rahani and T. Kundu. Gaussian-DPSM (G-DPSM) and Element Source Method (ESM) modifications to DPSM for ultrasonic field modeling. *Ultrasonics*, 51(5):625–631, 2011.

[77] A.J. Croxford, P.D. Wilcox, G. Konstantinidis, and B.W. Drinkwater. Strategies for Overcoming the Effect of Temperature on Guided Wave Structural

Health Monitoring. In *Proceedings of the SPIE*, volume 6532, page 65321T, 2007.

[78] C. Canali, G. De Cicco, B. Morten, M. Prudenziati, and A. Taroni. A Temperature Compensated Ultrasonic Sensor Operating in Air for Distance and Proximity Measurements. *IEEE Transactions on Industrial Electronics*, IE-29(4):336–341, 1982.

[79] S.W. Smith. *The Scientist and Engineer's Guide to Digital Signal Processing*. California Technical Publishing, San Diego, CA, 1997.

[80] D. Liu and R.C. Waag. Correction of ultrasonic wavefront distortion using backpropagation and a reference waveform method for time-shift compensation. *The Journal of the Acoustical Society of America*, 96(2):649–660, 1994.

[81] J.S. Bendat and A.G. Piersol. *Random Data: Analysis and Measurement Procedures*. Wiley, 2010.

[82] *DISPERSE User Manual, Version 2.0.16B*. Imperial College of Science, Technology and Medicine, London, London, UK, 2003.

[83] Y. Saad and M.H. Schultz. GMRES: A Generalized Minimal Residual Algorithm for Solving Nonsymmetric Linear Systems. *SIAM Journal on Scientific and Statistical Computing*, 7(3):856–869, 1986.

[84] M. Saillard and D. Maystre. Scattering from Random Rough Surface: A Beam Simulation Method. *Journal of Optics*, 19(4):173–176, 1988.

[85] C.J.R. Sheppard and T.J. Connolly. Imaging of Random Surfaces. *Journal of Modern Optics*, 42(4):861–881, 1995.

[86] J. Kvarekval. Morphology of Localised Corrosion Attacks in Sour Environments. In *Corrosion*, number 07659, pages 1–10, 2007.

[87] C. Shargay, K. Moore, and R. Colwell. Survey of Materials in Hydroheater Units Processing High TAN Feeds. In *Corrosion*, number 07573, pages 1–11, 2007.

[88] X. Wu, H. Jing, Y. Zheng, Z. Yao, and W. Ke. Erosion-corrosion of various oil-refining materials in naphthenic acid. *Wear*, 256(1-2):133–144, 2004.

[89] E. Slavcheva, B. Shone, and A. Turnbull. Factors Contolling Naphthenic Acid Corrosion. In *Corrosion*, number 579, pages 1–19, 1998.

[90] D.R. Qu, Y.G. Zheng, H.M. Jing, Z.M. Yao, and W. Ke. High temperature naphthenic acid corrosion and sulphidic corrosion of Q235 and 5Cr1/2Mo steels in synthetic refining media. *Corrosion Science*, 48(8):1960–1985, 2006.

[91] M.J. Zetlmeisl. Naphthenic Acid Corrosion and its Control. In *Corrosion*, number 218, pages 1–8, 1996.

[92] R.D. Kane and M.S. Cayard. A Comprehensive Study on Naphthenic Acid Corrosion. In *Corrosion*, number 02555, pages 1–16, 2002.

[93] W. Schwanghart. Ordinary kriging. *http://www.mathworks.com/matlabcentral/fileexchange/29025-ordinary-kriging*, October 2010.

[94] S. Nešić. Key issues related to modelling of internal corrosion of oil and gas pipelines - A review. *Corrosion Science*, 49(12):4308–4338, 2007.

[95] R. Nyborg. Field Data Collection, Evaluation and use for Corrosivity Prediction and Validation of Models. In *Corrosion*, number 06118, pages 1–15, 2006.

[96] S. Papavinasam, A. Doiron, and R.W. Revie. A Model to Predict Internal Pitting Corrosion of Oil and Gas Pipelines. In *Corrosion*, number 07658, pages 1–18, 2007.

[97] T. Johnsen and R. Hilfer. Statistical prediction of corrosion front penetration. *Physical Review E*, 55(5):5433–5442, 1997.

[98] A. Valor, F. Caleyo, L. Alfonso, D. Rivas, and J.M. Hallen. Stochastic modeling of pitting corrosion: A new model for initiation and growth of multiple corrosion pits. *Corrosion Science*, 49(2):559–579, 2007.

[99] J. Amri, E. Gulbrandsen, and R.P. Nogueira. Numerical simulation of a single corrosion pit in CO2 and acetic acid environments. *Corrosion Science*, 52(5):1728–1737, 2010.

[100] P. Meakin, T. Jøssang, and J. Feder. Simple passivation and depassivation model for pitting corrosion. *Physical Review E*, 48(4):2906–2916, 1993.

[101] R. Quimby. Practical limitations of TOFD on power station main steam pipework. *Insight*, 48(9):559–563, 2006.

[102] A.J.C. Jarvis and F.B. Cegla. Defect Monitoring at Elevated Temperatures (>500°C) Using an Array of Ultrasonic Waveguides. In *Review of Progress in Quantitative Nondestructive Evaluation*, volume 30, pages 1679–1686.

[103] F.B. Cegla, A.J.C. Jarvis, and J.O. Davies. High temperature ultrasonic crack monitoring using SH waves. *NDT & E International*, 44(8):669–679, 2011.

[104] J.P. Charlesworth and J.A.G. Temple. *Engineering Applications of Ultrasonic Time of Flight Diffraction*. Research Studies Press Ltd, Philadelphia, PA, 2 edition, 2001.

[105] J.A. Ogilvy and J.A.G. Temple. Diffraction of elastic-waves by cracks - application to time-of-flight inspection. *Ultrasonics*, 21(6):259–269, 1983.

[106] L. Capineri, H.G. Tattersall, M.G. Silk, and J.A.G. Temple. Time-of-flight diffraction tomography for ndt applications. *Ultrasonics*, 30(5):275–288, 1992.

[107] R.K. Chapman. Cegb report nw/ssd/rr/145/81. pages 16–17, 1981.

[108] M. Lorenz. Ultrasonic imaging for the characterization of defects in steel components, 1993. TU Delft digital repository [http://repository.tudelft.nl/oai] (Netherlands) ER.

[109] J. Zhang, B.W. Drinkwater, P.D. Wilcox, and A.J. Hunter. Defect detection using ultrasonic arrays: The multi-mode total focusing method. *NDT & E International*, 43(2):123–133, 2010.

[110] C. Holmes, B.W. Drinkwater, and P.D. Wilcox. Post-processing of the full matrix of ultrasonic transmit - receive array data for non-destructive evaluation. *NDT&E International*, 38:701–711, 2005.

[111] E. Papadakis, L.C. Lynnworth, K.A. Fowler, and E.H. Carnevale. Ultrasonic attenuation and velocity in hot specimens by the momentary contact method with pressure coupling, and some results on steel to 1200c. *The Journal of the Acoustical Society of America*, 52(3):850–857, 1972.

[112] R. Thomas, B.W. Drinkwater, and D. Liaptsis. The reflection of ultrasound from partially contacting rough surfaces. *The Journal of the Acoustical Society of America*, 117(2):638–645, 2005.

[113] T. Kim. Failure of piping by hydrogen attack. *Engineering Failure Analysis*, 9(5):571–578, 2002.

[114] G.R. Prescott and B. Shannon. Process Equipment Problems Caused by Interaction with Hydrogen-An Overview. *Process Safety Progress*, 20(1):63–72, 2001.

[115] A.S. Birring, M.L. Bartlett, and K. Kawano. Ultrasonic Detection of Hydrogen Attack in Steels. *Corrosion*, 45(3):259–263, 1989.

[116] D. Eliezer. High-temperature hydrogen attack of carbon steel. *Journal of Materials Science*, 16(11):2962–2966, 1981.

[117] A.S. Birring, M. Riethmuller, and K. Kawano. Ultrasonic Techniques for Detection of High Temperature Hydrogen Attack. *Material Evaluation*, pages 110–115, 2005.

[118] A. Gajdacsi, A.J.C. Jarvis, P.E. Huthwaite, and F.B. Cegla. Reconstruction of the Temperature Distribution in a Steel Block using an Ultrasonic Sensor Array. Submitted to. *NDT & E International*, 2013.

[119] R. Gordon and G.T. Herman. Reconstruction of pictures from their projections. *Communications of the ACM*, 14(12):759–768, 1971.

[120] G.T. Herman. Image Reconstruction From Projections. *Real-Time Imaging*, 1(1):3–18, 1995.

[121] S.J. Norton, L.R. Testardi, and H.N.G Wadley. Reconstructing Internal Temperature Distributions From Ultrasonic Time of Flight Tomography and Dimensional Resonance Measurements. *Journal Of Research Of The National Bureau Of Standards*, 89(1):65–74, 1984.

[122] P.E. Huthwaite. Quantitative imaging with mechanical waves, 2012. Imperial College London PhD Thesis [http://www3.imperial.ac.uk/nde/publications].

[123] M. Jiang and G. Wang. Development of iterative algorithms for image reconstruction. *Journal of X-Ray Science and Technology*, 10:77–86, 2002.

[124] A.K. Chatterjee, A.K. Mal, and L. Knopoff. Elastic Moduli of Two-Component Systems. *Journal of Geophysical Research*, 83(7):1785–1792, 1978.

[125] J.R. Simonson. *Engineering Heat Transfer*. Macmillan Education Ltd, London, UK, 2 edition, 1988, pp. 39-57.

[126] P.E. Huthwaite, A.A. Zwiebel, and F. Simonetti. A New Regularization Technique for Limited-View Sound-Speed Imaging. *IEEE Transactions on Ultrasonics, Ferroelectrics and Frequency Control*, 60(3):TBC–TBC, 2013.

Publication List

[P1] A.J.C Jarvis and F.B. Cegla. Defect Monitoring at Elevated Temperatures (>500°C) Using an Array of Ultrasonic Waveguide Transducers. In *Review of Progress in Quantitative Nondestructive Evaluation*, San Diego CA, USA. Volume 30, pages 1679-1686. Edited by D.O. Thompson, D.E. Chimenti. 2010

[P2] A.J.C Jarvis and F.B. Cegla. Simulation of the Variation of Ultrasonically Monitored Thickness due to the Effects of Roughness. In *Review of Progress in Quantitative Nondestructive Evaluation*, Burlington VT, USA. Volume 31, pages 713-720. Edited by D.O. Thompson, D.E. Chimenti. 2011

[P3] F.B. Cegla, A.J.C. Jarvis and J.O. Davies. High Temperature Ultrasonic Crack Monitoring Using SH Waves. In *NDT&E International*, 44(8):669-679, 2011

[P4] A.J.C Jarvis and F.B. Cegla. Monitoring Pitting Corrosion in High Temperature Environments. Submitted to *Review of Progress in Quantitative Nondestructive Evaluation*, Denver CO, USA. Volume 33, pages 1433-1440. Edited by D.O. Thompson, D.E. Chimenti. 2012

[P5] A.J.C Jarvis and F.B. Cegla. Application of the Distributed Point Source Method to Rough Surface Scattering and Ultrasonic Wall Thickness Measurement. In *Journal of the Acoustical Society of America*, 132(3):1325-1335, 2012

[P6] A.J.C. Jarvis and F.B. Cegla. Scattering of SH Waves by Sinusoidal and Rough Surfaces in 3D: Comparison to the Scalar Wave Approximation. Submitted to *IEEE Transactions on Ultrasonics, Ferroelectrics and Frequency Control*, 2013

[P7] A. Gajdacsi, A.J.C. Jarvis, P.E. Huthwaite and F.B. Cegla. Reconstruction of the Temperature Distribution in a Steel Block using an Ultrasonic Sensor Array. Submitted to *IEEE Transactions on Ultrasonics, Ferroelectrics and Frequency Control*, 2013